Analysis and Design of Wideband Phased Arrays for Ku- and Ka-band Satcom Applications

van Katwijk, Alexander J.

Citation (APA)
van Katwijk, A. J. (2024). *Analysis and Design of Wideband Phased Arrays for Ku- and Ka-band Satcom Applications*. [Dissertation (TU Delft), Delft University of Technology]. https://doi.org/10.4233/uuid:b6c5adfb-9f02-48c1-9aed-fa55aa8d05e8

Important note
To cite this publication, please use the final published version (if applicable).
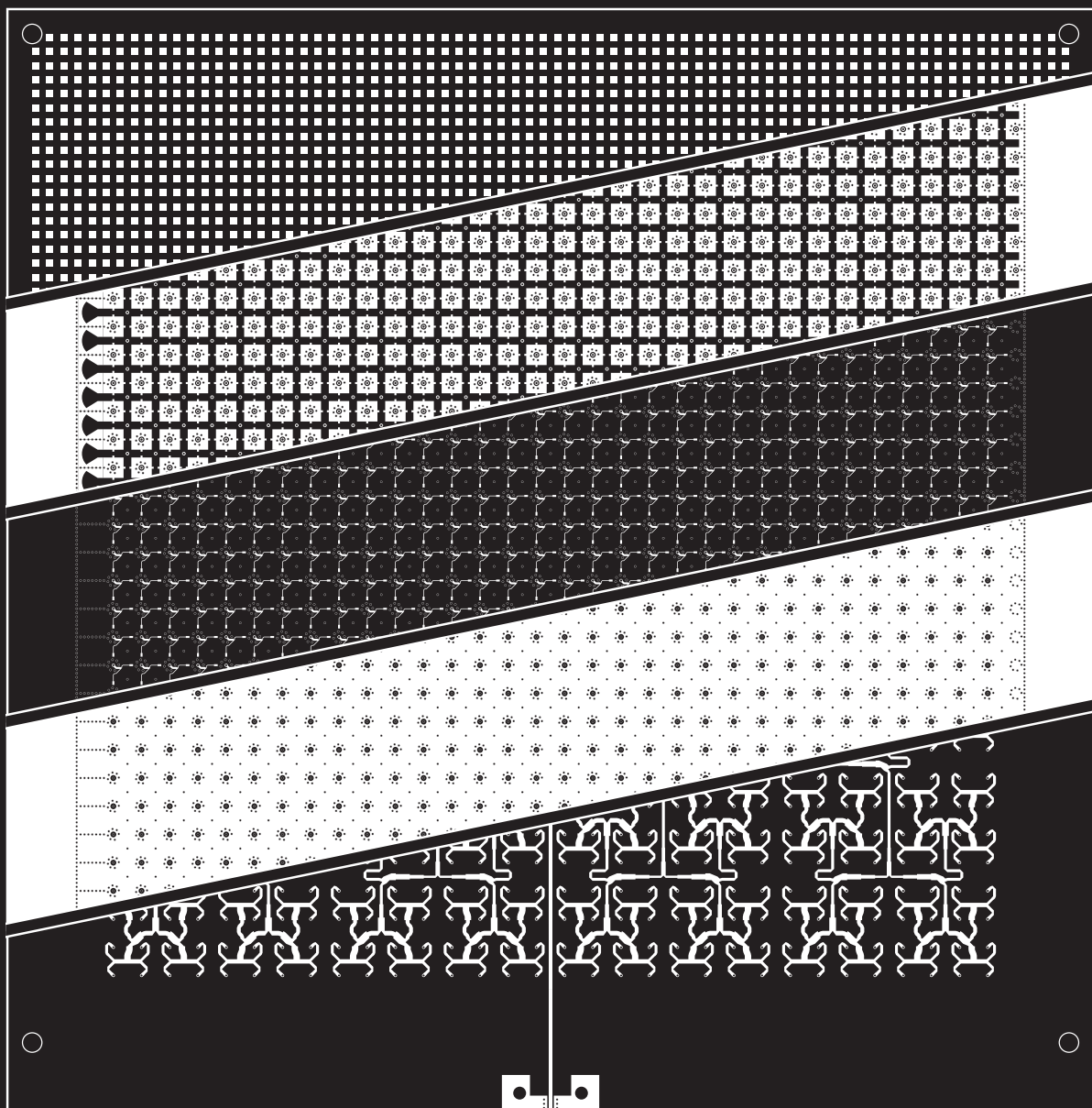Please check the document version above.

Analysis and Design of Wideband Phased Arrays for Ku- and Ka-band Satcom Applications

Alexander J. van Katwijk

Analysis and Design of Wideband Phased Arrays for Ku- and Ka-band Satcom Applications

Analysis and Design of Wideband Phased Arrays for Ku- and Ka-band Satcom Applications

DISSERTATION

for the purpose of obtaining the degree of doctor
at Delft University of Technology
by the authority of the Rector Magnificus, Prof. dr. ir. T. H. J. J. van der Hagen,
Chair of the Board for Doctorates,
to be defended publicly on
Wednesday October 30th, 2024, at 17:30

by

Alexander Jacob VAN KATWIJK

Master of Science in Electrical Engineering,
Delft University of Technology, the Netherlands,
born in Takoma Park, United States of America.

This dissertation has been approved by the promotors.

Composition of the doctoral committee:

Rector Magnificus,	Chairman
Prof. dr. ing. A. Neto	Delft University of Technology, promotor
Dr. D. Cavallo	Delft University of Technology, promotor

Independent members:

Prof. dr. N. Llombart Juan	Delft University of Technology
Prof. dr. C. Craeye	Université Catholique de Louvain
Prof. dr. ir. F. E. van Vliet	University of Twente
Dr. E. Martini	Università degli Studi di Siena
Prof. dr. ir. B. Smolders	Eindhoven University of Technology

Reserve member:

Prof. dr. ir. J. J. A. Baselmans	Delft University of Technology

TUDelft   **·e**esa

PDF version

An electronic version of this dissertation is available at
https://repository.tudelft.nl/

Contents

Chapter 1

Introduction

1.1 Wideband Wide-Scanning Antenna Arrays

Wideband wide-scanning antenna arrays have been gaining popularity in the past decade due to their applicability in multiple fields and applications. They have already been used in military applications for multiple decades [1] due to their ability to combine multiple functions such as electronic warfare [2, 3], target tracking [4], and situational awareness [5] in a single aperture, drastically reducing the number of antenna systems necessary on the platform [6]. More recently, they have started to be used in radio astronomy [7, 8] and in civilian applications such as security imaging [9], wireless communication [10, 11], and satellite communication (Satcom) [12]. Wideband arrays are desired for communications because their large bandwidths can enable multiple services by covering several bands [13]. For radio astronomy, the wide bandwidth enables a single receiver to cover multiple astronomical phenomena, which ensures that certain red-shifted emissions can be accurately identified [14].

The need for ultra-wideband capability is often paired to the ability to scan over a large conical region. Wide-scanning arrays enable tracking of multiple targets simultaneously, which can be important for radar systems. Here, the ability to steer a beam instantaneously enables the quick target switching required to identify and track multiple targets [3, 4]. A wide-scanning array is also desired in astronomy, where a received signal can be tracked in a larger field of view or a sector of the sky can be surveyed faster [15]. Communication systems can utilize arrays with wide-scanning capabilities for multibeam connections [16], to track users [17] or, vice versa, track the transmitters from the user side [18]. Wide-scanning Satcom arrays can guarantee agile connection to different satellites, also on mobile platforms such as aircraft.

For Satcom on-the-move systems on aircraft, wideband wide-scanning antenna arrays are especially interesting. Mechanical systems that are able to point an antenna in a desired direction can be bulky, heavy and expensive to maintain. For satellite tracking, electronic beam steering antennas offer advantages over mechanical systems in terms of reliability and beam agility. A low-profile phased array can be utilized to rapidly track a satellite while the platform is moving. Electronic steering can also

1

enable multiple-beam generation, wide-scanning, radiation pattern shaping, reconfig-urability, or power sharing among multiple beams. Terminal antenna arrays have been demonstrated for the Ku- [19–25] and Ka-band [26–28], which are the Satcom bands of interest in this thesis.

Despite these advantages, planar phased array antennas typically exhibit limita-tions when steering a pencil beam in a large field of view. These limitations are due to uncontrolled waves that are excited in the aperture such as surface waves or waves generated by the edges of the array, and are noticed as deterioration of the antenna active reflection coefficient. Another problem of terminal antennas, especially on mo-bile platforms, is the limited space allocated to cover multiple required bands. In this regard, it is beneficial to use a wideband array covering simultaneously multiple bands [12, 29], to provide significant reduction of the overall cost and volume of the system operating in the Ku- and/or Ka-bands.

Covering multiple bands in a single antenna poses challenges not only in terms of bandwidth, but also in polarization. Due to the use of different polarizations in various bands – e.g. linear in the Ku- and circular in the Ka-band – polarization agility is desired in terminal antennas that cover multiple bands. This can be realized using polarization-reconfigurable surfaces [30, 31], but can also be achieved through the use of dual-polarized antenna apertures. Dual-polarized antenna apertures can offer challenges when pushed to higher frequencies due to the limited space available to connect the two radiators in each unit cell.

1.2 State-of-the-Art Wideband Arrays and Selected Antenna Concept

Wideband arrays have been demonstrated using various technologies, such as tapered slot antennas [32–40], long-slot arrays [41, 42], and tightly-coupled or connected dipole arrays [10, 43–47]. These designs have been shown to cover multi-octave bandwidths and large scan ranges. However, typically such bandwidths come at the cost of reduced efficiency or higher cross-polarization (X-pol). Examples of arrays in literature can also be compared in terms of manufacturing complexity. Most of the designs are realized using vertical printed circuit boards (PCBs) that implement the antennas and their feeding structure, which can result in a costly and complex assembly process. Additionally, many of the proposed designs require vertical radiators of significant length, which increases their volume and mass. These tall radiating structures can also give rise to higher X-pol [33, 48–52], which can degrade their usability for various applications. For this reason, arrays implemented in planar technology [53, 54] are favorable and will be used in this work.

One of the proposed concepts to realize a wideband wide-scanning terminal an-tenna is the connected slot array [55–59], which will be used in this thesis because it offers the required bandwidths and scan ranges. Moreover, a major advantage of connected slot arrays is their planar structure, which gives them a low profile and vol-ume. Their planar structure also enables manufacturing of entire arrays on a single

1
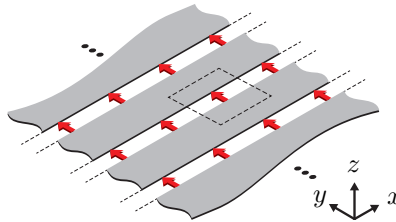
Figure 1.1: Connected slot array in free space with three slots illustrated, each including four feeding points. The slots extend to infinity, and are infinitely repeated in the other dimension. The unit cell is highlighted by the dashed square.

multi-layer PCB using traditional PCB manufacturing techniques, enabling low-cost and low-complexity manufacturing. Connected slots have also been used in conformal designs [60], which allows them to be integrated in various structures such as the aircraft fuselage.

Another advantage of connected slot arrays is that they can be accurately described with analytical expressions [45, 61, 62], which allow efficient evaluation of relevant parameters such as active input impedance and radiation patterns of the array. This avoids the need for complex simulations in commercial tools in the early design stage, and enables rapid iteration to form an optimized design. While the analysis method only supports single-polarized slots, the extension to a dual-polarized slot plane does not significantly alter the antenna behavior, so the single polarized design provides an excellent stating point. The method uses the stratified media Green's function, and can therefore include the effect of various stratifications around the array.

1.3 Connected Slot Array with Artificial Dielectrics

A connected slot array utilizes a set of long slots which are periodically fed to realize the antenna aperture. An illustration of such an aperture is shown in Fig. 1.1, where the unit cell is highlighted. The periodic feeding points on the long, continuous slots generate a flat non-resonant current profile, which enables a theoretically infinite bandwidth [63]. The aperture of these arrays can be designed with the inclusion of capacitive or parasitic components [55, 64], or a superstrate can be included that matches it to a desired impedance [54, 58]. The stratification around such antennas and the finite aperture size imposes the bandwidth limitation.

To provide uni-directional radiation and shield the antenna from its feeding electronics, a ground plane is usually included, but its resonance imposes a bandwidth limitation. To mitigate this limitation, a dense superstrate is desired to increase the front-to-back ratio and reduce the impact of the ground plane on the array impedance. One such superstrate is the wide angle impedance matching (WAIM) [65] layer, which uses an air gap followed by a dense dielectric to provide a superstrate whose impedance depends on the scan angle and can therefore match an array for larger angles.

TM Incidence   TE Incidence
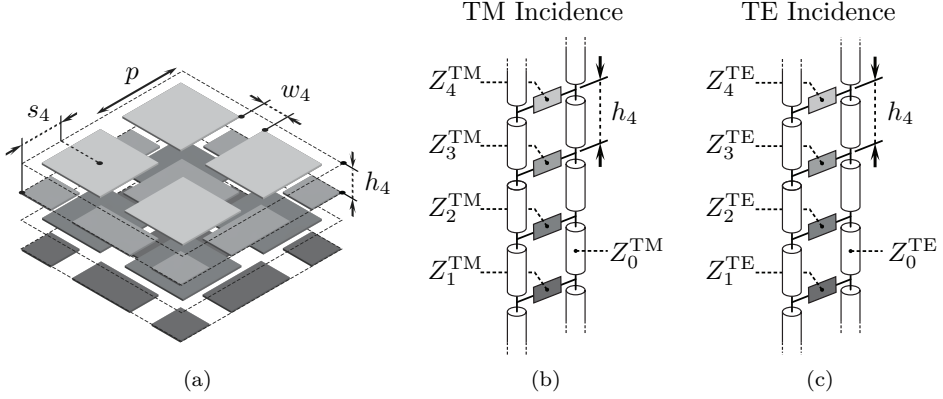
Figure 1.2: (a) Four-layer ADL stack with annotated geometrical parameters of the topmost layer. (b) Equivalent transmission line models for TE and (c) TM incidence.

However, dense dielectrics can cause issues in wideband wide-scanning arrays due to their ability to support surface waves [66]. These surface waves can reduce the bandwidth of the array or cause scan blindness. To avoid surface waves, a superstrate is desired that can provide the effect of the WAIM, but also prevents surface waves from propagating for large scan angles. One method to realize such a superstrate is by utilizing artificial dielectrics [67, 68] or, more specifically, artificial dielectric layers (ADLs) [54, 58, 59, 69], which consist of several layers of sub-wavelength flat metal patches, arranged in a periodic rectangular lattice. Such ADLs do not support the transverse magnetic (TM) surface wave [70], even for large incidence angles, and therefore enable large scan volumes. ADLs can be designed to implement a wideband impedance transformer.

An example ADL is shown in Fig. 1.2(a), where four layers of ADL are illustrated. The four geometrical parameters used to describe a layer of ADL are highlighted and represent the following;

- p is the periodicity of the lattice,

- w is the gap width between two adjacent patches,

- h is the vertical distance with respect to the previous layer,

- s is the shift in x and y with respect to the previous layer.

If the patches or their lattice are not square, the geometrical parameters are represented using separate values along x or y, so eight parameters are necessary. The behavior of the ADL can vary greatly depending on each of these parameters, so each parameter must be chosen carefully. For the four-layer ADL shown in the figure, 16 parameters are used to fully define the stack. Optimizing the value of each parameter with a full-wave solver becomes infeasible due to the huge number of evaluations required.

1

For this reason, a closed-form method to analyze artificial dielectrics was developed. The development of the method was done in various stages, where the number of degrees of freedom was increased with every stage. First, the analysis assumed an aligned set of identical layers [70, 71], which was extended to allow for non-aligned layers [72]. The method was then generalized to allow non-identical layers [73] – where the geometrical parameters vary per layer – and non-square patches [74] – where the geometrical parameters vary between x and y. These methods are able to fully characterize the behavior of an arbitrary stack of ADLs using only the four (or eight) geometrical parameters per layer shown in Fig. 1.2(a). When the patches are square, the layers are modeled using two decoupled transmission lines for TM and TE incidence, which are shown in Fig. 1.2(b) and Fig. 1.2(c), respectively. In these transmission lines, $Z_0^{\mathrm{TM/TE}}$ is the free-space impedance for TM or TE incidence, and the values of the shunt impedances are given by

$$Z_n^{\mathrm{TM}} = \frac{-j}{B_n} \tag{1.1}$$

$$Z_n^{\mathrm{TE}} = \frac{-j}{B_n \left(1 - \frac{\sin^2\theta}{2}\right)} \, , \tag{1.2}$$

where the susceptance B of each layer is known in closed form as a function of on the four parameters [73].

As more degrees of freedom are added to the ADL stack, more complex geometries can be modeled, and fewer layers are required to obtain a certain response. For example, an ADL with non-identical layers can be used to form a superstrate with improved bandwidth for the same number of layers or to reduce the number of layers required to cover a desired band. The equivalent transmission line model of the ADLs can be used to find the stratified media Green's function to use in conjunction with the connected slot array method. The combination of these two methods enable analysis of the entire antenna in milliseconds. This enables the use of iterative techniques to rapidly design an antenna with a certain desired bandwidth and even offers the possibility of using genetic algorithms or other optimization techniques to design an arbitrary frequency response.

1.4 Need for Accurate Modeling Techniques

While a unit cell can be accurately described using analytical expressions, the periodic unit cell approximation does not properly represent the performance in finite wideband arrays. Edge effects can significantly alter the behavior of individual elements in the array, potentially causing them to become mismatched. For this reason, various efforts have gone into the modeling of the behavior of semi-finite [75, 76] and finite arrays [7, 77–81]. These edge effects are particularly important in connected arrays because the inter element connection allows guided waves generated at the edges of the array to travel along the array and influence the impedance behavior of large portions of the array [82–84]. For this reason, various numerical methods were

1

developed to model the behavior of semi-infinite connected arrays [83, 85]. However, these methods take into account only the finiteness along either the E- or H-plane, and assume an infinite array in the other dimension. As such, they cannot fully take into account the effects from the corners of the array. Therefore efficient methods to analyze 2D-finite connected arrays are necessary.

Moreover, the analysis shown in the past for artificial dielectric layers only considered horizontal patches. The behavior of ADLs can be augmented to provide advantageous behavior through the inclusion of different structures. In this dissertation, the presence of vertical pins within the ADL is investigated and shown to provide improved X-pol performance. As such, to enable designs of antennas using this structure, methods to analyze these more general artificial dielectric structures are of interest.

1.5 Novel Contributions in the Thesis

In this work, different research topics related to connected arrays for Satcom applications are investigated, involving both design and modeling aspects. Novel design concepts are introduced to enhance the array performance and reduce its complexity. Regarding the modeling efforts, methods to analyze the finite array performance and the scattering from ADLs are developed. More specifically, the main contributions of this thesis can be summarized as follows:

- A dual-polarized phased array is designed for use in Satcom applications. The array is designed to cover both the Ku- and Ka-transmit bands, which span 13.75–14.5 GHz and 28–31 GHz, respectively. The design targets a scan volume of $\pm 60°$ for all azimuths. The design is based on the connected array with ADL concept to achieve this bandwidth. It differs from previous works in that it uses non-identical layers in the ADL to achieve a wide bandwidth with a significantly reduced number of layers. Additionally, it is designed to operate at higher frequency than previously demonstrated, which presents challenges due to limitations imposed by the PCB manufacturing technology. Experimental validation is also presented based on a 32×32 dual-polarized array. Wideband corporate feeding networks are developed to validate the array for different scanning conditions.

- An efficient method is developed for the analysis of large finite connected slot arrays, by accurately taking into account the finiteness along both dimensions. A spectral method of moments approach is proposed using only a single basis function per element, to reduce the computational complexity. Moreover, some mutual impedance integrals are solved in closed-form to efficiently analyze large arrays. It utilizes the stratified media Green's function to accurately take into account the stratification in which the array is embedded, such as an ADL stratification and a backing reflector.

1

- The stability of X-pol reduction using signal processing based cancellation is investigated. The cancellation is achieved by combining two orthogonal radiators, of which the radiated field is known in detail, to cancel an undesired polarization. Here, the two orthogonal slots in each unit cell of the connected array are combined with the proper excitation weights to achieve an arbitrary polarization at a certain frequency and scan angle. The X-pol and axial ratio are used to determine the resulting polarization purity in slant linear and circular polarization, respectively. The stability of the cancellation procedure with respect to frequency and scan angle is studied, as well as the effect of this technique on the matching efficiency of a connected slot array.

- A study on the effect of various superstrates on the X-pol of an ideal linearly polarized source is performed. The study is done using a magnetic Wheeler current sheet [86] and pinpoints the main contributor to the increased X-pol that is found in antennas that utilize superstrates. It is found that the increased X-pol is linked to the anisotropy of the superstrates.

- A pin-patch structure is proposed to control the anisotropy of a superstrate utilizing ADLs and can effectively reduce the X-pol. The structure consists of two layers of metal patches in a periodic lattice connected by a vertical pin. The new structure is compatible with existing designs. Measurements of two ADL superstrates – one with pins and one without – are used to demonstrate the effectiveness of the X-pol reduction.

- An efficient method is presented for the analysis of a pin-patch structure consisting of two square patches connected by a vertical pin, placed in a 2D-periodic rectangular lattice. The method uses a method of moments approach with nine independent basis functions to model the entire structure and can accurately estimate the scattering of a plane wave incident on the structure. Basis functions with known Fourier or Hankel transforms are used to close all integrals, resulting in a closed-form expression for each of the mutual impedance matrix elements. An auxiliary circular pin-patch structure is used in combination with a cylindrical method of moments to accurately model the vertical current on the pin and the cylindrical spreading of the current on the patches.

1.6 Outline of the Thesis

A brief description of the chapters in this dissertation is given in the following. The reader may notice the order of presentation is different from above, which was done to facilitate the reading process.

- **Chapter 2** discusses the analysis method for large 2D-finite connected slot arrays [Fig. 1.3(a)]. A spectral domain method of moments formulation is applied, where only a single basis function is considered per element in the array, plus
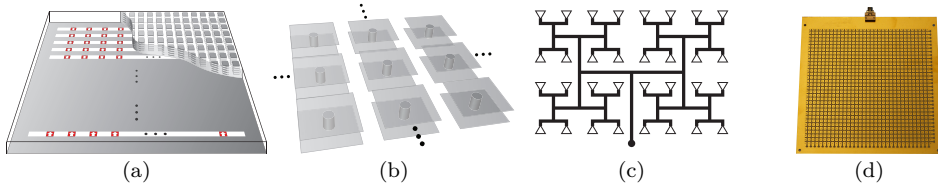
Figure 1.3: Representations of various major components described in this thesis. (a) Illustration of a large finite connected slot array embedded in an ADL stratification. (b) Illustration of the pin-patch structure that is used to reduce the X-pol of ADL superstrates. (c) Illustration of a corporate feeding network that feeds many elements from a single point. (d) Photo of the slot plane of a prototype connected slot array antenna demonstrator.

two at the ends of each slot. The Fourier transforms of the basis functions are known in closed form, and asymptotic techniques are used to reduce computation time of one of the integrals. The input impedance of a 5×5 finite array with ADLs is compared to the results found by a commercial solver, and the input impedance and radiation patterns of a large 32×32 finite array are studied.

- **Chapter 3** discusses the technique to reduce the intrinsic X-pol of the ADL superstrate. It contains a detailed analysis of the behavior of the X-pol of various superstrates over a magnetic Wheeler current sheet. The key reason for the increased X-pol of the ADLs is highlighted, and a novel structure that connects two layers of ADL together with a pin is introduced [Fig. 1.3(b)]. An ADL design using the pins to reduce X-pol is presented and verified using measurements.

- **Chapter 4** discusses the analysis method for the pin-patch structure introduced in Chapter 3. The structure is analyzed in a spectral domain method of moments where nine spectral domain basis functions are used, of which the Fourier transforms are presented in closed form. All integrals required for the evaluation of elements in the mutual impedance matrix are closed, and the values are calculated using Floquet sums only. An auxiliary circular pin-patch structure is used with a method of moments in cylindrical coordinates to evaluate the vertical current on the pin, which is compared to those found by a full-wave simulation. To demonstrate the validity of the method, scattering parameters of pin-patch structures of various sizes are compared to those obtained by a full-wave solver.

- **Chapter 5** discusses the design of a wideband, wide-scan connected slot array covering the Ku- and Ka-Satcom bands. The methods used to design various parts of the array are discussed in detail, starting from the design of the ADLs, and continuing into the design of the radiating element, its feeding structure, and finally the corporate feeding networks [Fig. 1.3(c)]. The results of a failed manufacturing attempt are briefly discussed and suggestions for changes are given. A study into the possibilities of canceling X-pol is detailed, and complex excitation weights are derived to achieve radiation along a certain polarization.

Various results are shown for the quality of the resulting polarization versus frequency or scanning angle.

- **Chapter 6** discusses the design of an antenna [Fig. 1.3(d)] with reduced manufacturing complexity that uses the suggestions from Chapter 5 to improve the chances of a successful manufacturing run. The stratification is greatly simplified, and the unit cell is designed to have a single input and to radiate circular polarization in the Ka-band. A new set of corporate feeding networks is briefly shown, and experimental results of the prototype are shown. The VSWR, radiation patterns, axial ratio, directivity and gain of a set of prototype boards are detailed.

Chapter 2

Efficient Semi-Analytical Method for the Analysis of Large Finite Connected Slot Arrays

An efficient method for the analysis of finite connected slot arrays in the presence of stratified media is presented. The formulation is based on a spectral method of moments, where only one basis function is considered for each array element and one for each slot edge. An expression for the mutual impedance is derived in terms of a double spectral integral. Asymptotic extraction techniques are employed to largely reduce the computation time of one of the spectral integrals. For the other integral, when a guided wave contribution dominates the mutual coupling between two array elements, the result can be approximated as the residue of the spectral polar singularity, providing a closed-form solution of the coupling for elements at electrically large distances. The complete method enables simulations of entire finite arrays with hundreds or even thousands of elements in minutes. The same structure would require impractical computation time when analyzed with a general purpose commercial software. The method allows estimating the performance of finite connected arrays. This is particularly relevant because wideband connected arrays are known to exhibit higher edge effects compared to narrowband arrays, due to the high inter-element mutual coupling.

2
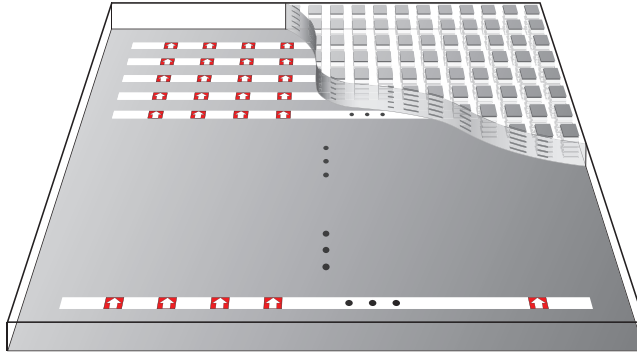
Figure 2.1: Finite connected slot array with artificial dielectric superstrate.

2.1 Introduction

The active input impedance of the elements can be written in closed form as a function of the geometrical parameters, as described in [45, 61, 63]. The analytical model enables computation of the array unit cell main performance parameters within very little computation time, allowing the design of an array using a fast optimization procedure. However, the periodic unit cell approximation does not always represent the performance in finite wideband arrays. Edge effects can be significant, and the active impedance of the individual elements can be considerably different from the infinite array approximation. This is especially true in connected arrays because the inter-element connection allows guided waves generated at the edges to propagate along the array surface, affecting the impedance behavior of large portions of the array [82–84].

For this reason, numerical methods for the analysis of finite arrays [82, 87–91] are needed to evaluate the variation of the output impedance seen by the transmit/receive modules connected to the antenna elements. Numerical methods specific for connected arrays are introduced in [83, 85], but they are limited to finite-by-infinite arrays, which are assumed to be finite only in the H-plane and still periodic in the E-plane.

An attempt to include the finiteness in the E-plane was reported in [57]. However, this method used a discrete space Fourier transform to account for the finiteness of the slots, which assumed the spectral current in each slot to be the same except for a phase shift. This approximation was accurate enough in [57], because a high permittivity lens was considered above the array, and one could safely assume that waves launched from the center of the array would not reach the edges. In more general stratifications, the current spectra cannot be assumed equal on the slots.

In this chapter, a semi-analytical method for the analysis of finite-by-finite connected slot arrays is introduced, which does not rely on the approximation of equal current spectra on the slots. The method can be used for generic stratified media, so it can for example be combined with the known spectral Green's function of artificial dielectrics [72, 73] to simulate an entire array structure such as the one depicted in Fig. 2.1. Different acceleration techniques are implemented to speed up the computa-
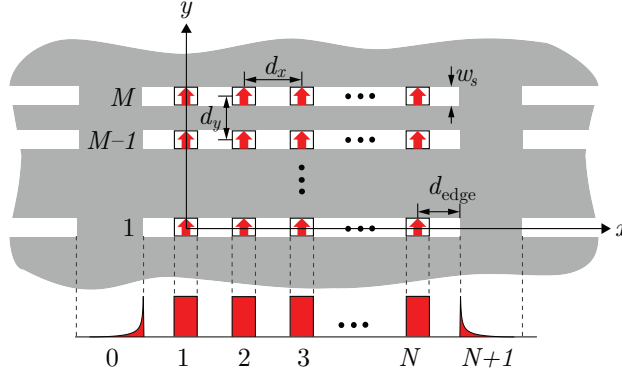
Figure 2.2: Finite connected slot array with geometrical parameters and x-dependent basis functions on the feeding gaps and slot terminations, on each slot axis.

tion of the coupling integrals. As a consequence, large arrays with hundreds or even thousands of elements can be analyzed with moderate computational resources. The complete method enables simulations of entire finite arrays using orders of magnitude less computational resources than a commercial software. The finite array current distribution and all the relevant parameters, such as active impedances and radiation patterns, can be estimated using this method for generic complex excitation of the array elements.

2.2 Analysis Method

We consider an array of connected slots, as depicted in Fig. 2.2. The array consists of M parallel x-oriented slots, with indexes $m \in \{1, ..., M\}$ and centered at periodic locations $y = m\,d_y$. Each slot is fed by delta-gap generators at N locations spaced by d_x and is interrupted by metal terminations. The method assumes that the metal terminations are of a finite length such that the spectral solution for infinite slots can be used as in [85]. The array plane can be embedded within a general stratified medium along z that can, for instance, include dielectric substrates or superstrates, a backing reflector, or ADLs.

2.2.1 Space Domain Integral Equation

Following the procedure described in [57], an integral equation can be set up by imposing the continuity of the x-component of the magnetic field across the slots:

$$\iint m_x(x', y')g_{xx}(x - x', md_y - y')dx'dy' = -j_{y,\text{gaps}}(x, md_y) \tag{2.1}$$
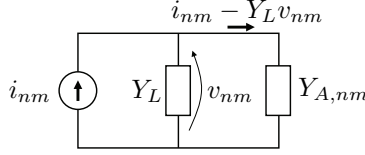
Figure 2.3: Norton equivalent circuit of the feeding port of the array with indexes nm. $Y_{A,mn}$ is the active input admittance for the active port with indexes nm.

where the left-hand side represents the magnetic field scattered by all the slots and observed on the axis of the m-th slot ($y = m\,d_y$). The scattered field is written as a convolution between the equivalent magnetic current density on the slots (m_x) and the xx-component of the dyadic spectral Green's function (g_{xx}), relating the magnetic field to magnetic currents and accounting for the stratified medium above and below the slots. The right-hand side of (2.1) represents the sum of all surface electric currents flowing in the feeding gaps and the metal terminations:

$$j_{y,\mathrm{gaps}}(x, md_y) = \sum_{n'=0}^{N+1} (i_{n'm} - Y_L v_{n'm}) f_{n'}(x - x_{n'}) \tag{2.2}$$

where we assume the currents to be written as basis functions $f_{n'}$, defined on the feeds and terminations and centered at $x_{n'}$, multiplied by unknown coefficients. The basis functions are chosen as constant on the feeding gaps and edge singular on the metal terminations (see Fig. 2.2) and they are defined in closed form as in [85], both in space and spectral domain. The assumption of a single basis function per feed is accurate enough under the condition that the delta gaps are small compared to the wavelength, such that the current and voltage can be averaged on each gap. This choice of basis functions is not valid for the general shape of the slots, but specific for uniform slot width and rectangular delta-gap feeds.

The weights of the basis functions depend on the impressed currents $i_{n'm}$, the unknown average voltages in the gaps $v_{n'm}$, and the load admittance Y_L, according to the Norton equivalent circuit of the feeding ports as in Fig. 2.3. The impressed currents $i_{n'm}$ are imposed to be 0 for the passive metal terminations, that is $i_{0\,m} = i_{N+1\,m} = 0$.

To solve the integral equation, we assume that the magnetic current is a separable-variable function on each slot:

$$m_x(x', y') = \sum_{m'=1}^{M} v_{m'}(x') m_t(y' - m'd_y) \tag{2.3}$$

where $v_{m'}$ are unknown voltage distributions on the slots, while $m_t(y) = 2/(w_s\pi) \times (1 - (2y/w_s)^2)^{-1/2}$ is an edge singular transverse distribution. The assumption that the magnetic current is variable separable and only oriented along x is valid under the condition that the slot width is uniform and narrow with respect to the wavelength. By replacing (2.3) and (2.2) in (2.1) and defining the function

$$d_{m'm}(x - x') = \int\limits_{m'd_y - \frac{w_s}{2}}^{m'd_y + \frac{w_s}{2}} g_{xx}(x - x', md_y - y')m_t(y' - m'd_y)dy' \qquad (2.4)$$

one can simplify the integral equation as follows:

$$\sum_{m'=1}^{M} \int\limits_{-\infty}^{\infty} d_{m'm}(x - x')v_{m'}(x')dx' = \sum_{n'=0}^{N+1} (Y_L v_{n'm} - i_{n'm})f_{n'}(x - x_{n'}). \qquad (2.5)$$

The function in (2.4) can be interpreted as the connected-array Green's function, associated with the field radiated by slot m' onto slot m. The introduction of this function enables the description of the magnetic current on the slots using only a limited number of basis functions located on the feeds and terminations. A more standard spectral domain approach would require discretization of the entire slot domain resulting in a large number of basis functions and heavy computation requirements.

2.2.2 Spectral Domain Integral Equation and Solution

Equation (2.5) can be written in the spectral domain as

$$\sum_{m'=1}^{M} D_{m'm}(k_x)V_{m'}(k_x) = \sum_{n'=0}^{N+1} (Y_L v_{n'm} - i_{n'm}) F_{n'}(k_x)e^{jk_x x_{n'}} \qquad (2.6)$$

where $V_{m'}(k_x)$ is the spectrum of the unknown voltage along the axis of each slot, k_x is the spectral counterpart of the spatial variable x, and $F_{n'}$ is the Fourier transform of the basis function $f_{n'}$. $D_{m'm}$ is the spectral version of (2.4) and is given by the k_y-spectral integral

$$D_{m'm}(k_x) = \frac{1}{2\pi} \int\limits_{-\infty}^{\infty} G_{xx}(k_x, k_y)J_0\left(\frac{w_s k_y}{2}\right) e^{-jk_y(y_m - y_{m'})}dk_y \qquad (2.7)$$

where J_0 is the zeroth-order Bessel function, representing the Fourier transform of the edge singular distribution across the slot, and G_{xx} is the xx-component of the dyadic spectral Green's function. The Green's function can be found as $G_{xx}(k_x, k_y) = (-i_{TE}k_x^2 + i_{TM}k_y^2)/(k_x^2 + k_y^2)$, where i_{TE} and i_{TM} are the current solutions of the equivalent transmission lines representing the layered medium for TE and TM modes, respectively. The equivalent transmission lines for the ADL stratification were derived in [73].

When considering observation on the axes of all slots, (2.6) can be compactly written in matrix form as

$$\mathbf{D}(k_x)\mathbf{V}(k_x) = \sum_{n'=0}^{N+1} (Y_L \mathbf{v}_{n'} - \mathbf{i}_{n'}) F_{n'}(k_x)e^{jk_x x_{n'}} \qquad (2.8)$$

where $\mathbf{D}(k_x)$ is an M by M matrix consisting of the elements $D_{m'm}(k_x)$, $\mathbf{V}(k_x) = \{V_1(k_x), ..., V_M(k_x)\}$, $\mathbf{i}_{n'} = \{i_{n'1}, ..., i_{n'M}\}$, and $\mathbf{v}_{n'} = \{v_{n'1}, ..., v_{n'M}\}$. Inverting the D matrix leads to an expression for the voltage spectra as

$$\mathbf{V}(k_x) = \sum_{n'=0}^{N+1} \mathbf{D}^{-1}(k_x) \left(Y_L \mathbf{v}_{n'} - \mathbf{i}_{n'} \right) F_{n'}(k_x) e^{jk_x x_{n'}} . \tag{2.9}$$

Projecting both LHS and RHS onto the n-th test function (chosen as equal to the basis function, according to the Galerkin projection method) allows us to define a mutual impedance

$$Z_{n'nm'm} = -\frac{1}{2\pi} \int_{-\infty}^{\infty} \left(D^{-1}(k_x) \right)_{m'm} F_{n'}(k_x) F_n(-k_x) e^{-jk_x(x_n - x_{n'})} dk_x . \tag{2.10}$$

The mutual impedances in (2.10) fill the impedance matrix $\mathbf{Z}$, with which the unknown voltage vector can be found as

$$\mathbf{v} = (\mathbf{Z}_L + \mathbf{Z})^{-1} \mathbf{Z}_L \mathbf{Z} \mathbf{i} \tag{2.11}$$

where $\mathbf{v}$ and $\mathbf{i}$ are $(N+2) \times M$-element vectors describing the unknown voltages and the impressed currents at all basis functions. $\mathbf{Z}_L$ is a diagonal matrix containing the load impedance at each basis function, equal to $1/Y_L$ for the active feeds and 0 for the metal terminations. The currents flowing into each port are then given by $\mathbf{i}_A = \mathbf{Z}^{-1}\mathbf{v}$ and the active impedance at each of the feeds can be found as

$$Z_{A,nm} = \frac{v_{nm}}{i_{A,nm}} . \tag{2.12}$$

2.3 Analysis of the Spectral Integrals

The numerical method introduced in the previous section requires the computation of the spectral integrals in k_y and k_x, given by (2.7) and (2.10), respectively. These spectral integrals can be further studied to reduce computation time and to highlight the different contributions.

2.3.1 Acceleration by Extraction of Asymptotic Part

For large values of k_y, the spectral Green's function is dominated by the reactive field surrounding the slot. For complex stratification such as the ADL in Fig. 2.4(a), the Green's function tends asymptotically to the Green's function G_{xx}^∞ associated with a set of two homogeneous semiinfinite half-spaces as in Fig. 2.4(b). The media in these half-spaces are taken as the closest media above and below the slot, with wavenumbers k_1 and k_2, respectively.
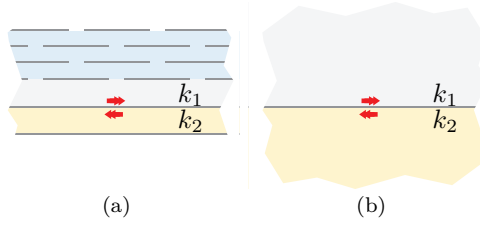
Figure 2.4: (a) Initial stratification with ADL and backing reflector to define the stratified media Green's function for the problems above and below the slots. (b) Semi-infinite media to define the asymptotic Green's function for the upper and lower problems.

By subtracting and adding the homogeneous semi-infinite Green's function, (2.7) can be written as the sum of two integrals

$$
D_{m'm}(k_x) = \frac{1}{2\pi} \int\limits_{-\infty}^{\infty} (I_{m'm}(k_x, k_y) - I^{\infty}_{m'm}(k_x, k_y)) dk_y + \frac{1}{2\pi} \int\limits_{-\infty}^{\infty} I^{\infty}_{m'm}(k_x, k_y)) dk_y
$$

$$
= D^{\text{diff}}_{m'm}(k_x) + D^{\infty}_{m'm}(k_x)
$$

(2.13)

with

$$
I_{m'm}(k_x, k_y) = G_{xx}(k_x, k_y) J_0\left(\frac{w_{\text{s}} k_y}{2}\right) e^{-jk_y(y_m - y_{m'})}
$$

(2.14)

$$
I^{\infty}_{m'm}(k_x, k_y) = G^{\infty}_{xx}(k_x, k_y) J_0\left(\frac{w_{\text{s}} k_y}{2}\right) e^{-jk_y(y_m - y_{m'})}.
$$

(2.15)

The first integral in (2.13) ($D^{\text{diff}}_{m'm}$) converges faster than the original integral ($D_{m'm}$) and can be evaluated over a reduced integration domain. The second integral ($D^{\infty}_{m'm}$) represents the spectral Green's function of slot pairs located at the interface between two semi-infinite homogeneous half-spaces and can be evaluated in closed form as [61]

$$
D^{\infty}_{m'm}(k_x) \approx \frac{-1}{2k_0\zeta_0} \sum_{i=1}^{2} \kappa_i^2 \times \begin{cases} J_0\left(\frac{w_{\text{s}}}{4}\kappa_i\right) H_0^{(2)}\left(\frac{w_{\text{s}}}{4}\kappa_i\right) & \text{for } m = m' \\ H_0^{(2)}\left((y_{m'} - y_m)\kappa_i\right) & \text{for } m \neq m', \end{cases}
$$

(2.16)

where $\kappa_i = (k_i^2 - k_x^2)^{1/2}$, the subscripts $i = \{1, 2\}$ represent the upper and lower half-spaces, respectively, $H_0^{(2)}$ is the Hankel function of zeroth order and the second kind, and k_0 and ζ_0 are the free-space wave number and impedance.

An example is shown for the 5-layer ADL shown in Fig. 2.5. The metal patches of the ADL are assumed to be in free space, and the media above and below the slot are also free space ($k_1 = k_2 = k_0$). The integrand as a function of the spectral variable k_y is shown in Fig. 2.6 for both the real stratification and the semi-infinite media. It can be seen that the difference between the two integrands becomes very small for $k_y > 10k_0$. This is confirmed by the relative error in Fig. 2.6(c) and (d), defined as $|I_{m'm} - I^{\infty}_{m'm}|/|I_{m'm}|$, which is below 1% for $k_y > 10k_0$.

2

(a)   (b)
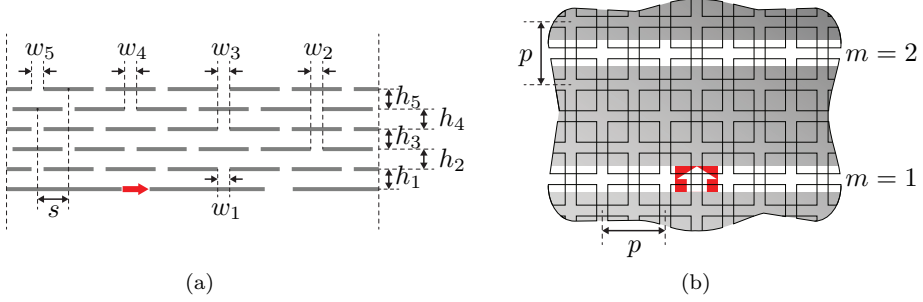
Figure 2.5: (a) Side view and (b) top view of the ADL geometry considered, with two slots ($d_y = 0.19\lambda$, $w_s = 0.06\lambda$, where λ is the wavelength at the calculation frequency) and five-layer ADL ($p = 0.173\lambda$, $w_1 = w_2 = w_3 = 0.013\lambda$, $w_4 = w_5 = 0.022\lambda$, $h_1 = 0.009\lambda$, $h_2 = h_3 = 0.017\lambda$, $h_4 = 0.035\lambda$, $h_5 = 0.052\lambda$, $s = 0.5p$).

(a)   (b)   (c)
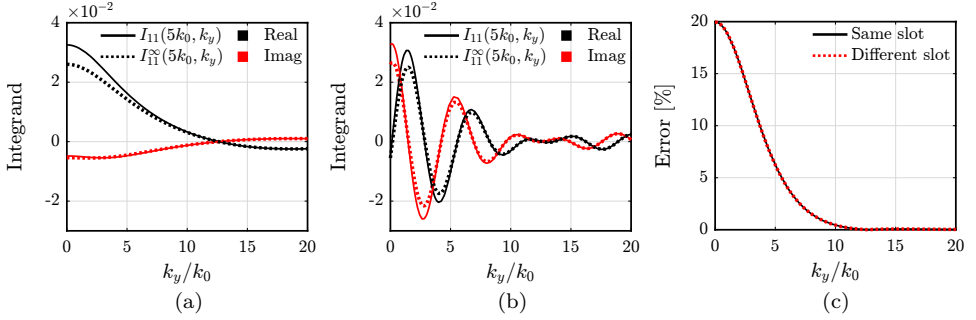
Figure 2.6: Integrand as a function of k_y for $k_x = 5k_0$. (a) Comparison between total integrand and semi-infinite dielectric case for two feeds on the same slot ($m = m' = 1$) and (b) for two feeds on different slots ($m = 1 \neq m' = 2$). (c) Relative error between total integrand and semi-infinite dielectric case for the same two cases.

Table 2.1: Time spent on the calculation of $D^{-1}(k_x)$ in (2.10) without and with use of the asymptotic extraction described in (2.13).

	Without Acceleration	With Acceleration
5 slots	3 min, 14 sec	40 sec
20 slots	79 min, 23 sec	8 min, 39 sec

Extraction of the asymptotic part can be used to accelerate the integral in (2.7). The calculation time related to the matrix $\mathbf{D}^{-1}(k_x)$ is shown in Table 2.1 to be significantly reduced for arrays of 5 or 20 slots under the ADL in Fig. 2.5.

2.3.2 Residue Contribution

The integrand of the k_x-integral in (2.10) is characterized by a number of polar and branch singularities that represent guided and radiated waves, respectively. The na-
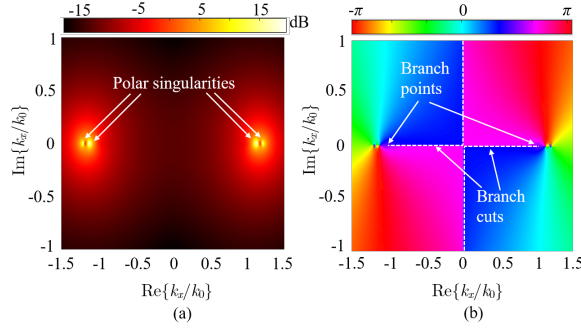
Figure 2.7: Integrand of (2.10) in the k_x-complex plane for the stratification shown in Fig. 2.5: (a) amplitude in dB and (b) phase of $(D^{-1}(k_x))_{12}$.

ture and the number of poles are related to the specific dielectric stratification above and below the slot array. When the polar singularities are located on the real axis in the k_x-complex plane, they represent guided waves with no attenuation and are the dominant contribution to the mutual impedance between basis functions at electrically large distances. As such, the mutual impedance between such elements can be approximated using the poles' residual contributions. This analytical approximation replaces the numerical computation of the integral, thus greatly simplifying the evaluation of the mutual impedances.

Assuming that the function $D_{m'm}$ has L poles indicated as $k_{xp1}, k_{xp2}, ..., k_{xpL}$, the residue contribution of the integral in (2.10) can be written as

$$Z_{n'nm'm} \approx \sum_{l=1}^{L} \frac{jF_{n'}(k_{xpl})F_n(-k_{xpl})e^{-jk_{xpl}(x_n-x_{n'})}}{\left.\frac{d(D^{-1}(k_x))_{m'm}}{dk_x}\right|_{k_x=k_{xpl}}} \; . \qquad (2.17)$$

As an example, a 2×2 array is considered under the stratification shown in Fig. 2.5, and the function $(D^{-1}(k_x))_{12}$ is shown in the k_x-complex plane in Fig. 2.7. The polar and branch singularities are highlighted in the figure. A comparison between the complete integral and the residual contributions of the two poles is shown in Fig. 2.8 as a function of the distance between the two basis functions on the slot. The comparison is shown for basis functions in [Fig. 2.8(a)] the same slot and [Fig. 2.8(b)] different slots. For both cases, it can be seen that the mutual impedance is well approximated by the residue contribution for distances above a quarter wavelength.

2.3.3 Physical Meaning of Poles

A physical interpretation can be given to the polar singularities. Each pole can be associated with a guided mode supported by the combination of the various slots. To highlight this aspect, the voltage distribution along the slots is calculated on a set of two slots when only one feed is present on each slot. The voltage is calculated as the
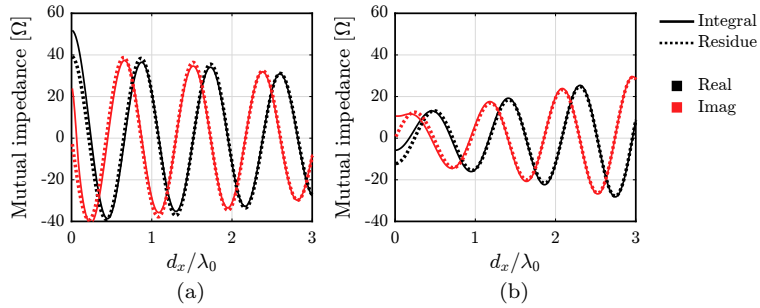
Figure 2.8: Comparison between the complete integral and the residual contributions of the two poles is shown as a function of the distance between the two basis functions on (a) the same slot and (b) different slots.
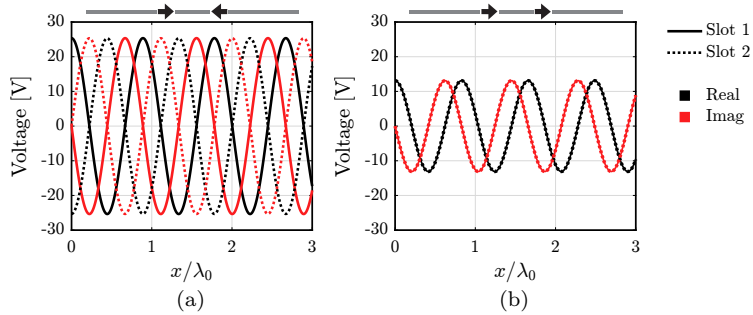
Figure 2.9: Voltage distribution along a set of two slots in free space, considering (a) only the first polar contribution and (b) only the second polar contribution.

inverse Fourier transform of (2.9) and is equal to

$$v_m(x) = \frac{1}{2\pi} \int\limits_{-\infty}^{\infty} V_m(k_x) e^{-jk_x x} dk_x \,. \tag{2.18}$$

The total voltage is computed using the residue theorem and the contribution from each of the two poles is plotted separately in Fig. 2.9. The voltage distributions on the two slot due to each pole are either equal or opposite, so the two poles correspond to the common and differential modes supported by the pair of slots.

While the closed-form solution of the integral as in (2.17) avoids the numerical computation of the coupling integrals, it must be noted that the number of poles is proportional to the number of slots composing the array. This aspect is illustrated in Fig. 2.10 where the position of the poles is shown in the complex plane for three and four slots. Each pole represents a quasi-transverse electromagnetic (TEM) mode supported by the slots. This is in line with the expectation that N_c-1 TEM modes are supported by a transmission line with N_c conductors. Therefore for large arrays, the search of the poles can become more complex than the original numerical integration and may thus no longer be convenient. Moreover, when a large number of poles occur
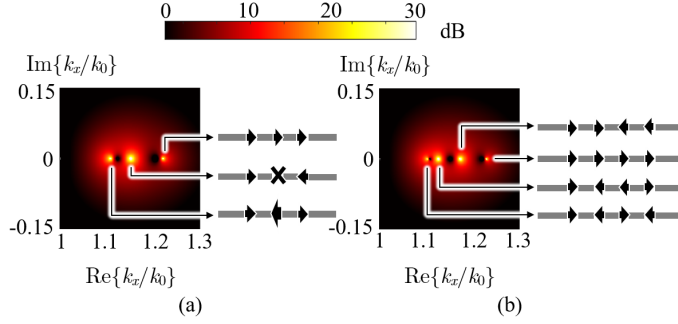
Figure 2.10: Amplitude of $(D^{-1}(k_x))_{11}$ in the k_x-complex plane: Location of the polar singularities for (a) three and (b) four slots under the ADL structure as in Fig. 2.5. Each pole represents a quasi-TEM mode supported by the ensemble of the slots.
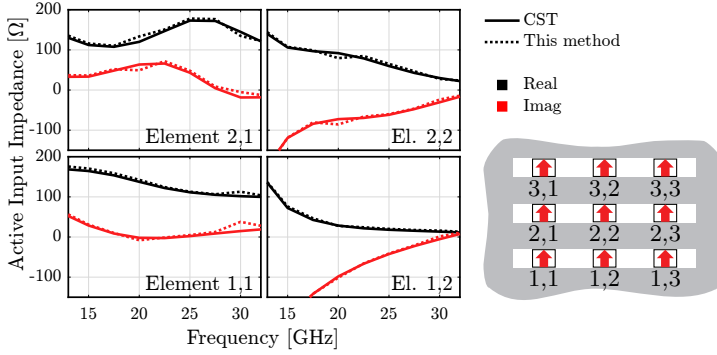
Figure 2.11: Comparison between CST and MoM of the active input impedance of each element of a 3×3 array in free space, with $d_x = d_y = 0.45\lambda$, $w_{\rm s} = 0.05\lambda$, $\delta = 0.05\lambda$, $d_{\rm edge} = 0.25\lambda$, and $Z_L = 100\,\Omega$, where λ is the wavelength at $31\,{\rm GHz}$.

in the range $k_0 < k_x < 1.3k_0$, it can become difficult to distinguish them and isolate the individual contributions.

2.4 Validation

2.4.1 Impedance

The method is validated using the commercial solver CST Microwave Studio. First, a 3×3 array is considered in free space, with $d_x = d_y = 0.45\lambda$, $w_{\rm s} = 0.05\lambda$, $\delta = 0.05\lambda$, $d_{\rm edge} = 0.25\lambda$, and $Z_L = 100\,\Omega$. The active input impedance of the elements for broadside scanning is presented in Fig. 2.11, showing a very good agreement between our model and CST. Only four elements of the array are shown, since all the others are included by symmetry.
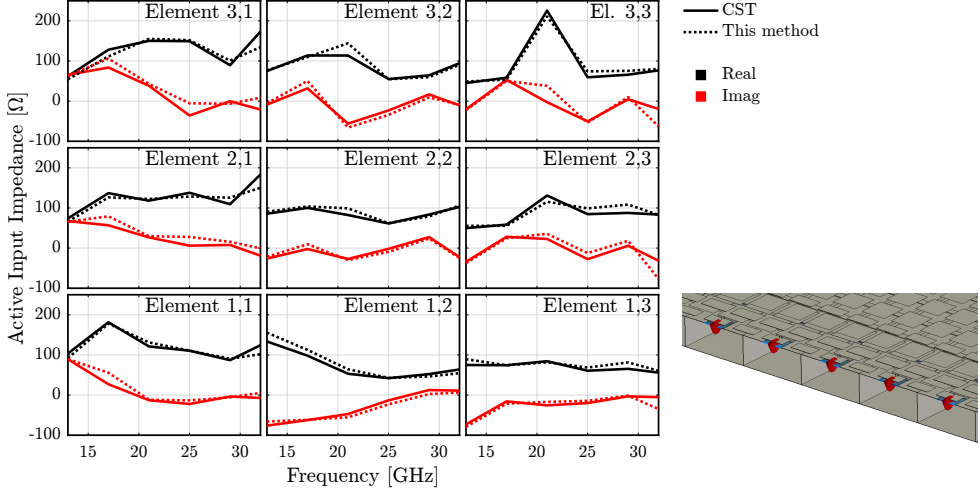
Figure 2.12: Comparison between CST and MoM of the active input impedance of each element of a 5×5 array with a backing reflector and a five-layer ADL superstrate. Vertical walls are included below the slot plane. The geometrical parameters are $d_x = d_y = 4.35$ mm, $w_s = 1.4$ mm, $\delta = 2$ mm, $d_{\text{edge}} = 2.4$ mm, distance from backing reflector $h = 1.9$ mm, relative permittivity of the substrate $\varepsilon_r = 2.2$. The ADL is in free space with $p = d_x/2$, $w_1 = 0.64$ mm, $w_2 = w_3 = 0.32$ mm, $w_4 = w_5 = 0.5$ mm, $d_1 = 0.23$ mm, $d_2 = d_3 = 0.45$ mm, $d_4 = 0.83$ mm, $d_5 = 1.2$ mm, $s = 0.5p$.

A 5×5 finite array with a backing reflector and loaded by a 5-layer artificial dielectric is simulated in CST and using our method. Vertical walls are considered between parallel slots as in [58]. Fig. 2.12 shows a good agreement between the results given by CST and those generated by our method. For this example, the computation time was 2 min for seven frequency points with our method, versus 2 h in CST.

2.4.2 Radiation Patterns

The radiation patterns can also be computed from the voltage spectrum in (2.9) by using the stationary phase point method. The generic component of the radiated magnetic field can be expressed as

$$H_{\{x,y,z\}}(\theta_o, \phi_o, r) \approx jk_{zo}G_{\{x,y,z\}x}(k_{xo}, k_{yo})M(k_{xo}, k_{yo})\frac{e^{-jk_0r}}{2\pi r} \tag{2.19}$$

where (θ_o, ϕ_o, r) refers to an observation point in the far field and $k_{xo} = k_0 \sin\theta_o \cos\phi_o$, $k_{yo} = k_0 \sin\theta_o \sin\phi_o$, $k_{zo} = k_0 \cos\theta_o$. The 2-D magnetic current spectrum on the array aperture is

$$M(k_x, k_y) = \sum_{m=1}^{M} V_m(k_x)J_0(k_yw/2)e^{jk_ym\,d_y} \ . \tag{2.20}$$
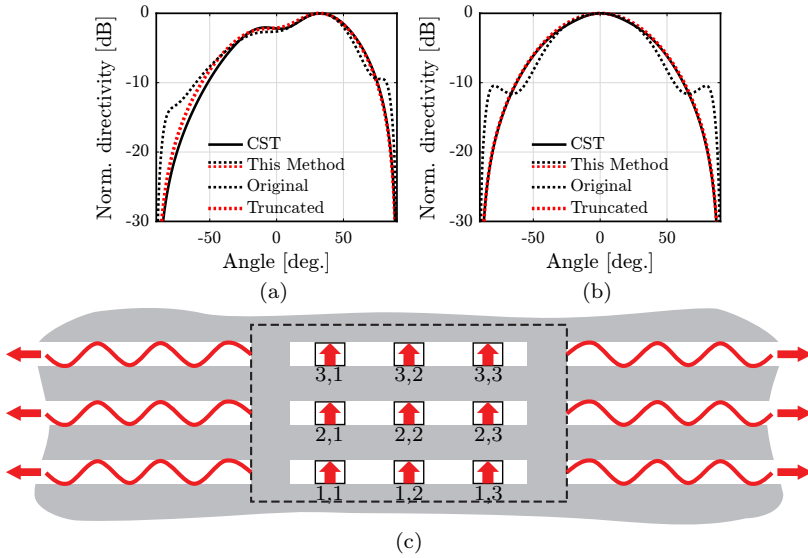
Figure 2.13: 3×3 connected slot array in free space: H-plane embedded patterns of the (a) corner (1,1) and (b) central (2,2) elements, with and without windowing of the aperture field. Patterns are calculated at 31 GHz. (c) Finite length metal terminations at the slot edges with fictitious waves propagating in the slots outside the array. A rectangular window (dashed rectangle) is used to exclude these waves from the results.

For example, for the 3×3 array in free space considered in the previous section, the H-plane embedded patterns of the corner and central elements are shown as red dotted curves in Fig. 2.13(a) and (b). It can be seen that a discrepancy with CST occurs at large angles close to 90°. This discrepancy arises due to the assumption of finite length metal terminations at the slot edges, which is used to simplify the procedure by exploiting the spectral solutions of the infinite slot. The extension of the slots after this finite termination enables the propagation of fictitious residual waves along the infinite slots outside the array [see Fig. 2.13(c)].

This effect can be removed from the results by replacing the total spectrum V_m with a truncated version $V_{m,\text{trunc}}$ that includes only the array aperture (dashed rectangle in Fig. 2.13(c)) and cuts out the aperture field in the passive slots outside the array. This can be obtained mathematically by applying the inverse Fourier transform $(\mathcal{F}^{-1}\{\cdot\})$ of (2.9), multiplying by a rectangular window $\text{rect}_{\text{array}}(x)$ including only the finite slot region and re-applying the Fourier transform $(\mathcal{F}\{\cdot\})$:

$$V_{m,\text{trunc}}(k_x) = \mathcal{F}\{\mathcal{F}^{-1}\{V_m(k_x)\}\,\text{rect}_{\text{array}}(x)\}. \tag{2.21}$$

The patterns after truncation are also shown in Fig. 2.13(a) and (b), and they are closer to the CST solutions.

The patterns in the presence of the ADL can also be calculated since the spectral Green's function of ADLs is known. For the same 5×5 array with ADL considered in Fig. 2.12, the patterns on the two main planes are shown in Fig. 2.14.
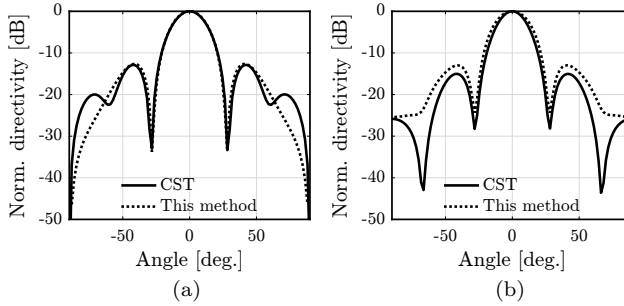
Figure 2.14: Radiation patterns at 29 GHz for the 5×5 array with ADL considered in Fig. 2.12: (a) H-plane ($\phi = 0°$) and (b) E-plane ($\phi = 90°$).

2.5 Large Array Performance

2.5.1 Impedance Matching

To show the capabilities of the method, a large array is simulated containing 32×32 elements. The array is based on the same unit cell as in Fig. 2.12. Our method is used to analyze the effects of the finiteness on such an array. The resulting active VSWR of each element is shown in Fig. 2.15(a)-(c) for various scanning conditions. It is seen that, while most elements are close to the infinite array approximation, some deviate from it quite significantly. This information is relevant in array design to estimate the amount of power that is reflected in the output of the power amplifiers feeding the individual elements. On the other hand, the total matching efficiency of the array, determined from the total input and reflected power as $(P_{in} - P_{reflected})/P_{in}$, is shown in Fig. 2.15(d) to be within a few percent of the infinite array.

To determine the position of the elements that exhibit a higher VSWR, colormaps of the VSWR for each element (n, m) are shown in Fig. 2.16 for two different scanning conditions. The greatest mismatch is seen at the edges of the array while the majority of elements have a VSWR lower than 3.

2.5.2 Radiation Patterns

The proposed spectral method also provides the radiation patterns of the finite array. The standard approach for estimating the pattern of finite arrays is the windowing techniques [77, 92], which simply multiplies the unit cell active element pattern by the array factor. However, this technique does not account for the variations of the impedance across the array. The radiation patterns of the finite array for scanning to 60° in the two main planes are shown in Fig. 2.17, where they are compared to the windowing approximation. It is evident that for large arrays the two methods provide a similar estimation of the patterns with differences primarily in the sidelobes.
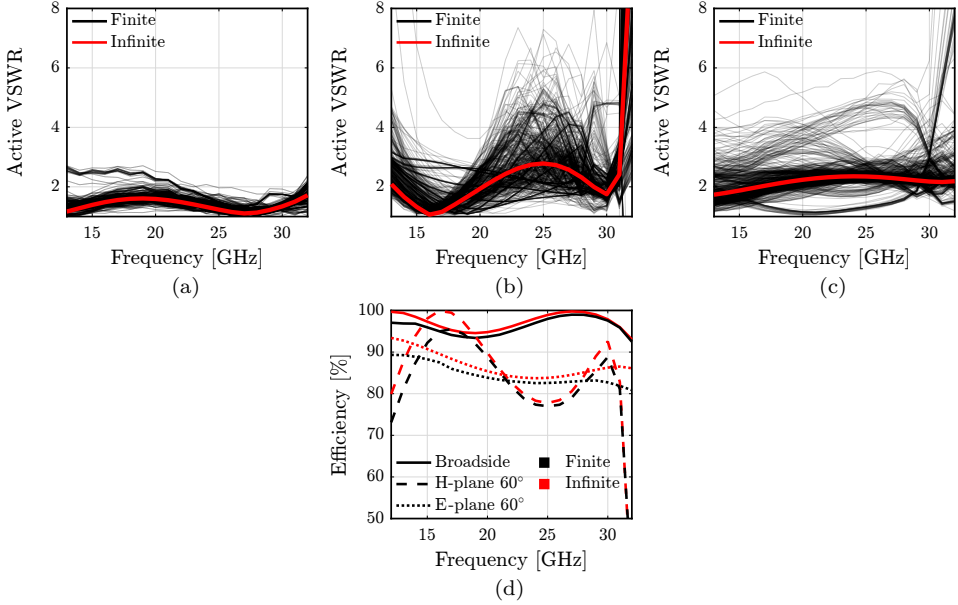
Figure 2.15: Active VSWR for each element in a 32×32 connected slot array when scanning to (a) broadside, (b) 60° on the H-plane, and (c) 60° on the E-plane; (d) resulting matching efficiency.
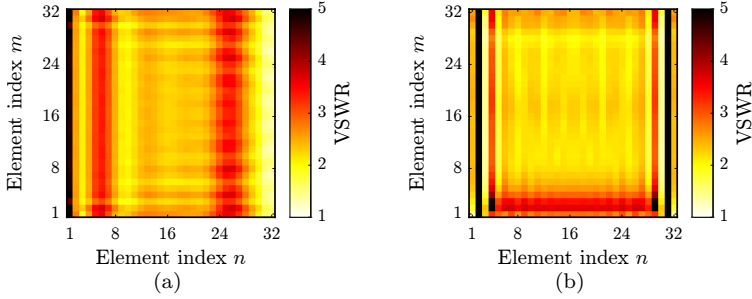
Figure 2.16: Maps of the active VSWR of the elements across the array for scanning to 60° at 31 GHz in the (a) H-plane and (b) E-plane.
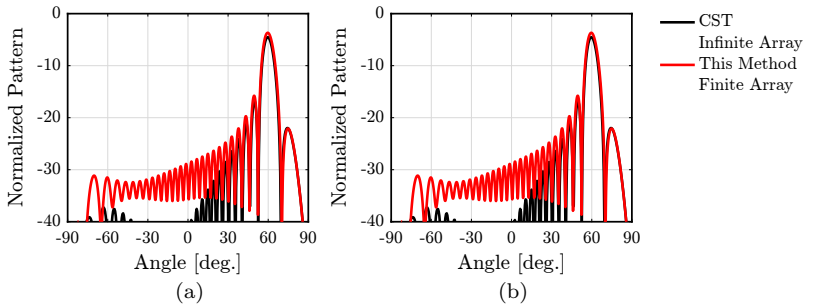
Figure 2.17: Radiation patterns at 30 GHz of a 32×32 finite array based on the unit cell shown in 2.12 scanning to 60° on the (a) H-plane and (b) E-plane. The patterns are normalized to the maximum at broadside.

2.6 Conclusions

A numerical method to analyze planar connected arrays with ADLs was presented. The method is based on a spectral domain approach with a limited number of basis functions, equal to $(N + 2) \times M$, for an array of $N \times M$ elements. The mutual impedance is efficiently evaluated by extraction of asymptotic parts and residue contributions of the polar singularities.

The method was validated using CST Microwave Studio and enables finite array simulations with large numbers of elements to estimate the effects of the finiteness on the active impedance and the radiation patterns.

Chapter 3

On the Cross-Polarization Levels of Arrays With Wide Angle Impedance Matching Layers

The characteristic cross-polarization (X-pol) behavior of wide angle impedance matching (WAIM) structures is investigated. The study considers an ideal linearly polarized current sheet in the presence of various dielectric and artificial dielectric superstrates, analyzed using transmission line models representing the stratified media. The main mechanism that causes increased X-pol is highlighted and linked to the anisotropy of the superstrate. An approach to reduce the X-pol is proposed, which involves including vertical vias within the WAIM dielectrics to control the vertical component of the permittivity tensor. The intrinsic X-pol performance of a set of artificial dielectric layers with and without vias is experimentally verified by placing the WAIM above an open- ended waveguide that acts as a linearly polarized source. The proposed WAIM with vias can be used in wideband wide-scanning array designs to improve polarization purity.

3.1 Introduction

Planar array designs often utilize dielectric slabs or metal structures placed above the antenna (superstrates) to improve the matching performance and the scanning capability [46, 47]. One such superstrate is the wide angle impedance matching (WAIM) layer [65], which consists of an electrically thin dielectric layer located in the close vicinity of the array to mitigate the impedance mismatch while scanning. Since its introduction, various research efforts have gone into exploiting metasurfaces in WAIM designs to improve the array performance in terms of scanning range or operational bandwidth [93, 94].

Another approach to realizing superstrates was presented in [54, 58, 95] and proposes using artificial dielectric layers (ADLs) rather than homogeneous isotropic dielectrics. ADLs consist of periodic metallic patches, small with respect to the wavelength, embedded in a host material to create an equivalent material with modified properties. The effective electromagnetic parameters of the artificial material can be engineered by properly designing the spatial density of the metallic inclusions. ADLs are anisotropic, which is a key advantage that helps avoid the occurrence of surface waves and scan blindness, even for very large scanning angles.

Although dielectric and metal WAIMs have been extensively studied with a focus on the matching and scan performance, they have not been thoroughly investigated in terms of polarization properties. On the other hand, it is known that dielectric slabs can influence the polarization performance of antennas, e.g., dielectric substrates increase the cross-polarization (X-pol) levels of microstrip antennas, especially in the diagonal planes [96]; also, dielectric superstrates increase the axial ratio in circularly polarized arrays [97].

This chapter first describes the fundamental limits of dielectric and artificial dielectric superstrates in terms of X-pol. To highlight the main mechanism, an ideal Wheeler current sheet [86] is considered in the presence of different superstrates. The X-pol behavior is then studied using transmission line models representing stratified media. Based on this study, the effective anisotropy of WAIMs is identified as the main cause of X-pol deterioration. An approach to reduce the X-pol levels while maintaining comparable bandwidth performance is proposed. To do so, vias are added in some parts of the dielectrics to enhance the vertical component of the effective permittivity tensor. To validate the proposed concept, an ADL superstrate with and without vias is manufactured and tested, showing reduced X-pol when vias are included.

3.2 Cross-Polarization of Wheeler's Current Sheet with a Superstate

To better understand the intrinsic polarization properties of common superstrates, it is convenient to first introduce the polarization characteristics of an ideal source. To this aim, we consider a Wheeler's current sheet [86], which represents a current
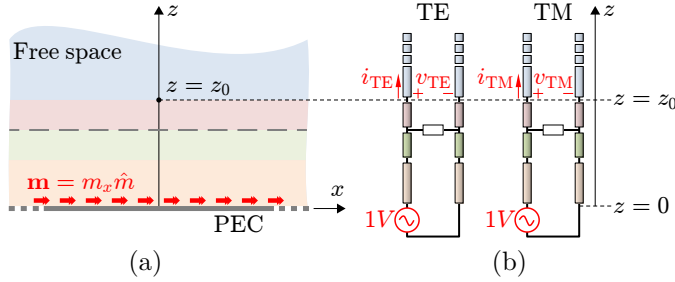
Figure 3.1: (a) Illustration of a Wheeler current sheet on a PEC plane, loaded with a generic dielectric/metal stratification and (b) equivalent transmission lines for TE and TM modes.

distribution with constant amplitude over an infinite plane and with a continuous linear phase distribution. For example, we can consider an x-oriented magnetic current sheet with constant amplitude V_0 in the xy-plane, infinitesimally thin in z, and with a phase distribution to point its radiated field to the angle θ, ϕ:

$$\mathbf{m}(x, y, z) = m_x(x, y, z)\hat{\mathbf{x}} = V_0 e^{-jk_{x0}x} e^{-jk_{y0}y} \delta(z)\hat{\mathbf{x}} \tag{3.1}$$

where $k_{x0} = k_0 \sin\theta \cos\phi$, $k_{y0} = k_0 \sin\theta \sin\phi$, k_0 is the free-space wave number, and $\delta(\cdot)$ represents the Dirac delta function. The Wheeler current is equivalent to a phased array with infinitesimally small spacing, yielding a continuous phase distribution rather than discrete.

Generally, the radiated X-pol from a current sheet depends on the stratification above and below. However, for the sake of simplicity, we assume that the magnetic current is located on a perfect electric conductor (PEC) sheet so that only the stratification above the radiating plane is considered. This assumption is relevant in the context of slot arrays because the metallic plate in which the slots are etched typically decouples the radiation in the half spaces above and below the slots.

To find the field radiated by the Wheeler current sheet in the presence of a dielectric or metal stratification, such as the one shown in Fig. 3.1(a), one can make use of the spectral Green's function for stratified media $\bar{\bar{\mathbf{G}}}^{em}$ [98] that relates the electric field to a magnetic source. The x-, y-, and z-components of the electric field can be calculated as described in Appendix A and are given by

$$\begin{aligned}
e_x &= V_0 G_{xx}^{em}(k_{x0}, k_{y0}) = V_0 \left(v_{\text{TM}} - v_{\text{TE}}\right) \sin\phi \cos\phi \\
e_y &= V_0 G_{yx}^{em}(k_{x0}, k_{y0}) = V_0 \left(v_{\text{TE}} \cos^2\phi + v_{\text{TM}} \sin^2\phi\right) \\
e_z &= V_0 G_{zx}^{em}(k_{x0}, k_{y0}) = -V_0 \zeta_0 i_{\text{TM}} \sin\theta \sin\phi
\end{aligned} \tag{3.2}$$

where G_{xx}^{em}, G_{yx}^{em} and G_{zx}^{em} are the relevant components of the dyadic Green's function for an x-oriented magnetic current. These components can be expressed in terms of the current and voltage solutions (i_{TE}, i_{TM}, v_{TE}, and v_{TM}) of the equivalent transmission lines representing the stratification, as depicted in Fig. 3.1(b). Two transmission lines are considered for the transverse electric (TE) and transverse magnetic (TM) modes, with characteristic impedances $Z_{\text{TE}} = \zeta_0 k_0 / k_z$ and $Z_{\text{TM}} =$

$\zeta_0 k_z / (k_0 \varepsilon_r)$, respectively, where $\zeta_0 = 120\pi\,\Omega$ is the free-space medium impedance, $k_z = (\varepsilon_r k_0^2 - k_{x0}^2 - k_{y0}^2)^{0.5}$ is the propagation constant in the transmission line section, and ε_r is the relative permittivity of the dielectric layer. The currents and voltages can be calculated at any point $z > z_0$ above the stratification, assuming a normalized voltage generator of 1V. It should be noted that in (3.2), we omit the phase term $\exp(-jk_0 r)$ that multiplies all the components, with r being the distance from the observation point to the point $(x, y, z) = (0, 0, z_0)$.

The Cartesian components of the field can be projected onto the co- and cross-polarized vectors, defined according to the third definition of Ludwig [99]. Following the steps reported in Appendix A, the X-pol ratio can be written as

$$\mathrm{Xpol}(\theta, \phi) = \frac{e_{\mathrm{cr}}}{e_{\mathrm{co}}} = \frac{\frac{\sin(2\phi)}{2}(v_{\mathrm{TM}} \sec\theta - v_{\mathrm{TE}})}{v_{\mathrm{TM}} \sin^2\phi \sec\theta + v_{\mathrm{TE}} \cos^2\phi}. \tag{3.3}$$

It is evident from (3.3) that for scanning in the main planes ($\phi = 0°$ or $\phi = 90°$) the X-pol is always 0 for any planar stratification. Another specific case is the diagonal plane ($\phi = 45°$), typically associated with the highest X-pol levels, for which the expression of the X-pol becomes

$$\mathrm{Xpol}(\theta, \phi = 45°) = \frac{v_{\mathrm{TM}} \sec\theta - v_{\mathrm{TE}}}{v_{\mathrm{TM}} \sec\theta + v_{\mathrm{TE}}}. \tag{3.4}$$

3.2.1 Free-Space Case

In the case of a Wheeler's current sheet radiating in free space [Fig. 3.2(a)], the voltages v_{TE} and v_{TM} are equal to 1, yielding a simple expression for the X-pol:

$$\mathrm{Xpol}(\theta, \phi) = \frac{\frac{\sin(2\phi)}{2}(\sec\theta - 1)}{\sin^2\phi \sec\theta + \cos^2\phi}. \tag{3.5}$$

For the diagonal plane, this simplifies to

$$\mathrm{Xpol}(\theta, \phi = 45°) = \frac{\sec\theta - 1}{\sec\theta + 1} = \tan^2\frac{\theta}{2}. \tag{3.6}$$

In free space, v_{TE} and v_{TM} are constant with frequency, so the X-pol is also frequency-independent. In Fig. 3.2(b), the X-pol is plotted as a function of the scan angle θ, for $\phi = 45°$. It is visible that, even for a perfectly linear polarized array radiating in free space, the X-pol increases with θ and reaches about $-9.5\,\mathrm{dB}$ for $\theta = 60°$ in the diagonal plane. This value represents a benchmark to assess the performance of a wide-scanning array. The curve in Fig. 3.2(c) shows the X-pol for $\theta = 60°$ and varying ϕ. As expected, the maximum X-pol occurs around the diagonal planes.
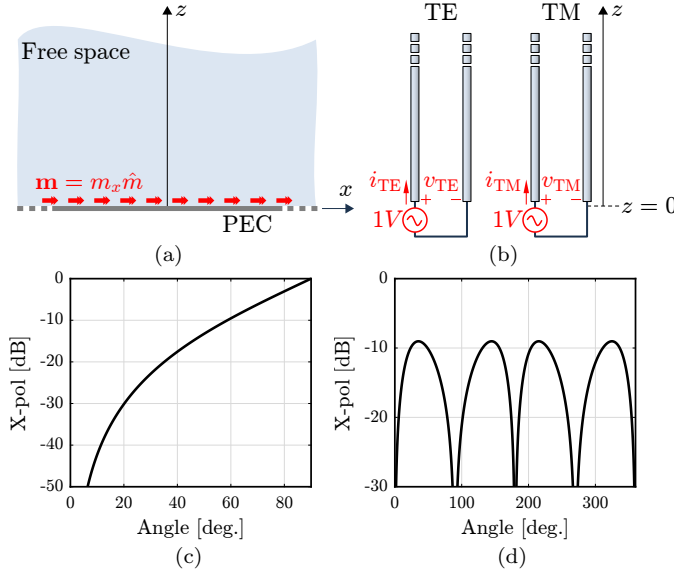
Figure 3.2: (a) Illustration of a Wheeler current sheet on a PEC plane, radiating into free space and (b) equivalent transmission lines for TE and TM modes. (c) X-pol for fixed $\phi = 45°$ and varying θ and (d) for fixed $\theta = 60°$ and varying ϕ.

3.2.2 Dielectric Superstrate

When adding a homogeneous dielectric slab above the current, the radiated fields vary with frequency and depend on the permittivity and thickness of the superstrate. A schematic drawing of the structure and the corresponding equivalent circuit is given in Fig. 3.3(a). To calculate the voltages v_{TE} and v_{TM}, we can define the ABCD matrix of the slab as

$$\begin{bmatrix} A & B \\ C & D \end{bmatrix}_{\text{slab}} = \begin{bmatrix} \cos(k_z h) & jZ_{Ti}\sin(k_z h) \\ jY_{Ti}\sin(k_z h) & \cos(k_z h) \end{bmatrix} \tag{3.7}$$

where 'Ti' can indicate TE or TM and $Y_{Ti} = 1/Z_{Ti}$. The voltage and current at $z = 0$ are

$$v_{Ti}(z = 0) = 1 \qquad i_{Ti}(z = 0) = 1/Z_{\text{in},Ti} \tag{3.8}$$

with

$$Z_{\text{in},Ti} = Z_{Ti}\frac{Z_{0Ti} + jZ_{Ti}\tan(k_z h)}{Z_{Ti} + jZ_{0Ti}\tan(k_z h)} . \tag{3.9}$$

Z_{0Ti} is the characteristic impedance for the free space transmission line. The voltage and current above the slab are found as

$$\begin{bmatrix} v_{Ti}(z = z_0) \\ i_{Ti}(z = z_0) \end{bmatrix} = \begin{bmatrix} A & B \\ C & D \end{bmatrix}_{\text{slab}}^{-1} \begin{bmatrix} v_{Ti}(z = 0) \\ i_{Ti}(z = 0) \end{bmatrix} . \tag{3.10}$$
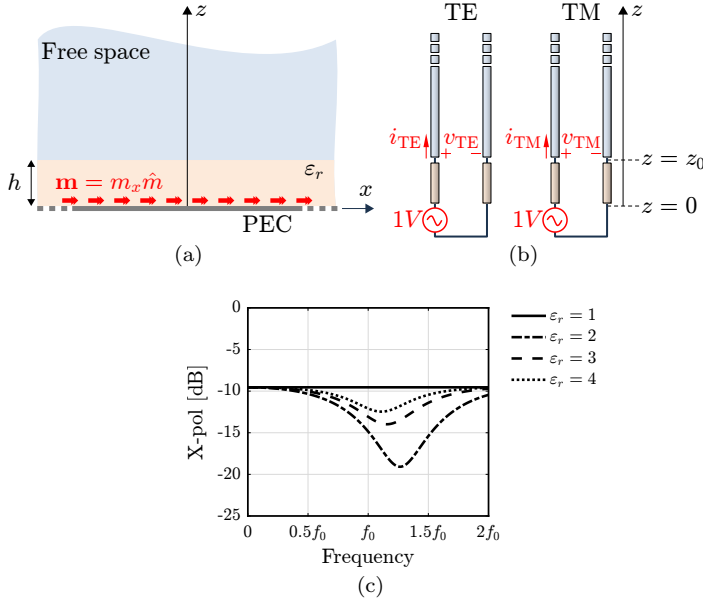
Figure 3.3: (a) Illustration of a Wheeler current sheet on a PEC plane, loaded with a dielectric superstrate and (b) equivalent transmission lines for TE and TM modes. (c) X-pol at $\phi = 45°$ and $\theta = 60°$, for various dielectric permittivities.

With some algebraic steps, we obtain

$$v_{Ti}(z = z_0) = \frac{V_0 Z_{0Ti}}{Z_{0Ti}\cos(k_z h) + j Z_{Ti}\sin(k_z h)}. \tag{3.11}$$

The X-pol at $\phi = 45°$ and $\theta = 60°$ for superstrates with $h = \lambda_d/4$ and various relative permittivities is shown in Fig. 3.3(b). In these examples, λ_d is the wavelength in the dielectric at the frequency f_0. The free-space case ($\varepsilon_r = 1$) is also shown for comparison, corresponding to the constant curve. It can be observed that the X-pol of the dielectric slabs is always lower than the one of free space, with the case of $\varepsilon_r = 2$ being the one that gives the lowest values. Therefore, low permittivity superstrates could be used to reduce the X-pol of the array in specific frequency ranges. However, in realistic array designs with periodic elements, including such slabs would limit the scan range by supporting surface waves and causing scan blindness.

3.2.3 Wide Angle Impedance Matching Layer

Another interesting case is where an air gap between the array and the dielectric slabs is included to implement a WAIM layer [65]. This stratification is shown in Fig. 3.4(a). In this case

$$\begin{bmatrix} A & B \\ C & D \end{bmatrix}_{\text{strat}} = \begin{bmatrix} A & B \\ C & D \end{bmatrix}_{\text{gap}} \begin{bmatrix} A & B \\ C & D \end{bmatrix}_{\text{slab}} \tag{3.12}$$
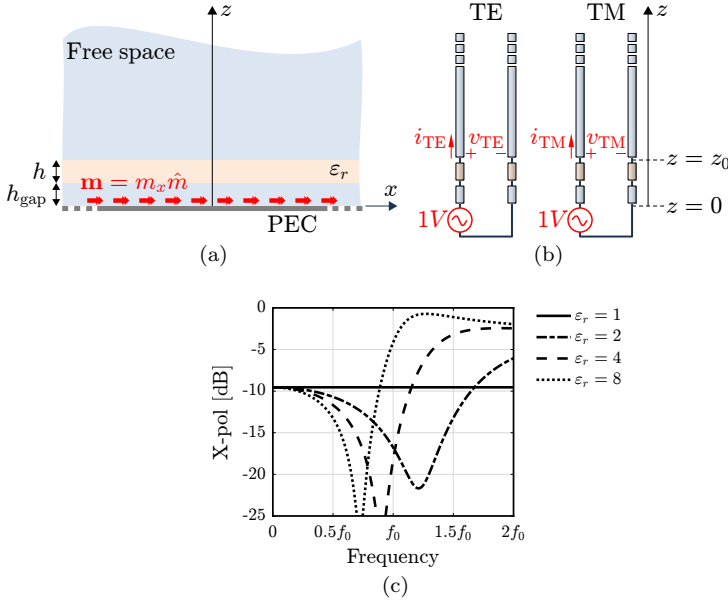
Figure 3.4: (a) Illustration of a Wheeler current sheet on a PEC plane, loaded with a dielectric WAIM and (b) equivalent transmission lines for TE and TM modes. (b) X-pol at $\phi = 45°$ and $\theta = 60°$, for various dielectric permittivities.

where the [ABCD] matrix of the slab is defined in (3.7) and

$$
\begin{bmatrix} A & B \\ C & D \end{bmatrix}_{\text{gap}} = \begin{bmatrix} \cos(k_{z0}h_{\text{gap}}) & jZ_{0Ti}\sin(k_{z0}h_{\text{gap}}) \\ jY_{0Ti}\sin(k_{z0}h_{\text{gap}}) & \cos(k_{z0}h_{\text{gap}}) \end{bmatrix} .
\tag{3.13}
$$

The current at $z = 0$ is given by $i_{Ti}(z = 0) = 1/Z_{\text{in},Ti}$, where the input impedance is given by

$$
Z_{\text{in},Ti} = Z_{0Ti}\frac{Z'_{\text{in},Ti} + jZ_{0Ti}\tan(k_{z0}h_{\text{gap}})}{Z_{0Ti} + jZ'_{\text{in},Ti}\tan(k_{z0}h_{\text{gap}})}
\tag{3.14}
$$

with

$$
Z'_{\text{in},Ti} = Z_{Ti}\frac{Z_{0Ti} + jZ_{Ti}\tan(k_z h)}{Z_{Ti} + jZ_{0Ti}\tan(k_z h)} .
\tag{3.15}
$$

Fig. 3.4(b) shows the resulting X-pol at $\phi = 45°$ and $\theta = 60°$, calculated for dielectric slabs with $h = \lambda_d/10$ and $h_{\text{gap}} = \lambda_0/10$, where λ_0 is the wavelength in free space. It can be observed that the X-pol exceeds the free-space values for the higher frequencies and can approach $0\,\text{dB}$ for high permittivity. This observation is relevant because typical WAIM layers are characterized by high permittivity values [65].

The increase in X-pol can be explained by looking at the equivalent refractive index of the combination of the air gap and the dielectric. Using the method described in [100] and fine-tuning the parameters, the two slabs [Fig. 3.5(a)] can be replaced by a single homogenized slab [Fig. 3.5(b)]. When $\varepsilon_r = 4$, the equivalent permittivity and
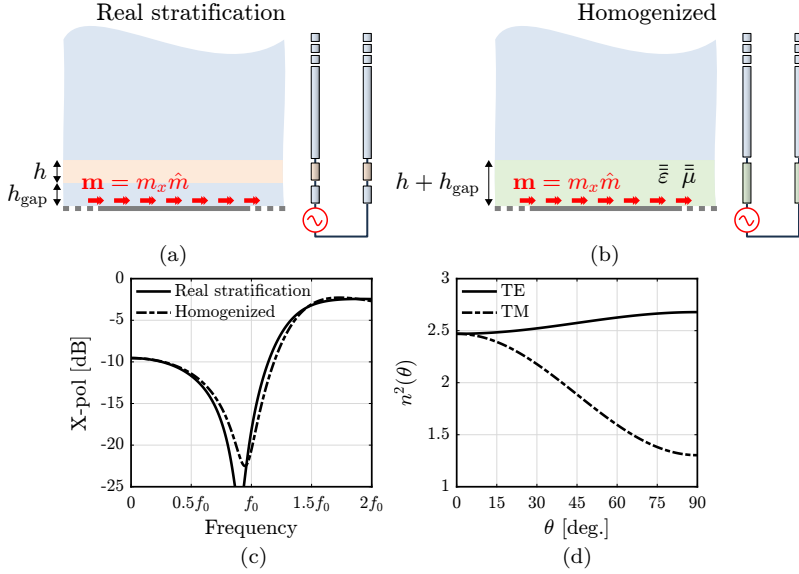
Figure 3.5: (a) Real two-slab stratification with equivalent transmission line and (b) homogenized equivalent anisotropic slab; (c) X-pol at $\phi = 45°$ and $\theta = 60°$ for the two structures and (d) equivalent refractive index of the homogenized slab for TE and TM modes.

permeability tensors of the homogenized slab are given by

$$\begin{bmatrix} \varepsilon_x & 0 & 0 \\ 0 & \varepsilon_y & 0 \\ 0 & 0 & \varepsilon_z \end{bmatrix} = \begin{bmatrix} 2.6 & 0 & 0 \\ 0 & 2.6 & 0 \\ 0 & 0 & 1.2 \end{bmatrix} \tag{3.16}$$

$$\begin{bmatrix} \mu_x & 0 & 0 \\ 0 & \mu_y & 0 \\ 0 & 0 & \mu_z \end{bmatrix} = \begin{bmatrix} 0.95 & 0 & 0 \\ 0 & 0.95 & 0 \\ 0 & 0 & 1.2 \end{bmatrix}. \tag{3.17}$$

The X-pol radiated by the two structures is shown in Fig. 3.5(c) to be similar. One can write the refractive index for the TE and TM modes as [100]

$$n_{\text{TE}} = \sqrt{\varepsilon_y \mu_x + (1 - \mu_x/\mu_z)\sin^2\theta} \tag{3.18}$$

$$n_{\text{TM}} = \sqrt{\varepsilon_x \mu_y + (1 - \varepsilon_x/\varepsilon_z)\sin^2\theta}, \tag{3.19}$$

where θ is the free-space propagation angle with respect to the axis of the material (z-axis). These indexes are shown as a function of the angle in Fig. 3.5(d). It is seen that the equivalent slab is characterized by an anisotropic behavior, where the TE and TM components of the field experience different refractive indexes at oblique incidence. Since the X-pol is given by the ratio of the TE and TM voltages in the equivalent transmission line, the different refractive indexes cause an increase in X-pol.
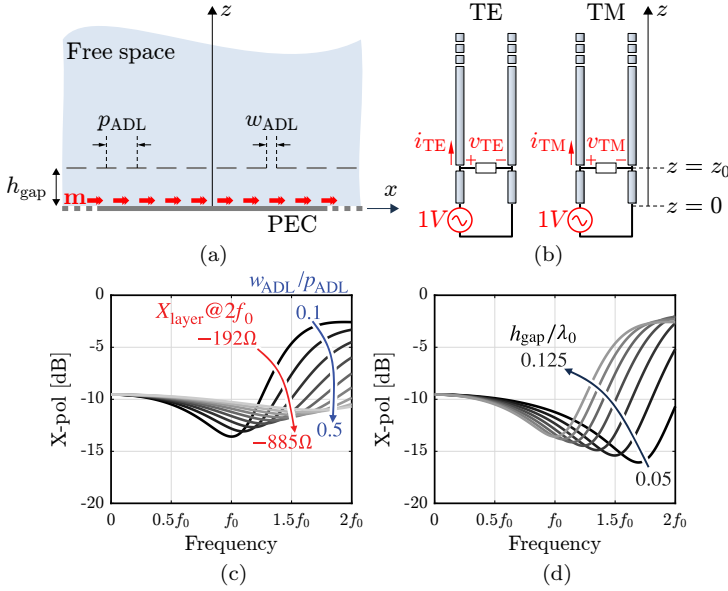
Figure 3.6: (a) Wheeler current sheet radiating in the presence of a capacitive grid and equivalent transmission lines for TE and TM modes; X-pol at $\phi = 45°$ and $\theta = 60°$, for different values of (b) the gap width to period ratio $w_{\mathrm{ADL}}/p_{\mathrm{ADL}}$, which corresponds to varying layer reactance, and (c) the distance from the current.

3.2.4 Single Layer of Artificial Dielectric

A similar effect as the dielectric WAIM is observed when a capacitive grid is placed at a certain distance from the radiating current, as depicted in Fig. 3.6(a). The capacitive grid is an array of sub-wavelength square patches, which form a single layer of ADLs. The ABCD matrix of the stratification is given by

$$\begin{bmatrix} A & B \\ C & D \end{bmatrix}_{\mathrm{strat}} = \begin{bmatrix} A & B \\ C & D \end{bmatrix}_{\mathrm{gap}} \begin{bmatrix} A & B \\ C & D \end{bmatrix}_{\mathrm{layer}} \tag{3.20}$$

where the ABCD matrix of the gap is defined in (3.13) and the ABCD matrix of the layer is given by

$$\begin{bmatrix} A & B \\ C & D \end{bmatrix}_{\mathrm{layer}} = \begin{bmatrix} 1 & 0 \\ Y_{\mathrm{layer},Ti} & 1 \end{bmatrix} . \tag{3.21}$$

The layer admittance is given by $Y_{\mathrm{layer,TM}} = jB_{\mathrm{layer}}$ and $Y_{\mathrm{layer,TE}} = jB_{\mathrm{layer}}(1 - 0.5\sin^2\theta)$, where B_{layer} is the susceptance of a layer, known in closed form [71, 85].

The current at $z = 0$ is given by $i_{Ti}(z = 0) = 1/Z_{\mathrm{in},Ti}$, with input impedance $Z_{\mathrm{in},Ti}$ equal to

$$Z_{\mathrm{in},Ti} = Z_{0Ti} \frac{Z'_{\mathrm{in},Ti} + jZ_{0Ti}\tan(k_{z0}h_{\mathrm{gap}})}{Z_{0Ti} + jZ'_{\mathrm{in},Ti}\tan(k_{z0}h_{\mathrm{gap}})} \tag{3.22}$$

where

$$Z'_{\mathrm{in},Ti} = \frac{1}{1/Z_{0Ti} + Y_{\mathrm{layer},Ti}} . \tag{3.23}$$
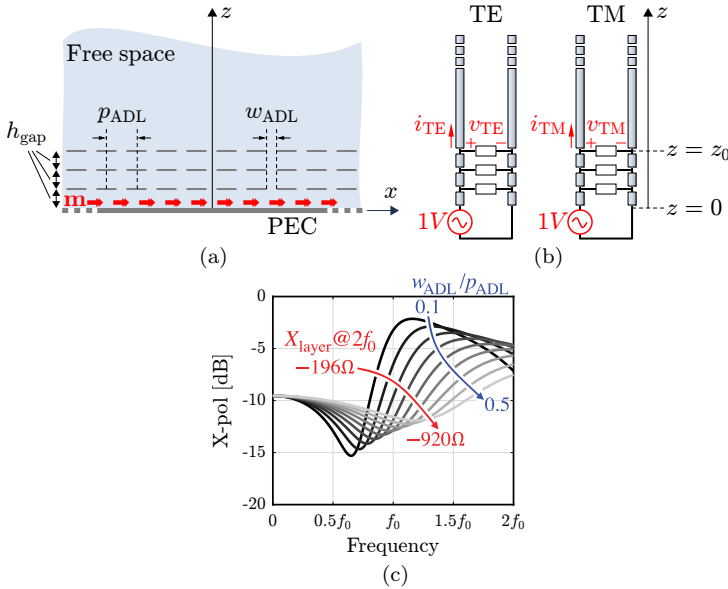
Figure 3.7: (a) Wheeler current sheet radiating in the presence of a three-layer capacitive grid and equivalent transmission lines for TE and TM modes. (b) X-pol at $\phi = 45°$ and $\theta = 60°$, for different values of the gap width to period ratio $w_{\text{ADL}}/p_{\text{ADL}}$, which corresponds to varying layer reactance.

The X-pol of a single metal layer with period $p_{\text{ADL}} = \lambda_0/8$, for $\phi = 45°$ and $\theta = 60°$, is shown in Fig. 3.6. Similar to how the dielectric WAIM yields higher X-pol for higher permittivity, the X-pol of the metal layer increases for smaller layer reactance $X_{\text{layer}} = -1/B_{\text{layer}}$, which corresponds to narrower gaps w_{ADL} between patches. Fig. 3.6(b) shows the X-pol for a layer placed at a distance $h_{\text{gap}} = \lambda_0/8$ from the current sheet and different values of w_{ADL}. When fixing the gap width to $w_{\text{ADL}} = 0.1p_{\text{ADL}}$ while varying the distance h_{gap}, the X-pol in Fig. 3.6(c) is obtained, which is shown to increase with the gap height.

When considering ADLs consisting of multiple metal layers, a similar effect occurs. The total ABCD matrix of the stratification can be found by cascading three times the air gap and the shunt layer capacitance in the equivalent transmission line. In Fig. 3.7 the X-pol for $\phi = 45°$ and $\theta = 60°$ of a three-layer ADL with period $p_{\text{ADL}} = \lambda_0/8$, inter-layer distance $h_{\text{gap}} = \lambda_0/16$, and varying w_{ADL} is plotted. The X-pol increases for ADLs with higher metal density, which corresponds to higher effective permittivity.

3.3 Relation Between X-Pol and Anisotropy

Similar to the WAIM, the higher X-pol in the presence of ADLs is caused by their anisotropy. The characteristic equivalent refractive index of ADLs as a function of incidence angle is shown in Fig. 3.8(a). It is seen that an ADL slab has an equivalent refractive index that changes with the incidence angle and changes differently for
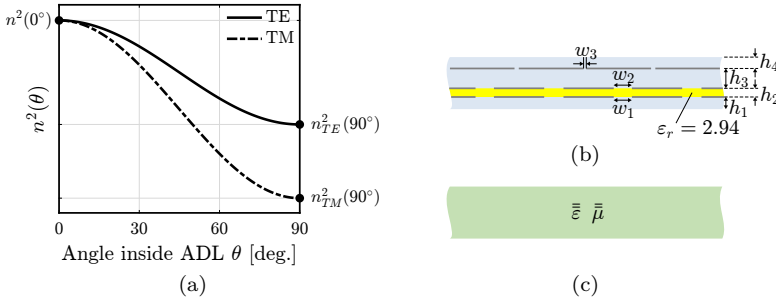
Figure 3.8: (a) Equivalent refractive index of a plane wave propagating through an ADL as a function of the angle inside the material. (b) Considered ADL stratification and (c) equivalent anisotropic material resulting from the homogenization.

the TE and TM modes. Similar to the dielectric WAIM example, the difference in refractive index for the TE and TM modes causes the ADL to exhibit higher X-pol as compared to an isotropic dielectric slab.

As an example, let us consider the ADL structure shown in Fig. 3.8(b), with $p_{\mathrm{ADL}} = 0.15\lambda_0$, $w_1 = w_2 = 0.03\lambda_0$, $w_3 = 0.007\lambda_0$, $h_1 = 0.033\lambda_0$, $h_2 = 0.013\lambda_0$, $h_3 = 0.043\lambda_0$, and $h_4 = 0.013\lambda_0$. The lower two ADLs are separated by a dielectric slab with relative permittivity $\varepsilon_r = 2.94$. The ADL can be homogenized as in Fig. 3.8(c) using the following equivalent relative permittivity and permeability tensors:

$$\begin{bmatrix} \varepsilon_x & 0 & 0 \\ 0 & \varepsilon_y & 0 \\ 0 & 0 & \varepsilon_z \end{bmatrix} = \begin{bmatrix} 9.4 & 0 & 0 \\ 0 & 9.4 & 0 \\ 0 & 0 & 1.2 \end{bmatrix} \tag{3.24}$$

$$\begin{bmatrix} \mu_x & 0 & 0 \\ 0 & \mu_y & 0 \\ 0 & 0 & \mu_z \end{bmatrix} = \begin{bmatrix} 1 & 0 & 0 \\ 0 & 1 & 0 \\ 0 & 0 & 0.2 \end{bmatrix}. \tag{3.25}$$

As evident from (3.19), the z-component of the permittivity tensor ε_z only affects the refractive index for the TM mode. If one imposes the condition $n_{\mathrm{TE}} = n_{\mathrm{TM}}$, and assumes that the ADLs consist of square patches (i.e., $\varepsilon_x = \varepsilon_y$ and $\mu_x = \mu_y$), we obtain

$$\varepsilon_z = \mu_z \varepsilon_x / \mu_x. \tag{3.26}$$

To illustrate the effect of this condition, Fig. 3.9(a) compares the X-pol of the homogenized slab with the values in (3.24), (3.25) to the ones obtained by applying (3.26). Without the condition, the X-pol increases to approximately $-2\,\mathrm{dB}$ near f_0. With the condition in (3.26), which gives $n_{\mathrm{TE}} = n_{\mathrm{TM}}$, the X-pol is reduced to below the free-space value, similar to an isotropic slab.

3.4 Superstrates with Reduced X-Pol

One possible method to alter the z-component of the permittivity tensor is by including vertical metallic insertions such as vias, as shown in Fig. 3.9(c). These vias
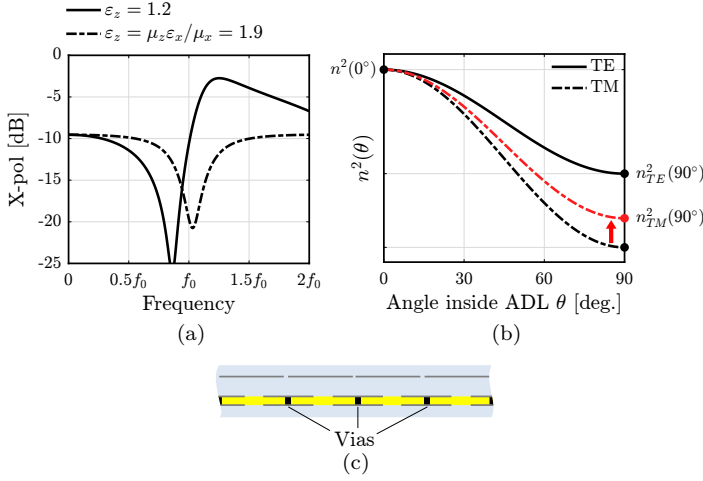
Figure 3.9: (a) X-pol for anisotropic slab above a grounded magnetic Wheeler current sheet, for different values of ε_z. (b) Effect of increased ε_z on the equivalent TM refractive index of an ADL. (c) Physical implementation of structure to increase ε_z, formed by connecting two layers of ADL together with vertical vias.

interact with the electric field along z and thereby increase ε_z. This reduces the difference between the TE and TM equivalent refractive indexes of the ADLs, as depicted in Fig. 3.9(b). Since an excessive increase of ε_z would cause surface waves in a realistic array, vias are placed only between the two lowest layers of the ADL.

3.4.1 Wire Medium

Such vertical metal pins can be placed in a periodic square lattice along x and y to form a wire medium. This structure is illustrated in Fig. 3.10(a). The z-component of the permittivity can be tuned by adjusting the spacing between the pins or their length. If the wire medium is inserted as a separate slab between the metal layers of the ADL, the maximum length of the pins is limited. To sufficiently increase the value of ε_z would require a very large number of closely spaced pins.

Fortunately, the effect of each pin on ε_z can be enhanced by connecting the vertical pins to the patches in the ADL, similar to the geometry proposed by [101]. This adds capacitive loading to the pins and makes them behave as if they are effectively longer, so fewer pins can be used to achieve the same enhancement of ε_z. This combination of ADL and the wire medium is illustrated in Fig. 3.10(b), where vias are added to implement the vertical metal pins.

3.4.2 Application to Wideband Arrays

To give a realistic example of how the ADL is used in wideband array design, we consider the unit cell as it is designed in Chapter 5. The unit cell is shown in Fig. 3.11(a), which shows a cavity-backed connected slot element, loaded with a four-layer ADL.
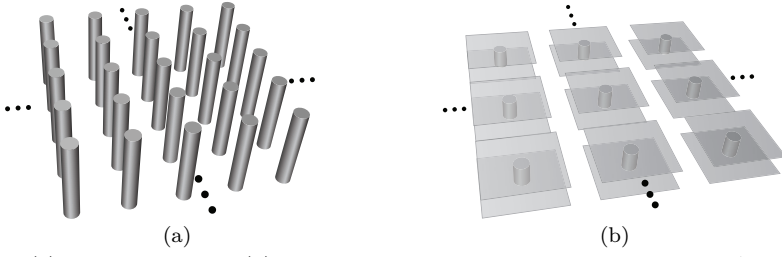
Figure 3.10: (a) Wire medium and (b) combination of wire medium and square-patch ADLs, resulting in a capacitively loaded wire medium.
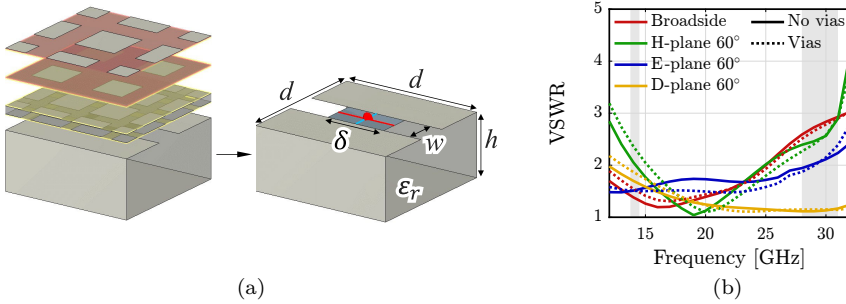
Figure 3.11: (a) 3D view of the connected array unit cell with ADL superstrate and (b) the simulated active VSWR (referred to $100\,\Omega$).

The unit cell with periodicity $d = 4.35\,\text{mm}$ consists of a connected slot with width $w = 1\,\text{mm}$, a delta-gap feed of length $\delta = 1.87\,\text{mm}$, placed at a distance of $h = 1.91\text{mm}$ from a backing reflector. The substrate between the backing reflector and the slot plane has a relative permittivity of $\varepsilon_r = 1.7$ and contains vertical walls along the direction of the slots.

The design example covers simultaneously the Ku- and the Ka-transmit SatCom bands, 13.75–14.5 GHz (for Ku) and 28–31 GHz (for Ka). The design is discussed in more detail in Chapters 5. In Fig. 3.11(b), the unit cell's active voltage standing wave ratio (VSWR) reported. The VSWR of the unit cell is lower than 3 for scanning up to $55°$ in the H-plane, and up to $60°$ in the D- and E-planes, for the two bands of interest (highlighted in grey).

The X-pol of this unit cell is calculated when scanning to $60°$ in the diagonal plane ($\phi = 45°$) for the stratification without vias [side view in Fig. 3.12(a)] and with vias [Fig. 3.12(b)]. The X-pol of the unit cell without vias in Fig. 3.12(c) exceeds $-5\,\text{dB}$ for the upper frequencies. The X-pol of the unit cell with vias is shown to be significantly lowered due to the presence of the vias. As shown by the dotted lines in Fig. 3.11(b), the VSWR is not adversely affected by the inclusion of the vias.

<table>
<tr><td>(a)</td><td>(b)</td><td>(c)</td></tr>
</table>
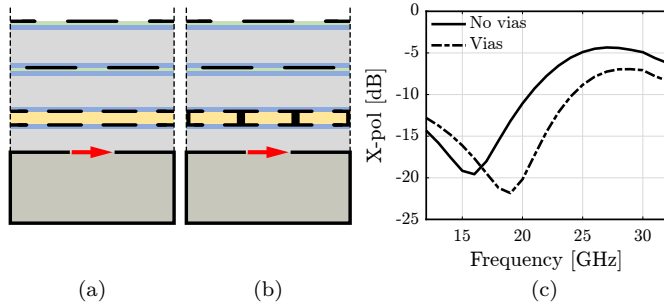
Figure 3.12: Side view of the connected slot unit cell with an artificial dielectric (a) without and (b) with vertical vias. (c) Simulated X-pol for scanning to 60° on the diagonal plane.

Table 3.1: ADL Dimensions [mm]

	p	h	w	s
Layer 4	2.175	0.8	0.75	1.09
Layer 3	2.175	0.8	1.1	0
Layer 2	1.45	0.254	0.36	0
Layer 1	1.45	0.5	0.36	0

Geometrical Parameters of the ADL

The artificial dielectric is designed following the procedure that will be described in Chapter 5 and consists of 4 layers which are defined by the unit cell periodicity p, their distance from the previous layer h, gap width w and shift with respect to the previous layer s. The values for each layer are listed in Table 3.1. Between layers 1 and 2, a dielectric with relative permittivity $\varepsilon_r = 2.2$ is present. In the ADL with vias, the patches in layers 1 and 2 are connected by a via with a diameter of 0.2 mm.

The materials used in the construction of the ADL are listed in Table 3.2, where the colors match those illustrated in Table 3.1. The thickness of the Rohacell 31 HF is not listed, as it varies to ensure the metal layers are separated by the distances listed in Table 3.1.

3.5 Experimental Validation

3.5.1 Measurement Setup

To independently assess the X-pol properties of the two ADLs, they are illuminated by a WR28 open-ended waveguide. A ground plane is placed under the ADL board, in which a hole is present through which the waveguide probe is inserted, as shown in the Fig. 3.13(a). Although the behavior of the X-pol with respect to frequency is different compared to the array case, the improvement in terms of X-pol reduction

Table 3.2: ADL Materials

		ε_r	Thickness
🟩	DuPont™ Pyralux® AP	3.4	25µm
🟦	Rogers CuClad® 6250	2.32	38µm
🟨	Rogers RT/duroid® 5880	2.2	254µm
⬜	Rohacell 31 HF®	1.04	Varies
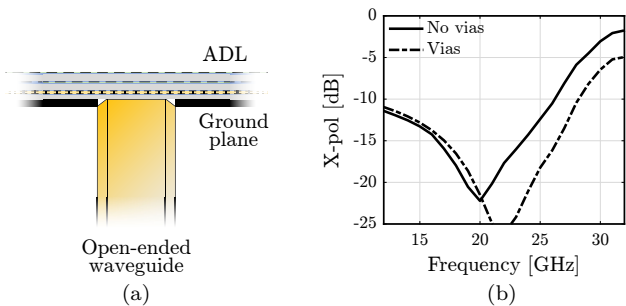
Figure 3.13: (a) Open-ended waveguide loaded with the ADL structure and (b) simulated X-pol with and without vias.
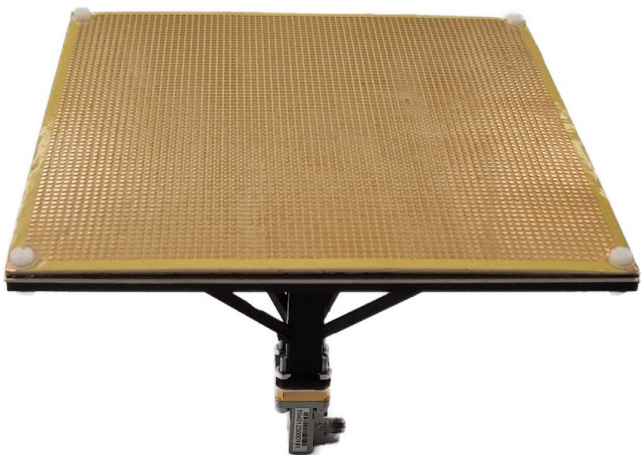
Figure 3.14: Photo of the assembled prototype showing the top layer of the 4-layer ADL over a ground plane in a mount that holds the WR28 waveguide.

achieved with the vias is similar in the two cases, as shown by the simulated X-pol in Fig. 3.13(b).

Two ADL boards were manufactured to experimentally verify the result: one with vias and one without. A photo of the assembled sample, including the ADL board, a ground plane, and the waveguide probe, is shown in Fig. 3.14. Since the X-pol levels in the Ku-band are comparable between the two boards, the measurements are only done for the Ka-band. A far-field measurement over a 26–36 GHz bandwidth is done.
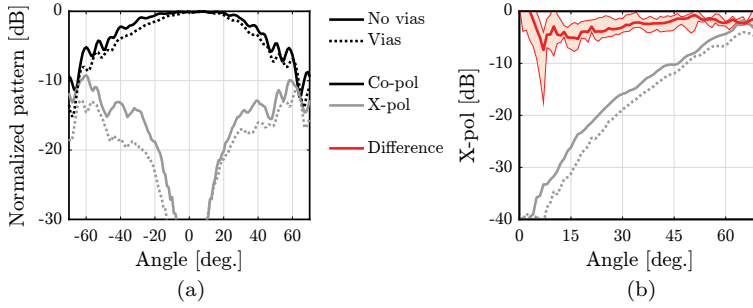
Figure 3.15: (a) Measured normalized patterns at 34 GHz of the prototype in the diagonal plane ($\phi = 45°$). (b) The average X-pol ratio over the 26–36 GHz range and the change in cross-polarization on the diagonal plane between the ADL without and the ADL with wire medium.

3.5.2 Results

The measured co- and cross-components of the electric field are shown for the diagonal plane at 34 GHz in Fig. 3.15(a). It can be observed that a lower X-pol level is obtained in the case of vias. The X-pol ratio for both versions of the ADL is shown for the diagonal plane in Fig. 3.15(b), along with the change in X-pol between the boards. To show the improvement both in frequency and in scanning angle, the figure shows the average X-pol ratio in the 26–36 GHz band over a range of 0-70 degrees. The red line shows the mean change in X-pol over that frequency band and the shaded region shows the range of values found in the averaged band. It is seen that the mean change ranges from -5 dB to -2 dB. Despite some discrepancy between the simulated and measured values, the X-pol is consistently reduced by the presence of the vias over the entire band and scanning range. It can be noted that the X-pol increases at angles close to broadside, but this corresponds to very low levels of X-pol (< -35 dB).

The reduction of 2–5 dB may not be sufficient for some applications, but the improvement shown here was mainly limited by the required bandwidth and scan range. In this example, the goal was to show that some X-pol reduction is possible while maintaining the scan range of $\pm 60°$ and the bandwidth 13.75–31 GHz. More significant reduction of X-pol is possible by placing more vias in each unit cell, at the expense of a reduced bandwidth or scan range.

3.6 Conclusion

A method for improving cross-polarization in wideband arrays that employ artificial dielectrics in their superstrate was presented. It was shown that the difference in the behavior of artificial dielectrics for TE and TM, which is desired for its positive effect on the scan volume and bandwidth, is also responsible for increased cross-polarization. A solution that employs vertical vias in the lower layers of the artificial dielectric has been shown to reduce the difference between the effective refractive index for the TE and TM modes. Simulations were presented to show this structure's effectiveness, and measurements showed a reduction in cross-polarization of 2–5 dB for up to 70° on the diagonal plane over a frequency range of 26–36 GHz.

Chapter 4

Efficient Analysis Method for Artificial Dielectric Layers with Vertical Metal Inclusions

Artificial dielectric superstrates have recently been studied due to their ability to enhance the bandwidth and scanning range of antenna arrays. One such superstrate consists of artificial dielectric layers (ADLs) and forms an effective medium that is anisotropic, which enables a larger scanning volume without supporting surface waves. When arrays that employ these ADLs scan to large angles on the diagonal plane, this anisotropy increases the cross-polarization of the array. This problem can be reduced by introducing vertical metal pins in the ADL superstrate which enables control over the vertical component of the permittivity tensor. This work describes an efficient analysis method based on a spectral domain method of moments. Entire-domain basis functions are used in a hybrid Cartesian and cylindrical method of moments to accurately model the currents on the structure and scattering parameters under plane wave incidence.

4.1 Introduction

The design process of wideband wide-scanning phased arrays is generally focused on increasing the bandwidth or scan volume. Even though many applications require polarization agility, polarization purity is generally only secondary. In planar wideband wide-scanning arrays, their coverage of large bandwidths and large scanning volumes is often achieved with dielectric superstrates or metal structures. In Chapter 3 it was shown that these superstrates can have a detrimental effect on the polarization purity.

Chapter 3 also proposed and demonstrated a novel structure that is able to reduce the X-pol caused by the superstrate. The structure is formed by connecting two layers of the ADL together using a vertical pin to form a pin-patch structure. The design used in the demonstration was optimized using a full-wave solver which means considerable time was spent on simulations. Since the structure has been proven to be effective, it is interesting to use it in future array designs that use ADL superstrates. To this end, a more efficient method to analyze and design these structures is desired.

In this chapter, such a method is developed based on a spectral domain method of moments. To this end, the currents on the structure are analyzed and appropriate entire-domain basis functions are proposed. An auxiliary cylindrical structure is used to accurately model the vertical current on the pin and the radial currents on the patches. Finally, to demonstrate the validity of the method, the scattering from an example structure is compared to results obtained from a commercial full-wave solver.

4.2 Effect of Vertical Pins on Cross-Polarization

While the benefit of the vertical pins in an ADL superstrate was already demonstrated in Chapter 3, an additional example is presented here. This example is based on a connected array design shown in [102]. The array covers both the Ku- and Ka-transmit bands while scanning up to 60°. The design is shown in Fig. 4.1(a) and consists of 6 metal layers over a dual-polarized slot plane, which is placed over a dielectric substrate with a backing reflector. Its X-pol when it is scanned to 60° in the diagonal plane is shown in black in Fig. 4.1(c) to exceed $-10\,\mathrm{dB}$ at the higher frequencies. To show the effect of the pins on the cross-polarization, a dielectric slab with a relative permittivity of 2.2 and metal vias are added between the first two ADLs, as illustrated in Fig. 4.1(b). The X-pol of the new unit cell is shown in Fig. 4.1(c) to be reduced by about $5\,\mathrm{dB}$ over most of the band.

4.3 Spectral Domain Method of Moments for Hybrid Artificial Dielectric Layers

The proposed analysis method uses a spectral domain method of moments to model the currents that are excited on the structure by the incident plane wave. The struc-
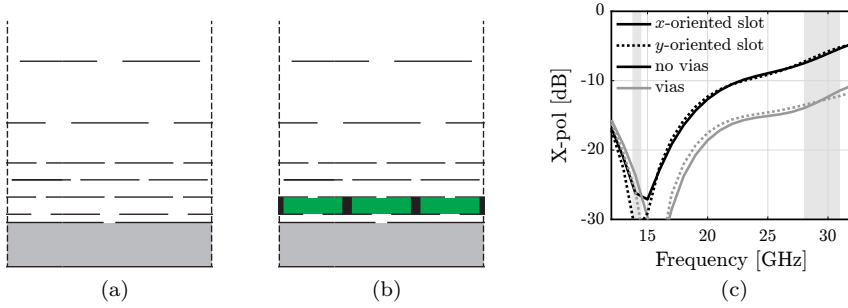
Figure 4.1: Side view of a connected array unit cell with artificial dielectric layers (a) without and (b) with vertical pins. (c) The X-pol for both unit cells when scanned to 60° in the diagonal plane.
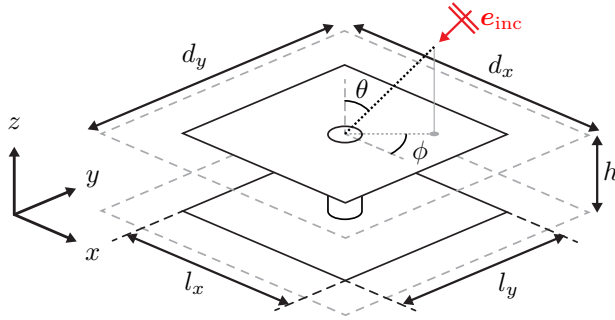
Figure 4.2: Geometry of the pin-patch structure with geometrical parameters. The incident field e_{inc} is illustrated as a plane wave with incidence angles θ and ϕ.

ture under investigation is illustrated in Fig. 4.2 and consists of two metal patches connected by a vertical pin, periodic along x and y with period d_x and d_y, respectively. The two patches are located at $x = y = 0$ and $z = \pm d/2$ and are assumed to rectangular with sides l_x by l_y and infinitesimally thin in z. The pin is taken as circular with radius r_1 and height h, located at $x = y = z = 0$. A plane wave incident from the angles θ and ϕ with wave number k_0 is considered.

To find the currents on the structure, an electric field integral equation is set up based on the requirement that the tangential electric field vanishes on the metal. This means the scattered field must be equal and opposite to the incident field

$$-e_{\text{scat}}(r) = e_{\text{inc}}(r). \tag{4.1}$$

The scattered field is given by the convolution of the currents on the structure with the Green's function, so we find the electric field integral equation

$$-\bar{\bar{g}} * j = -\iiint\limits_{-\infty}^{\infty} \bar{\bar{g}}(r, r')j(r)dr' = e_{\text{inc}}(r), \tag{4.2}$$

where $\bar{\bar{g}}$ is the dyadic Green's function and j are the equivalent currents on the structure. Assuming the equivalent current $j(r)$ is given by a set of N basis functions,

periodic in x and y

$$\boldsymbol{j}(\boldsymbol{r}) = \sum_{n_x=-\infty}^{\infty} \sum_{n_y=-\infty}^{\infty} \sum_{n=1}^{N} I_n \boldsymbol{b}_n(x-x_n-n_x d_x, y-y_n-n_y d_y, z-z_n) e^{-jk_{x0} n_x d_x} e^{-jk_{y0} n_y d_y}$$

(4.3)

where d_x, d_y are the periodicity in x and y, respectively, and I_n is the unknown complex amplitude of the nth basis function. Each basis function $\boldsymbol{b}_n$ is centered in $\boldsymbol{r}_n = (x_n, y_n, z_n)$. According to the Galerkin projection method, the test functions are chosen to be equal to the basis functions. It follows that

$$\sum_{n=1}^{N} I_n \left\langle -\bar{\bar{g}} * \boldsymbol{b}_n, \boldsymbol{b}_{n'} \right\rangle = \left\langle \boldsymbol{e}_{\text{inc}}, \boldsymbol{b}_{n'} \right\rangle , \qquad (4.4)$$

where $\langle \boldsymbol{a}, \boldsymbol{b} \rangle = \iiint \boldsymbol{a}(\boldsymbol{r}) \cdot \boldsymbol{b}(\boldsymbol{r}) d\boldsymbol{r}$ is the projection operator. The first projection is the mutual impedance between two basis functions, and is defined as

$$Z_{n'n} = \left\langle -\bar{\bar{g}} * \boldsymbol{b}_n, \boldsymbol{b}_{n'} \right\rangle . \qquad (4.5)$$

Following the steps reported in Appendix C, which involve applying the spectral domain method and the Floquet theorem, we find

$$Z_{n'n} = -\frac{1}{2\pi} \frac{1}{d_x d_y} \sum_{m_x=-\infty}^{\infty} \sum_{m_y=-\infty}^{\infty} e^{jk_{xm}(x_n-x_{n'})} e^{jk_{ym}(y_n-y_{n'})}$$

$$\int_{-\infty}^{\infty} \bar{\bar{\boldsymbol{G}}}(k_{xm}, k_{ym}, k_z) \boldsymbol{B}_n(k_{xm}, k_{ym}, k_z) \boldsymbol{B}_{n'}(-k_{xm}, -k_{ym}, -k_z) e^{jk_z(z_n-z_{n'})} dk_z , \quad (4.6)$$

where $k_{xm} = k_0 \sin\theta \cos\phi - 2\pi m_x/d_x$, $k_{ym} = k_0 \sin\theta \sin\phi - 2\pi m_x/d_y$ are the Floquet wavenumbers, $\boldsymbol{B}_n$ and $\boldsymbol{B}_{n'}$ are the three-dimensional Fourier transforms of the basis functions, and $\bar{\bar{\boldsymbol{G}}}$ is the spectral free-space dyadic Green's function.

Using the mutual impedance matrix, the unknown current weights $\boldsymbol{I}$ for the basis functions on the structure can be found using

$$\boldsymbol{I} = \boldsymbol{Z}^{-1} \boldsymbol{v}_{\text{inc}} , \qquad (4.7)$$

where the mutual impedance matrix $\boldsymbol{Z}$ for the basis functions is given by (4.6), and $\boldsymbol{v}_{\text{inc}}$ is the vector of incident voltages with elements $v_{\text{inc},n'} = \langle \boldsymbol{e}_{\text{inc}}, \boldsymbol{b}_{n'} \rangle$. For all expressions used in this work, the integral in k_z can be closed using a residue calculation, which is described in detail in Section C.9. Since the basis functions are also chosen such that their relevant transforms are known in closed form, the computation of the mutual impedance matrix purely analytical.

The basis functions can be freely chosen and a common choice is small-domain basis functions such as Rao-Wilton-Glisson [103]. However, to enable efficient evaluation of the matrix inversion that is required to solve the matrix equation, the number

of basis functions should be minimized. In this work, entire domain basis functions are defined that closely resemble the actual shape of the currents that are excited on the structure. This results in a method that is able to analyze the proposed geometry using only 9 basis functions.

4.3.1 Incident Field

The second projection in (4.4) projects the incident field onto the basis functions and gives the incident voltage on the basis functions. Suppose the incident field $e_{\text{inc}}(r)$ is a generic plane wave, which can be expressed as the superposition of transverse magnetic (TM) and transverse electric (TE) components

$$e_{\text{inc}}(r) = e_{\text{inc,TM}}(r) + e_{\text{inc,TE}}(r) = (V_{\text{TM}}\hat{\theta} + V_{\text{TE}}\hat{\phi})e^{-jk_{x0}x}e^{-jk_{y0}y}e^{+jk_{z0}z} \quad (4.8)$$

where the sign of k_{z0} represents the plane wave traveling in the $-z$-direction. The propagation constants along x, y and z can be defined as $k_{x0} = k\sin\theta\cos\phi$, $k_{y0} = k\sin\theta\sin\phi$ and $k_{z0} = k\cos\theta$, where k is the wave number in the homogeneous medium hosting the wires, and θ and ϕ are the elevation and azimuth of the incident plane wave, respectively.

The incident voltage is given by the spectral domain projection of the incident field onto the test functions, and the expressions to calculate it depend on the type of test function, as well as their direction. For a Cartesian test function, the incident voltage on the n'-th basis function is given by

$$\begin{aligned} v_{\text{inc},n'} = [&(V_{\text{TM}}\cos\theta\cos\phi - V_{\text{TE}}\sin\phi)\hat{x} + (V_{\text{TM}}\cos\theta\sin\phi + V_{\text{TE}}\cos\phi)\hat{y} \\ &+ (-V_{\text{TM}}\sin\theta)\hat{z}] \cdot \boldsymbol{B}_{n'}(-k_{x0}, -k_{y0}, +k_{z0})e^{-jk_{x0}x_{n'}}e^{-jk_{y0}y_{n'}}e^{+jk_{z0}z_{n'}} . \quad (4.9) \end{aligned}$$

4.3.2 Scattering Parameters

The scattered field can be found from the currents from the fundamental mode of the EFIE. For a Cartesian basis function, we find

$$\begin{aligned} e_{\text{scat}}(x, y, z) = \frac{1}{d_x d_y} \sum_{n=1}^{N} I_n B_{nxy}(k_{x0}, k_{y0})e^{-jk_{x0}(x-x_n)}e^{-jk_{y0}(y-y_n)} \\ \cdot \frac{1}{2\pi} \int\limits_{-\infty}^{\infty} \bar{\bar{\boldsymbol{G}}}(k_{x0}, k_{y0}, k_z)\hat{b}B_{nz}(k_z)e^{-jk_z(z-z_n)}dk_z \quad (4.10) \end{aligned}$$
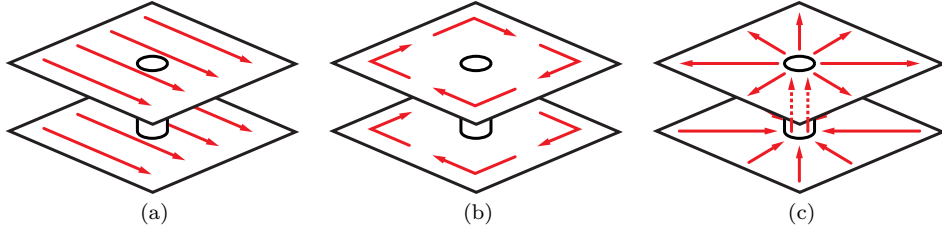
Figure 4.3: Shapes of the currents that are excited on the structure. (a) Linear current, (b) loop current, and (c) radial current.

The scattering parameters can be found from the incident and scattered fields by projecting them onto cylindrical coordinates, and taking the ratio

$$\Gamma_{\mathrm{TM}} = \frac{e_{\mathrm{scat},TM}}{e_{\mathrm{inc},TM}} \tag{4.11}$$

$$\Gamma_{\mathrm{TE}} = \frac{e_{\mathrm{scat},TE}}{e_{\mathrm{inc},TE}} \tag{4.12}$$

where

$$e_{TM} = \quad e_x \cos\phi + e_y \sin\phi \tag{4.13}$$
$$e_{TE} = -e_x \sin\phi + e_y \cos\phi \tag{4.14}$$

4.4 Entire-Domain Basis Functions

An incident plane wave can give rise to three currents on the patches, which are illustrated in Fig. 4.3. To model these three currents, three groups of basis functions are defined. The currents induced on the two square patches is represented by four basis functions per patch. The currents are assumed to be variable separable, so the basis functions are each defined by the product of different functions along the x, y, z, or ρ-direction. Since the patches are assumed to be infinitesimally thin, the current distribution along z for all basis functions on the patches is given by

$$b_z(z) = \delta(z), \tag{4.15}$$

where $\delta(z)$ is the Dirac delta function. Each basis function is assumed to be oriented along a specific axis, so along $\hat{x}$, $\hat{y}$, $\hat{z}$, or $\hat{\rho}$.

4.4.1 Linear Current

When the incident field is near broadside, the primary current excited on each patch is a linear current, as illustrated in Fig. 4.3(a). The direction of this linear current depends on the azimuth and polarization of the incident field. The component of

Figure 4.4: Basis functions used to model the linear currents on the pin-patch ADL. (a) Three-dimensional visualization of the shape of the basis function along $\hat{x}$, (b) inverse edge singular distribution, (c) adjustable edge singular distribution.

this current along $\hat{x}$ is modeled with an inverse edge singular distribution along x, and an adjustable edge singular distribution along y. The adjustable edge singular [104] is chosen to more accurately model the flattening of the current due to the capacitive effect between neighboring patches. The component along $\hat{y}$ is modeled with an adjustable edge singular along x, and an inverse edge singular along y. A 3D visualization of the shape of the linear basis function along $\hat{x}$ is shown in Fig. 4.4(a).

The inverse edge singular distribution is shown in Fig. 4.4(b) and given by

$$e(u) = \frac{4}{\pi l} \sqrt{1 - \left(\frac{2u}{l}\right)^2} \, \mathrm{rect}\left(\frac{u}{l}\right) \tag{4.16}$$

where u is either x or y, l is the length of the function, and the factor $4/(\pi l)$ is used to normalize the area of the basis function to 1. Here, rect is the unit rectangular function

$$\mathrm{rect}(u) = \begin{cases} 1 & \text{for } |u| < 0.5 \\ \frac{1}{2} & \text{for } |u| = 0.5 \\ 0 & \text{for } |u| > 0.5 \end{cases} \tag{4.17}$$

The adjustable edge singular distribution is shown in Fig. 4.4(c) and is given by

$$a_\kappa(u) = \frac{\mathrm{rect}\left(\frac{2u+l}{l\kappa} - \frac{1}{2}\right)}{\sqrt{1 - \left(\frac{2u+l}{\kappa l} - 1\right)^2}} + \frac{\mathrm{rect}\left(\frac{2u-l}{l\kappa} + \frac{1}{2}\right)}{\sqrt{1 - \left(\frac{2u-l}{\kappa l} + 1\right)^2}} + \mathrm{rect}\left(\frac{u}{l(1-\kappa)}\right) \mathrm{sign}(1-\kappa), \tag{4.18}$$

where

$$\mathrm{sign}(x) = \begin{cases} -1 & \text{if } x < 0 \\ 0 & \text{if } x = 0 \\ 1 & \text{if } x > 0. \end{cases} \tag{4.19}$$

The parameter κ defines the fraction of the function that is edge singular, and was found to be linear with the ratio of the patch size and the unit cell size. A linear fit of the values of κ that best describe the current on the patch yields $\kappa = 1.226 - 1.1489 l/d$, where l and d are the length and the periodicity of the basis function.

The linear basis functions along $\hat{x}$ and $\hat{y}$ can be written as

$$\boldsymbol{b}_{\text{linear},\hat{x}}(x, y, z) = e(x)a_\kappa(y)\delta(z)\hat{x} \tag{4.20}$$

$$\boldsymbol{b}_{\text{linear},\hat{y}}(x, y, z) = a_\kappa(x)e(y)\delta(z)\hat{y}. \tag{4.21}$$

The linear currents on the patches also give rise to vertical currents on the pin. The vertical currents are equal and opposite on either side of the pins so, assuming the pins are small with respect to wavelength, will not contribute to the scattering. As such, these currents can be neglected in the analysis.

Since the basis function are to be used in a spectral domain method of moments, the Fourier transforms of the functions are determined in closed-form to reduce the computational complexity of the method. The Fourier transform of an inverse edge singular distribution of length l is given by

$$E(k) = \frac{4}{\pi l}\frac{\pi}{k}J_1\left(k\frac{l}{2}\right), \tag{4.22}$$

where J_ν is the ν-th order Bessel function of the first kind, and $\lim_{k\to 0} E(k) = 1$. The Fourier transform of the adjustable edge singular distribution of length l is given by

$$A_\kappa(k) = lk\frac{\pi}{2}\left[J_0\left(k\frac{l}{2}\kappa\right)\cos\left(k\frac{l}{2}(1-\kappa)\right) - \mathbf{H}_0\left(k\frac{l}{2}\kappa\right)\sin\left(k\frac{l}{2}(1-\kappa)\right)\right]$$
$$+ l(1-\kappa)\operatorname{sinc}\left(k\frac{l}{2}(1-\kappa)\right) \tag{4.23}$$

where $\mathbf{H}_\alpha$ is the α-th order Struve function of the first kind. With these definitions, the spectral domain linear basis functions can be written as

$$\boldsymbol{B}_{\text{linear},\hat{x}}(k_x, k_y, k_z) = E(k_x)A_\kappa(k_y)\hat{x} \tag{4.24}$$

$$\boldsymbol{B}_{\text{linear},\hat{y}}(k_x, k_y, k_z) = A_\kappa(k_x)E(k_y)\hat{y}. \tag{4.25}$$

4.4.2 Loop Current

For grazing TE incidence, a loop current is excited on the patches, as illustrated in Fig. 4.3(b). This loop current can be modeled using another pair of basis functions along $\hat{x}$ and $\hat{y}$ on each patch. The current along $\hat{x}$ is modeled using an inverse edge singular along x, and an odd edge singular along y. The current along $\hat{y}$ is modeled using an odd edge singular along x, and an inverse edge singular along x. A 3D visualization of the shape of the basis function along $\hat{x}$ is shown in Fig. 4.5(a). The loop is formed by the superposition of the two basis functions, and an example when the weight of the two basis functions is equal is shown in Fig. 4.5(b).

The odd edge singular distribution is shown in Fig. 4.5(c) and is given by

$$o(u) = \left[\frac{1}{\sqrt{1-\left(\frac{2u}{l}\right)^2}} - 1\right]\left(\operatorname{rect}\left(\frac{2u}{l}+\frac{1}{2}\right) - \operatorname{rect}\left(\frac{2u}{l}-\frac{1}{2}\right)\right), \tag{4.26}$$
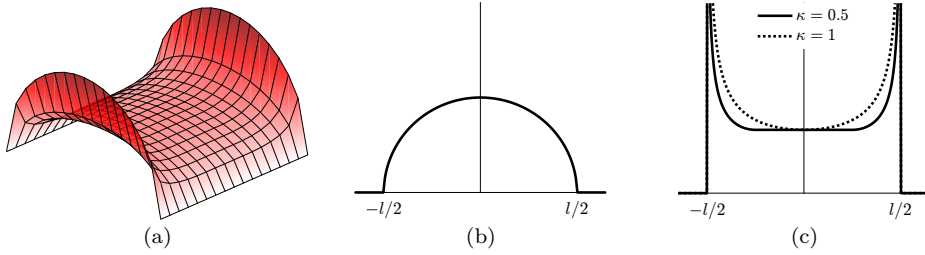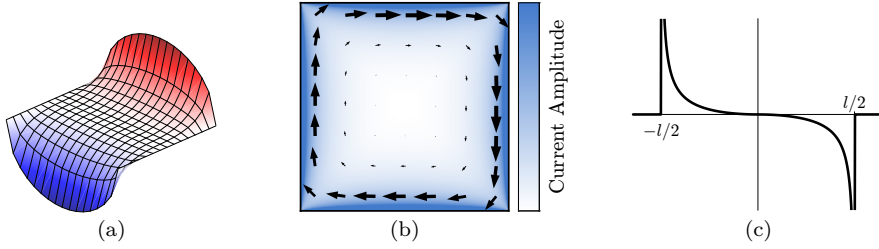
Figure 4.5: Basis functions used to model the linear currents on the pin-patch ADL. (a) Three-dimensional visualization of the shape of the basis function along $\hat{x}$, (b) color map of current amplitude when the two basis functions have equal weight, with arrows denoting the direction of the current, (c) odd edge singular distribution.

with Fourier transform

$$O(k) = e^{jkl/2}\left(J_0(kl) - j\mathbf{H}_0(kl)\right) - e^{-jkl/2}\left(J_0(-kl) - j\mathbf{H}_0(-kl)\right) . \tag{4.27}$$

The loop basis functions along $\hat{x}$ and $\hat{y}$ can be written as

$$\boldsymbol{b}_{\text{loop},\hat{x}}(x, y, z) = e(x)o(y)\delta(z)\hat{x} \tag{4.28}$$

$$\boldsymbol{b}_{\text{loop},\hat{y}}(x, y, z) = o(x)e(y)\delta(z)\hat{y} . \tag{4.29}$$

The loop current has a null in the center, so no current is excited on the pin. The spectral domain loop basis functions can be written as

$$\boldsymbol{B}_{\text{loop},\hat{x}}(k_x, k_y, k_z) = E(k_x)O(k_y)\hat{x} \tag{4.30}$$

$$\boldsymbol{B}_{\text{loop},\hat{y}}(k_x, k_y, k_z) = O(k_x)E(k_y)\hat{y} . \tag{4.31}$$

4.4.3 Currents due to the Pin

The vertical component of the field interacts with the pin and generates a vertical current on the pin itself. This vertical current terminates in the patches and spreads radially across the patches. This current is shown in Fig. 4.6(a) and can be described using the distribution

$$\frac{1}{\sqrt{x^2 + y^2}} \operatorname{rect}\left(\frac{x}{l_x}\right) \operatorname{rect}\left(\frac{y}{l_y}\right) . \tag{4.32}$$

This function has a discontinuity at the edge of the patch, so it is multiplied by the inverse edge singular function to force it to zero at the edges of the patch. The resulting function is given by

$$\frac{1}{\sqrt{x^2 + y^2}} \operatorname{rect}\left(\frac{x}{l_x}\right) \operatorname{rect}\left(\frac{y}{l_y}\right) \sqrt{1 - \left(\frac{2x}{l_x}\right)^2} \sqrt{1 - \left(\frac{2y}{l_y}\right)^2} . \tag{4.33}$$
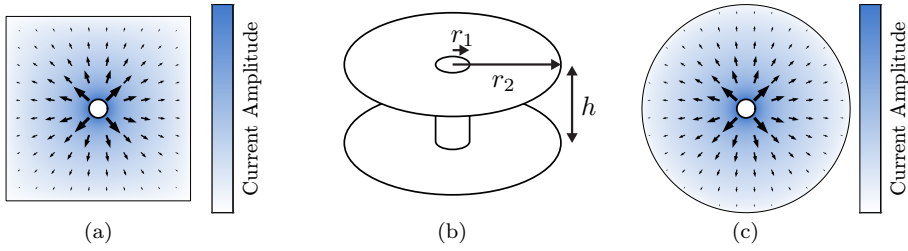
Figure 4.6: Current amplitude due to the radial spreading on the (a) square and (b) round patch, with arrows denoting the direction of the current. (c) Equivalent circular geometry used to model the current on the pin and the radial current on the patches.

However, the required transform of this function is not known in closed-form and would therefore require a computationally expensive numerical evaluation.

Since the current is along the radial direction, it is convenient to instead model it using cylindrical coordinates. This means that the pin and patches are modeled using an auxiliary circular structure, as shown in Fig. 4.6(b). The radial current is modeled with the product of $1/\rho$ and an inverse edge singular function, where the $1/\rho$ models the spreading of the current and the inverse edge singular function ensures that the current goes to zero at the edge of the patch. The current is assumed to be constant in azimuth ϕ. The resulting radial current on a circular patch is shown in Fig. 4.6(c).

The radial current on the patch inside the radius of the pin ($0 < \rho < r_1$) is zero due to symmetry, so the basis function must be set to zero for $\rho < r_1$. To retain the closed-form Hankel transforms, this zero was introduced by subtracting a second order Taylor expansion. The basis function shown in Fig. 4.7(a) and can be written as

$$\boldsymbol{b}_{\text{radial}}(\rho, z) = \left[\frac{1}{\rho} \sqrt{1 - \left(\frac{\rho}{r_2} \right)^2} \, \text{rect}\left(\frac{\rho}{2r_2} \right) - \left(1 - \frac{\rho^2}{2r_2^2} \right) \text{rect}\left(\frac{\rho}{2r_1} \right) \right] \delta(z) \hat{\rho}, \quad (4.34)$$

where r_2 is the radius of the equivalent circular patch. The radius of the equivalent circular patch is chosen such that the area of the circle matches that of the patch so, for a square patch ($l_x = l_y$), this yields $r_2 = l_x/\sqrt{\pi}$. To show the validity of this approach, a pin-patch structure is placed in a periodic environment and illuminated with a 30 GHz TM-polarized incident plane wave incident at a grazing angle (89°). The structure consists of two circular patches of radius $r_2 = 1$ mm or two square patches of length $l_x = l_y = 1.77$ mm. The patches are spaced $d = 0.2$ mm apart and placed in a periodic lattice of $d_x = d_y = 2.5$ mm. Figure 4.7(c) shows the currents on the pin as a function of patch area for square and circular patches, which are seen to be in close agreement.

The vertical current on the pin is assumed to be only on the surface of the pin (infinitesimal in ρ) and to be constant in z and ϕ. The shape of the current on the pin along z is shown in Fig. 4.7(b). The current is oriented along $\hat{z}$ and is given by

$$\boldsymbol{b}_{\text{pin}}(\rho, z) = \delta(\rho - r_1) \, \text{rect}\left(\frac{z}{d} \right) \hat{z}. \quad (4.35)$$
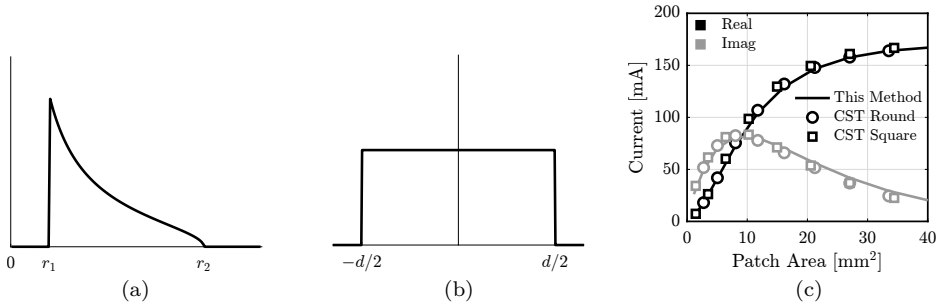
Figure 4.7: (a) $1/\rho$ distribution with forcing term and zeroed pin radius and (b) rectangular distribution. (c) Vertical current on the pin of the pin-patch structure versus patch area under plane-wave illumination. The plane-wave is TM-polarized and is incident at a grazing angle (89°). Results are compared between the method of moments and CST Microwave Studio for round patches and square patches.

The three basis functions that model the current on the pin and the current on the patches are discontinuous. To ensure continuity of the current, the amplitude of these basis functions are set to be equal. This is done by summing the rows and columns of the impedance matrix corresponding to these three basis functions. This ensures convergence of the Floquet sums, which is described in more detail in Appendix C. Additionally, due to symmetry, the current on the pin and the radial current on the patches do not couple to the linear and loop currents and the mutual impedances between them are zero. As a result, the method only requires an 8×8 matrix inversion.

To calculate the mutual and self impedances of the three cylindrical basis functions in the rectangular periodic lattice, a spectral domain method of moments was developed that accepts basis functions in Cartesian or in cylindrical coordinates. The derivation of this method of moments is shown in Appendix C and yields expressions for the mutual impedances and incident voltages of cylindrical basis functions that involve Hankel transforms of the basis functions. For this reason, the Hankel transforms of 0th and 1st order are shown below instead of the Fourier transforms that were shown for the Cartesian basis functions.

The Hankel transforms of the 0th and 1st order of a function $f(\rho)$ are denoted by

$$F_{J_0}(k_\rho) = \int_0^\infty f(\rho) J_0(k_\rho \rho) \rho d\rho \tag{4.36}$$

$$F_{J_1}(k_\rho) = \int_0^\infty f(\rho) J_1(k_\rho \rho) \rho d\rho \,. \tag{4.37}$$

In the cylindrical method of moments expression, the Hankel transform is applied to the ρ-dependence, and the Fourier transform is used for the z-dependence. The

resulting transforms of the radial basis function is given by

$$\boldsymbol{B}_{\text{radial},J_0}(k_\rho, k_z) = \left[-\frac{r_1}{2} J_0(k_\rho r_1)(2 - \pi \mathbf{H}_1(k_\rho r_1)\left(1 + \frac{1}{2k_\rho^2 r_2^2}\right) \right. \tag{4.38}$$

$$+ \frac{r_1}{2} J_1(k_\rho r_1)(k_\rho \frac{r_1}{r_2^2} - \pi \mathbf{H}_0(k_\rho r_1)\left(1 + \frac{1}{2k_\rho^2 r_2^2}\right)$$

$$\left. + \frac{r_2}{4}\pi \left(J_0\left(k_\rho \frac{r_2}{2}\right)^2 + J_1\left(k_\rho \frac{r_2}{2}\right)^2 \right) \right]\hat{\rho}$$

$$\boldsymbol{B}_{\text{radial},J_1}(k_\rho, k_z) = \frac{1}{k_\rho}\left(J_0(k_\rho r_1) + \frac{1}{2}\frac{r_1^2}{r_2^2} J_2(k_\rho r_1) - \text{sinc}(k_\rho r_2) \right)\hat{\rho}. \tag{4.39}$$

For the basis function that models the currents on the pin, the transforms are given by

$$\boldsymbol{B}_{\text{pin},J_0}(k_\rho, k_z) = \frac{1}{2\pi} J_0(k_\rho r_1) l \, \text{sinc}\left(k_z \frac{l}{2}\right) \hat{z} \tag{4.40}$$

$$\boldsymbol{B}_{\text{pin},J_1}(k_\rho, k_z) = \frac{1}{2\pi} J_1(k_\rho r_1) l \, \text{sinc}\left(k_z \frac{l}{2}\right) \hat{z}. \tag{4.41}$$

4.5 Validation

The method is validated by comparing the results calculated using this method to those obtained by simulating the structure in the commercial full-wave solver CST Microwave Studio. Validation is done in two parts; first the currents obtained using this method are compared, and then the full square pin-patch structure is analyzed under TE and TM plane-waves incident at various angles.

To verify the accuracy of the circular pin-patch analysis, the circular pin-patch structure in Fig. 4.7(c) is again considered with a 30 GHz TM-polarized plane wave incident at an elevation angle of $89°$. The currents on the patches and the pin are shown in Fig. 4.8(a) and in Fig. 4.8(b), respectively. It is seen that the method is able to accurately model the shape, amplitude, and phase of the current on the circular patches and on the pin.

Next, the square pin-patch structure used in Chapter 3 is analyzed. The structure consists of two square patches with sides $l_x = l_y = 1.09$ mm separated by a distance $d = 0.254$ mm. The two patches are connected by a pin with radius $r_1 = 0.1$ mm and height h. The structure is in a periodic environment along x and y with a periodicity of $d_x = d_y = 1.45$ mm. The structure is illuminated by a 30 GHz TE- or TM-polarized plane wave incident at an angle θ along the $\phi = 0°$ plane, and currents on the structure are found using the method and basis functions described above.

The currents on the top patch are shown on cuts along x and y in Fig. 4.9(a) and Fig. 4.9(b), respectively. A good agreement can be seen for most of the cut, but an increasing difference is seen near the pin. This difference is due to the current entering and exiting the pin, which was neglected for the linear current, but causes
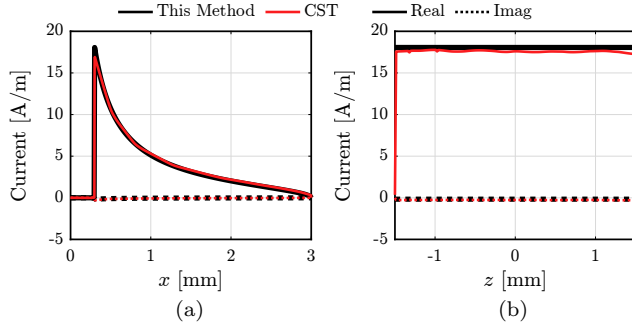
Figure 4.8: Current on a circular pin-patch structure under TM plane-wave illumination, incident at an elevation angle of $89°$. (a) Current along x on the top patch and (b) current along z on the pin.
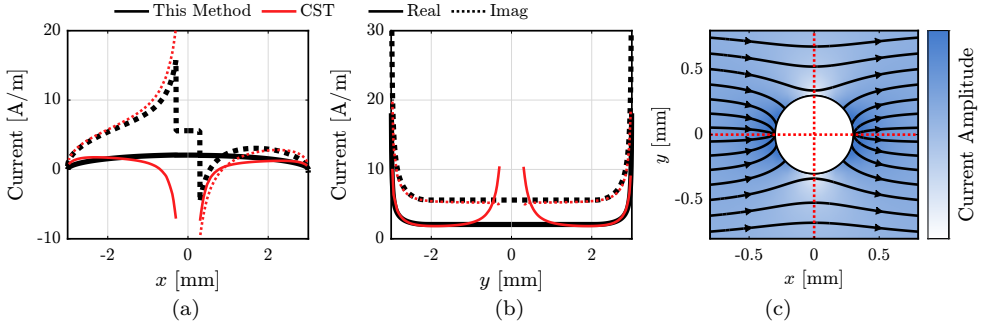
Figure 4.9: Current on a circular pin-patch structure under TM plane-wave illumination, incident at an elevation angle of $10°$. (a) Current on the top patch along $\hat{x}$ versus x and (b) versus y. (c) Shows a close-up of the real part of the current near the pin on the top patch with the paths of the current highlighted. The two cuts along which (a) and (b) are calculated are shown horizontally and vertically, respectively.

a crowding effect near the edge of the pin. To show this effect, the current on the patch is extracted from CST and the path of the currents is traced. A close-up of the region around the pin is shown in Fig. 4.9(c), where the crowding effect is clearly visible. This crowding is a local effect and does not influence the scattering of the structure, as will be shown by the scattering parameters.

The currents can be used to calculate the scattered field and scattering parameters using the expressions in Section 4.3.2. The structure for which the currents were shown in Fig. 4.9 is analyzed, and the scattering parameters are computed. The resulting reflection coefficients are shown in Fig. 4.10 to be in good agreement with those obtained using CST.

The results shown in Fig. 4.10 took 8 s for 90 scanning angles using the proposed method, and 40 min in CST. When optimizing a design, a single incidence angle is generally considered, and the geometrical parameters are changed for each iteration. Evaluating a single angle took 90 ms using the proposed method, and 4 min in CST. This means that the method is able to provide the computational efficiency that is required when optimizing a design, and enables the use of simple iterative techniques to design a particular behavior.
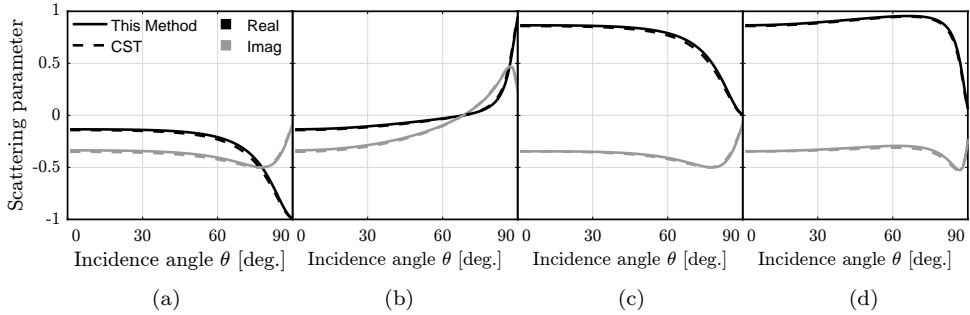
Figure 4.10: Scattering parameters at 30 GHz vs incidence angle for plane wave incidence on the pin-patch structure used in Chapter 3. (a) Reflection under TE and (b) TM incidence, and (c) transmission under TE and (d) TM incidence. The geometrical parameters of the structure are $l_x = l_y = 1.09$ mm, $d = 0.254$ mm, and $r_1 = 0.1$ mm. The structures are in a periodic environment along x and y with a periodicity of $d_x = d_y = 1.45$ mm.

4.6 Conclusion

A periodic structure consisting of set of two patches connected by a vertical pin was analyzed. Such a unit cell was shown to significantly reduce the cross-polarization in wideband arrays that use artificial dielectrics in their superstrate. An analysis technique is proposed based on the spectral domain method of moments. The key aspect of the procedure is the use of entire-domain basis functions to define the electric current distribution on the structure.

Three types of basis functions are defined and shown to describe accurately the currents:

- The first basis function represents a linear distribution on the patches, aligned with the polarization of the incident plane wave. To model patches with variable sizes, an adjustable edge singular profile is chosen as transverse distribution.

- The second basis function represents a loop current on the patches, which is only excited under TE incidence. Both the first and second basis functions are present on the patches also in absence of the vertical pin.

- The third basis function describes the current flowing on the pin and spreading radially across the patches. This current is excited by the vertical component of the electric field for oblique TM incidence. To simplify the analysis, a cylindrical analogy is used, by introducing equivalent circular patches. The analogy is shown to accurately model the current resulting from the pin.

Currents and reflection coefficients obtained with the proposed method are shown to be in good agreement with those obtained in a commercial full-wave solver. The method is able to speed up the analysis of the structure by a factor 2500 with respect to CST for a single incidence angle and frequency.

Chapter 5

Wideband Wide-Scanning Connected Slot Array Design Covering both the Ku- and Ka-Satcom Bands

The design of a dual-polarized broadband array that simultaneously covers the Ku- and Ka- satellite communication transmit bands is presented. The array element is a connected slot backed by a ground plane and loaded with artificial dielectric layers. The design includes the detailed feeding structure for the two polarizations and accounts for realistic manufacturing constraints in the definition of the layer stack-up. A conical scan volume of $\pm 60°$ is achieved with active voltage standing wave ratio (VSWR) below 2.5 in the Ku-band and below 2.8 in the Ka-band. A study on techniques to reduce X-pol or to achieve an arbitrary given polarization is detailed and it is shown that an arbitrary polarization can be achieved through the use of two orthogonal radiators. Various corporate feeding networks are detailed that scan the array to a set of fixed pointing angles. Measurements are presented for a test sample which demonstrate the feasibility of using a 1024-element feeding network and quantify the losses that can be expected from such a network.

5.1 Introduction

The connected slot array with artificial dielectrics concept has been demonstrated in the past. A prototype covering the 6–15 GHz band was presented in [54] with a dual-polarized aperture consisting of 16×16 elements. However, that design used 8 metal layers in the ADL superstrate to cover its 2.5:1 bandwidth. Here, a 2.25:1 bandwidth (13.75–31 GHz) is targeted and is covered using only 4 metal layers, through the use of the additional degrees of freedom offered by the ability to use different geometrical parameters for each individual layer. Additionally, the higher upper operational frequency offers challenges due to geometrical constraints that arise from the PCB manufacturing process.

The design shown in this chapter is dual-polarized, which allows flexibility in the polarization of the radiated fields. The radiated field should have slant linear polarization for the Ku- and in circular polarization for the Ka-band. The presence of the two orthogonal radiators in each unit cell enables them to be combined to achieve an arbitrary polarization. A study on cancellation techniques and their performance is presented.

The scan capability of the phased array prototype was to be demonstrated by designing and manufacturing a finite number of fixed beamforming feeding structures, each for a specific scan angle, including the most representative scanning conditions to assess the array performance: broadside, maximum scan on the main and diagonal planes. The feeding networks consists of 1 to N power combiners and implement static true time delay lines at the level of the individual array elements for the mentioned fixed scan conditions. A test printed circuit board with the feeding lines is manufactured and measured to quantify the losses.

5.2 Artificial Dielectric Design

5.2.1 Comparison of Transformers

The artificial dielectric slab is to implement an impedance transformer from the impedance of free space to a lower impedance at the slot plane. To determine the impedance of each section of the transformer, various canonical impedance transformers are considered [105]. The options that are considered are:

- Single-section quarter-wave

- Two-section Chebyshev with -14 dB passband

- Two-section Binomial

- Exponential taper

The transformers are designed to implement a transition from the impedance of free space ($377\,\Omega$) to $80\,\Omega$. The impedances used for the one- and two-section

Table 5.1: Impedance transformer section impedances.

Transformer	Z_1 [Ω]	Z_2 [Ω]
Single quarter-wave	173.7	
2-section Binomial	117.9	255.9
2-section Chebyshev	130.27	231.52
Exponential taper	$Z(x) = 80e^{1.55x/L}$	
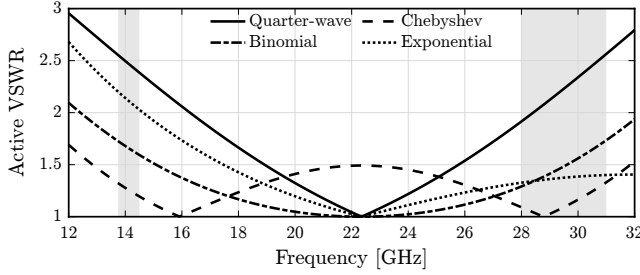
Figure 5.1: VSWR of the considered impedance transformers when normalized to $80\,\Omega$ and $377\,\Omega$.

5

transformers are shown in Table 5.1. The length of the sections is quarter-wave at the center frequency of the target bandwidth, 22.35 GHz. The resulting VSWR is shown in Fig. 5.1, where the shaded areas highlight the targeted Ku- and Ka-transmit bands. It can be observed that the single quarter-wave transformer is too narrow band to cover both bands. The two-section binomial transformer exhibits a wider bandwidth and VSWR below 2 in both bands. The Chebyshev transformer has an even lower VSWR in the bands of interest due to its two separate nulls. The position of the nulls can be tuned by changing the center frequency of design and the level of the pass band reflection coefficient. This control of the position of the nulls gives an advantage when optimizing the matching efficiency of the unit cell for large scanning ranges.

An exponentially tapered transformer is also reported for comparison, with the same length as the two-section transformers, $L = \lambda/2$ at 22.35 GHz. A continuous exponential taper does not have a high frequency limit, while for the given height the lower frequency limit (VSWR < 2) is about 15 GHz. To achieve the desired lower frequency of 13.75 GHz, the exponential transformer should be longer, resulting in a unit cell with higher profile. Moreover, implementing a nearly continuous impedance taper with an artificial dielectric would require a large number of metal layers, with increased costs and manufacturing complexity. Therefore, the two-section Chebyshev transformer is selected for the design.

The steps in Fig. 5.2 are used to convert the ideal transformer into an artificial dielectric stratification. From the two-section transformer in vacuum [Fig. 5.2(a)], the permittivity of the lines is changed and their length is adjusted accordingly to achieve the same behavior [Fig. 5.2(b)]. The transmission line in Fig. 5.2(b) is the equivalent circuit representation of a plane wave traveling through two dielectric slabs [Fig. 5.2(c)]. An ADL slab is then synthesized with an equivalent permittivity that
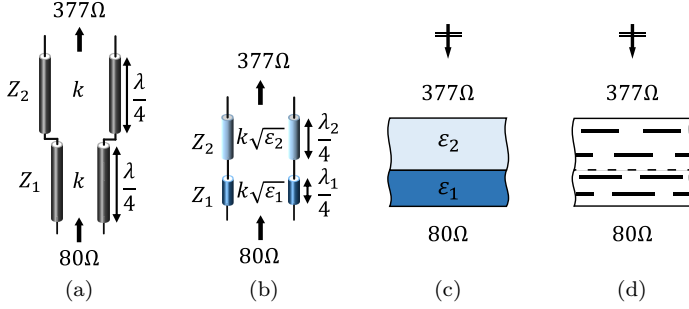
Figure 5.2: (a) Original two-section transformer with phase constant and wavelength in vacuum; (b) equivalent transformer achieved by changing the relative permittivity of the lines; (c) plane-wave incidence on two dielectric slabs represented by the transmission line model in (b); (d) artificial dielectric with the same equivalent parameters as the real dielectrics in (c).
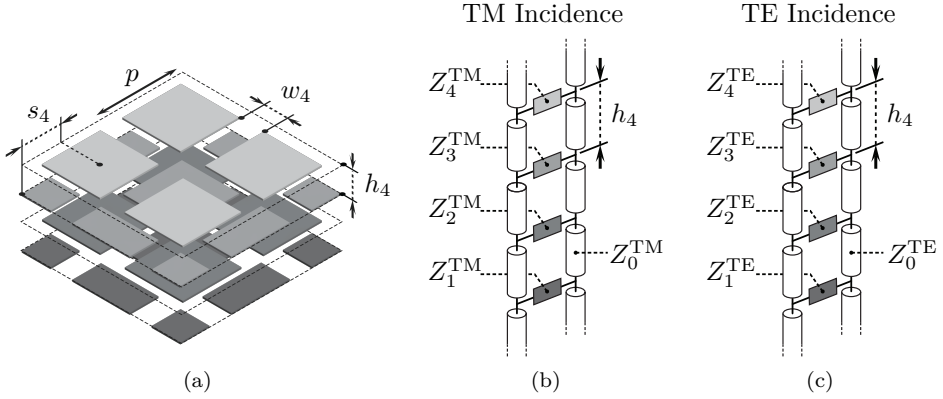
Figure 5.3: (a) Four-layer ADL stack with annotated geometrical parameters of the topmost layer. (b) Equivalent transmission line models for TE and (c) TM incidence.

matches the dielectric slabs [Fig. 5.2(d)]. For the synthesis of the artificial dielectric (AD) with the desired effective electrical parameters, the closed-form analysis described in [73] is used.

5.2.2 Synthesis of Artificial Dielectric Layers

Since the ADL transformer is to follow a Chebyshev impedance profile, the next step is to design the geometrical parameters of the AD slab such that it implements that profile. Each section of the transformer is implemented using multiple AD layers to realize an effective dielectric permittivity that corresponds to the desired impedance in that section. The effective dielectric permittivity of the layer is determined from its scattering (S-)parameters under plane wave incidence using a homogenization procedure [100]. The S-parameters are computed using the closed-form analysis described in [73].
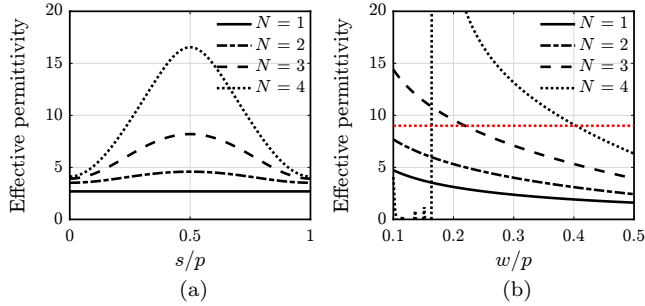
Figure 5.4: Relative permittivity vs (a) s or (b) w of an ADL slab consisting of N layers with $p = \lambda_0/4$, $L = \lambda_0/6$, $w = p/4$, $s = p/2$. The red dotted line shows the edge of the region assumed to no longer be invalid.

The AD has several geometrical parameters that can be used to design a desired permittivity. These parameters are illustrated in Fig. 5.3 and are listed below:

- Periodicity p: the distance between the centers of the patches.

- Shift s: The shift in horizontal position between the centers of the patches in two adjacent layers.

- Interlayer distance h: The vertical distance between the patches.

- Gap width w: The distance between the edges of the patches.

In general, the effective permittivity $\varepsilon_{r,\text{eff}}$ of the ADL slab increases with metal density. As such, it increases as a function of p and s and decreases as a function of w and h. To enable the use of unit cell simulations, the period p must be chosen as the array periodicity d_{array} divided by an integer. The patches must also be small in terms of wavelength ($p < \lambda/4$) to ensure the validity of the closed-form expressions. Since high permittivity values are desired, and the permittivity increases with p, the periodicity is maximized at $p = d_{\text{array}}/2 < \lambda/4$.

Larger shift between successive layers enhance the layer capacitance, and therefore result in a higher dielectric constant [72]. This can also be seen in Fig. 5.4(a), where the permittivity is seen to increase as the shift approaches $p/2$. As such, to minimize the number of layers, the shift between layers is half the unit cell size $s = p/2$.

Each section of a Chebyshev transformer has a fixed height $L = \lambda_{\text{d}}/4$ of a quarter wavelength in the dielectric. As such, the inter-layer distance h in the AD depends on the height of the transformer section and the number of layers N. Since an air-gap is included above and the set of layers with a height of $d/2$, the interlayer distance is given by $d = L/N$. Fig. 5.4 shows that the permittivity increases with the number of layers. The cost of an ADL slab is primarily determined by the number of metal layers in the stratification, so the number of layers should be minimized.

This leaves two free parameters that can be used to realize a certain given dielectric permittivity, N and w. Since the number of layers is to be minimized, w is primarily used and N is increased only if the permittivity cannot be achieved. Fig. 5.4 shows
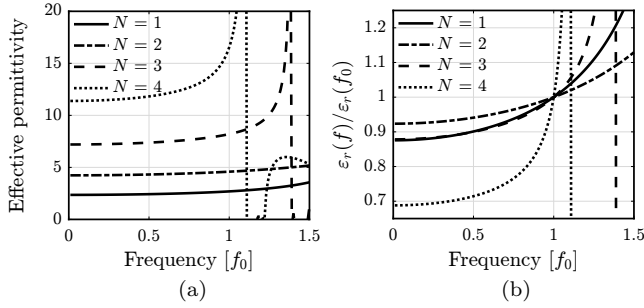
Figure 5.5: (a) Relative permittivity vs frequency of an ADL slab consisting of N layers with $p = \lambda_0/4$, $L = \lambda_0/6$, $w = p/4$, $s = p/2$. (b) Normalized to the permittivity at f_0.

Table 5.2: ADL impedance transformer section impedance and geometrical parameters.

	Z [Ω]	N	w_1 [mm]	w_2 [mm]	s	p [mm]	h [mm]
Section 1	130.27	2	0.221	0.111	$p/2$	2.175	0.617
Section 2	231.52	2	0.552	0.552	$p/2$	2.175	1.097

that the dielectric permittivity as a function of the gap width w is nonincreasing, which means that simple error minimization techniques such as Newton-Raphson can be used.

As is shown from the negative values obtained for $N = 4$, $w/p < 0.17$, the relative permittivity can not be accurately determined for very high densities. This is because the length of the section becomes electrically large and the assumptions made in the homogenization procedure [100] no longer hold. The retrieval method for deriving the effective permittivity of the AD sections [100] is valid for slabs with thickness smaller than half a wavelength. Larger thicknesses support resonances that create ambiguity in the estimation of the effective parameters. This is evident from Fig. 5.4 in the cases of 4 layers and frequency above f_0. In this work, it is assumed that the method is valid only for electric lengths of under half of the effective wavelength in the ADL. Since, $L = \lambda_0/6$ in this example, this condition holds for $\varepsilon_r < 9$, as highlighted by the red dotted line in Fig. 5.4(b).

Fig. 5.5 shows the effective permittivity of the ADL slab as a function of evaluation frequency. The effective permittivity is more dispersive for higher metal densities and can exceed the validity range of the homogenization for high frequencies, resulting in incorrect permittivities.

The ADL is synthesized following the guidelines above and its geometrical parameters are shown in Table 5.2. The section length is determined based on a center frequency of 21 GHz, and the ADL is synthesized with a design frequency of 29 GHz. The VSWR of the ADL impedance transformer when normalized to the impedance of free space (377 Ω) and 80 Ω is shown in Fig. 5.6(a) to closely resemble the VSWR of the ideal Chebyshev transformer. The difference is due to a slight frequency dispersion of the dielectric permittivity and intrinsic approximations of the retrieval procedure.
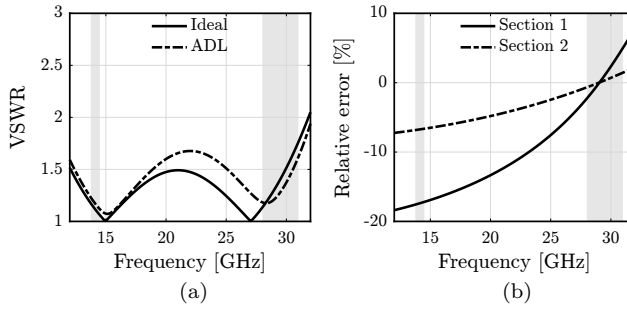
Figure 5.6: (a) Simulated VSWR of the ADL impedance transformer (referred to $80\,\Omega$ and $377\,\Omega$). (b) Normalized error in realized permittivity of section 1 and 2, shown as $(\varepsilon_r - \varepsilon_{\text{desired}})/\varepsilon_{\text{desired}}$.

The frequency dispersion of the two sections of the ADL is shown in Fig. 5.6(b), where the error is 0 at the design frequency.

5.3 Radiating Element Design

The radiating element, a connected slot, periodic in x and y is defined by four geometrical parameters. First, the initial design of the radiating element is done using unit cell simulations, with analytical expressions based on the geometrical parameters of the slot [58]. Next, the detail design is done in CST Microwave Studio [106] to include vias, a cavity, and a dual-polarized radiating element. Finally, a realistic feeding structure is implemented based on an integrated coaxial line.

5.3.1 Initial Design

While the ADL allows the array to avoid TM surface waves, the ADL can still support transverse electric (TE) surface waves. These appear at large scanning angles in the H-plane. To avoid these surface waves, the unit cell periodicity is chosen as $4.35\,\text{mm} = 0.45\lambda$ at the highest frequency, $31\,\text{GHz}$, which enables scanning to $60°$. The array is chosen to consist of 32×32 elements, so the radiating aperture is around $14\,\text{cm} \times 14\,\text{cm}$ in size. This size corresponds to a maximum directivity of $27\,\text{dB}$ to $34\,\text{dB}$ at the lowest and highest frequencies, respectively.

The dimensions are adjusted to optimize the matching efficiency when the array is scanned to broadside. The best values were found as $w = 1.4\,\text{mm}$, $\delta = 2\,\text{mm}$, $h = 1.9\,\text{mm}$, $d_x = d_y = 4.35\,\text{mm}$, where the space between the slot plane and backing reflector is filled with a dielectric with a relative permittivity of 2.2. The active VSWR of the array, normalized to $80\,\Omega$, is shown in Fig. 5.7(a) to be low for broadside, but to exhibit a resonance when the array is scanned to $60°$ on either the H- or the E-plane.

The resonance in the H-plane is due to a guided wave, schematically depicted in Fig. 5.7(b), that is supported by the slot. Because of the connection between
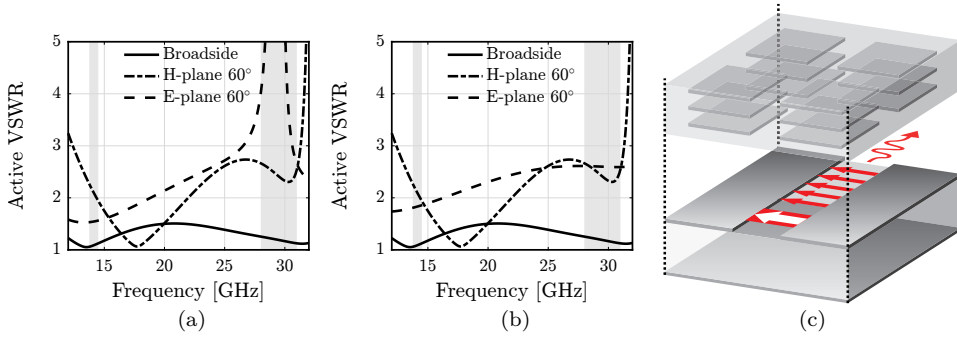
Figure 5.7: Simulated active VSWR (referred to $80\,\Omega$) of the unit cell (a) without and (b) with vertical walls. (c) Illustration of guided wave traveling along the connected slot.

slots, a quasi-transverse-electromagnetic (quasi-TEM) wave can be guided along the array. Similarly to surface waves in dielectric slabs, this mode is undesired as it can cause scan blindness and stronger finite edge effects when truncating the array. When designing the connected array, one should make sure that the propagation constant of this guided wave is as close as possible to the free space one. This can be achieved in three ways; by keeping the AD layers at a distance from the slot that is comparable with the slot width, by reducing the density of the layer closest to the slot, or by reducing the density of the material below the slot plane. The second option was already used in this design to ensure the resonance falls outside the target operational bandwidth.

The resonance in the E-plane is due to a parallel plate waveguide (PPW) mode that propagates between the slot plane and the backing reflector [58]. A common solution to prevent this resonance is to include vertical metal walls between each pair of slots. The VSWR of the array including these vertical metal walls is shown in Fig. 5.7(b) to be below 3 in the entire target operational bandwidth.

5.3.2 Detail Design

To include the details of the substrate and the feed structure that are not accounted by the analytical tool, the design is transferred to the commercial solver CST Microwave Studio. To evaluate the agreement between the analytical tool and CST, the unit cell is first simulated as-is and the active VSWR obtained when normalizing the input to $80\,\Omega$ is shown in Fig. 5.8(a) for various scanning conditions. The guided wave on the H-plane has appeared at slightly lower frequency than predicted by the analytical tool, causing a mismatch in the higher frequency band for H-plane scanning.

A narrow resonance is also observed for E-plane scanning at $23.7\,$GHz, which has appeared due to a cavity resonance below the slot, as illustrated in Fig. 5.8(b). This resonance can be shifted to a higher frequency in two ways; by reducing the size of the cavity by using thicker walls [Fig. 5.8(c)], or by reducing the density of the material below the slot plane by introducing an air cavity in the substrate [Fig. 5.8(d)]. Both
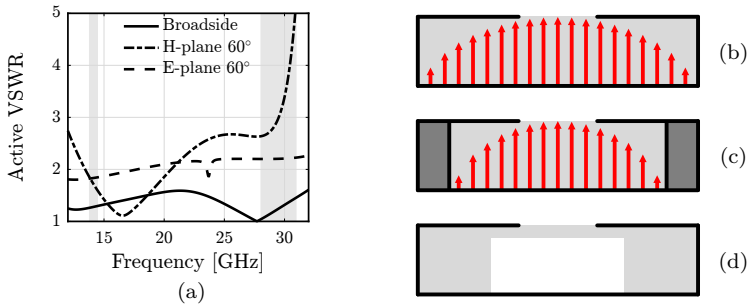
Figure 5.8: (a) Simulated active VSWR (referred to 80 Ω) and (b) illustration of the cause for the E-plane resonance around 24 GHz. The resonance can be shifted to a higher frequency using (c) increased wall thickness or (d) a perforated substrate.

of these approaches were used together to shift both resonances out of the target operational bandwidth. Additionally, the H-plane resonance is further shifted to higher frequencies by reducing the density of the ADL. Its density is reduced by changing the design impedance of the Chebyshev transformer from 80 Ω to 90 Ω. The resulting active VSWR (referred to 80 Ω) is shown in Fig. 5.9(a) to no longer exhibit the resonances, and to be below 2.6 in both bands of interest.

To implement a dual-polarized unit cell, the vertical walls are replaced by a set of vias that perform the same function. The active VSWR of the dual-polarized unit cell is shown in Fig. 5.9(b) to be similar to that of the single-polarized unit cell. However, to enable implementation of a feeding structure using vias, the backing reflector distance is reduced from $h_{\mathrm{br}} = 1.9\,\mathrm{mm}$ to 0.9 mm. The resulting unit cell is shown in Fig. 5.10, and its VSWR is shown in Fig. 5.11(a) to have higher values, especially for the lower frequency band. This is due to the inductive effect of the ground plane, which is electrically too close to the slot at the lower frequency. The matching is improved by adding a series capacitance to counteract the inductance of the backing reflector at low frequency, which will only affect the imaginary part of the input impedance. The resulting active input impedance is shown in Fig. 5.11(b), where the gray curve shows the imaginary part of the input impedance when the series capacitor is not present. The associated VSWR (referred to 80 Ω) is shown in Fig. 5.11(c) to be significantly improved in the Ku-band.

5.3.3 Realistic Feeding Structure

Until now, all simulations have been performed using a delta-gap feed in the slot plane. A more realistic feed needs to include a transition to connectors placed below the ground plane. In this work, several corporate feeding networks will be used to feed the entire array for various scanning conditions. The two polarizations will each have a corporate feeding network, realized on two different layers with fixed delay lines for scanning. There is a stripline layer that feeds one set of parallel slots and a microstrip layer that feeds the orthogonal slots. The networks are discussed in detail
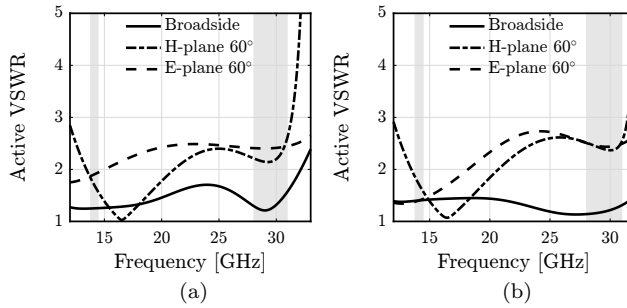
Figure 5.9: Simulated active VSWR (referred to $80\,\Omega$) of the unit cell with vias and a cavity with (a) single-polarized or (b) dual-polarized radiating element.
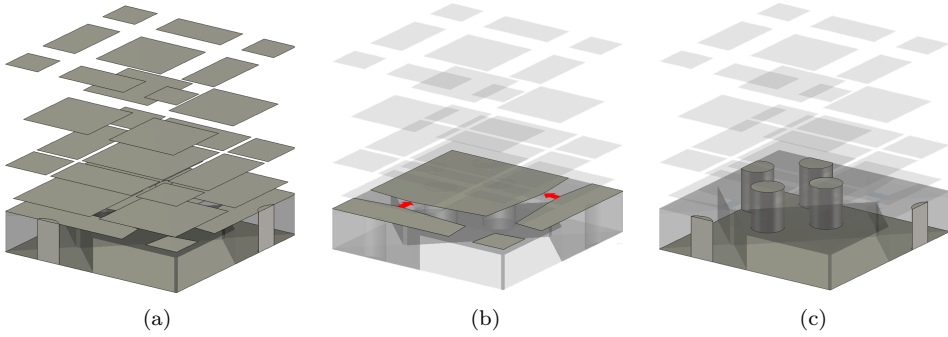
Figure 5.10: (a) Dual-polarized unit cell with (b) details of the orthogonal slots and (c) substrate with vias dielectric grid.

in Section 5.4. To connect to these networks, a transition from the slot plane to two separate layers containing a stripline and microstrip is added.

The feeding structure is implemented in three steps. First, the delta-gap feed is approximated using a microstrip terminated in an open-ended capacitive stub, which implements the series capacitance [Fig. 5.12(a)]. Second, two integrated coaxial lines to two holes in the ground plane are placed in the unit cell, one for each polarization [Fig. 5.12(b)]. The lines are implemented by replacing two of the large vias in each unit cell by two sets of four vias. The central conductor of a coaxial line is formed using a via that is connected to the microstrip, and three more vias implement the shield. These vias also perform the function of preventing the PPW mode from propagating between the ground and slot plane. Third, transitions to the stripline and microstrip layers, along with an extra ground plane to separate these two layers, are added to enable connection to the corporate feeding networks [Fig. 5.12(c)].

The active VSWR (referred to $80\,\Omega$) of the unit cells are also shown in Fig. 5.12. The VSWR of the microstrip-fed cell in Fig. 5.12(a) is below 3 across both the Ku- and Ka-band for scanning up to 60°. Fig. 5.12(b) demonstrates that the addition of the integrated coaxial line does not adversely affect the VSWR in the bands of interest. The transitions to the microstrip and stripline layers are seen to be well-matched to the rest of the unit cell in Fig. 5.12(c). Fig. 5.12(c) uses different curves
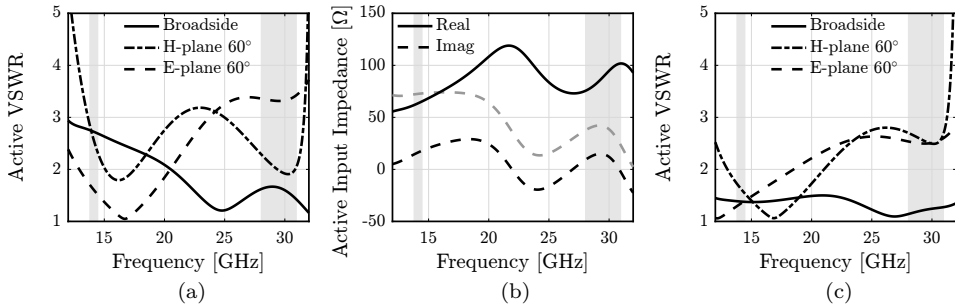
Figure 5.11: Simulated active VSWR (referred to $80\,\Omega$) of the unit cell with reduced backing reflector distance (a) without and (c) with series capacitance. (b) Active input impedance (black) with and (gray) without series capacitance.

for the $x-$ and $y-$oriented slots due to the loss of symmetry in the unit cell, and resulting different matching at the stripline and microstrip inputs.

5.3.4 Additional Elevation Angles

The active VSWR of the unit cell has always been shown for three scanning conditions (broadside, E-plane scan to 60° and H-plane scan to 60°). In this section, the simulated VSWR is shown for several more scanning conditions within the array field of view. The unit cell without the last transition to microstrip and stripline [Fig. 5.12(b)] is considered, so that the feeds are still symmetric and the number of simulations can be reduced by exploiting symmetry. It was shown that the last transition does not have a major effect on the matching performance.

The active VSWR of the unit cells in Fig. 5.12(b) is presented in Fig. 5.13(a)-(c) for several elevations angles, in steps of 10°, in the H-, E-, and D- ($\phi = 45°$) planes, respectively. It can be observed that the matching performance is excellent for most of the scanning conditions and degrade only when scanning beyond 50°. The active VSWR is below 2.8 for scanning up to 60° in all planes, which corresponds to a matching efficiency of 77%. Here, the slots are excited separately, with only one of the two orthogonal ports active and the other passively terminated. The matching when both slots are active is investigated in Section 5.5.2.

5.3.5 Unit Cell Losses

The simulations of the unit cell have thus far used lossless materials. To quantify the expected losses, the unit cell is simulated with lossy materials for various scanning conditions. Similar to Section 5.3.4, the unit cell without the last transition to microstrip and stripline [Fig. 5.12(b)] is considered. The infinitely thin perfect electric conductor metals are replaced with $18\,\mu m$ thick copper with a surface roughness of
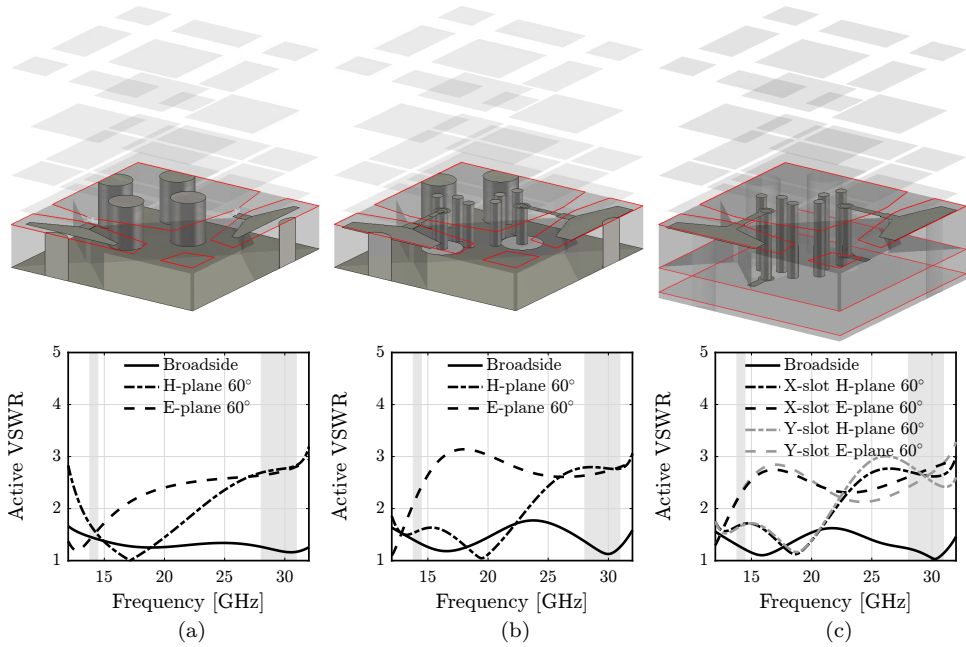
Figure 5.12: Geometry and VSWR (referred to $80\,\Omega$) of unit cell with (a) microstrip and open-ended capacitive stub, (b) integrated coaxial and (c) transition to stripline and microstrip layers. The red outline highlights when a metal layer is drawn transparently.

1.6. For the dielectrics, a dissipation factor of $\tan\delta = 9 \times 10^{-4}$ is considered, as is given for Rogers RT/duroid® 5880.

The radiation efficiency including ohmic and dielectric losses is shown in Fig. 5.14(a). The simulated losses are less than $0.5\,\mathrm{dB}$, which confirms the known low-loss characteristics of ADLs. The total losses including the mismatch are shown in Fig. 5.14(b) to be better than $1.2\,\mathrm{dB}$ for the Ku-band and better than $1.6\,\mathrm{dB}$ for the Ka-band. These values are the worst-case scenario, as they consider the maximum scanning angle of $60°$.

5.4 Corporate Feeding Networks

Each of the 32×32 unit cells contains two orthogonal radiators. This means that two connectors must be included in each unit cell, and a total of 2048 connectors would be required to connectorize the entire array. To simplify assembly and reduce cost of the prototype demonstrator, corporate feeding networks are developed to feed the entire array from a single point. The networks introduce a phase distribution that is chosen such that the array points at a specific scan angle. Multiple boards with separate feeding networks are used to test the array under various scanning conditions. The phase distribution is realized using true time delay lines that increase the path
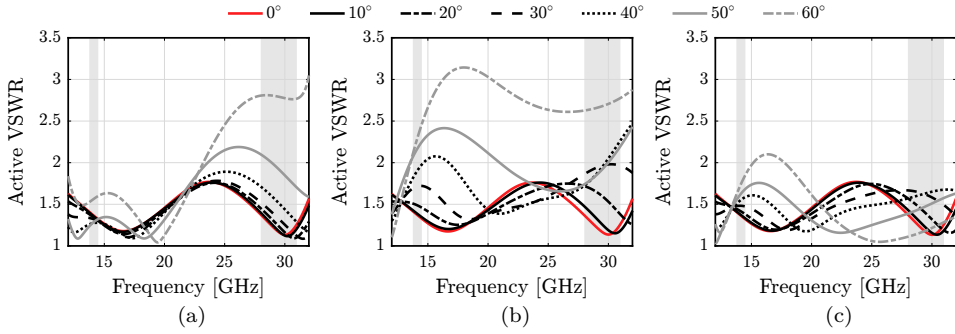
Figure 5.13: Simulated active VSWR (referred to $80\,\Omega$) of the unit cell in Fig. 5.12(b) when scanning to various elevation angles on the (a) H-plane, (b) E-plane, or (c) D-plane.
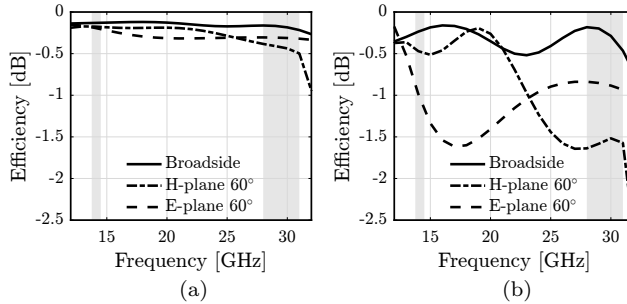
Figure 5.14: (a) Radiation efficiency (material losses) and (b) total efficiency (material and mismatch losses) for the unit cell in Fig. 5.12(b) when realistic materials are used.

length to specific elements to increase their phase. The use of true time delay lines enables the array to maintain a constant scan angle over the entire bandwidth. To test the feasibility of this concept, a test sample is developed to quantify the losses and to enable de-embedding the effects of the feeding network from the array prototype measurements.

The two separate feeding networks for the two polarizations enable the use of the techniques described in Section E.1 to realize an arbitrary polarization. Additionally, they enable characterization of the H- and E-plane in a certain scanning condition using only a single board.

5.4.1 Feeding Network Design

The feeding networks are to be embedded in the PCB that is used for the connected array, which imposes various constraints. The unit cell design also imposes several constraints on the feeding networks, illustrated in Fig. 5.15. Limits on the via aspect ratio by the manufacturer limit total PCB height. The bandwidth of 13–31 GHz should be covered with low insertion loss to minimize the impact of the feeding network on antenna gain. The resulting design guidelines are listed below

(a)   (b)
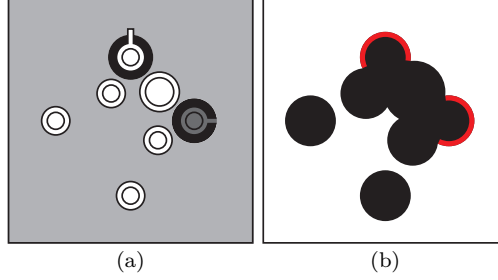
Figure 5.15: (a) Bottom view of the unit cell showing the positions of the vias and their pads. The via that ends in the stripline layer is darkened to highlight its different depth. (b) Illustration of the unavailable area (black) for the feeding network design, where the red edges show the two connection points for the two feeding networks.

- Distance between feeding points is 4.35 mm in both the x and y-direction.

- Position of feeding points is fixed by the unit cell feeding structure.

- Each unit cell contains seven vias, five imposed by the integrated coaxial line and two that are used to implement the vertical metal walls.

- Distance between lines and other structures must be at least 200 µm.

- Minimum trace width is 100 µm.

- The VSWR at the input of the network should be below 2.

The imposed constraints on the usable area of the unit cell made the implementation of a 1024-port network that scans in the diagonal plane infeasible. As such, the size of the array for scanning in the diagonal plane is reduced from 32×32 to 8×8.

Four different boards are designed that each scan to a different angle with both polarizations, where each polarization is fed using a separate network. The x-oriented slots are fed using microstrips, and the y-oriented slots are fed using striplines. The phase profile is realized using true time delay lines, whose inter-element delay length can be calculated from the scan angle as

$$\Delta l_x = \frac{d_x}{\sqrt{\varepsilon_{r,\text{eff}}}} \sin\theta \cos\phi \tag{5.1}$$

$$\Delta l_y = \frac{d_y}{\sqrt{\varepsilon_{r,\text{eff}}}} \sin\theta \sin\phi \,, \tag{5.2}$$

where θ and ϕ are the desired scan angles, $d_x = d_y = 4.35\,\text{mm}$ are the unit cell periodicities along x and y, and $\varepsilon_{r,\text{eff}}$ is the effective permittivity in the microstrip or stripline. The effective permittivities are around 1.8 and 2.2 for the microstrip and stripline layers, respectively. The total phase gradient across the array is then found using

$$\Delta\phi_{ij} = (n_{x,i} - n_{x,j})\frac{2\pi}{\lambda}\Delta l_x + (n_{y,i} - n_{y,j})\frac{2\pi}{\lambda}\Delta l_y \,, \tag{5.3}$$

Table 5.3: Desired scan angles and associated length differences and phases. The values are calculated using the effective permittivity for the microstrip network. The given phase is the maximum phase difference found in the array.

Scan angle		Δl [mm]		Phase [deg.]	
θ	ϕ	x	y	x	y
0	0	0	0	0	0
30	0	1.62	0	2506	0
60	0	2.81	0	4340	0
60	45	1.99	1.99	3069	3069
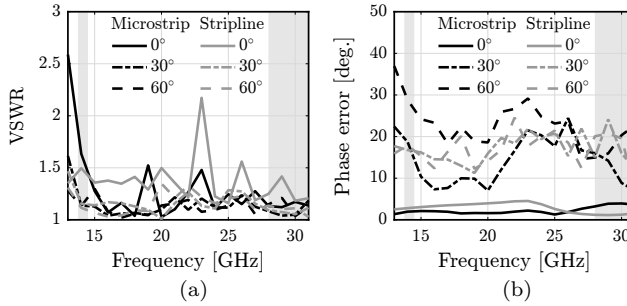
Figure 5.16: (a) Simulated VSWR (referred to $90\,\Omega$) at the input of the feeding networks and (b) maximum phase error of the entire network.

where n_x, n_y is the index of element i or j along x or y and $\lambda = \lambda_0/\sqrt{\varepsilon_{r,\text{eff}}}$ is the wavelength on the line. The desired scan angles and associated length differences and phases are shown in Table 5.3.

The networks contain a series of splits from the single input port. To ensure coverage of the very wide band, each split incorporates a multi-section Chebyshev impedance transformer. Due to the limited space in each unit cell, the last few splits cannot each fit a multi-section impedance transformer. As such, the three splits in the 1-to-8 network are spanned by a single five-section transformer, with every other split incorporating a three-section transformer. Due to memory limitations, networks larger than 128 elements were not simulated, but were instead simulated by cascading the scattering matrices of smaller subsections. The simulated VSWR for all 8 networks are shown in Fig. 5.16(a) to be below 1.9 in the Ku-band and below 1.4 in the Ka-band. Simulations were performed in Ansys HFSS.

Since the networks are to implement a certain phase gradient, the phase error is an important figure of merit. The phase error is the maximum deviation of any element in the network from the ideal phase according to (5.3), evaluated as

$$\text{Maximum phase error} = \max_{i,j} \Delta\phi_{ij,\text{ideal}} - \Delta\phi_{ij,\text{realized}} . \tag{5.4}$$

The maximum phase error of all networks is shown in Fig. 5.16(b) to be below 5° for the broadside networks, below 25° (1%) for the networks that scan to 30°, and below

Table 5.4: Material stack of feeding network test sample. Layers M1 and M4 host the microstrip networks, while M2 and M3 are ground planes.

Layer	Material	Thickness
M1	Copper	9 µm
D1	Rogers RT/duroid® 5880	127 µm
M2	Copper	9 µm
Bond	Rogers 2929 Bondply	38 µm
M3	Copper	9 µm
D2	Rogers RT/duroid® 5880	127 µm
M4	Copper	9 µm

(a)   (b)
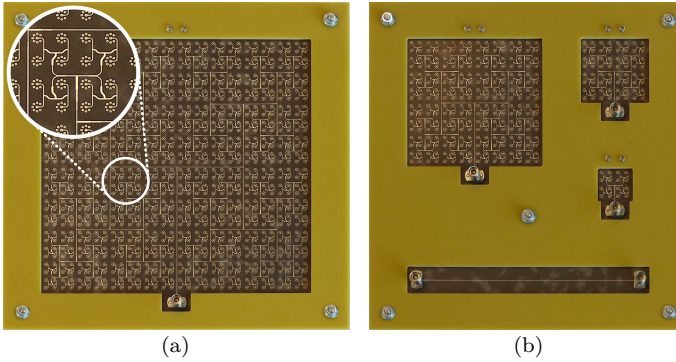
Figure 5.17: Photos of the feeding network prototype. The two boards house (a) a 1-1024-1 back-to-back feeding network and (b) a 1-256-1, 1-64-1, and 1-16-1 back-to-back feeding networks, as well as a 100 mm line.

$31°$ (0.7%) for the networks that scan to $60°$. The percentage values are relative to the total phase gradient that is implemented by the network.

5.4.2 Test Sample

To further evaluate the losses, a test sample was manufactured that contains networks of various sizes. These networks are placed in a back-to-back configuration to implement a transition from 1 to N to 1 (1-N-1) elements. The layer stackup is given in Table 5.4, and the 328 µm thick boards are supported by 2 mm thick FR-4 frames with cutouts to avoid influencing the networks. The networks are connected on either side to coaxial connectors[1]. The networks on either side are connected by vias through a hole in the two ground planes. These transitions are surrounded by extra vias to avoid a PPW mode between the two ground planes.

The networks are placed on two separate boards. The first board contains the 1-1024-1 back-to-back feeding network, and is shown in Fig. 5.17(a). An inset shows a closer look at the 1-16 network and the transition between the two 1-1024 networks.

---

[1] Rosenberger 02K722-40MS3 solderless RPC-2.92 mm
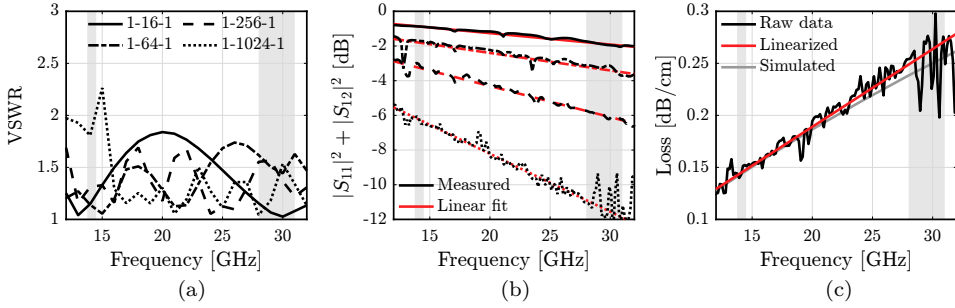
Figure 5.18: (b) Measured VSWR of the back-to-back feeding networks. (a) Measured losses for – from top to bottom – the 1-16-1, 1-64-1, 1-256-1, and 1-1024-1 networks, along with linear fits. (c) Measured loss per unit length in the line section compared to the loss per unit length of a simulated line section.

The second boards is shown in Fig. 5.17(b) and contains a 100 mm long line and three back-to-back networks. The networks in the second board are 1-256-1, 1-64-1, and 1-16-1 and are included to be able to determine the losses introduced by the connectors. The line is included to be able to measure the losses without the transition through the board, and without the effect of coupling between neighboring lines.

Measurements

The boards are measured and the VSWR of the networks is shown in Fig. 5.18(a) to be below 2 across both bands of interest. The losses are shown in Fig. 5.18(b) to increase with frequency and with network size. To be able to predict the losses that will be present in future prototypes, the loss per unit length is important. To estimate the loss per unit length, a linear fit $(ax + b)$ of the loss vs network length is done for each frequency point. The first parameter (a) gives the loss per unit length of line, and the second parameter of the fit (b) represents the losses in the connector. This fit is applied both to the raw data and to the linear fits vs frequency that are shown in red in Fig. 5.18(b). The resulting loss per cm is shown in Fig. 5.18(c). The results are compared to the loss of a simulated microstrip line, which is seen to be accurate for lower frequencies, but to underestimate the loss in the Ka-band.

5.5 Study on the Cross-Polarization

The Ku- and Ka- satellite transmit bands generally use linear and circular polarization, respectively. As such, the polarization purity of the terminal antenna is an important parameter in the design. The polarization purity of a linearly polarized antenna can be quantified through the use of the X-pol, given by

$$\text{X-pol}(\theta, \phi) = \frac{E_{\text{cx}}(\theta, \phi)}{E_{\text{co}}(\theta, \phi)}, \tag{5.5}$$
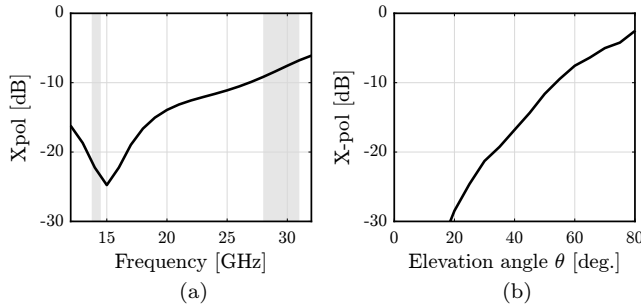
Figure 5.19: X-pol of the unit cell in Fig. 5.12(b), scanning on the diagonal ($\phi = 45°$) plane, versus (a) frequency at $\theta = 60°$ and (b) elevation angle at 30 GHz.

where E_{cx} and E_{co} are the co- and cross-components of the electric field according to Ludwig's third definition of cross-polarization [99]. Similar to Section 5.3.4, the unit cell without the last transition to microstrip and stripline [Fig. 5.12(b)] is considered. The X-pol is shown in Fig. 5.19 to increase with frequency and with elevation. To improve the polarization purity of the array, two methods to reduce the X-pol were studied, cancellation and reduction of intrinsic X-pol.

When two orthogonal ports can be independently excited in a dual-polarized unit cell, one can combine the two ports to generate a certain polarization for a specific scan angle and a specific frequency. By defining the excitation amplitudes of both radiators in the unit cell based on the electric field each radiator emits in their co- and cross-polarized direction, the total radiated field can be modified to include only a certain desired polarization. The complex excitation amplitudes to achieve linear, slant linear, or circular polarization are derived in Appendix E, and this section presents the results obtained using these weights.

5.5.1 Cross-Polarization Cancellation Results

The three excitation weights are applied to the unit cell under investigation, and the results are quantified using the X-pol for the linear and slant linear polarization cases, and using the axial ratio for the circular polarization case. Ideally, the weight would be calculated for each combination of frequency, elevation and azimuthal angle. However, this may be infeasible as it requires measurements for each of these points. To study the stability of the cancellation, the weight is calculated for a single frequency and scan angle and the results are shown as the frequency or scan angle move away from this ideal point. The behavior of the effectiveness of cancellation when both frequency and scan angle move away from the ideal point is shown in Appendix E.
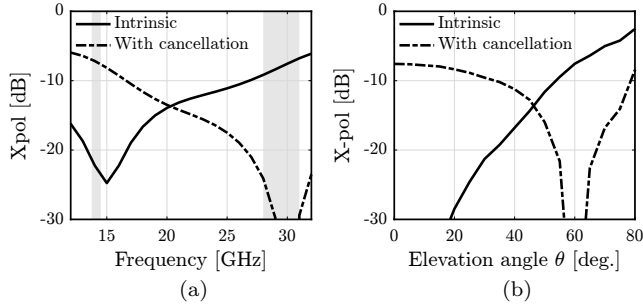
Figure 5.20: X-pol of the unit cell in Fig. 5.12(b) with the linear polarization weighting condition applied at 30 GHz, $\theta = 60°$, $\phi = 45°$, scanning on the diagonal ($\phi = 45°$) plane, versus (a) frequency at $\theta = 60°$ and (b) elevation angle at 30 GHz.
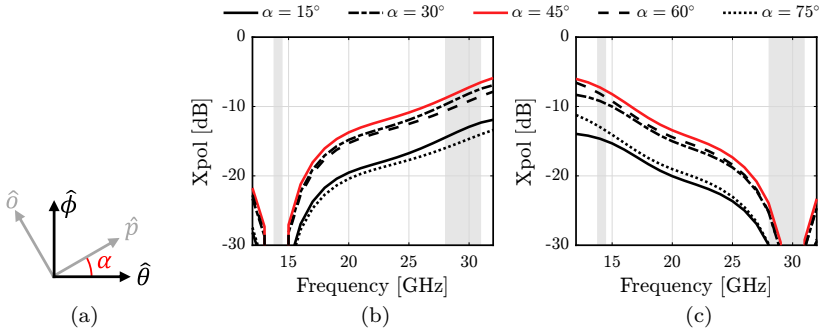
Figure 5.21: (a) Definition of $\hat{p}$ and $\hat{o}$ vectors with respect to the $\hat{\theta}$ and $\hat{\phi}$ vectors. (b) X-pol of the unit cell in Fig. 5.12(b) with the slant linear polarization weighting condition applied at $\theta = 60°$, $\phi = 45°$ and 14 GHz or (c) 30 GHz, scanning on the diagonal ($\phi = 45°$) plane.

Linear Polarization

The linear polarization weighting condition is applied at 30 GHz, $\theta = 60°$, $\phi = 45°$, and the resulting X-pol is shown as a function of frequency in Fig. 5.20(a). The X-pol without cancellation is replicated for ease of comparison. It is seen that the X-pol is effectively canceled (under -25 dB) in the Ka-band with a single choice of weights and that the band in which the X-pol is reduced is very wide. This yields two operating conditions for the two bands: for the Ku-band no cancellation is required to have low X-pol, while in the Ka-band cancellation can reduce the X-pol to < -25 dB. The X-pol versus elevation angle on the diagonal plane is shown in Fig. 5.20(b), and is seen to increase as the scan angle is moved away from the direction in which the cancellation weights are calculated.

Slant Linear Polarization

By applying the slant linear polarization weighting condition, the angle of α of the polarization vector $\hat{p}$ can specified, as illustrated in Fig. 5.21(a). The X-pol is defined here as the ratio of the field in the desired direction and the field orthogonal to it. The weighting condition is applied at 14 GHz in Fig. 5.21(b) and at 30 GHz in Fig. 5.21(c). A similar behavior versus frequency is seen as in the linear polarization case, where the X-pol is low in a wide band around the frequency at which the weights are calculated. Due to the symmetries in the connected slot elements in the unit cell, the $\alpha = 0°$ and $\alpha = 90°$ cases are below -45 dB across the entire frequency range and are therefore omitted. It can be noted that, as expected, the $\alpha = 45°$ case is identical to the linear polarization case seen in Fig. 5.20(a).

Circular Polarization

By applying the circular polarization weighting condition, a right-handed circular polarization can be realized. Here, the axial ratio is considered and is calculated according to the definition in (E.14). The behavior of the axial ratio when the weighting condition is applied at 14 GHz and at 30 GHz is shown in Fig. 5.22. For broadside scanning, the cancellation is nearly perfect and frequency independent. The frequency variation becomes larger for increasing scan angles, progressively reducing the axial ratio bandwidth. This frequency dependence is stronger for the E-plane scan compared to the D plane, and it is stronger at the higher frequency band.

The results in Fig. 5.22 use a different combination of weights for each elevation angle θ. This may not be desired as it requires a large look-up table for the weights, as well as exact knowledge of the radiation characteristics of the antenna at each of these angles. As such, the effect of applying the weighting for a single elevation angle θ is investigated, to better highlight the angular and frequency dependence of the polarization properties. The results are shown in Appendix E.

5.5.2 Effect on Impedance Matching

Since both slots are excited simultaneously, the VSWR shown in Section 5.3.4 is no longer applicable due to interactions between the two slots. Using the weight for the linear cancellation described in Section E.1.1, the active VSWR changes for various scanning conditions. The VSWR when both slots are active for broadside and for scanning to 60° on the H-plane are shown in Fig. 5.23(a). Two sets of curves are shown for the Ku- and Ka-bands, as the two bands use weights calculated at 14 GHz and 30 GHz, respectively. The active VSWR is seen to remain below 3 across both bands.

The VSWR for two active ports in the diagonal plane is shown in Fig. 5.23(b), where it is seen that the VSWR for the Ku-band is negative, and the VSWR for the Ka-band approaches 10. The negative VSWR arises due to the power coupling
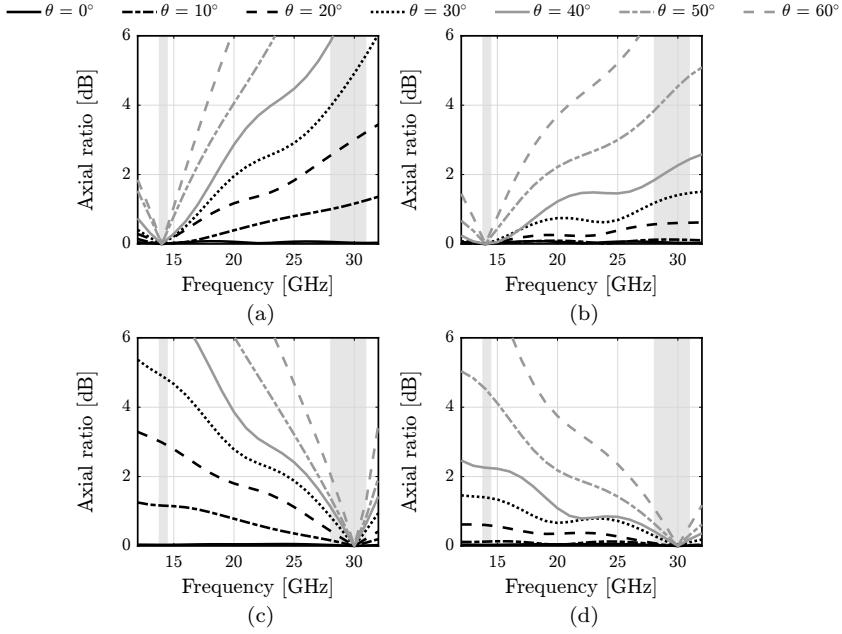
Figure 5.22: Axial ratio of the unit cell in Fig. 5.12(b) with the circular polarization weighting condition applied at (top) 14 GHz or (bottom) 30 GHz on the (left) H-plane and (right) D-plane. The results for the E-plane are identical to the H-plane and are therefore omitted.

from the other slot being higher than the excitation amplitude ($|a_y| = 0.075a_x$ in this example). Similarly, the very high VSWR also corresponds to a very low excitation amplitude. As such, the actual reflected power in the port can still be much lower than the total incident power in both ports. When the weights of the two slots are different, it is more relevant to look at the total matching efficiency, given by

$$\eta = \frac{\text{total reflected power}}{\text{total reflected power}} = \frac{|a_x|^2 + |a_y|^2}{|a_x \Gamma_{\text{active},x}|^2 + |a_y \Gamma_{\text{active},y}|^2} \,. \tag{5.6}$$

The efficiency corresponding to the VSWR curves in Fig. 5.23(a)-(b) is shown in Fig. 5.23(c) to be above 65%. A further study of the efficiency for slant linear and circular polarization is shown in Fig. 5.24(a)(b) for the D-plane and H-plane. The broadside case is omitted due to the low VSWR and resulting high efficiency (>95%). Separate weights are calculated for each of the two bands, so two separate sets of curves are shown. The efficiency for the slant linear polarization is shown for various slant angles α and is >80% when scanning to 60° on the diagonal plane, and >65% when scanning to 60° on the H-plane. The efficiency for the circular polarization case is shown in Fig. 5.24(c) to be >80% in the Ku-band and >75% in the Ka-band.
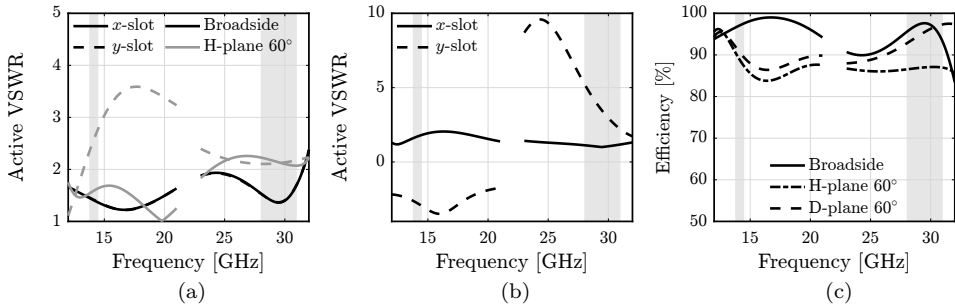
Figure 5.23: Active VSWR of the unit cell in Fig. 5.12(b) with the linear polarization weighting condition applied at 30 GHz. Results shown on for (a) broadside and scanning to 60° on the H-plane and (b) scanning to 60° on the diagonal plane. (c) Efficiency calculated according to (5.6).
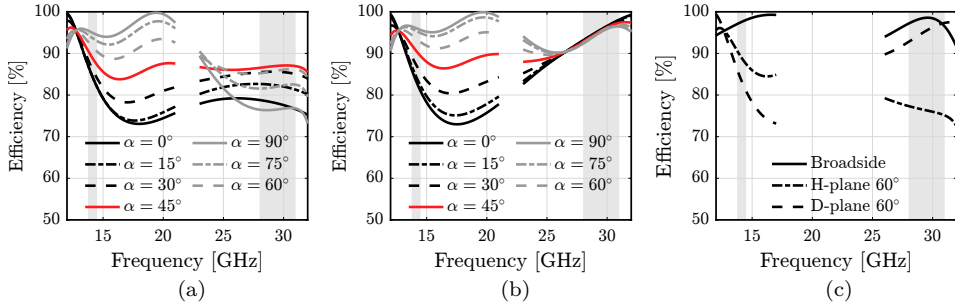
Figure 5.24: Efficiency of the unit cell in Fig. 5.12(b) calculated according to (5.6). Results shown for the slant linear polarization weighting condition with various slant angles α for (a) scanning to 60° on the H-plane and (b) scanning to 60° on the diagonal plane. (c) Efficiency when the circular polarization weighting condition is applied.

5.5.3 Reduction of Intrinsic Cross-Polarization

As shown in Chapter 3, including pins in the ADL can improve the intrinsic X-pol behavior of the superstrate. As such, pins were added to the superstrate of the proposed unit cell. Aside from the addition of the pins between the first two layers of ADL, there are no differences between the unit cell without and the unit cell with pins. For these simulations, the final unit cell is considered, as will be described and shown in Section 5.6. The VSWR of the two unit cells (referred to $80\,\Omega$) is shown in Fig. 5.25(a), and is seen to be below 3 in the bands of interest for all scanning conditions. It can be noted that the VSWR of the two unit cells is nearly identical, with a slight improvement in all scanning conditions when the vias are included, especially for the high frequency E-plane. Due to the different transitions to these two layers, the VSWR for the two orthogonal slots can vary slightly. The maximum VSWR of the two slots at each frequency is shown in the figure.

The X-pol of the unit cell without and with vias is shown in Fig. 5.25(b). It is seen that the X-pol levels are lower than those shown in Fig. 5.19. This is because the unit cell without pins still includes the dense dielectric between the first and second
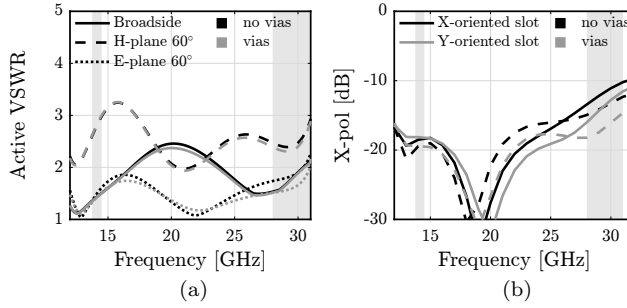
Figure 5.25: (a) Simulated VSWR (referred to $80\,\Omega$) of the final unit cell without or with vias for broadside and for scanning to $60°$ on the main planes. (b) X-pol of the two unit cells when scanned to $60°$ on the diagonal ($\phi = 45°$) plane.
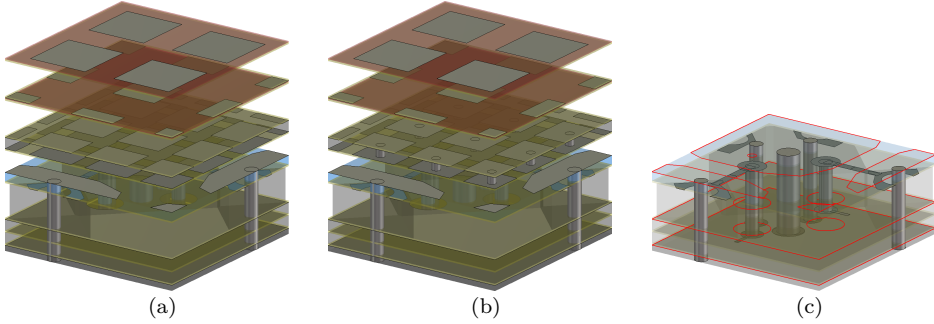
Figure 5.26: Unit cell after changes required by manufacturer. Unit cell is shown (a) without and (b) with vias in the ADL. (c) The feeding structure from the slot plane to the microstrip and stripline layers. The slot plane and two ground planes are shown using red outlines.

layer, which already improves the X-pol with respect to the free-space case. However, the pins still reduce the X-pol of both slots in the Ka-band by up to $3.3\,\text{dB}$.

5.6 Prototype

To validate the proposed antenna, a prototype demonstrator is designed and manufactured. The demonstrator consists of four separate boards, which each consist of 32×32 elements and include two of the feeding networks detailed in Section 5.4.

5.6.1 Prototype Materials

To enable manufacturing of the prototype, several adjustments and additions are made to the ideal unit cell design in Fig. 5.12(c). The ADL is implemented using foam layers with a minimum thickness of $500\,\mu\text{m}$, and is adapted to enable inclusion of the vertical pins described in Section 5.5.3. The dielectric between the feed microstrip and the slot plane is replaced by a denser dielectric (Rogers RO4003®, $\varepsilon_r = 3.55$)

for its mechanical rigidity. The extra vias are shrunk to match the diameter of the vias used for the integrated coaxial lines. During optimization for the new ADL and material, the integrated coaxial lines are each realized using 3 vias, one of which is shared between the two.

The unit cell after these changes is shown in Fig. 5.26(a), where the four layers of ADL are shown, including their glue and substrate layers. The unit cell when vias are added differs in no way other than the vias between the first and second layer, but is shown in Fig. 5.26(b). To show the geometry of the feeding structure with capacitive patch, microstrip, and integrated coax, the unit cell with transparent slot plane and ground planes is shown in Fig. 5.26(c), where the slot and ground planes are shown using a red outline.

The stack-up of the demonstrator boards is shown in Table 5.5, along with a brief description of what each metal layer is used for. The feeding networks are connected to Southwest Microwave 1092-02A-6 connectors. These are connected to the feeding networks through landing pads on the microstrip layer. To avoid the need for blind vias, the transition from the stripline layer to the microstrip layer is implemented using a capacitively coupled pad.

5.6.2 Manufacturing
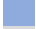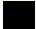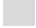
A manufacturing run was attempted, but was aborted after four failed attempts. The fourth attempt was shipped upon request. When measured, the feeding network provided high reflection and through investigation with the manufacturer it was found that the layer alignment and tolerances on line widths were worse than expected. Additionally, the glue layer was re-melting during the drilling of the vias, causing issues during metallization. Contact testing revealed that various vias in the board were shorted to incorrect layers, or did not properly connect.

Although additional iterations of manufacturing could have been successful, due to time constraints it was decided to redesign the prototype using a simpler stack-up and materials that are easier to process. The new prototype is described in Chapter 6.

Table 5.5: Stack-up of the radiating element, with metal (M), dielectric (D), and bonding layers. The total thickness is 1840 μm.

Layer	Material	Thickness	Description
M7	Copper	9 μm	Slot plane
D5	Rogers RO4003C®	203 μm	
Bond	Rogers CuClad® 6250	38 μm	
M6	Copper	9 μm	Feeding microstrips
D4	Rogers RT/duroid® 5880	787 μm	Air cavities
Bond	Rogers CuClad® 6250	38 μm	
M5	Copper	9 μm	Ground plane
D3	Rogers RT/duroid® 5880	254 μm	
M4	Copper	9 μm	Stripline layer
Bond	Rogers CuClad® 6250	38 μm	
M3	Copper	9 μm	Capacitively coupled pad
D2	Rogers RT/duroid® 5880	254 μm	
Bond	Rogers CuClad® 6250	38 μm	
M2	Copper	9 μm	Ground plane
D1	Rogers RT/duroid® 5880	127 μm	
M1	Copper	9 μm	Microstrip layer

Table 5.6: Stack-up of the ADL design, with metal (M), dielectric (D), foam (F), and bonding layers. The total thickness is 2640 μm.

	Layer	Material	Thickness
	M4	Copper	9 μm
	S2	Dupont™ Pyralux® AP	25 μm
	Bond	Rogers CuClad® 6250	38 μm
	F3	ROHACELL® 31 HF	800 μm
	Bond	Rogers CuClad® 6250	38 μm
	M3	Copper	9 μm
	S1	Dupont™Pyralux® AP	25 μm
	Bond	Rogers CuClad® 6250	38 μm
	F2	ROHACELL® 31 HF	800 μm
	Bond	Rogers CuClad® 6250	38 μm
	M2	Copper	9 μm
	D1	Rogers RT/duroid® 5880	254 μm
	M1	Copper	9 μm
	Bond	Rogers CuClad® 6250	38 μm
	F1	ROHACELL® 31 HF	500 μm

Chapter 6

Antenna Design with Reduced Manufacturing Complexity and Experimental Validation

The design and measurements of a dual-polarized broadband array that simultaneously covers the Ku- and Ka-satellite communication transmit bands is presented. This design is a variation on the design presented in Chapter 5 and uses a simplified stratification to avoid manufacturing difficulties that were observed in a previous design. Corporate feeding networks are included to feed the entire 32×32 array from a single point, where different networks implement different phase gradients that scan the array to a set of two angles. The measured results are in good agreement with expectation from the simulations.To simplify the array PCB stack-up, a single feeding network is used for both polarizations. Circular polarization is implemented in the Ka-band directly in the unit cell by means of a 1-to-2 power splitter and a delay line to feed the two orthogonal slots with a 90 degree phase shift.

6.1 Introduction

Connected slot array antennas that employ artificial dielectric layers typically use substrates with a low permittivity to avoid a surface wave that is guided by the combination of the slot and the superstrate. This low permittivity is generally achieved by perforating the substrate [54, 59]. This was attempted in the previous design but caused issues in manufacturing as described in Section 5.6. The example design presented in Chapter 3 also used a substrate material with the same relative permittivity as previous designs, which assumed a perforated substrate in each unit cell to reduce the effective permittivity.

A new connected slot array is designed which, to reduce the complexity of the manufacturing process and limit the risk of major issues, does not include perforations but instead uses a solid dielectric substrate. The dielectric material in the substrate is chosen for ease of manufacturing, and has a relatively high relative permittivity of 3. This reduces the scan range and continuous bandwidth that can be covered by the antenna.

Another simplification with respect to the design presented in Chapter 5 is a reduction in the complexity and number of feeding networks. The previous design has two feeding networks per board, implemented in a stripline or microstrip layer. This is reduced to a single network per board, implemented in the microstrip layer. The constraints placed on this new design by other structures in each unit cell are reduced to allow for a simpler design, and a larger minimum line width and spacing is used to reduce difficulty of manufacturing.

The array aperture is still dual-polarized and, to still utilize both slots simultaneously, an extra feeding line is added in each unit cell. This line feeds both slots in the unit cell and implements the appropriate phase shift to radiate circular polarization directly. Since the phase delay of the fixed line will vary as a function of frequency, the fixed delay line is not able to realize circular polarization across the entire bandwidth. As a proof of concept, the design focuses on achieving right-handed circular polarization in the Ka-band.

This chapter details the design and measurements of a connected slot array and can be divided into three parts. First, the design of the radiating aperture is detailed, where the new unit cell is described along with the feeding structure that feeds the two polarizations. Next, the design of two corporate feeding networks is discussed that scan the antenna array to broadside and to $30°$, and key performance metrics are shown. Finally, near- and far-field measurements of the prototype array are presented, including return loss, directivity, axial ratio, and gain.

6.2 Radiating Element Design

Since the ADL already exists, the first step is to design the radiating element.

Table 6.1: Stack-up of the radiating element, with metal (M), dielectric (D), and bonding layers. The total thickness is 1202 µm.

Layer	Material	Thickness [µm]	Description
M4	Copper	18	Slot plane
D3	Rogers RO3003™	130	
M3	Copper	18	Microstrip feed
Bond	*fast*Rise™ FR-27-0030-25 (F)	91	
D2	Rogers RO3003™	760	
M2	Copper	18	Ground plane
Bond	*fast*Rise™ FR-27-0030-25 (F)	91	
D1	Rogers RO3003™	130	
M1	Copper	18	Feeding network

The substrate consists of a single dielectric material[1] interspersed with bonding[2] layers. Four metal layers are used to house - from top to bottom - the slot plane, the microstrip feeding the slots, the backing reflector, and the corporate feeding networks. The layer stack-up of the prototype boards is shown in Table 6.1.

The unit cell with annotated geometrical parameters is shown in Fig. 6.1(a). Both the broadside and scanning board use the same slot plane geometry, given by periodicity $d = 4.35$ mm, slot width $w_s = 1.2$ mm, feed gap length $\delta_f = 0.3$ mm and feed gap width $w_f = 0.6$ mm. The used vias have a radius of 0.2 mm and the radius of the integrated coaxial line is 0.85 mm. Both the extra via and the central conductor of the integrated coaxial line have a pad with a radius of 0.28 mm. The pad of the central conductor of the integrated coaxial line is separated from the slot plane by a 0.17 mm gap.

The dense substrate material causes the guided wave described in Section 5.3 to be excited at significantly lower frequency. It causes a resonant behavior at a specific frequency between the two bands where the antenna is completely mismatched, resulting in a dual-band design. The resonance is close to the the Ka-band, so an extra via is placed in the unit cell to shift this resonance to a lower frequency. The active VSWR of the two unit cells (referred to $56\,\Omega$) is shown in Fig. 6.1(f) to be below 1.7 in the bands of interest. The guided wave is at 24 GHz, so it will not adversely affect the performance of the antenna in the bands of interest.

The unit cell is designed to radiate circular polarization directly, using a delay line between the integrated coaxial line and one of the two slots. The length of the delay line is chosen such that the array emits circular polarization with minimized axial ratio in the Ka-band. Since the two radiators in each unit cell are offset with respect to each other, the required phase difference for circular polarization is different for the two scanning conditions. To account for this, the length of the delay line is adjusted between the design of the broadside [Fig. 6.1(a)(b)] and scanning [Fig. 6.1(d)(e)] boards. The simulated axial ratio of the unit cell is shown in Fig. 6.1(c) to be below 2.5 dB at broadside, and below 1.6 dB for scanning to 30°.

---

[1] Rogers RO3003™, $\varepsilon_r = 3.0$
[2] *fast*Rise™ FR-27-0030-25 (F), $\varepsilon_r = 2.7$
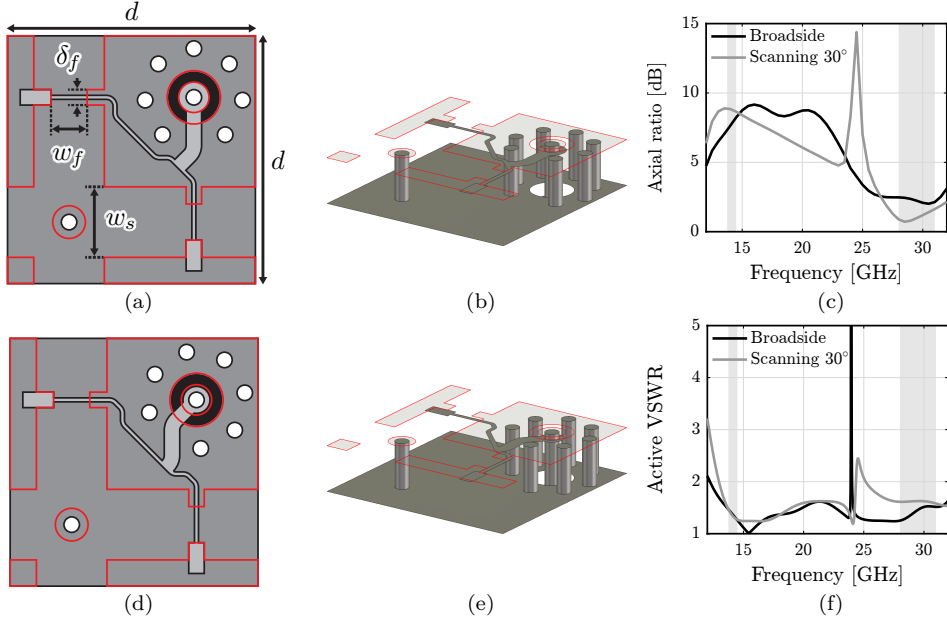
Figure 6.1: Top and perspective views of the redesigned unit cell for (a)(b) broadside and (d)(e) scanning to 30°, where the red outline illustrates the slot plane. The unit cell is loaded with the ADL described in Chapter 3. (c) Axial ratio of the unit cells. (f) Active VSWR (referred to 56 Ω) of the unit cells.

6.3 Corporate Feeding Networks

The prototype demonstrator consists of two boards with 32×32 elements. Each board contains a corporate feeding network that feeds every element in the array and implements a phase profile to point the array at broadside or to scan it to 30°. These two boards will be referred to as the broadside and scanning boards, respectively.

In the previous feeding network design (Section 5.4), the space in each unit cell for the feeding network was restricted primarily by the large number of vias that had to be avoided. To reduce the constraints on the usable area, the vias used in the unit cell are all resin filled plated through holes and all end at the ground plane, except for the central conductor of the integrated coaxial line. This means that the extra vias do not have to be avoided in the feeding network design.

To ensure a good impedance match between the input and the 1024 outputs, multi-section Chebyshev impedance transformers are used at each junction to transform the impedance back to a nominal value of 60 Ω. The broadside feeding network is shown in Fig. 6.2(a), where a 1-16 section is shown. The three-section impedance transformer shown in the center of the image is replicated for all other splits. The scanning feeding network is shown in Fig. 6.2(b), where a 1-32 section is shown. The off-center attachment on the horizontal axis and the additional delay lines are used to
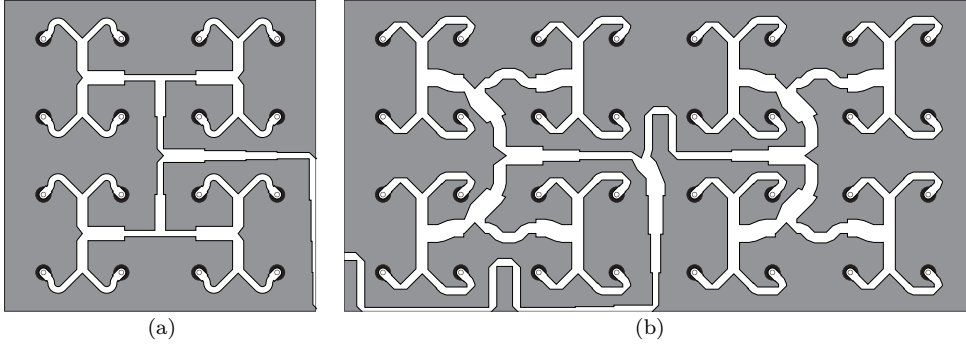
Figure 6.2: Illustration of a small section of (a) the broadside feeding network for up to 16 elements and (b) the scanning feeding network up to 32 elements.
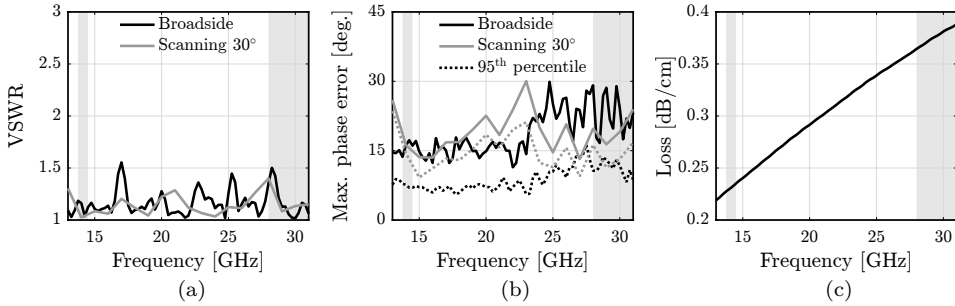
Figure 6.3: (a) Simulated VSWR (referred to $60\,\Omega$ input, $56\,\Omega$ outputs) at the input of two feeding networks and (b) maximum phase error across the network. (c) Simulated loss per cm for the stratification used for the feeding network.

implement the phase difference horizontally. The two impedance transformers shown in the figure are replicated for all other splits.

The VSWR of the two networks (referred to $60\,\Omega$ at the input, and $56\,\Omega$ at the outputs) is shown in Fig. 6.3(a) to be below 1.6 across the entire 13–31 GHz band. The $60\,\Omega$ line is matched to a $50\,\Omega$ connector[3] with a reflection coefficient of $< -20\,\text{dB}$ and is not included in the network simulations.

The phase profile is implemented using true time delay lines to each element in the array. To quantify the accuracy of the phase distribution, the phase error is calculated as

$$\epsilon_{\phi,i} = |\phi_i - \phi_{i,\text{ideal}}| \; , \tag{6.1}$$

where ϕ_i is the phase of S_{1i}, and $\phi_{i,\text{ideal}}$ is the ideal phase at that port according to the phase gradient to be implemented. The maximum phase error across the two designs is shown in Fig. 6.3(b) to be below $30°$ for all elements. The variations arise mostly from coupling between neighboring lines in the dense network, which is worse for certain elements near transformer sections. To illustrate the error for the majority of elements in the array, the 95th percentile is also shown. In the bands of interest,

---

[3]Southwest 1092-02A-6 2.92mm end launch connector

<center>(a)   (b)   (c)</center>
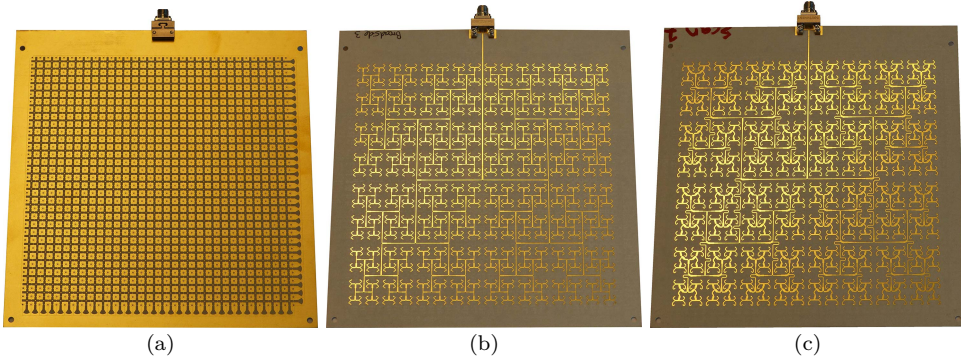
Figure 6.4: Photos of prototype boards. (a) Slot plane of the broadside board, which is identical to the slot plane of the scanning board. (b) Feeding network of the broadside and (c) scanning board.

95 % of the elements are fed with a phase within 14° and 17° of the ideal for the broadside and scanning boards, respectively. This corresponds to 0.7 % of the 2506° phase gradient required to scan the array to 30°.

To estimate the losses, the loss per unit length is calculated by simulating a line with realistic material properties. The loss tangent used for the dielectric and bonding layers are given in their data sheets to be 9×10^{-4} and 16×10^{-4}, respectively. The surface roughness and conductivity of the copper are given as $2\,\mu\text{m}$ and $5.8 \times 10^{7}\,\text{S/m}$. Surface roughness for the ground plane is not supported in Ansys HFSS, and is therefore neglected. The simulated losses per cm are shown in Fig. 6.3(c) to be $0.23\,\text{dB/cm}$ in the Ku-band, and $0.38\,\text{dB/cm}$ in the Ka-band. The line length between input and output is $22.5\,\text{cm}$ for the broadside board and, on average, $24.5\,\text{cm}$ in the scanning board. As such, the expected losses in the Ku- and Ka-bands for the two networks are $5.3\,\text{dB}$ and $8.7\,\text{dB}$ for broadside, and $5.8\,\text{dB}$ and $9.5\,\text{dB}$ for scanning.

The loss simulations shown above are done using pure copper metal traces. However, due to the ENIG surface finish applied by the manufacturer, a layer of nickel is added, which reduces the conductivity. Simulations show that the losses increase by approximately 20 %.

6.4 Prototype and Measurements

The two boards were manufactured and the slot plane of the broadside board is shown in Fig. 6.4(a). The slot plane is identical in both boards. The feeding networks on the other side are shown for the broadside and scanning boards in Fig. 6.4(b) and Fig. 6.4(c), respectively.

Both the broadside and scanning board were measured in two different measurement setups. First, both boards are measured in a near-field scan setup, where WR28 open-ended waveguide is used to perform a scan of the antenna aperture. The near-field scan allows calculation of the full hemispherical radiation pattern and can give an indication of sidelobe levels outside the principal planes.
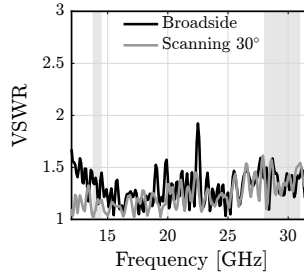
Figure 6.5: Measured VSWR at the inputs of the two prototype boards.

Next, they are measured using a far-field measurement setup in an anechoic chamber. For the broadside board, the two principal planes ($\phi = 0°, 90°$) are measured, and for the scanning board only the scanning plane ($\phi = 0°$) is measured. The far-field measurement enables a more accurate measurement of the principal planes of the radiation pattern. Additionally, the axial ratio can be more accurately determined due to the low cross-polarization of the receiver horn[4].

The measured VSWR is identical between the two setups, so only one measurement is shown in Fig. 6.5(a). The VSWR is seen to be below 1.6 in the entire 13–31 GHz band, aside from the resonance between the two bands. The guided wave is seen to have shifted from 24 GHz to 22.5 GHz, which is still outside the bands of interest and therefore does not adversely affect the performance of the array.

6.4.1 Radiation Patterns

The far-field pattern for the broadside board is calculated at 30 GHz and shown in Fig. 6.6(a), where the UV plane is truncated to more clearly show the main beam and principal sidelobes. A cut of the main planes from the near-field scan is shown in Fig. 6.6(b) and shows sidelobe levels of -12.6 dB and -10.4 dB for the $\phi = 0°$ and $\phi = 90°$ cuts, respectively. The far-field scan in Fig. 6.6(c) shows lower sidelobes in both cuts of -12.3 dB. The far-field pattern of the scanning board is shown in Fig. 6.6(d) to be pointed in the desired $\theta = 30°$, $\phi = 0°$ direction. The sidelobe levels from the near-field scan are shown in Fig. 6.6(e) to be under -13.3 dB, but are seen to be slightly higher (-11.7 dB) in the far-field scan in Fig. 6.6(f).

The radiation pattern for the scanning board has a -12 to -15dB spurious lobe that points to $\theta = -40°$. The origin of this extra lobe is the mismatch between the feeding network and the array impedance. To illustrate this, the array factor pattern is calculated from the excitation weights provided by the feeding network simulations in two situations, and each is compared to the pattern obtained using an ideal linear phase profile. The ideal phase difference between neighboring columns in the array

---

[4]Flann 22240 standard gain horn [107].
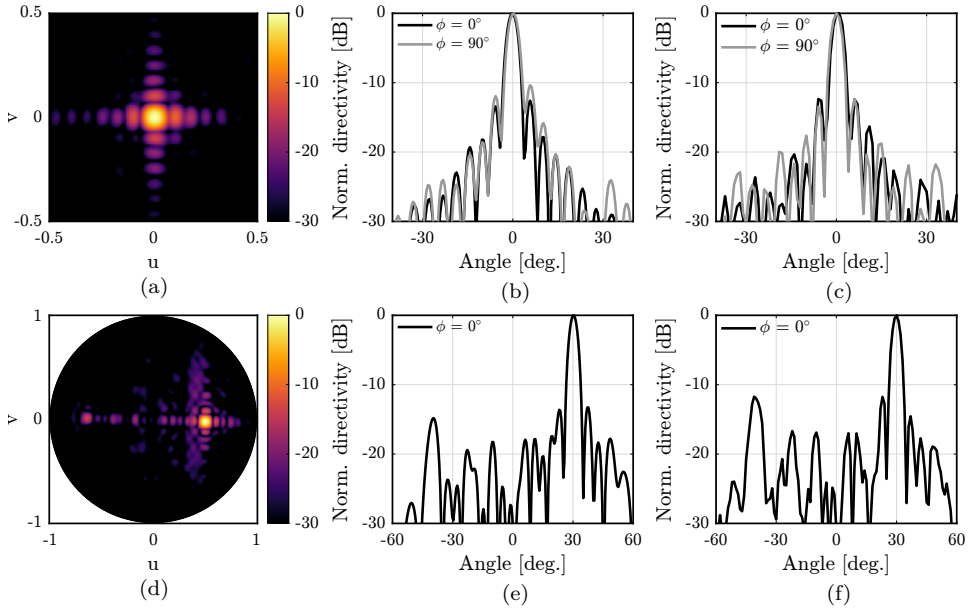
Figure 6.6: Radiation pattern measurements at 30 GHz of the (top) broadside and (bottom) scanning boards. The pattern is shown as a (left) UV map of the near-field scan data, and as cuts along the principal planes of the (mid) near-field and (right) far-field scan.

at 30 GHz is easily found using

$$\Delta\phi_{\text{ideal}} = k_x d_x = \frac{2\pi}{\lambda} d_x \sin\theta_{\text{scan}} = 78.3° \,, \tag{6.2}$$

where λ is the wavelength and $d_x = 4.35$ mm is the column spacing.

First, the scattering matrix of the feeding network is terminated with $60\,\Omega$ at the input and $56\,\Omega$ at the outputs, and the average phase difference between neighboring columns $\overline{\Delta\phi}_{56}$ is shown in Fig. 6.7(a) to be close to the ideal value. The resulting pattern is shown in Fig. 6.7(b) to closely resemble the pattern obtained from the ideal phase distribution. Next, the scattering matrix is terminated with $60\,\Omega$ at the input and loaded with the simulated input impedance of the unit cell, which is complex and frequency dependent, at the outputs. The phase difference between neighboring elements $\overline{\Delta\phi}_Z$ is shown to oscillate significantly around the ideal value, and the resulting array factor pattern is seen in Fig. 6.7(c) to exhibit the spurious lobe pointing in the $\theta = -40°$ direction.

To isolate the spurious lobe, the difference between the complex excitation weights (S_{1n}) at the outputs of the two networks is taken, and the average phase difference $\overline{\Delta\phi}_{\text{diff}}$ is shown in Fig. 6.7(a) to oscillate around $-98.5°$, which corresponds to a scan angle of $-39°$. The array factor pattern of only this difference excitation is shown in Fig. 6.7(c) to form only the spurious lobe.

The radiation patterns of the two boards, measured in the far-field at 14 GHz are shown in Fig. 6.8(b) and Fig. 6.8(b). The main beam width and sidelobe levels are
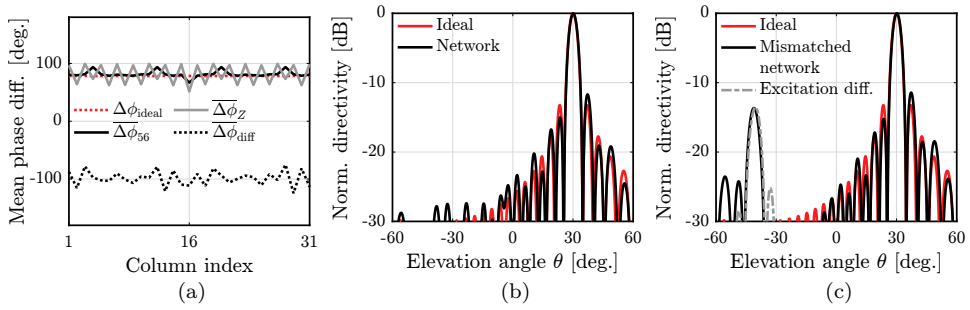
Figure 6.7: (a) Mean phase difference between the outputs of the scanning feeding network in each column of the array. Results are shown for different loading conditions at the outputs of the feeding network when it is loaded with $56\,\Omega$ or with the simulated input impedance (Z) of a unit cell simulation. Also shown is the mean phase difference between columns of the difference between the aforementioned excitations. (b) Array factor directivity pattern at $30\,$GHz for an ideal excitation as well as feeding network terminated with $60\,\Omega$ at the input and $56\,\Omega$ at the outputs or (c) the simulated input impedance of the unit cell at the outputs. Also shown in (c) is the array factor directivity pattern of the difference excitation.
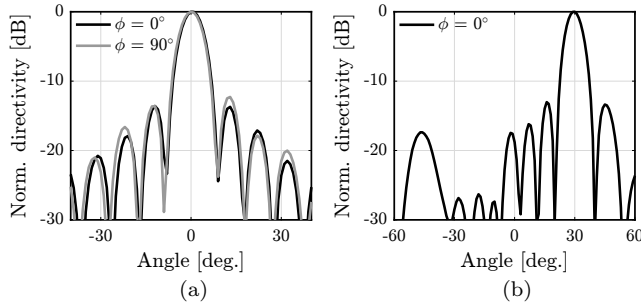
Figure 6.8: Far-field radiation pattern measurements at $14\,$GHz of the (a) broadside and (b) scanning boards.

very close to the ideal pattern expected from the aperture size. A similar spurious lobe is seen in the scanning pattern, which is caused by the same effect.

6.4.2 Directivity, Axial Ratio and Gain

The directivity is calculated from the near-field measurement and shown in Fig. 6.9(a), where it is compared to the ideal directivity of an aperture of this size. It is seen to be $1\,$dB to $2\,$dB below the maximum theoretical curve.

The axial ratio of the two boards is measured by Wave Up and is shown in Fig. 6.9(b). The measured values are in good agreement with the simulated values, with axial ratios below $2.5\,$dB and $1.8\,$dB for the broadside and scanning boards, respectively.

The gain of the broadside antenna is measured in the far-field using the gain-transfer method [108]. The measurement is done using three standard gain horns
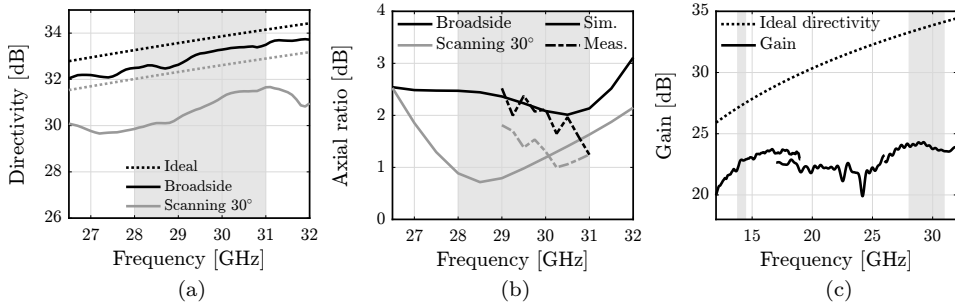
Figure 6.9: (a) Measured directivity and (b) axial ratio for the broadside and scanning boards. (c) Measured gain of the broadside board.

covering the 12–19 GHz, 17–26 GHz, and 26–40 GHz bands. The gain of the broadside board is shown in Fig. 6.9(c) to be around 5 dB below the ideal directivity in the Ku-band, and around 10 dB under the ideal in the Ka-band. This difference is attributed to phase errors, losses in the feeding network and the finite array edge effects.

6.5 Conclusion

A dual-polarized planar connected slot array has been designed for Satcom applications. The array is designed to cover the Ku- (13.75–14.5 GHz) and Ka-transmit (28–31 GHz) bands. Each unit cell contains two orthogonal connected slot elements that are combined with a fixed delay line to radiate circular polarization in the Ka-band.

The design is demonstrated using two prototype boards that each consist of 32×32 elements. Each board hosts a true time delay feeding network that implements the phase profile to scan it to either broadside or to a scan angle of $30°$. A VSWR of < 1.6 at the input of the feeding network is shown for the broadside and scanning boards in the 13–31 GHz band, except for a narrow band around 24 GHz. The two orthogonal radiators in each unit cell are fed using a delay line that implements circular polarization in the Ka-band. The measured axial ratio of the circular polarization closely matches simulations and is under 2.5 dB and 1.8 dB for the broadside and scanning boards, respectively. Radiation patterns, directivity, and gain measurements are also presented.

Chapter 7

Conclusion

This dissertation describes the research work carried out over a period of five years (September 2019 to July 2024) at the Terahertz Sensing Group of the Delft University of Technology. The work was partly supported by the European Space Agency (ESA) for the project "Antenna User Terminal with Wide Angle Impedance Matching Metamaterial Radome" under Contract 4000127381/19/NL/AF.

The main focus of this work is on the development of a wideband wide-scanning connected slot array for the Ku- and Ka-Satcom transmit bands. The work describes the design procedure of the various sub-components required for such an antenna array. The work also details two analysis techniques that can support the design and can help improve the performance of such arrays.

This work was part of a larger project in collaboration with WaveUp and University of Siena. In the collaborative project, the goal is to combine an active phased array with a set of passive metalenses to achieve low-cost beamforming by mechanical rotation of the lenses [109–111]. This will be achieved over a small part of the bandwidth covered by this array.

In this chapter, the conclusion and most significant findings are summarized and future outlooks for the continuation of this research are discussed.

7.1 Analysis of Large Finite Antenna Arrays

Phased array antennas are being developed with increasing number of elements and are typically simulated using a unit cell representation, where the array is assumed to be infinite. While this approximation is valid for central elements in an array, elements near the edge can behave significantly differently. This is especially true for connected array geometries where edge effects can propagate across the array and affect large portions of it.

To accurately estimate the effect of edge effects on the individual elements in a 2D-finite array, MoM procedures using basis functions that represent the spatial vari-

ability of the fields have been studied for decades but they remain of limited utility when the dimensions of the arrays and details of the structures combine to form unsolvable systems of equations. The simulations of the large finite arrays with complex artificial dielectric stratification that are of interest in this work would be impractical with any currently available commercial software. To address this problem, this work presents a MoM procedure in which the basis functions represent the spectra of the fields that needs to be described. This drastically reduces the numerical complexity by exploiting the spectral properties of the field distributions that emerge from both the periodicity and the geometries used.

Instead of using the stratified media Green's function as kernel of the MoM directly, the method uses the Green's function of the slots, which is known analytically in the spectral domain. This choice allowed to reduce the number of unknowns to the number of feeding points in the array plus two per slot. This choice implies that the MoM matrix needs to be solved for every spatial spectral wave number, k_x, k_y. Another feature that renders the method particularly effective is that the Green's function of an arbitrary stratification can be introduced, such as the closed-form Green's function of the ADLs. The developed method enable analysis of finite connected slot arrays of essentially arbitrary size. The relevant parameters of finite arrays are also calculated, such as active input impedance, voltage spectrum, and radiation patterns. The technique is validated by comparing the active input impedance of the elements in various example structures to those obtained using the commercial solver CST Microwave Studio, where a good agreement is found.

It should be noted that while the method considers a finite number of finite-length slots, it assumes an infinite ground plane and that the array is embedded in an infinitely extended stratification. Nevertheless, the truncation effect considered are the dominant ones.

7.2 Improving the X-Pol of WAIM Superstrates

Wide angle impedance matching (WAIM) layers are interesting in the design of wide-scanning antenna arrays due to their ability to improve the impedance matching of an array when it is scanned to a large angle. A WAIM consists of a dense dielectric placed at a certain distance from the radiating aperture. However, the anisotropy that is created by the combination of the air-gap and the dense dielectric increases the X-pol of the radiated field. This work presents a study of the cross-polarization behavior of various superstrates, and proposes a pin-patch structure to reduce the X-pol of an ADL-based WAIM superstrate. A prototype and experimental results are shown to prove the effectiveness of the structure.

Additionally, to facilitate the use of the pin-patch structure in future antenna array designs, an efficient technique is developed to simulate the structure. The technique utilizes a compact space domain Method of Moments (MoM), with 9 basis functions to analyze the pin-patch structure in a computationally efficient way. The reaction integrals of the MoM procedure are performed efficiently in the spectral domain. The

method is able to accurately represent the currents on the pin-patch structure and the resulting scattered fields. The scattering parameters of an example structure calculated using this method are compared to results obtained in CST, and a good agreement is demonstrated.

Finally, the use of cancellation to improve the X-pol of a connected slot array is investigated. The two orthogonal radiators in a dual-polarized configuration are used with proper complex excitations to cancel the X-pol of the radiated field. Various polarizations are considered and the effectiveness of the cancellation is studied for each. The stability of the cancellation with respect to frequency and scanning angle when the weights are calculated at a specific frequency and/or scanning angle are shown. The effect of cancellation on the matching efficiency of a dual-polarized connected slot array is also shown to be small.

7.3 Design of a Wideband Wide-Scanning Connected Slot Array

This work describes the design of two dual-polarized wideband wide-scanning antenna arrays for use in Satcom systems. Both designs cover the Ku- and Ka-Satcom transmit bands and are based on the connected slot array concept. The design process of the array is described, where a unit cell is designed in various stages. First, the design of a ADL-based WAIM superstrate that implements a Chebyshev impedance transformer is detailed. Next, the dual-polarized radiating aperture is introduced and a feeding structure based on an integrated coaxial line and a microstrip is shown. Finally, several corporate feeding networks are developed that implement the phase profile to steer the beam of the array to certain angles. The corporate feeding networks are used to develop a low-cost prototype demonstrator, which unfortunately was not successfully manufactured.

Issues that arose during manufacturing were primarily related to the choice of the materials to be used in a multi-layer stack-up. The materials chosen did not provide the mechanical and thermal stability that was required by the design. The inclusion of cavities in the substrate material is shown to pose even more stringent requirements on the thermal properties of the materials used. The use of foam spacers to build an ADL stack also presents difficulties at higher frequencies, primarily due to the limited minimum manufacturable thickness and the high fabrication tolerance of the thickness with respect to the desired value.

A second prototype is presented in this work that has significantly lower manufacturing complexity and solved most of the issues encountered during the first manufacturing run. While the first design used a perforated substrate with a low-permittivity dielectric, this new design uses a substrate without perforations and with a material that is easier to handle in manufacturing. Due to the dense dielectric, a resonance exists between the Ku- and Ka-bands, which does not affect the performance of the array within the two bands. The array is designed to radiate circular polarization in the Ka-band using a delay line in one of the microstrips feeding the slots.

Two prototype boards are manufactured – one pointing at broadside and one pointing at 30° – and near-field and far-field measurements are presented. Measurements of the prototypes show fair comparison with simulated results. A directivity close to the theoretical maximum is observed. Active VSWR is below 1.6 for the bands of interest, which demonstrates successful manufacturing of the corporate feeding networks. An extra lobe pointing at −40° is present in the scanning board, and is found to be the result of mismatch between the feeding network and the radiating aperture. The axial ratio of the circular polarization closely matches simulations and is under 2.5 dB and 1.8 dB for the broadside and scanning boards, respectively. The gain of the array is 5–10 dB lower than the directivity due to significant losses in the 1-to-2048 elements feeding network.

7.4 Future Outlooks

The future outlooks of this thesis are summarized in the following:

- The finite array method currently assumes an infinitely extended ground plane and stratification. The method could be extended to also take into account finiteness in the ground plane or stratification.

- To demonstrate the ability of the pin-patch structure to reduce the X-pol of an antenna that uses a WAIM, vias could be placed throughout the stratification in a design where the refractive index for the TM wave is made equal to that of the TE wave. While this would limit the bandwidth, that trade off may be worthwhile for polarization-sensitive applications.

- The analysis technique for the pin-patch structure in this thesis assumes that the structure is in free space, so that the integral in k_z can be closed. A possible generalization for future studies is the case in which the structure is embedded in a stratified medium, which requires alternative computation of the k_z-integrals [112].

- The pin-patch analysis technique currently assumes that it is the only layer in the stratification. It could be extended to support multiple layers, similar to [70], taking into account the reactive coupling between layers.

- The number of independent basis functions in the pin-patch structure could be reduced through further investigation of the coupling between them. It is believed that some of the basis functions can be combined to produce a smaller set of orthogonal functions.

- An equivalent circuit representation of the pin-patch layer was not provided in this work. It can be interesting to develop such an equivalent circuit to use in combination with the available transmission line models of ADLs [73].

- An alternative feeding structure could be used to avoid a perforated substrate while still achieving 60°, as described in [113].

- For applications with lower requirements on scan volume, array thinning could be used to reduce the number of feeding points in the array.

- The demonstrated antenna array will be tested in conjunction with the rotating metalenses described in [111] to achieve low-cost beamforming in a large field of view in the Ka-band.

7.5 Impact of the Research

The work described in this dissertation has led to 3 journal and 11 conference publications (see page 163). Two MSc. theses were co-supervised with topics related to Chapter 3 and Chapter 5 of this dissertation.

The analysis methods developed in this thesis have been used for the design of connected arrays for various applications in multiple projects in the group. The inclusion of vertical pins has become a common feature in ADL superstrate designs to control the polarization performance. The finite array method is being used to analyze arrays of resonant slots feeding lenses for mm-wave radar applications. A code that provides an easy to use interface between Matlab and CST was developed during this project and is currently in use by various members of the group.

7

Appendix A

Field Radiated by a Wheeler's Current

We consider an ideal x-oriented magnetic Wheeler's current sheet on a PEC plane with amplitude V_0:

$$m_x(x, y, z) = V_0 e^{-jk_{x0}x} e^{-jk_{y0}y} \delta(z), \qquad (A.1)$$

where $k_{x0} = k_0 \sin\theta \cos\phi$, $k_{y0} = k_0 \sin\theta \sin\phi$ are the x- and y-components of the propagation vector, and δ represents a Dirac distribution. The quantity in (A.1) is a magnetic volume current density, with unit V/m^2. The Wheeler current radiates in the presence of a generic superstrate made of dielectrics or metal layers. The field radiated by such a current can be defined as

$$\mathbf{e}_{\text{scat}}(\mathbf{r}) = \iiint \bar{\bar{\mathbf{g}}}^{em}(\mathbf{r} - \mathbf{r}') m_x(\mathbf{r}') \hat{\mathbf{x}} d\mathbf{r}', \qquad (A.2)$$

where $\bar{\bar{\mathbf{g}}}^{em}$ is the dyadic Green's function of the medium. Because the current is infinitesimally thin in z, from the volume current density $m_x(x, y, z)$, with units V/m^2, we can consider a surface magnetic current density $m_{s,x}(x, y)$, with units V/m. Hence, the radiation integral becomes

$$\mathbf{e}_{\text{scat}}(\mathbf{r}) = \int\limits_{-\infty}^{\infty} \int\limits_{-\infty}^{\infty} \bar{\bar{\mathbf{g}}}^{em}(x - x', y - y', z) m_{s,x}(\mathbf{r}') \hat{\mathbf{x}} dx' dy', \qquad (A.3)$$

where

$$m_{s,x}(x, y) = V_0 e^{-jk_{x0}x} e^{-jk_{y0}y}. \qquad (A.4)$$

We can now write the Green's function $\bar{\bar{\mathbf{g}}}^{em}$ as the inverse Fourier Transform of the two-dimensional spectral Green's function $\bar{\bar{\mathbf{G}}}^{em}$:

$$\bar{\bar{\mathbf{g}}}^{em}(x - x', y - y', z) =$$
$$\frac{1}{4\pi^2} \int\limits_{-\infty}^{\infty} \int\limits_{-\infty}^{\infty} \bar{\bar{\mathbf{G}}}^{em}(k_x, k_y, z) e^{-jk_x(x-x')} e^{-jk_y(y-y')} dx' dy'. \quad (A.5)$$

A

The components of the dyadic spectral Green's function for an x-oriented magnetic current can be expressed in terms of the current and voltage solutions (i_{TE}, i_{TM}, v_{TE}, and v_{TM}) of the equivalent transmission lines representing the stratification [see Fig. 3.1(b)]:

$$\begin{bmatrix} G_{xx}^{em}(k_x, k_y, z) \\ G_{yx}^{em}(k_x, k_y, z) \\ G_{zx}^{em}(k_x, k_y, z) \end{bmatrix} = \begin{bmatrix} \frac{(v_{\text{TM}} - v_{\text{TE}})k_x k_y}{k_\rho^2} \\ \frac{v_{\text{TE}}k_x^2 + v_{\text{TM}}k_y^2}{k_\rho^2} \\ -\frac{\zeta k_y}{k} i_{\text{TM}} \end{bmatrix} . \tag{A.6}$$

where ζ is the medium impedance at z. A step-by-step derivation of the spectral Green's function for stratified media can be found in [98].

Substituting (A.5) in the radiation integral (A.3) and recognizing that the Fourier transform of a constant distribution with a linear phase term is a Dirac δ, i.e.:

$$\int_{-\infty}^{\infty} \int_{-\infty}^{\infty} e^{-jk_{x0}x'} e^{-jk_{y0}y'} e^{jk_x x'} e^{jk_y y'} dx' dy' = 4\pi^2 \delta(k_x - k_{x0})\delta(k_y - k_{y0}), \tag{A.7}$$

the scattered field becomes

$$\mathbf{e}_{\text{scat}}(\mathbf{r}) = V_0 \int_{-\infty}^{\infty} \int_{-\infty}^{\infty} \bar{\bar{\mathbf{G}}}^{em}(k_x, k_y, z)\hat{\mathbf{x}}$$
$$\delta(k_x - k_{x0})\delta(k_y - k_{y0})e^{-jk_x x} e^{-jk_y y} dk_x dk_y . \tag{A.8}$$

From the property of the Dirac δ, we can then close the integral as follows

$$\mathbf{e}_{\text{scat}}(\mathbf{r}) = V_0 \bar{\bar{\mathbf{G}}}^{em}(k_{x0}, k_{y0}, z)\hat{\mathbf{x}} e^{-jk_{x0}x} e^{-jk_{y0}y} . \tag{A.9}$$

Assuming that the Green's function is calculated on the top of the dielectric stratification (at $z = z_0$) and there is free space above, we can write

$$\mathbf{e}_{\text{scat}}(x, y, z_0) = V_0 \bar{\bar{\mathbf{G}}}^{em}(k_{x0}, k_{y0}, z_0)\hat{\mathbf{x}} e^{-jk_{x0}x} e^{-jk_{y0}y} e^{-jk_{z0}(z-z_0)} , \tag{A.10}$$

with $k_{z0} = k_0 \cos\theta$, or in a more compact form

$$\mathbf{e}_{\text{scat}}(x, y, z_0) = V_0 \bar{\bar{\mathbf{G}}}^{em}(k_{x0}, k_{y0}, z_0)\hat{\mathbf{x}} e^{-jk_0 r} , \tag{A.11}$$

where $r = \sqrt{x^2 + y^2 + (z - z_0^2)}$. When calculating the X-pol levels of the Wheeler current, the term $\exp(-jk_0 r)$ can be omitted without loss of generality since it multiplies both the co-polar and cross-polar components, and thus it cancels out in the expression of the X-pol ratio.

A

Ludwig 3 Components of the Radiation from Wheeler's Current

From (A.11) and (A.6), the Cartesian components of the radiated field from an x-oriented magnetic Wheeler current can be written explicitly as

$$
\begin{aligned}
e_x &= V_0(v_{\mathrm{TM}} - v_{\mathrm{TE}})\sin\phi\cos\phi \\
e_y &= V_0(v_{\mathrm{TE}}\cos^2\phi + v_{\mathrm{TM}}\sin^2\phi) \\
e_z &= -V_0\zeta_0 i_{\mathrm{TM}}\sin\theta\sin\phi\,.
\end{aligned}
\tag{A.12}
$$

One can relate the Cartesian components of the field vector to the spherical components as

$$
\begin{aligned}
e_\theta &= \cos\theta\cos\phi\,e_x + \cos\theta\sin\phi\,e_y - \sin\theta\,e_z \\
e_\phi &= -\sin\phi\,e_x + \cos\phi\,e_y\,.
\end{aligned}
\tag{A.13}
$$

Since the fields are evaluated in free space, we can write the current i_{TM} in terms of the voltage v_{TM} as follows

$$
i_{\mathrm{TM}} = \frac{v_{\mathrm{TM}}}{Z_{\mathrm{TM}}} = \frac{v_{\mathrm{TM}}}{\frac{\zeta_0 k_z}{k_0}} = \frac{v_{\mathrm{TM}}}{\frac{\zeta_0 k_0 \cos\theta}{k_0}} = \frac{v_{\mathrm{TM}}}{\zeta_0 \cos\theta}\,.
\tag{A.14}
$$

By substituting (A.12) and (A.14) in (A.13) and using some algebraic steps, one finds the simple expressions

$$
\begin{aligned}
e_\theta &= V_0 v_{\mathrm{TM}}\sin\phi\sec\theta \\
e_\phi &= V_0 v_{\mathrm{TE}}\cos\phi\,.
\end{aligned}
\tag{A.15}
$$

From the spherical components, one can find the projection on the co- and cross-polarization vectors, defined according to the third definition of Ludwig [99]:

$$
\begin{aligned}
e_{\mathrm{co}} &= V_0(v_{\mathrm{TM}}\sin^2\phi\sec\theta + v_{\mathrm{TE}}\cos^2\phi) \\
e_{\mathrm{cr}} &= V_0\frac{\sin(2\phi)}{2}(v_{\mathrm{TM}}\sec\theta - v_{\mathrm{TE}})\,.
\end{aligned}
\tag{A.16}
$$

Appendix B

Derivation of Finite Array Method

The analysis method for an $N \times M$ finite connected slot array is derived below, starting from the integral equation and resulting in expressions for the active input impedance and voltage spectrum. It models the array using the connected array Green's function, and defines one basis function per feeding point plus two basis functions that model the terminations of each slot. As a result, it uses $(N + 2) \times M$ basis functions to model the entire finite connected slot array.

B.1 Integral Equation

We use the equivalence theorem, and define equivalent currents j_s and m_s on the surface surrounding the slots. The field inside the surface is arbitrary and assumed to be 0, so that

$$\boldsymbol{j}_s = \hat{z} \times \boldsymbol{h} \tag{B.1}$$

$$\boldsymbol{m}_s = -\hat{z} \times \boldsymbol{e}, \tag{B.2}$$

The material inside the surface is also arbitrary, so we choose PEC, which means that the field contribution due to the electric field cancels with their image, so we can consider only m_s. The magnetic field jumps by an amount proportional to the current on the surface, so

$$\hat{z} \times (\boldsymbol{h}^+ - \boldsymbol{h}^-) = \boldsymbol{j}_s. \tag{B.3}$$

The current on the surface is given by the surface impedance (or termination) and the tangential electric field

$$\boldsymbol{j}_s = Y_l \boldsymbol{e}_{\text{tang}}. \tag{B.4}$$

It follows that

$$\hat{z} \times (\boldsymbol{h}^+ - \boldsymbol{h}^-) = Y_l \boldsymbol{e}_{\text{tang}}. \tag{B.5}$$

The field above and below can be written as the sum of the scattered and incident field

$$\hat{z} \times (h_{\text{scat}}^+ - h_{\text{scat}}^-)a + \hat{z} \times (h_{\text{inc}}^+ - h_{\text{inc}}^-)a = Y_l e_{\text{tang}}. \tag{B.6}$$

Using the cyclical property of the cross-product

$$h^+_{\text{scat}} - h^-_{\text{scat}} = -(h^+_{\text{inc}} - h^-_{\text{inc}})a \times \hat{z} + Y_l e_{\text{tang}} \times \hat{z}\,. \tag{B.7}$$

The incident field jumps by the impressed current, so $h^+_{\text{inc}} - h^-_{\text{inc}} = j_{\text{inc}}$ and

$$h^+_{\text{scat}} - h^-_{\text{scat}} = -j_{\text{inc}} \times \hat{z} + Y_l e_t \times z\,. \tag{B.8}$$

The scattered field is given by the convolution of the magnetic current with the Green's function

$$m_s * (g^{hm}_{\text{up}} + g^{hm}_{\text{down}})a = -j_{\text{inc}} \times \hat{z} + Y_l e_t \times \hat{z}\,. \tag{B.9}$$

Observing on the axis of the slot yields

$$m_x * (g^{hm}_{xx,\text{up}} + g^{hm}_{xx,\text{down}})a(x,y) = -j_{y,\text{inc}}(x,y) + Y_l v(x,y)\,. \tag{B.10}$$

Define $g_{xx} = g_{xx,\text{up}} + g_{xx,\text{down}}$

$$(m_x * g^{hm}_{xx})a(x) = -j_{y,\text{inc}}(x,y) + Y_l v(x,y)\,. \tag{B.11}$$

B.2 Left-Hand Side

Taking the left-hand side of (B.11), and writing out the convolution

$$\iint\limits_{-\infty}^{\infty} g^{hm}_{xx}(x - x', y - y')m_x(x',y')\,.dx'dy' \tag{B.12}$$

Assuming the current is variable separable, let the distribution of the current be given by separated transverse and longitudinal distributions, summed over all slots $m' = 1, ..., M$

$$m_x(x',y')a = \sum_{m'=1}^{M} v_{m'}(x')m_{m'}(y')\,. \tag{B.13}$$

Assuming the transverse distribution is identical per slot, exists only inside the slot and differs by a spatial shift

$$m_{m'}(y')a = m_t(y' - m'd_y)\,\text{rect}_w(y' - m'd_y)\,. \tag{B.14}$$

We find

$$\sum_{m'=1}^{M} \iint\limits_{-\infty}^{\infty} g^{hm}_{xx}(x - x', y - y')v_{m'}(x')m_{m'}(y')dx'dy'\,. \tag{B.15}$$

Observing along the axis of the mth slot

$$\sum_{m'=1}^{M} \iint\limits_{-\infty}^{\infty} g^{hm}_{xx}(x - x', md_y - y')v_{m'}(x')m_{m'}(y')dx'dy'\,, \tag{B.16}$$

and rearranging to isolate the integral in y'

$$\sum_{m'=1}^{M} \int_{-\infty}^{\infty} \left[\int_{-\infty}^{\infty} g_{xx}^{hm}(x - x', md_y - y')m_{m'}(y')dy' \right] v_{m'}(x')dx'.$$ (B.17)

We define the connected array Green's function, where the domain of integration is limited to the region where m_t is defined, $-\frac{w}{2} \leq y' \leq \frac{w}{2}$,

$$d_{m'm}(x - x') = \int_{m'd_y - \frac{w}{2}}^{m'd_y + \frac{w}{2}} g_{xx}^{hm}(x - x', md_y - y')m_t(y' - m'd_y)dy',$$ (B.18)

and find

$$\sum_{m'=1}^{M} \int_{-\infty}^{\infty} d_{m'm}(x - x')v_{m'}(x')dx'.$$ (B.19)

B.3 Right-Hand Side

Taking the left-hand side of (B.11)

$$-j_{y,\text{inc}}(x, y) + Y_l v(x, y).$$ (B.20)

Assuming the first term, the impressed current:

- Is variable separable

$$j_{y,\text{inc}}(x, y) = j_{y,\text{inc},x}(x)j_{y,\text{inc},y}(x, y).$$ (B.21)

- Is constant in y over the slot width w

$$j_{y,\text{inc},y}(x, y) = \sum_{m'=1}^{M} \text{rect}_w(y - m'd_y).$$ (B.22)

- Is given in x by $N + 2$ basis function $f_{n'}(x)$ placed at $x_{n'}$ with amplitude $i_{n'm'}$

$$j_{y,\text{inc},x}(x) = \sum_{n'=0}^{N+1} i_{n'm'}f_{n'}(x - x_{n'}).$$ (B.23)

We find that the impressed current can be written as

$$j_{y,\text{inc}}(x, y) = \sum_{n'=0}^{N+1} \sum_{m'=1}^{M} i_{n'm'}f_{n'}(x - x_{n'})\text{rect}_w(y - m'd_y).$$ (B.24)

The second term is the current due to the voltage across the loads. Assuming the impressed voltage:

- Is variable separable

$$v(x, y) = v_x(x)v_y(y) \,. \tag{B.25}$$

- Is periodic in y with the feeding points in locations md_y.

- Is constant in y across the width w of the slot

$$v_y(y) = \sum_{m'=1}^{M} \mathrm{rect}_w(y - m'd_y) \,. \tag{B.26}$$

- Is given in x by a sum of basis functions $f_{n'}(x)$ placed at $x_{n'}$ with amplitude $v_{n'm'}$

$$v_x(x) = \sum_{n'=-1}^{N} v_{n'm'} f_{n'} \left(x - x_{n'} \right) \,. \tag{B.27}$$

We find that the impressed voltage can be written as

$$v(x, y) = \sum_{n'=-1}^{N} \sum_{m'=1}^{M} v_{n'm'} f_{n'} \left(x - x_{n'} \right) \mathrm{rect}_w(y - m'd_y) \,. \tag{B.28}$$

Combining (B.24) and (B.28) and observing on the axis of the mth slot

$$\sum_{n'=0}^{N+1} \sum_{m'=1}^{M} \left(-i_{n'm'} + Y_l v_{n'm'} \right) f_{n'} \left(x - x_{n'} \right) \mathrm{rect}_w(md_y - m'd_y) \,. \tag{B.29}$$

Assuming $w < d_y$, the rect_w function becomes a Kronecker delta δ in $m - m'$

$$\sum_{n'=0}^{N+1} \sum_{m'=1}^{M} \left(-i_{n'm'} + Y_l v_{n'm'} \right) f_{n'} \left(x - x_{n'} \right) \delta(m - m') \,, \tag{B.30}$$

and the sum in m' can be evaluated to find only element m

$$\sum_{n'=0}^{N+1} \left(-i_{n'm} + Y_l v_{n'm} \right) f_{n'} \left(x - x_{n'} \right) \,. \tag{B.31}$$

B.4 Combining the Left- and Right-Hand Sides

Substituting the left-hand side (B.19) and the right-hand side (B.31) into the integral equation (B.11) yields

$$\sum_{m'=1}^{M} \int_{-\infty}^{\infty} d_{m'm}(x - x')v_{m'}(x')dx' = \sum_{n'=0}^{N+1} \left(-i_{n'm} + Y_l v_{n'm} \right) f_{n'} \left(x - x_{n'} \right) \,. \tag{B.32}$$

Writing $d_{m'm}$ and $f_{n'}$ as inverse Fourier transforms

$$d_{m'm}(x - x') = \frac{1}{2\pi} \int\limits_{-\infty}^{\infty} D_{m'm}(k_x) e^{-jk_x(x-x')} dk_x \qquad (B.33)$$

$$f_{n'}(x - x_{n'} = \frac{1}{2\pi} \int\limits_{-\infty}^{\infty} F_{n'}(k_x) e^{-jk_x(x-x_{n'})} dk_x . \qquad (B.34)$$

Substituting these into (B.32)

$$\sum_{m'=1}^{M} \int\limits_{-\infty}^{\infty} \left[\frac{1}{2\pi} \int\limits_{-\infty}^{\infty} D_{m'm}(k_x) e^{-jk_x(x-x')} dk_x \right] v_{m'}(x') dx'$$

$$= \sum_{n'=0}^{N+1} (-i_{n'm} + Y_l v_{n'm}) \left[\frac{1}{2\pi} \int\limits_{-\infty}^{\infty} F_{n'}(k_x) e^{-jk_x(x-x_{n'})} dk_x \right] , \quad (B.35)$$

and rearranging to isolate the integral in x'

$$\frac{1}{2\pi} \int\limits_{-\infty}^{\infty} \sum_{m'=1}^{M} D_{m'm}(k_x) \left[\int\limits_{-\infty}^{\infty} v_{m'}(x') e^{jk_x x'}) dx' \right] e^{-jk_x x} dk_x$$

$$= \frac{1}{2\pi} \int\limits_{-\infty}^{\infty} \sum_{n'=0}^{N+1} (-i_{n'm} + Y_l v_{n'm}) F_{n'}(k_x) e^{jk_x x_{n'}} e^{-jk_x x} dk_x . \quad (B.36)$$

The integral in x' is a Fourier transform

$$\frac{1}{2\pi} \int\limits_{-\infty}^{\infty} \sum_{m'=1}^{M} D_{m'm}(k_x) V_{m'}(k_x) e^{-jk_x x} dk_x$$

$$= \frac{1}{2\pi} \int\limits_{-\infty}^{\infty} \sum_{n'=0}^{N+1} (-i_{n'm} + Y_l v_{n'm}) F_{n'}(k_x) e^{jk_x x_{n'}} e^{-jk_x x} dk_x . \quad (B.37)$$

This expression must be valid for all x, so we can equate the spectra

$$\sum_{m'=1}^{M} D_{m'm}(k_x) V_{m'}(k_x) = \sum_{n'=0}^{N+1} (-i_{n'm} + Y_l v_{n'm}) F_{n'}(k_x) e^{jk_x x_{n'}} . \qquad (B.38)$$

Since this must be valid for all m, this can be written in matrix form as

$$\boldsymbol{D}(k_x) \boldsymbol{V}(k_x) = \sum_{n'=0}^{N+1} (-\boldsymbol{i}_{n'} + Y_l \boldsymbol{v}_{n'}) F_{n'}(k_x) e^{jk_x x_{n'}} . \qquad (B.39)$$

B

Multiplying both sides by $\boldsymbol{D}^{-1}$ yields

$$\boldsymbol{V}(k_x) = \boldsymbol{D}^{-1}(k_x) \sum_{n'=0}^{N+1} \left(-\boldsymbol{i}_{n'} + Y_l \boldsymbol{v}_{n'} \right) F_{n'}(k_x) e^{j k_x x_{n'}} \, . \tag{B.40}$$

Projecting onto the nth gap gives the voltage on the left-hand side

$$\boldsymbol{v}_n = \frac{1}{2\pi} \int_{-\infty}^{\infty} \boldsymbol{V}(k_x) F_n(-k_x) e^{-j k_x x_n} dk_x$$

$$= \frac{1}{2\pi} \int_{-\infty}^{\infty} \boldsymbol{D}^{-1}(k_x) \sum_{n'=0}^{N+1} \left(-\boldsymbol{i}_{n'} + Y_l \boldsymbol{v}_{n'} \right) F_{n'}(k_x) e^{j k_x x_{n'}} F_n(-k_x) e^{-j k_x x_n} dk_x \, . \tag{B.41}$$

Taking element m of the voltage and expanding the matrix equation back into a sum in m'

$$v_{nm} = \frac{1}{2\pi} \int_{-\infty}^{\infty} \sum_{m'=1}^{M} \sum_{n'=0}^{N+1} \left(\boldsymbol{D}^{-1}(k_x) \right)_{m'm} \left(-i_{n'm'} + Y_l v_{n'm'} \right)$$

$$\cdot F_{n'}(k_x) F_n(-k_x) e^{j k_x (x_{n'} - x_n)} dk_x \, . \tag{B.42}$$

Rearranging to isolate the integral in k_x

$$v_{nm} = \sum_{m'=1}^{M} \sum_{n'=0}^{N+1} - \left(-i_{n'm'} + Y_l v_{n'm'} \right)$$

$$\cdot \left[-\frac{1}{2\pi} \int_{-\infty}^{\infty} \left(\boldsymbol{D}^{-1}(k_x) \right)_{m'm} F_{n'}(k_x) F_n(-k_x) e^{j k_x (x_{n'} - x_n)} dk_x \right] \, . \tag{B.43}$$

Define the mutual impedance matrix

$$Z_{n'nm'm} = -\frac{1}{2\pi} \int_{-\infty}^{\infty} \left(\boldsymbol{D}^{-1}(k_x) \right)_{m'm} F_{n'}(k_x) F_n(-k_x) e^{j k_x (x_{n'} - x_n)} dk_x \, , \tag{B.44}$$

to find

$$v_{nm} = \sum_{m'=1}^{M} \sum_{n'=0}^{N+1} Z_{n'nm'm} \left(i_{n'm'} - Y_l v_{n'm'} \right) \, . \tag{B.45}$$

This is a set of equations, which can be written in matrix form as

$$\boldsymbol{v} = \boldsymbol{Z} \boldsymbol{i} - \boldsymbol{Z} \boldsymbol{Y}_l \boldsymbol{v} \, , \tag{B.46}$$

where $\boldsymbol{Y}_l$ is a diagonal matrix describing the loads on the elements. Multiplying by $\boldsymbol{Z}_l = \boldsymbol{Y}_l^{-1}$ and solving for v yields

$$\boldsymbol{v} = (\boldsymbol{Z} + \boldsymbol{Z}_l)^{-1} \boldsymbol{Z}_l \boldsymbol{Z} \boldsymbol{i} \, , \tag{B.47}$$

and the active current can be found as

$$i_a = Z^{-1}v \, ,$$

(B.48)

and the active input impedance for element nm can be written as

$$Z_{a,nm} = \frac{v_{nm}}{i_{a,nm}} \, .$$

(B.49)

B

B.5 Fourier Transform of d

Starting from the connected array Green's function in (B.18)

$$d_{m'm}(x - x') = \int_{m'd_y - \frac{w}{2}}^{m'd_y + \frac{w}{2}} g_{xx}^{hm}(x - x', md_y - y')m_t(y' - m'd_y)dy' \, ,$$

(B.50)

and writing g_{xx}^{hm} as inverse 2D Fourier transform

$$d_{m'm}(x - x') = \int_{m'd_y - \frac{w}{2}}^{m'd_y + \frac{w}{2}} \frac{1}{2\pi} \int_{-\infty}^{\infty} \frac{1}{2\pi} \int_{-\infty}^{\infty} G_{xx}^{hm}(k_x, k_y)e^{-jk_y(md_y - y')}dk_y e^{jk_x(x - x')}dk_x$$

$$m_t(y' - m'd_y)dy' \, . \quad \text{(B.51)}$$

Rearranging to isolate the integral in y', and performing a change of variables $y' = y'' + m'd_y$

$$d_{m'm}(x - x') = \frac{1}{2\pi} \int_{-\infty}^{\infty} \frac{1}{2\pi} \int_{-\infty}^{\infty} G_{xx}^{hm}(k_x, k_y)$$

$$\left[\int_{-\frac{w}{2}}^{\frac{w}{2}} m_t(y'')e^{jk_y y''} dy'' \right] e^{-jk_y(m - m')d_y}dk_y e^{jk_x(x - x')}dk_x \, . \quad \text{(B.52)}$$

The integral in y'' is a Fourier transform of the transverse current distribution on the slot

$$d_{m'm}(x - x') = \frac{1}{2\pi} \int_{-\infty}^{\infty} \frac{1}{2\pi} \int_{-\infty}^{\infty} G_{xx}^{hm}(k_x, k_y)M_t(k_y)e^{-jk_y(m - m')d_y}dk_y e^{jk_x(x - x')}dk_x \, .$$

(B.53)

Fourier transform both sides in $x - x'$

$$D_{m'm}(k_x) = \frac{1}{2\pi} \int_{-\infty}^{\infty} G_{xx}^{hm}(k_x, k_y)M_t(k_y)e^{-jk_y(m - m')d_y}dk_y \, .$$

(B.54)

Since the transverse current distribution was assumed to be an edge-singular of length w, its Fourier transform $M_t(k_y)$ is a 0th order Bessel function of the first kind. We find the final expression for the spectral connected array Green's function D

$$D_{m'm}(k_x) = \frac{1}{2\pi} \int\limits_{-\infty}^{\infty} G_{xx}^{hm}(k_x, k_y) J_0\left(k_y \frac{w}{2}\right) e^{-jk_y(m-m')d_y} dk_y. \qquad \text{(B.55)}$$

Appendix C

Derivation of Periodic Spectral Method of Moments

This appendix describes the derivation of the mutual impedance for a Cartesian or cylindrical basis or test function embedded in a rectangular periodic environment. Expressions are derived for basis and test functions oriented along a Cartesian axis $(\hat{x}, \hat{y}, \hat{z})$ or a cylindrical axis $(\hat{\rho}, \hat{z})$.

C.1 Integral Equation

To ensure the tangential component of the current goes to zero on the metal, the scattered field must be equal and opposite to the incident field

$$-\boldsymbol{e}_{\text{scat}}(\boldsymbol{r}) = \boldsymbol{e}_{\text{inc}}(\boldsymbol{r}) \,. \tag{C.1}$$

The scattered field is given by the convolution of the currents on the structure with the Green's function, so we find the electric field integral equation

$$-\bar{\bar{\boldsymbol{g}}} * \boldsymbol{j} = -\iiint\limits_{-\infty}^{\infty} \bar{\bar{\boldsymbol{g}}}(\boldsymbol{r}, \boldsymbol{r}')\boldsymbol{j}(\boldsymbol{r})d\boldsymbol{r}' = \boldsymbol{e}_{\text{inc}}(\boldsymbol{r}) \,, \tag{C.2}$$

where $\bar{\bar{\boldsymbol{g}}}$ is the dyadic Green's function and j are the equivalent currents on the structure.

C.2 Current Distribution

Assuming the equivalent current $\boldsymbol{j}(\boldsymbol{r})$ is given by a set of N basis functions, periodic in x and y

$$\boldsymbol{j}(\boldsymbol{r}) = \sum_{n_x=-\infty}^{\infty} \sum_{n_y=-\infty}^{\infty} \sum_{n=1}^{N} I_n \boldsymbol{b}_n(x - x_n - n_x d_x, y - y_n - n_y d_y, z - z_n) e^{-jk_{x0}n_x d_x} e^{-jk_{y0}n_y d_y} ,$$

(C.3)

where d_x, d_y are the periodicity in x and y, respectively, and I_n is the unknown complex amplitude of the basis function. Each basis function $\boldsymbol{b}_n$ is centered in $\boldsymbol{r}_n = (x_n, y_n, z_n)$.

C.3 Solution of integral equation

Substituting the current into the EFIE, we obtain

$$-\iiint_{-\infty}^{\infty} \bar{\bar{g}}(\boldsymbol{r}, \boldsymbol{r}') \sum_{n_x=-\infty}^{\infty} \sum_{n_y=-\infty}^{\infty} \sum_{n=1}^{N} I_n \boldsymbol{b}_n(x - x_n - n_x d_x, y - y_n - n_y d_y, z - z_n)$$

$$e^{-jk_{x0}n_x d_x} e^{-jk_{y0}n_y d_y} d\boldsymbol{r}' = \boldsymbol{e}_{\text{inc}}(\boldsymbol{r}) . \quad \text{(C.4)}$$

The spatial Green's function $\bar{\bar{g}}(\boldsymbol{r}, \boldsymbol{r}')$ can be written as the inverse Fourier transform of the spectral Green's function $\bar{\bar{G}}(k_x, k_y, k_z)$.

$$\bar{\bar{g}}(\boldsymbol{r}, \boldsymbol{r}') = \frac{1}{(2\pi)^3} \iiint_{-\infty}^{\infty} \bar{\bar{G}}(k_x, k_y, k_z) e^{-jk_x(x-x')} e^{-jk_y(y-y')} e^{-jk_z(z-z')} dk_x dk_y dk_z .$$

(C.5)

Substituting the Green's function into the EFIE

$$-\iiint_{-\infty}^{\infty} \left[\frac{1}{(2\pi)^3} \iiint_{-\infty}^{\infty} \bar{\bar{G}}(k_x, k_y, k_z) e^{-jk_x(x-x')} e^{-jk_y(y-y')} e^{-jk_z(z-z')} dk_x dk_y dk_z \right]$$

$$\cdot \sum_{n_x=-\infty}^{\infty} \sum_{n_y=-\infty}^{\infty} \sum_{n=1}^{N} I_n \boldsymbol{b}_n(x' - x_n - n_x d_x, y' - y_n - n_y d_y, z' - z_n) e^{-jk_{x0}n_x d_x} e^{-jk_{y0}n_y d_y} d\boldsymbol{r}'$$

$$= \boldsymbol{e}_{\text{inc}}(\boldsymbol{r}) . \quad \text{(C.6)}$$

For simplicity we only consider the left hand side (LHS). Using

$$\begin{aligned}
-(x - x') &= (x' - x_n - n_x d_x) - (x - x_n) + n_x d_x \\
-(y - y') &= (y' - y_n - n_y d_y) - (y - y_n) + n_y d_y \\
-(z - z') &= (z' - z_n) - (z - z_n) .
\end{aligned}$$

(C.7)

The exponential terms become

$$e^{jk_x(x'-x_n-n_xd_x)}e^{-jk_x(x-x_n)}e^{jk_xn_xd_x}e^{jk_y(y'-y_n-n_yd_y)}e^{-jk_y(y-y_n)}e^{jk_yn_yd_y}$$

$$e^{jk_z(z'-z_n)}e^{-jk_z(z-z_n)}\,. \quad \text{(C.8)}$$

We can rearrange to isolate the integrals in x', y', z'

$$-\frac{1}{(2\pi)^3}\sum_{n_x=-\infty}^{\infty}\sum_{n_y=-\infty}^{\infty}\sum_{n=1}^{N}I_n\iiint_{-\infty}^{\infty}\bar{\bar{\boldsymbol{G}}}(k_x,k_y,k_z)$$

$$\cdot\left[\iiint_{-\infty}^{\infty}\boldsymbol{b}_n(x'-x_n-n_xd_x,y'-y_n-n_yd_y,z'-z_n)\right.$$

$$\cdot\left.e^{jk_x(x'-x_n-n_xd_x)}e^{jk_y(y'-y_n-n_yd_y)}e^{jk_z(z'-z_n)}dx'dy'dz'\right]$$

$$\cdot e^{-jk_{x0}n_xd_x}e^{-jk_{y0}n_yd_y}e^{-jk_x(x-x_n)}e^{jk_xn_xd_x}e^{-jk_y(y-y_n)}e^{jk_yn_yd_y}e^{-jk_z(z-z_n)}dk_xdk_ydk_z\,.$$
$$\text{(C.9)}$$

Rearranging to isolate the sums in n_x, n_y, where the triple integral in x', y', z' is abbreviated for convenience

$$-\frac{1}{(2\pi)^3}\sum_{n=1}^{N}I_n\iiint_{-\infty}^{\infty}\bar{\bar{\boldsymbol{G}}}(k_x,k_y,k_z)\Big[\cdots\Big]e^{-jk_x(x-x_n)}e^{-jk_y(y-y_n)}e^{-jk_z(z-z_n)}$$

$$\cdot\left[\sum_{n_x=-\infty}^{\infty}e^{j(k_x-k_{x0})n_xd_x}\right]\left[\sum_{n_y=-\infty}^{\infty}e^{j(k_y-k_{y0})n_yd_y}\right]dk_xdk_ydk_z\,. \quad \text{(C.10)}$$

The Poisson formula states

$$\sum_{n_x=-\infty}^{\infty}e^{j(k_x-k_{x0})n_xd_x}=\frac{2\pi}{d_x}\sum_{m_x=-\infty}^{\infty}\delta(k_x-k_{xm})$$
$$\sum_{n_y=-\infty}^{\infty}e^{j(k_y-k_{y0})n_yd_y}=\frac{2\pi}{d_y}\sum_{m_y=-\infty}^{\infty}\delta(k_y-k_{ym})\,, \quad \text{(C.11)}$$

where $k_{xm}=k_{x0}-\frac{2\pi m_x}{d_x}$ and $k_{ym}=k_{y0}-\frac{2\pi m_y}{d_y}$. Substituting this into the expression above and evaluating the integrals in k_x, k_y yields

$$-\frac{1}{2\pi}\frac{1}{d_xd_y}\sum_{m_x=-\infty}^{\infty}\sum_{m_y=-\infty}^{\infty}\sum_{n=1}^{N}I_n\int_{-\infty}^{\infty}\bar{\bar{\boldsymbol{G}}}(k_{xm},k_{ym},k_z)\Big[\cdots\Big]$$

$$e^{-jk_{xm}(x-x_n)}e^{-jk_{ym}(y-y_n)}e^{-jk_z(z-z_n)}dk_z\,. \quad \text{(C.12)}$$

C.4 Mutual impedances

The goal is to define an impedance $Z_{n'n}$ that relates the current I_n to the projection of the field onto the test function $\boldsymbol{t}_{n'}$. This is done by projecting both sides onto that test function.

Element n', n of the mutual impedance matrix is found by projecting the n-th element of the sum above onto the n'-th test function $\boldsymbol{t}_{n'}(\boldsymbol{r} - \boldsymbol{r}_{n'})$

$$
Z_{n'n} = \left\langle -\frac{1}{2\pi}\frac{1}{d_x d_y} \sum_{m_x=-\infty}^{\infty} \sum_{m_y=-\infty}^{\infty} \right.
$$
$$
\left. \int_{-\infty}^{\infty} \bar{\bar{\boldsymbol{G}}}(k_{xm}, k_{ym}, k_z) \left[\cdots\right] e^{-jk_{xm}(x-x_n)} e^{-jk_{ym}(y-y_n)} e^{-jk_z(z-z_n)} dk_z, \boldsymbol{t}_{n'}(\boldsymbol{r} - \boldsymbol{r}_{n'}) \right\rangle.
$$
$$(C.13)$$

Writing this in integral form using $\langle a(\boldsymbol{r}), b(\boldsymbol{r}) \rangle = \iiint a(\boldsymbol{r}) b(\boldsymbol{r}) d\boldsymbol{r}$

$$
Z_{n'n} = \iiint_{-\infty}^{\infty} -\frac{1}{2\pi}\frac{1}{d_x d_y} \sum_{m_x=-\infty}^{\infty} \sum_{m_y=-\infty}^{\infty}
$$
$$
\int_{-\infty}^{\infty} \bar{\bar{\boldsymbol{G}}}(k_{xm}, k_{ym}, k_z) \left[\cdots\right] e^{-jk_{xm}(x-x_n)} e^{-jk_{ym}(y-y_n)} e^{-jk_z(z-z_n)} dk_z \cdot \boldsymbol{t}_{n'}(\boldsymbol{r} - \boldsymbol{r}_{n'}) d\boldsymbol{r}.
$$
$$(C.14)$$

We can write

$$
\begin{aligned}
-(x - x_n) &= -(x - x_{n'}) + (x_n - x_{n'}) \\
-(y - y_n) &= -(y - y_{n'}) + (y_n - y_{n'}) \\
-(z - z_n) &= -(z - z_{n'}) + (z_n - z_{n'}).
\end{aligned}
$$
$$(C.15)$$

Restore the integral in x', y', z' from (C.9) in the expression and apply the effects of the Poisson theorem to it. Then rearrange to also isolate the integral in x, y, z

$$
Z_{n'n} = -\frac{1}{2\pi} \frac{1}{d_x d_y} \sum_{m_x=-\infty}^{\infty} \sum_{m_y=-\infty}^{\infty} \int_{-\infty}^{\infty} \bar{\bar{\boldsymbol{G}}}(k_{xm}, k_{ym}, k_z)
$$

$$
\cdot \left[\iiint_{-\infty}^{\infty} \boldsymbol{b}_n(x' - x_n - n_x d_x, y' - y_n - n_y d_y, z' - z_n) \right.
$$

$$
\left. \cdot e^{jk_{xm}(x'-x_n-n_x d_x)} e^{jk_{ym}(y'-y_n-n_y d_y)} e^{jk_z(z'-z_n)} dx' dy' dz' \right]
$$

$$
\left[\iiint_{-\infty}^{\infty} \boldsymbol{t}_{n'}(\boldsymbol{r} - \boldsymbol{r}_{n'}) e^{-jk_{xm}(x-x_{n'})} e^{-jk_{ym}(y-y_{n'})} e^{-jk_z(z-z_{n'})} dx dy x dz \right]
$$

$$
\cdot e^{jk_{xm}(x_n-x_{n'})} e^{jk_{ym}(y_n-y_{n'})} e^{jk_z(z_n-z_{n'})} dk_z . \quad \text{(C.16)}
$$

C.4.1 Integral in x', y', z'

The integral in x', y', z' yields a different result based on whether the basis function $\boldsymbol{b}_n$ is defined in Cartesian coordinates or in cylindrical coordinates. It also varies based on the direction of the basis function.

Basis function in Cartesian coordinates

Starting with the integral in x', y', z'

$$
\iiint_{-\infty}^{\infty} \boldsymbol{b}_n(x' - x_n - n_x d_x, y' - y_n - n_y d_y, z' - z_n)
$$

$$
\cdot e^{jk_{xm}(x'-x_n-n_x d_x)} e^{jk_{ym}(y'-y_n-n_y d_y)} e^{jk_z(z'-z_n)} dx' dy' dz' . \quad \text{(C.17)}
$$

Assuming the basis function is defined in Cartesian coordinates, this is simply a Fourier transform

$$
\boldsymbol{B}_n(k_{xm}, k_{ym}, k_z) . \quad \text{(C.18)}
$$

Basis function in cylindrical coordinates

Starting again with the integral in x', y', z'

$$\iiint\limits_{-\infty}^{\infty} \boldsymbol{b}_n(x' - x_n - n_x d_x, y' - y_n - n_y d_y, z' - z_n)$$

$$\cdot e^{jk_{xm}(x'-x_n-n_x d_x)} e^{jk_{ym}(y'-y_n-n_y d_y)} e^{jk_z(z'-z_n)} dx' dy' dz' \, . \quad \text{(C.19)}$$

Change of variables to go to cylindrical coordinates

$$\begin{aligned}
x' - x_n - n_x d_x &= \rho' \cos \phi' \\
y' - y_n - n_y d_y &= \rho' \sin \phi' \\
k_{xm} &= k_{\rho m} \cos \alpha_m \\
k_{ym} &= k_{\rho m} \sin \alpha_m \\
dx' dy' &= J(\rho', \phi') d\rho' d\phi' = \rho' d\rho' d\phi' \, .
\end{aligned} \quad \text{(C.20)}$$

Where $J(\rho, \phi)$ is the Jacobian

$$J(\rho, \phi) = \begin{vmatrix} \frac{\partial x}{\partial \rho} & \frac{\partial x}{\partial \phi} \\ \frac{\partial y}{\partial \rho} & \frac{\partial y}{\partial \phi} \end{vmatrix} = \begin{vmatrix} \cos \phi & -\rho \sin \phi \\ \sin \phi & \rho \cos \phi \end{vmatrix} = \rho \left(\cos^2 \phi + \sin^2 \phi \right) = \rho \, . \quad \text{(C.21)}$$

The integral becomes

$$\int\limits_{-\infty}^{\infty} \int\limits_{0}^{2\pi} \int\limits_{0}^{\infty} \boldsymbol{b}_n(\rho', \phi', z' - z_n) e^{jk_{\rho m}\rho' \cos \alpha_m \cos \phi'} e^{jk_{\rho m}\rho' \sin \alpha_m \sin \phi'} e^{jk_z(z'-z_n)} \rho' d\rho' d\phi' dz' \, .$$

$$\text{(C.22)}$$

Using the trigonometric identity $\cos \alpha \cos \beta \mp \sin \alpha \sin \beta = \cos(\alpha \pm \beta)$

$$\int\limits_{-\infty}^{\infty} \int\limits_{0}^{2\pi} \int\limits_{0}^{\infty} \boldsymbol{b}_n(\rho', \phi', z' - z_n) e^{jk_{\rho m}\rho' \cos(\alpha_m - \phi')} e^{jk_z(z'-z_n)} \rho' d\rho' d\phi' dz' \, . \quad \text{(C.23)}$$

Assuming $\boldsymbol{b}_n$ is separable and constant in ϕ'

$$\boldsymbol{b}_n(\rho', \phi', z') = b_{n\rho}(\rho') b_{nz}(z') \hat{b}_n \, , \quad \text{(C.24)}$$

where $\hat{b} \in \{x, y, z\}$ is the unit vector describing the direction of the basis function. The integral can be rearranged into

$$\int\limits_{0}^{\infty} b_{n\rho}(\rho') \int\limits_{0}^{2\pi} e^{jk_{\rho m}\rho' \cos(\alpha_m - \phi')} \hat{b}_n d\phi' \rho' d\rho' \int\limits_{-\infty}^{\infty} b_{nz}(z' - z_n) e^{jk_z(z'-z_n)} dz' \, . \quad \text{(C.25)}$$

The integral in z' is a Fourier transform in k_z

$$\int\limits_0^\infty b_{n\rho}(\rho') \int\limits_0^{2\pi} e^{jk_{\rho m}\rho'\cos(\alpha_m-\phi')}\hat{b}_n d\phi'\rho' d\rho' B_{nz}(k_z)\,. \tag{C.26}$$

This expression can be further simplified by making an assumption on the orientation of the basis function. Here, two cases will be considered; a basis function along $\hat{\rho}$ and a basis function along $\hat{z}$.

Cylindrical basis function along $\hat{\rho}$

Assuming $\boldsymbol{b}_n$ is separable, constant in ϕ, and along $\hat{\rho}$

$$\hat{b}_n = b_{n\rho}(\rho')b_{nz}(z')\hat{\rho}\,. \tag{C.27}$$

Projecting this onto a Cartesian coordinate system yields $\hat{\rho} = \hat{x}\cos\phi' + \hat{y}\sin\phi'$, and we find

$$\int\limits_0^\infty b_{n\rho}(\rho') \int\limits_0^{2\pi} e^{jk_{\rho m}\rho'\cos(\alpha_m-\phi')}\left(\hat{x}\cos\phi' + \hat{y}\sin\phi'\right)d\phi'\rho' d\rho' B_{nz}(k_z)\,. \tag{C.28}$$

Expanding and considering the two integrals in ϕ'

$$\hat{x}\int\limits_0^{2\pi} e^{jk_{\rho m}\rho'\cos(\alpha_m-\phi')}\cos\phi' d\phi' + \hat{y}\int\limits_0^{2\pi} e^{jk_{\rho m}\rho'\cos(\alpha_m-\phi')}\sin\phi' d\phi'\,. \tag{C.29}$$

These integrals appear to match the following definition

$$j2\pi J_1(k_{\rho m}\rho)\left(\hat{x}\cos\alpha_m + \hat{y}\sin\alpha_m\right)\,. \tag{C.30}$$

Returning this to the integral and rearranging to isolate the integral in ρ'

$$j2\pi\left[\int\limits_0^\infty b_{n\rho}(\rho')J_1(k_{\rho m}\rho)\rho' d\rho'\right]B_{nz}(k_z)\left(\hat{x}\cos\alpha_m + \hat{y}\sin\alpha_m\right)\,. \tag{C.31}$$

The integral in the brackets is the Hankel transform of order 1 of the basis function

$$B_{n\rho,J_1}(k_{\rho m}) = \int\limits_0^\infty b_{n\rho}(\rho')J_1(k_{\rho m}\rho)\rho' d\rho'\,. \tag{C.32}$$

The integral in x', y', z' when $\boldsymbol{b}_n$ is along $\hat{\rho}$ becomes

$$\iiint\limits_{-\infty}^\infty \boldsymbol{b}_n(x' - x_n - n_x d_x, y' - y_n - n_y d_y, z' - z_n)$$

$$\cdot\, e^{jk_{xm}(x'-x_n-n_x d_x)}e^{jk_{ym}(y'-y_n-n_y d_y)}e^{jk_z(z'-z_n)}dx' dy' dz'$$

$$= j2\pi B_{n\rho,J_1}(k_{\rho m})B_{nz}(k_z)\left(\hat{x}\cos\alpha_m + \hat{y}\sin\alpha_m\right)\,. \tag{C.33}$$

Cylindrical basis function along $\hat{z}$

Assuming $\boldsymbol{b}_n$ is separable, constant in ϕ, and along $\hat{z}$

$$\hat{b}_n = b_{n\rho}(\rho')b_{nz}(z')\hat{z} \tag{C.34}$$

The integral is

$$\int\limits_0^\infty b_{n\rho}(\rho') \int\limits_0^{2\pi} e^{jk_{\rho m}\rho'\cos(\alpha_m - \phi')}d\phi'\rho'd\rho' B_{nz}(k_z)\hat{z}\,. \tag{C.35}$$

Focusing on the integral in ϕ', rewriting it to a form similar to [114, Eq. 9.1.18], and then noticing that α_m has no effect on the result

$$\int\limits_0^{2\pi} e^{jk_{\rho m}\rho'\cos(\alpha_m - \phi')}d\phi' = 2\pi J_0(k_{\rho m}\rho')\,. \tag{C.36}$$

Returning this to the integral

$$2\pi \left[\int\limits_0^\infty b_{n\rho}(\rho')J_0(k_{\rho m}\rho')\rho'd\rho'\right] B_{nz}(k_z)\hat{z}\,. \tag{C.37}$$

The integral in the brackets is the Hankel transform of order 0 of the basis function

$$B_{n\rho,J_0}(k_{\rho m}) = \int\limits_0^\infty b_{n\rho}(\rho')J_0(k_{\rho m}\rho')\rho'd\rho'\,. \tag{C.38}$$

The integral in x', y', z' when $\boldsymbol{b}_n$ is along $\hat{z}$ becomes

$$\iiint\limits_{-\infty}^\infty \boldsymbol{b}_n(x' - x_n - n_x d_x, y' - y_n - n_y d_y, z' - z_n)$$

$$\cdot e^{jk_{xm}(x' - x_n - n_x d_x)}e^{jk_{ym}(y' - y_n - n_y d_y)}e^{jk_z(z' - z_n)}dx'dy'dz'$$

$$= 2\pi B_{n\rho,J_0}(k_{\rho m})B_{nz}(k_z)\hat{z}\,. \tag{C.39}$$

C.4.2 Integral in x, y, z

The integral in x, y, z yields a different result based on whether the test function $\boldsymbol{t}_{n'}$ is defined in Cartesian coordinates or in cylindrical coordinates. For cylindrical coordinates, it also varies based on the direction of the test function.

Test function in Cartesian coordinates

Isolating the integral in x, y, z from the expression in (C.16)

$$\iiint\limits_{-\infty}^{\infty} \boldsymbol{t}_{n'}(\boldsymbol{r} - \boldsymbol{r}_{n'})e^{j(-k_{xm})(x-x_{n'})}e^{j(-k_{ym})(y-y_{n'})}e^{j(-k_z)(z-z_{n'})}dxdydz\,. \qquad \text{(C.40)}$$

Assuming the test function is defined in Cartesian coordinates, this is simply a Fourier transform

$$\boldsymbol{T}_{n'}(-k_{xm}, -k_{ym}, -k_z)\,, \qquad \text{(C.41)}$$

where the $-$ signs arise from the signs of the exponentials.

Test function in cylindrical coordinates

Starting from (C.40), perform a change of variables

$$\begin{aligned}
x - x_{n'} - n_x d_x &= \rho\cos\phi \\
y - x_{n'} - n_y d_y &= \rho\sin\phi \\
k_{xm} &= k_{\rho m}\cos\alpha_m \\
k_{ym} &= k_{\rho m}\sin\alpha_m \\
dxdy &= J(\rho,\phi)d\rho d\phi = \rho d\rho d\phi\,,
\end{aligned} \qquad \text{(C.42)}$$

where the Jacobian $J(\rho, \phi) = \rho$ is the same as in (C.21). The integral becomes

$$\int\limits_{-\infty}^{\infty}\int\limits_{0}^{2\pi}\int\limits_{0}^{\infty} \boldsymbol{t}_{n'}(\rho, \phi, z - z_{n'})e^{-jk_{\rho m}\rho\cos\alpha_m\cos\phi}e^{-jk_{\rho m}\rho\sin\alpha_m\sin\phi}e^{-jk_z(z-z_{n'})}\rho d\rho d\phi dz\,.$$
$$\text{(C.43)}$$

Using the trigonometric identity $\cos\alpha\cos\beta \mp \sin\alpha\sin\beta = \cos(\alpha\pm\beta)$

$$\int\limits_{-\infty}^{\infty}\int\limits_{0}^{2\pi}\int\limits_{0}^{\infty} \boldsymbol{t}_{n'}(\rho, \phi, z - z_{n'})e^{-jk_{\rho m}\rho\cos(\alpha_m-\phi)}e^{-jk_z(z-z_{n'})}\rho d\rho d\phi dz\,. \qquad \text{(C.44)}$$

Assuming $\boldsymbol{t}_{n'}$ is separable and constant in ϕ

$$\boldsymbol{t}_{n'}(\rho, \phi, z) = t_{n'\rho}(\rho)t_{n'z}(z')\hat{t}_{n'}\,, \qquad \text{(C.45)}$$

where $\hat{t} \in \{x, y, z\}$ is the unit vector describing the direction of the test function. The integral can be rearranged into

$$\int\limits_{0}^{\infty} t_{n'\rho}(\rho)\rho \int\limits_{0}^{2\pi} e^{-jk_{\rho m}\rho\cos(\alpha_m-\phi)}\hat{t}_{n'}d\phi d\rho \int\limits_{-\infty}^{\infty} t_{n'z}(z - z_{n'})e^{-jk_z(z-z_{n'})}dz\,. \qquad \text{(C.46)}$$

The integral in z' is a Fourier transform in $-k_z$

$$\int\limits_0^\infty t_{n'\rho}(\rho)\rho \int\limits_0^{2\pi} e^{-jk_{\rho m}\rho\cos(\alpha_m - \phi)}\hat{t}_{n'}d\phi d\rho T_{n'z}(-k_z)\,. \tag{C.47}$$

This expression can be further simplified by making an assumption on the orientation of the test function. Here, two cases will be considered; a test function along $\hat{\rho}$ and a test function along $\hat{z}$.

Cylindrical test function along $\hat{\rho}$

Assuming $\boldsymbol{t}_{n'}$ is separable, constant in ϕ, and along $\hat{\rho}$

$$\hat{t}_{n'} = t_{n'\rho}(\rho)t_{n'z}(z')\hat{\rho}\,. \tag{C.48}$$

Projecting $\hat{\rho}$ onto the Cartesian coordinate system yields $\hat{\rho} = \hat{x}\cos\phi + \hat{y}\sin\phi$, and the integral in (C.47) becomes

$$\int\limits_0^\infty t_{n'\rho}(\rho)\rho \int\limits_0^{2\pi} e^{-jk_{\rho m}\rho\cos(\alpha_m - \phi)}\left(\hat{x}\cos\phi + \hat{y}\sin\phi\right)d\phi d\rho T_{n'z}(-k_z)\,. \tag{C.49}$$

The same methodology as was used for $\boldsymbol{b}_n$ in Section C.4.1 can be used to find

$$\iiint\limits_{-\infty}^\infty \boldsymbol{t}_{n'}(\boldsymbol{r} - \boldsymbol{r}_{n'})e^{j(-k_{xm})(x-x_{n'})}e^{j(-k_{ym})(y-y_{n'})}e^{j(-k_z)(z-z_{n'})}dxdydz$$

$$= j2\pi T_{n'\rho,J_1}(-k_{\rho m})T_{n'z}(-k_z)\left(\hat{x}\cos\alpha_m + \hat{y}\sin\alpha_m\right)\,, \tag{C.50}$$

where the $-$ signs arise from the minus signs in the exponentials, and $T_{n'\rho,J_1}(k_{\rho m})$ is the Hankel transform of order 1 of the test function.

Cylindrical test function along $\hat{z}$

Assuming $\boldsymbol{t}_{n'}$ is separable, constant in ϕ, and along $\hat{z}$

$$\hat{t}_{n'} = t_{n'\rho}(\rho)t_{n'z}(z')\hat{z} \tag{C.51}$$

The integral in (C.47) becomes

$$\int\limits_0^\infty t_{n'\rho}(\rho) \int\limits_0^{2\pi} e^{-jk_{\rho m}\rho\cos(\alpha_m - \phi)}\rho d\phi d\rho T_{n'z}(-k_z)\hat{z}\,. \tag{C.52}$$

The same methodology as was used for $\boldsymbol{b}_n$ in Section C.4.1 can be used to find

$$
\int\limits_0^\infty t_{n'\rho}(\rho) \int\limits_0^{2\pi} e^{-jk_{\rho m}\rho\cos(\alpha_m-\phi)}\hat{z}\,d\phi\rho d\rho \int\limits_{-\infty}^\infty t_{n'z}(z-z_{n'})e^{-jk_z(z-z_{n'})}dz
$$

$$
= 2\pi T_{n'\rho,J_0}(-k_{\rho m})T_{n'z}(-k_z)\hat{z}\,, \quad \text{(C.53)}
$$

where the $-$ signs arise from the signs of the exponentials, and $T_{n'\rho,J_0}(k_{\rho m})$ is the Hankel transform of order 0 of the test function.

C.4.3 Mutual Impedances

The resulting expressions of the mutual impedance for various orientations of the basis and test function are obtained by placing the various results of the integrals into the expression for $Z_{n'n}$. Substituting the correct solutions for the integrals into (C.16), this becomes:

- Cartesian basis and test function

$$
Z_{n'n,zz} = -\frac{1}{d_x d_y} \sum_{m_x=-\infty}^\infty \sum_{m_y=-\infty}^\infty B_{nxy}(k_{xm},k_{ym})T_{n'xy}(-k_{xm},-k_{ym})
$$

$$
e^{jk_{xm}(x_n-x_{n'})}e^{jk_{ym}(y_n-y_{n'})}
$$

$$
\cdot\frac{1}{2\pi}\int\limits_{-\infty}^\infty \bar{\bar{\boldsymbol{G}}}(k_{xm},k_{ym},k_z)\hat{b}\hat{t}B_{nz}(k_z)T_{n'z}(-k_z)e^{jk_z(z_n-z_{n'})}dk_z \quad \text{(C.54)}
$$

- Cylindrical basis function along $\hat{\rho}$ and cylindrical test function along $\hat{\rho}$

$$
Z_{n'n,\rho\rho} = -\frac{(2\pi)^2}{d_x d_y} \sum_{m_x=-\infty}^\infty \sum_{m_y=-\infty}^\infty jB_{n\rho,J_1}(k_{\rho m})jT_{n'\rho,J_1}(-k_{\rho m})
$$

$$
e^{jk_{xm}(x_n-x_{n'})}e^{jk_{ym}(y_n-y_{n'})}
$$

$$
\cdot\frac{1}{2\pi}\int\limits_{-\infty}^\infty \bar{\bar{\boldsymbol{G}}}(k_{xm},k_{ym},k_z)[\hat{x}\cos\alpha_m+\hat{y}\sin\alpha_m]^2 B_{nz}(k_z)T_{n'z}(-k_z)e^{jk_z(z_n-z_{n'})}dk_z
$$

$$
\text{(C.55)}
$$

- Cylindrical basis function along $\hat{\rho}$ and cylindrical test function along $\hat{z}$

$$Z_{n'n,\rho z} = -\frac{(2\pi)^2}{d_x d_y} \sum_{m_x=-\infty}^{\infty} \sum_{m_y=-\infty}^{\infty} jB_{n\rho,J_1}(k_{\rho m})T_{n'\rho,J_0}(-k_{\rho m})$$

$$e^{jk_{xm}(x_n-x_{n'})}e^{jk_{ym}(y_n-y_{n'})}$$

$$\cdot \frac{1}{2\pi} \int_{-\infty}^{\infty} \bar{\bar{G}}(k_{xm},k_{ym},k_z)[\hat{x}\cos\alpha_m + \hat{y}\sin\alpha_m]\hat{z}B_{nz}(k_z)T_{n'z}(-k_z)e^{jk_z(z_n-z_{n'})}dk_z \tag{C.56}$$

- Cylindrical basis function along $\hat{z}$ and cylindrical test function along $\hat{\rho}$

$$Z_{n'n,z\rho} = -\frac{(2\pi)^2}{d_x d_y} \sum_{m_x=-\infty}^{\infty} \sum_{m_y=-\infty}^{\infty} B_{n\rho,J_0}(k_{\rho m})jT_{n'\rho,J_1}(-k_{\rho m})$$

$$e^{jk_{xm}(x_n-x_{n'})}e^{jk_{ym}(y_n-y_{n'})}$$

$$\cdot \frac{1}{2\pi} \int_{-\infty}^{\infty} \bar{\bar{G}}(k_{xm},k_{ym},k_z)\hat{z}[\hat{x}\cos\alpha_m + \hat{y}\sin\alpha_m]B_{nz}(k_z)T_{n'z}(-k_z)e^{jk_z(z_n-z_{n'})}dk_z \tag{C.57}$$

- Cylindrical basis function along $\hat{z}$ and cylindrical test function along $\hat{z}$

$$Z_{n'n,zz} = -\frac{(2\pi)^2}{d_x d_y} \sum_{m_x=-\infty}^{\infty} \sum_{m_y=-\infty}^{\infty} B_{n\rho,J_0}(k_{\rho m})T_{n'\rho,J_0}(-k_{\rho m})$$

$$e^{jk_{xm}(x_n-x_{n'})}e^{jk_{ym}(y_n-y_{n'})}$$

$$\cdot \frac{1}{2\pi} \int_{-\infty}^{\infty} \bar{\bar{G}}(k_{xm},k_{ym},k_z)\hat{z}\hat{z}B_{nz}(k_z)T_{n'z}(-k_z)e^{jk_z(z_n-z_{n'})}dk_z \tag{C.58}$$

For all these cases, $\alpha_m = atan2(k_{ym}/k_{xm})$, $k_{\rho m} = \sqrt{k_{xm}^2 + k_{ym}^2}$ and the Hankel transforms $F_{\rho,J_0}(k_\rho)$ and $F_{\rho,J_1}(k_\rho)$ are given by (C.38) and (C.32), respectively. When the structure is in free space, the integral in k_z can be closed for many basis functions, and the relevant case for this thesis is described in Section C.9.

C.5 Projection of the Right Hand Side onto a Test Function

The right-hand side consists of the incident electric field.

$$e_{\text{inc}}(r).$$

This can be represented by a plane-wave incidence, or by a certain set of excited basis functions.

C.5.1 Plane-wave Incidence

Suppose the incident field $\boldsymbol{e}_{\text{inc}}(\boldsymbol{r})$ is a generic plane wave, which can be expressed as the superposition of transverse magnetic (TM) and transverse electric (TE) components

$$\boldsymbol{e}_{\text{inc}}(\boldsymbol{r}) = \boldsymbol{e}_{\text{inc,TM}}(\boldsymbol{r}) + \boldsymbol{e}_{\text{inc,TE}}(\boldsymbol{r}) = (V_{\text{TM}}\hat{\theta} + V_{\text{TE}}\hat{\phi})e^{-jk_{x0}x}e^{-jk_{y0}y}e^{+jk_{z0}z} \quad \text{(C.59)}$$

where the sign of k_{z0} represents the plane wave traveling in the $-z$-direction. The propagation constants along x, y and z can be defined as $k_{x0} = k\sin\theta\cos\phi$, $k_{y0} = k\sin\theta\sin\phi$ and $k_{z0} = k\cos\theta$, where k is the wave number in the homogeneous medium hosting the wires, and θ and ϕ are the elevation and azimuth of the incident plane wave, respectively. When projecting the incident field on the Cartesian coordinate system, we find

$$e_{\text{inc},x} = (V_{\text{TM}}\cos\theta\cos\phi - V_{\text{TE}}\sin\phi)e^{-jk_{x0}x}e^{-jk_{y0}y}e^{+jk_{z0}z}$$
$$e_{\text{inc},y} = (V_{\text{TM}}\cos\theta\sin\phi + V_{\text{TE}}\cos\phi)e^{-jk_{x0}x}e^{-jk_{y0}y}e^{+jk_{z0}z} \quad \text{(C.60)}$$
$$e_{\text{inc},z} = -V_{\text{TM}}\sin\theta e^{-jk_{x0}x}e^{-jk_{y0}y}e^{+jk_{z0}z}\,.$$

To solve the EFIE, the right-hand side should also be projected onto the test function.

$$\langle \boldsymbol{e}_{\text{inc}}(\boldsymbol{r}), \boldsymbol{t}_{n'}(\boldsymbol{r} - \boldsymbol{r}_{n'})\rangle \quad \text{(C.61)}$$

Writing this in integral form yields

$$\iiint\limits_{-\infty}^{\infty} (V_{\text{TM}}\hat{\theta} + V_{\text{TE}}\hat{\phi})e^{-jk_{x0}x}e^{-jk_{y0}y}e^{+jk_{z0}z}\boldsymbol{t}_{n'}(\boldsymbol{r} - \boldsymbol{r}_{n'})d\boldsymbol{r}\,. \quad \text{(C.62)}$$

Let

$$-x = -(x - x_{n'}) - x_{n'}$$
$$-y = -(y - y_{n'}) - y_{n'} \quad \text{(C.63)}$$
$$+z = +(z - z_{n'}) + z_{n'}\,,$$

to find

$$\iiint\limits_{-\infty}^{\infty} (V_{\text{TM}}\hat{\theta} + V_{\text{TE}}\hat{\phi})e^{-jk_{x0}(x-x_{n'})}e^{-jk_{y0}(y-y_{n'})}e^{+jk_{z0}(z-z_{n'})}$$

$$e^{-jk_{x0}x_{n'}}e^{-jk_{y0}y_{n'}}e^{+jk_{z0}z_{n'}}\boldsymbol{t}_{n'}(\boldsymbol{r} - \boldsymbol{r}_{n'})d\boldsymbol{r}\,. \quad \text{(C.64)}$$

Rearranging to isolate the integrals in x, y, z

$$(V_{\text{TM}}\hat{\theta} + V_{\text{TE}}\hat{\phi})e^{-jk_{x0}x_{n'}}e^{-jk_{y0}y_{n'}}e^{+jk_{z0}z_{n'}}$$

$$\cdot \left[\iiint\limits_{-\infty}^{\infty} \boldsymbol{t}_{n'}(\boldsymbol{r} - \boldsymbol{r}_{n'})e^{-jk_{x0}(x-x_{n'})}e^{-jk_{y0}(y-y_{n'})}e^{+jk_{z0}(z-z_{n'})}d\boldsymbol{r}\right]\,. \quad \text{(C.65)}$$

Focusing on the integral in x, y, z

$$\iiint\limits_{-\infty}^{\infty} \boldsymbol{t}_{n'}(\boldsymbol{r} - \boldsymbol{r}_{n'})e^{-jk_{x0}(x-x_{n'})}e^{-jk_{y0}(y-y_{n'})}e^{+jk_{z0}(z-z_{n'})}d\boldsymbol{r} \,. \tag{C.66}$$

If the test function is in Cartesian coordinates, this integral is simply a Fourier transform, and we find

$$v_{n'} = (V_{\text{TM}}\hat{\theta} + V_{\text{TE}}\hat{\phi})\boldsymbol{T}_{n'}(-k_{x0}, -k_{y0}, +k_{z0})e^{-jk_{x0}x_{n'}}e^{-jk_{y0}y_{n'}}e^{+jk_{z0}z_{n'}} \,, \tag{C.67}$$

which, when projected on the Cartesian coordinate system, becomes

$$v_{n'} = [(V_{\text{TM}}\cos\theta\cos\phi - V_{\text{TE}}\sin\phi)\hat{x} + (V_{\text{TM}}\cos\theta\sin\phi + V_{\text{TE}}\cos\phi)\hat{y}$$
$$+ (-V_{\text{TM}}\sin\theta)\hat{z}] \cdot \boldsymbol{T}_{n'}(-k_{x0}, -k_{y0}, +k_{z0})e^{-jk_{x0}x_{n'}}e^{-jk_{y0}y_{n'}}e^{+jk_{z0}z_{n'}} \,. \tag{C.68}$$

If the basis function is in cylindrical coordinates, this integral is practically the same as it was in (C.40) so, for a test function along $\hat{\rho}$

$$v_{n'} = (V_{\text{TM}}\hat{\theta} + V_{\text{TE}}\hat{\phi})2\pi j T_{n'\rho, J_1}(-k_{\rho0})T_{n'z}(+k_{z0})$$
$$\cdot (\hat{x}\cos\alpha_0 + \hat{y}\sin\alpha_0)\, e^{-jk_{x0}x_{n'}}e^{+jk_{y0}y_{n'}}e^{+jk_{z0}z_{n'}} \,, \tag{C.69}$$

where $k_{\rho0} = \sqrt{k_{x0}^2 + k_{y0}^2}$ and $\alpha_0 = \text{atan2}\,(k_{y0}, k_{x0})$. For a test function along $\hat{z}$

$$v_{n'} = (V_{\text{TM}}\hat{\theta} + V_{\text{TE}}\hat{\phi})2\pi T_{n'\rho, J_0}(-k_{\rho0})T_{n'z}(+k_{z0})\hat{z}e^{-jk_{x0}x_{n'}}e^{-jk_{y0}y_{n'}}e^{+jk_{z0}z_{n'}} \,. \tag{C.70}$$

When projecting the field onto the cylindrical coordinate system, we find, for a test function along $\hat{\rho}$

$$v_{n'} = [(V_{\text{TM}}\cos\theta\cos\phi - V_{\text{TE}}\sin\phi)\cos\alpha_0 + (V_{\text{TM}}\cos\theta\sin\phi + V_{\text{TE}}\cos\phi)\sin\alpha_0]$$
$$2\pi j T_{n'\rho, J_1}(-k_{\rho0})T_{n'z}(-k_{z0})e^{-jk_{x0}x_{n'}}e^{+jk_{y0}y_{n'}}e^{+jk_{z0}z_{n'}} \,, \tag{C.71}$$

and, for a test function along $\hat{z}$,

$$v_{n'} = -V_{\text{TM}}\sin\theta 2\pi T_{n'\rho, J_0}(-k_{\rho0})T_{n'z}(+k_{z0})e^{-jk_{x0}x_{n'}}e^{-jk_{y0}y_{n'}}e^{+jk_{z0}z_{n'}} \,. \tag{C.72}$$

Under plane-wave impedance, the load impedance of each basis function is $z_l = 0$, so the load impedance matrix Z_l is zero and can be omitted from the matrix equation.

C.5.2 Delta-gap Excitation

Assuming the delta-gap excitation with length δ and width w is defined in the $\{u, v\} \in \{x, y, z\}_{\neq}$ plane

$$V_\delta(u, v) = \text{rect}(u, \delta)\,\text{rect}(v, w) \,. \tag{C.73}$$

The excitation voltage is given by the fraction of the delta-gap that is covered by a basis function

$$v_{n'} = \sqrt{2z_l} \frac{a_{n'}}{\sum_n a_n} \, , \qquad (C.74)$$

where $a_{n'}$ is area of the basis function that overlaps the delta-gap, given by

$$a_{n'} = \iint\limits_{-\infty}^{\infty} b_{n'u}(u - u_{n'}) b_{n'v}(v - v_{n'}) \operatorname{rect}(u, \delta) \operatorname{rect}(v, w) du dv \, . \qquad (C.75)$$

And the load is given by

$$z_{l,n'} = z_l \frac{a_n'}{\sum_n a_n} \, . \qquad (C.76)$$

With a resulting load impedance matrix

$$\boldsymbol{Z}_l = \operatorname{diag}(\boldsymbol{z}_l) \, . \qquad (C.77)$$

C.6 Matrix Equation

To find the currents from the mutual impedance matrix, we simply use

$$\boldsymbol{I} = (\boldsymbol{Z} + \boldsymbol{Z}_l)^{-1} \boldsymbol{v} \, , \qquad (C.78)$$

where $\boldsymbol{Z}$ is the mutual impedance matrix for which the elements are given by the expression in Section C.4.3, $\boldsymbol{Z}_l$ is the diagonal load impedance matrix, and $\boldsymbol{v}$ is the excitation voltage for each basis function.

C.7 Scattered Field

The EFIE is built through the assumption that $-\boldsymbol{e}_s(\boldsymbol{r}) = \boldsymbol{e}_{\mathrm{inc}}(\boldsymbol{r})$. As such, the radiating scattered field is given by $-$ the fundamental mode in the LHS, so

$$\boldsymbol{e}_s(x, y, z) = \frac{1}{2\pi} \frac{1}{d_x d_y} \sum_{n=1}^{N} I_n \int\limits_{-\infty}^{\infty} \bar{\bar{\boldsymbol{G}}}(k_{x0}, k_{y0}, k_z) \left[\cdots \right]$$
$$e^{-jk_{x0}(x-x_n)} e^{-jk_{y0}(y-y_n)} e^{-jk_z(z-z_n)} dk_z \, , \qquad (C.79)$$

where the term in brackets is the integral

$$\iiint\limits_{-\infty}^{\infty} \boldsymbol{b}_n(x' - x_n - n_x d_x, y' - yi - n_y d_y, z' - z_n)$$
$$\cdot e^{jk_{xm}(x'-x_n-n_x d_x)} e^{jk_{ym}(y'-y_n-n_y d_y)} e^{jk_z(z'-z_n)} dx' dy' dz' \, , \qquad (C.80)$$

which is solved in Section C.4.1. For a Cartesian basis function, assuming the basis function is separable, we find

$$\boldsymbol{e}_s(x, y, z) = \frac{1}{d_x d_y} \sum_{n=1}^{N} I_n B_{nxy}(k_{x0}, k_{y0}) e^{-jk_{x0}(x-x_n)} e^{-jk_{y0}(y-y_n)}$$

$$\cdot \frac{1}{2\pi} \int_{-\infty}^{\infty} \bar{\bar{\boldsymbol{G}}}(k_{x0}, k_{y0}, k_z) \hat{b} B_{nz}(k_z) e^{-jk_z(z-z_n)} dk_z. \quad \text{(C.81)}$$

For a cylindrical basis function, assuming the basis function is separable and constant in ϕ, it follows that, for $\hat{b} = \hat{\rho}$

$$\boldsymbol{e}_s(x, y, z) = \frac{2\pi}{d_x d_y} \sum_{n=1}^{N} I_n B_{n\rho, J_1}(k_{\rho 0}) e^{-jk_{x0}(x-x_n)} e^{-jk_{y0}(y-y_n)}$$

$$\cdot \frac{1}{2\pi} \int_{-\infty}^{\infty} \bar{\bar{\boldsymbol{G}}}(k_{x0}, k_{y0}, k_z) B_{nz}(k_z) \left(\hat{x} \cos \alpha_0 + \hat{y} \sin \alpha_0 \right) e^{-jk_z(z-z_n)} dk_z, \quad \text{(C.82)}$$

and, for $\hat{b} = \hat{z}$

$$\boldsymbol{e}_s(x, y, z) = \frac{2\pi}{d_x d_y} \sum_{n=1}^{N} I_n B_{n\rho, J_0}(k_{\rho m}) e^{-jk_{x0}(x-x_n)} e^{-jk_{y0}(y-y_n)}$$

$$\cdot \frac{1}{2\pi} \int_{-\infty}^{\infty} \bar{\bar{\boldsymbol{G}}}(k_{x0}, k_{y0}, k_z) B_{nz}(k_z) \hat{z} e^{-jk_z(z-z_n)} dk_z. \quad \text{(C.83)}$$

The integrals in k_z can all be closed using the expressions derived in Section C.9.

C.8 Reflection Coefficient

The reflection coefficients can be found using by projecting the incident and scattered fields onto cylindrical coordinates, and taking the ratio

$$\Gamma_{\text{TM}} = \frac{e_{s,\rho}}{e_{i,\rho}} \quad \text{(C.84)}$$

$$\Gamma_{\text{TE}} = \frac{e_{s,\alpha}}{e_{i,\alpha}}, \quad \text{(C.85)}$$

where

$$e_\rho = \quad \cos \phi e_x + \sin \phi e_y \quad \text{(C.86)}$$

$$e_\alpha = -\sin \phi e_x + \cos \phi e_y. \quad \text{(C.87)}$$

C.9 Closing the Integral in k_z

With a proper choice of basis functions, the only integral that remains for the mutual impedances is the integral in k_z. Assuming the basis and test functions are in free space, the integral in k_z can be closed using a residue calculation. Whether or not this is possible depends on the basis function in z, but it is possible for rectangular, triangular, and for infinitesimally thin basis functions. In this work, only the rectangular and infinitesimal basis functions are used, so only those cases are considered below.

All integrals in k_z in the expressions for the mutual impedance are of the form

$$\frac{1}{2\pi}\int_{-\infty}^{\infty} \bar{\bar{G}}(k_{xm}, k_{ym}, k_z)\hat{b}\hat{t}B_{nz}(k_z)T_{n'z}(-k_z)e^{jk_z(z_n - z_{n'})}dk_z \,. \tag{C.88}$$

Assuming the structure is in free space, we can use the free-space Green's function

$$\bar{\bar{G}}_{fs}(k_x, k_y, k_z) = j\frac{\zeta}{k_0}\begin{bmatrix} k_0^2 - k_x^2 & -k_x k_y & -k_x k_z \\ -k_y k_x & k_0^2 - k_y^2 & -k_y k_z \\ -k_z k_x & -k_z k_y & k_0^2 - k_z^2 \end{bmatrix}\frac{1}{k_0^2 - k_x^2 - k_y^2 - k_z^2} \,. \tag{C.89}$$

For convenience of notation, define

$$C_{bt}(k_z) = \left(k_0^2 - k_x^2 - k_y^2 - k_z^2\right)\bar{\bar{G}}_{fs}(k_x, k_y, k_z)\cdot\hat{b}\hat{t} \,. \tag{C.90}$$

The integral becomes

$$\frac{1}{2\pi}\int_{-\infty}^{\infty} \frac{C_{bt}(k_z)}{k_0^2 - k_x^2 - k_y^2 - k_z^2}B_{nz}(k_z)T_{n'z}(-k_z)e^{jk_z(z_n - z_{n'})}dk_z \,. \tag{C.91}$$

This integral is closed for various combinations of basis and test functions below.

C.9.1 Mutual and Self Impedance Between Infinitesimal and Infinitesimal

Suppose we have an basis function and test function that are infinitesimally thin in z, which are given by

$$\boldsymbol{b}_{nz}(z) = \delta(z)\hat{b} \tag{C.92}$$

$$\boldsymbol{t}_{n'z}(z) = \delta(z)\hat{t} \,, \tag{C.93}$$

with Fourier transforms

$$\boldsymbol{B}_{nz}(k_z) = 1\hat{b} \tag{C.94}$$

$$\boldsymbol{T}_{n'z}(k_z) = 1\hat{t} \,. \tag{C.95}$$

The integral in (C.91) becomes

$$\frac{1}{2\pi} \int\limits_{-\infty}^{\infty} \frac{C_{bt}(k_z)}{k_0^2 - k_x^2 - k_y^2 - k_z^2}(-k_z)e^{jk_z(z_n - z_{n'})}dk_z \,. \tag{C.96}$$

This integrand has poles in $k_z = \pm\sqrt{k_0^2 - k_x^2 - k_y^2} := \pm k_{zp}$ due to the Green's function. To take the residue at this pole, the integrand must go to zero for $k_z \to -j\infty$ or $k_z \to +j\infty$. We consider three scenarios:

a) The basis function is above the test function;

b) The basis function is below the test function;

c) The basis function is at the same height as the test function.

Scenario a

Assuming the basis function is above the test function

$$(z_n - z_{n'}) > 0 \tag{C.97}$$

We must take the residue on the half-space where $\mathrm{re}\,(jk_z\,(z_n - z_{n'})) < 0$. Since we assume $(z_n - z_{n'}) > 0$, we need $\mathrm{re}\,(jk_z) < 0 \Rightarrow \mathrm{im}\,(k_z) > 0$, so we must take the upper half-space. The integral then becomes a counter-clockwise contour around $k_z = -k_{zp}$

$$\begin{aligned}
\frac{1}{2\pi} \oint_{-k_{zp}} \frac{C_{bt}(k_z)}{k_0^2 - k_x^2 - k_y^2 - k_z^2}e^{jk_z(z_n - z_{n'})}dk_z &= \frac{1}{2\pi}(+j2\pi)C_{bt}(k_z)\frac{e^{jk_z(z_n - z_{n'})}}{\frac{\partial}{\partial k_z}k_{zp}^2 - k_z^2}\bigg|_{k_z = -k_{zp}} \\
&= jC_{bt}(k_z)\frac{e^{jk_z(z_n - z_{n'})}}{-2k_z}\bigg|_{k_z = -k_{zp}} \\
&= jC_{bt}(-k_{zp})\frac{e^{-jk_{zp}(z_n - z_{n'})}}{2k_{zp}} \\
&= jC_{bt}(-k_{zp})\frac{e^{-jk_{zp}|z_n - z_{n'}|}}{2k_{zp}} \,,
\end{aligned} \tag{C.98}$$

where the last step is valid because we assumed $(z_n - z_{n'}) > 0$

Scenario b

Assuming the basis function is below the test function

$$(z_n - z_{n'}) < 0 \,. \tag{C.99}$$

We must take the residue on the half-space where $\text{re}(jk_z(z_n - z_{n'})) < 0$. Since we assume $(z_n - z_{n'}) < 0$, we need $\text{re}(-jk_z) < 0 \Rightarrow \text{im}(k_z) < 0$, so we must take the upper half-space. The integral lower becomes a clockwise contour around $k_z = +k_{zp}$

$$
\frac{1}{2\pi} \oint_{+k_{xp}} \frac{C_{bt}(k_z)}{k_0^2 - k_x^2 - k_y^2 - k_z^2} e^{jk_z(z_n-z_{n'})} dk_z = \frac{1}{2\pi}(-j2\pi)C_{bt}(k_z)\frac{e^{jk_z(z_n-z_{n'})}}{\frac{\partial}{\partial k_z}k_{zp}^2 - k_z^2}\Bigg|_{k_z=+k_{zp}}
$$

$$
= -jC_{bt}(k_z)\frac{e^{jk_z(z_n-z_{n'})}}{-2k_z}\Bigg|_{k_z=+k_{zp}}
$$

$$
= jC_{bt}(+k_{zp})\frac{e^{jk_{zp}(z_n-z_{n'})}}{2k_{zp}}
$$

$$
= jC_{bt}(+k_{zp})\frac{e^{-jk_{zp}|z_n-z_{n'}|}}{2k_{zp}} \, ,
$$

(C.100)

where the last step is valid because we assumed $(z_n - z_{n'}) < 0$

Scenario c

Assuming the basis function is at the same height as the test function

$$
(z_n - z_{n'}) = 0
$$

(C.101)

In this case, the exponent is 0, so the exponential is 1, and the integral converges both up and down

$$
\frac{1}{2\pi} \oint_{+k_{xp}} \frac{C_{bt}(k_z)}{k_0^2 - k_x^2 - k_y^2 - k_z^2} e^{jk_z(z_n-z_{n'})} dk_z = \frac{1}{2\pi}(-j2\pi)C_{bt}(k_z)\frac{1}{\frac{\partial}{\partial k_z}k_{zp}^2 - k_z^2}\Bigg|_{k_z=+k_{zp}}
$$

$$
= -jC_{bt}(k_z)\frac{1}{-2k_z}\Bigg|_{k_z=+k_{zp}}
$$

$$
= jC_{bt}(+k_{zp})\frac{1}{2k_{zp}}
$$

$$
= jC_{bt}(+k_{zp})\frac{e^{-jk_{zp}|z_n-z_{n'}|}}{2k_{zp}} \, ,
$$

(C.102)

where the last step is valid because we assumed $(z_n - z_{n'}) = 0$.

Combined situations

Combining the three situations yields, when both basis and test functions are infinitesimal in z

$$\frac{1}{2\pi} \int\limits_{-\infty}^{\infty} \frac{C_{bt}(k_z)}{k_0^2 - k_x^2 - k_y^2 - k_z^2} e^{jk_z(z_n - z_{n'})} dk_z$$

$$= jC_{bt}(-\operatorname{sign}(z_n - z_{n'})k_{zp}) \frac{e^{-jk_{zp}|zj - z_{n'}|}}{2k_{zp}} . \quad \text{(C.103)}$$

C

C.9.2 Mutual Impedance Between Rectangular and Infinitesimal

Suppose we have a basis function that is rectangular in z and a test function that is infinitesimal in z, we have

$$\boldsymbol{b}_{nz}(z) = \operatorname{rect}(l_{nz}, z)\hat{b} \quad \text{(C.104)}$$

$$\boldsymbol{t}_{n'z}(z) = \delta(z)\hat{t}, \quad \text{(C.105)}$$

with Fourier transforms

$$\boldsymbol{B}_{nz}(k_z) = l_{nz} \operatorname{sinc}(k_z l_{nz}/2)\,\hat{b} \quad \text{(C.106)}$$

$$\boldsymbol{T}_{n'z}(k_z) = 1\hat{t}. \quad \text{(C.107)}$$

The integral becomes

$$\frac{1}{2\pi} \int\limits_{-\infty}^{\infty} \frac{C_{bt}(k_z)}{k_0^2 - k_x^2 - k_y^2 - k_z^2} l_{nz} \operatorname{sinc}\left(k_z \frac{l_{nz}}{2}\right) e^{jk_z(z_n - z_{n'})} dk_z . \quad \text{(C.108)}$$

This integrand has poles in $k_z = \pm\sqrt{k_0^2 - k_x^2 - k_y^2} := \pm k_{zp}$ due to the Green's function, and a pole in 0 due to the basis function. To ensure convergence, we check the limit of this integrand for k_z going to infinity in the complex plane

$$\lim_{k_z \to -\infty} \frac{C_{bt}(k_z)}{k_0^2 - k_x^2 - k_y^2 - k_z^2} l_{nz} \operatorname{sinc}\left(k_z \frac{l_{nz}}{2}\right) e^{jk_z(z_n - z_{n'})} = 0$$

$$\lim_{k_z \to +\infty} \cdots = 0$$

$$\lim_{k_z \to -j\infty} \cdots = \begin{cases} 0 & \text{when } (z_n - z_{n'}) \leq -l_{nz}/2 \\ \infty & \text{when } (z_n - z_{n'}) > -l_{nz}/2 \end{cases} \quad \text{(C.109)}$$

$$\lim_{k_z \to +j\infty} \cdots = \begin{cases} \infty & \text{when } (z_n - z_{n'}) < l_{nz}/2 \\ 0 & \text{when } (z_n - z_{n'}) \geq l_{nz}/2 \end{cases} .$$

We consider two scenarios:

a) The test function intersects the basis function;

b) The basis function is entirely above or below the test function.

Scenario a

This scenario is not used in this thesis, so this appendix does not treat it. However, this scenario can be solved by splitting the rectangular basis function into two parts and taking the residue for the two halves.

C

Scenario b

Assuming the vertical basis function is entirely above or below the plane of the horizontal one

$$|z_n - z_{n'}| \geq l_{nz}/2\,. \tag{C.110}$$

In this situation, the limit of $k_z \to \pm j\infty$ goes to zero for either half-space, depending on $(z_n - z_{n'})$. The residue is done in the same way as in the infinitesimal-infinitesimal case, and yields

$$\frac{1}{2\pi} \int\limits_{-\infty}^{\infty} \frac{C_{bt}(k_z)}{k_0^2 - k_x^2 - k_y^2 - k_z^2} B_{nz}(k_z) e^{jk_z(z_n - z_{n'})} dk_z$$

$$= jC_{bt}(-\operatorname{sign}(z_n - z_{n'})k_{zp}) B_{nz}(-\operatorname{sign}(z_n - z_{n'}) \cdot +k_{zp}) \frac{e^{-jk_{zp}|z_n - z_{n'}|}}{2k_{zp}}\,. \tag{C.111}$$

Now consider the reverse - the basis function is infinitesimal and the test function is rectangular. The result is very similar

$$\frac{1}{2\pi} \int\limits_{-\infty}^{\infty} \frac{C_{bt}(k_z)}{k_0^2 - k_x^2 - k_y^2 - k_z^2} T_{n'z}(-k_z) e^{jk_z(z_n - z_{n'})} dk_z$$

$$= jC_{bt}(-\operatorname{sign}(z_n - z_{n'})k_{zp}) T_{n'z}(-\operatorname{sign}(z_n - z_{n'}) \cdot -k_{zp}) \frac{e^{-jk_{zp}|z_n - z_{n'}|}}{2k_{zp}}\,. \tag{C.112}$$

Since the other basis function is infinitesimal, these two scenarios can be combined into a single expression.

$$\frac{1}{2\pi} \int\limits_{-\infty}^{\infty} \frac{C_{bt}(k_z)}{k_0^2 - k_x^2 - k_y^2 - k_z^2} B_{nz}(k_z) T_{n'z}(-k_z) e^{jk_z(z_n - z_{n'})} dk_z$$

$$= jC_{bt}(-\operatorname{sign}(z_n - z_{n'})k_{zp}) B_{nz}(-\operatorname{sign}(z_n - z_{n'})k_{zp})$$

$$\cdot T_{n'z}(-\operatorname{sign}(z_n - z_{n'}) \cdot -k_{zp}) \frac{e^{-jk_{zp}|z_n - z_{n'}|}}{2k_{zp}}\,. \tag{C.113}$$

C.9.3 Mutual Impedance Between Rectangular and Rectangular

Suppose we have a basis function that is rectangular in z and a test function that is also rectangular in z, we have

$$\boldsymbol{b}_{nz}(z) = \text{rect}(l_{nz}, z) \tag{C.114}$$

$$\boldsymbol{t}_{n'z}(z) = \text{rect}(l_{n'z}, z)\,, \tag{C.115}$$

with Fourier transforms

$$\boldsymbol{B}_{nz}(k_z) = l_{nz}\,\text{sinc}\,(k_z l_{nz}/2)\,\hat{b} \tag{C.116}$$

$$\boldsymbol{T}_{n'z}(k_z) = l_{n'z}\,\text{sinc}\,(k_z l_{n'z}/2)\,\hat{t}\,. \tag{C.117}$$

The integral becomes

$$\frac{1}{2\pi}\int\limits_{-\infty}^{\infty}\frac{C_{bt}(k_z)}{k_0^2 - k_x^2 - k_y^2 - k_z^2}l_{nz}\,\text{sinc}\left(k_z\frac{l_{nz}}{2}\right)l_{n'z}\,\text{sinc}\left(k_z\frac{l_{n'z}}{2}\right)e^{jk_z(-z_{n'})}dk_z\,. \tag{C.118}$$

This integrand has poles in $k_z = \pm\sqrt{k_0^2 - k_x^2 - k_y^2} := \pm k_{zp}$ due to the Green's function, and a pole in 0 due to the basis function. To ensure convergence, we check the limit of this integrand for k_z going to infinity in the complex plane.

$$\lim_{k_z \to -\infty}\frac{C_{bt}(k_z)}{k_0^2 - k_x^2 - k_y^2 - k_z^2}B_{nz}(k_z)T_{n'z}(k_z)e^{jk_z(z_n - z_{n'})} \quad = 0 \tag{C.119}$$

$$\lim_{k_z \to +\infty}\cdots \qquad\qquad = 0 \tag{C.120}$$

$$\lim_{k_z \to -j\infty}\cdots \qquad = \begin{cases} 0 & \text{when } (z_n - z_{n'}) \leq -(l_{nz} + l_{n'z})/2 \\ \infty & \text{when } (z_n - z_{n'}) > -(l_{nz} + l_{n'z})/2 \end{cases} \tag{C.121}$$

$$\lim_{k_z \to +j\infty}\cdots \qquad = \begin{cases} \infty & \text{when } (z_n - z_{n'}) < (l_{nz} + l_{n'z})/2 \\ 0 & \text{when } (z_n - z_{n'}) \geq (l_{nz} + l_{n'z})/2 \end{cases}\,. \tag{C.122}$$

We consider two scenarios:

a) The basis function and test function partially overlap;

b) The basis function is entirely above or below the test function.

Scenario a

This scenario is not used in this thesis, so this appendix does not treat it. However, this scenario can be solved by splitting the two rectangular functions into separate overlapping and non-overlapping parts and doing the residues for the four components separately.

Scenario b

Assuming the basis function is entirely above or below the test function, the residue is done in the same way as in the infinitesimal-infinitesimal case, and yields the following expression

$$\frac{1}{2\pi}\int\limits_{-\infty}^{\infty}\frac{C_{bt}(k_z)}{k_0^2-k_x^2-k_y^2-k_z^2}B_{nz}(k_z)T_{n'z}(-k_z)e^{jk_z(z_n-z_{n'})}dk_z$$

$$= jC_{bt}(-\operatorname{sign}(z_n-z_{n'})k_{zp})B_{nz}(-\operatorname{sign}(z_n-z_{n'})k_{zp})$$

$$\cdot T_{n'z}(-\operatorname{sign}(z_n-z_{n'})\cdot -k_{zp})\frac{e^{-jk_{zp}|z_n-z_{n'}|}}{2k_{zp}}\,,\quad \text{(C.123)}$$

C

which is the same as the mutual between the infinitesimal and rectangular basis functions in (C.113).

C.9.4 Self Impedance of Rectangular

Suppose we have a basis function that is rectangular in z and we are calculating the self-impedance. In this situation, we have $(z_n-z_{n'})=0$, so the residue above cannot be used. To close the integral, we split the sinc functions into exponentials and do the residue for the separate components. Using $l_{nz}=l_{n'z}$ and $z_n=z_{n'}$, we can write the integral as follows

$$\frac{1}{2\pi}\int\limits_{-\infty}^{\infty}\frac{C_{bt}(k_z)}{k_0^2-k_x^2-k_y^2-k_z^2}l_{nz}^2\operatorname{sinc}^2\left(k_z\frac{l_{nz}}{2}\right)dk_z$$

$$=\frac{1}{2\pi}\int\limits_{-\infty}^{\infty}\frac{C_{bt}(k_z)}{k_0^2-k_x^2-k_y^2-k_z^2}\frac{2-e^{-jk_zl_{nz}}-e^{jk_zl_{nz}}}{k_z^2}dk_z\,.\quad \text{(C.124)}$$

This expression has poles in $k_z=\pm\sqrt{k_0^2-k_x^2-k_y^2}:=\pm k_{zp}$ and a double pole in $k_z=0$. We consider the three parts in $\left(2-e^{-jk_zl_{nz}}-e^{jk_zl_{nz}}\right)$ separately

Part I

The first part of the integral is

$$\frac{1}{2\pi}\int\limits_{-\infty}^{\infty}\frac{C_{bt}(k_z)}{k_0^2-k_x^2-k_y^2-k_z^2}\frac{2}{k_z^2}dk_z\,.\quad \text{(C.125)}$$

This converges both up and down. We choose down, so we consider the clockwise contour around $+k_{zp}$. The integral can be written as the sum of the contour integrals around the two poles.

$$
\frac{1}{2\pi} \int\limits_{-\infty}^{\infty} \frac{C_{bt}(k_z)}{k_0^2 - k_x^2 - k_y^2 - k_z^2} \frac{2}{k_z^2} dk_z
$$
$$
= \frac{1}{2\pi} \oint\limits_{+k_{zp}} \frac{C_{bt}(k_z)}{k_0^2 - k_x^2 - k_y^2 - k_z^2} \frac{2}{k_z^2} dk_z + \frac{1}{2\pi} \oint\limits_{0} \frac{C_{bt}(k_z)}{k_0^2 - k_x^2 - k_y^2 - k_z^2} \frac{2}{k_z^2} dk_z . \quad \text{(C.126)}
$$

We consider the pole in $+k_{zp}$ and in 0 separately.

Pole in $+k_{zp}$

We first consider the pole in $+k_{zp}$

$$
\frac{1}{2\pi} \oint\limits_{+k_{zp}} \frac{C_{bt}(k_z)}{k_0^2 - k_x^2 - k_y^2 - k_z^2} \frac{2}{k_z^2} dk_z
$$
$$
= \frac{1}{2\pi}(-j2\pi) \lim_{k_z \to +k_{zp}} (k_z - k_{zp}) \frac{C_{bt}(k_z)}{k_{zp}^2 - k_z^2} \frac{2}{k_z^2}
$$
$$
= -j \lim_{k_z \to +k_{zp}} 2(k_z - k_{zp}) \frac{C_{bt}(k_z)}{-(k_z - k_{zp})(k_z + k_{zp})k_z^2}
$$
$$
= -j \lim_{k_z \to +k_{zp}} 2 \frac{C_{bt}(k_z)}{-(k_z + k_{zp})k_z^2}
$$
$$
= -j \frac{C_{bt}(+k_{zp})}{2k_{zp}^3} 2 .
$$
$$\text{(C.127)}$$

Pole in 0

Next, we consider the second order pole in 0.

$$\frac{1}{2\pi}\oint_0 \frac{C_{bt}(k_z)}{k_0^2 - k_x^2 - k_y^2 - k_z^2}\frac{2}{k_z^2}dk_z$$

$$= \frac{1}{2\pi}(-j\pi)\lim_{k_z\to 0}\frac{\partial}{\partial k_z}(k_z - 0)^2\frac{C_{bt}(k_z)}{k_{zp}^2 - k_z^2}\frac{2}{k_z^2}$$

$$= -\frac{j}{2}\lim_{k_z\to 0}\frac{\partial}{\partial k_z}2\frac{C_{bt}(k_z)}{k_{zp}^2 - k_z^2}$$

$$= -\frac{j}{2}\lim_{k_z\to 0}\frac{C_{bt}(k_z)4k_z - 2(k_{zp}^2 - k_z^2)\frac{\partial}{\partial k_z}C_{bt}(k_z)}{(k_{zp}^2 - k_z^2)^2} \quad \text{(C.128)}$$

$$= -\frac{j}{2}\cdot j\frac{\zeta}{k_0}\cdot\frac{1}{k_{zp}^2}\begin{bmatrix} 0 & 0 & -2k_x \\ 0 & 0 & -2k_y \\ -2k_x & -2k_y & 0 \end{bmatrix}\hat{b}\hat{t}.$$

Part II

The second part of the integral is

$$\frac{1}{2\pi}\int_{-\infty}^{\infty}\frac{C_{bt}(k_z)}{k_0^2 - k_x^2 - k_y^2 - k_z^2}\frac{-e^{-jk_z l_{nz}}}{k_z^2}dk_z. \quad \text{(C.129)}$$

This converges down, so we consider the clockwise contour around $+k_{zp}$.

$$\frac{1}{2\pi}\oint_{+k_{zp}}\frac{C_{bt}(k_z)}{k_0^2 - k_x^2 - k_y^2 - k_z^2}\frac{-e^{-jk_z l_{nz}}}{k_z^2}dk_z = -j\frac{C_{bt}(+k_{zp})}{2k_{zp}^3}e^{-jk_{zp}l_{nz}}, \quad \text{(C.130)}$$

and in 0

$$\frac{1}{2\pi}\oint_0 \frac{C_{bt}(k_z)}{k_0^2 - k_x^2 - k_y^2 - k_z^2}\frac{-e^{-jk_z l_{nz}}}{k_z^2}dk_z$$

$$= -\frac{j}{2}\cdot j\frac{\zeta}{k_0}\cdot\frac{1}{k_{zp}^2}\begin{bmatrix} j(k_0^2 - k_x^2)l_{nz} & -jk_x k_y l_{nz} & k_x \\ -jk_x k_y l_{nz} & j(k_0^2 - k_y^2)l_{nz} & k_y \\ k_x & k_y & jk_0^2 l_{nz} \end{bmatrix}\hat{b}\hat{t}. \quad \text{(C.131)}$$

Part III

The third part of the integral is

$$\frac{1}{2\pi} \int\limits_{-\infty}^{\infty} \frac{C_{bt}(k_z)}{k_0^2 - k_x^2 - k_y^2 - k_z^2} \frac{-e^{jk_z l_{nz}}}{k_z^2} dk_z \qquad (C.132)$$

This converges up, so we consider the counter-clockwise contour around $-k_{zp}$

$$\frac{1}{2\pi} \oint\limits_{-k_{zp}} \frac{C_{bt}(k_z)}{k_0^2 - k_x^2 - k_y^2 - k_z^2} \frac{-e^{jk_z l_{nz}}}{k_z^2} dk_z = -j \frac{C_{bt}(-k_{zp})}{2k_{zp}^3} e^{-jk_{zp} l_{nz}}, \qquad (C.133)$$

and in 0

$$\frac{1}{2\pi} \oint\limits_{0} \frac{C_{bt}(k_z)}{k_0^2 - k_x^2 - k_y^2 - k_z^2} \frac{-e^{jk_z l_{nz}}}{k_z^2} dk_z$$

$$= \frac{j}{2} \cdot j \frac{\zeta}{k_0} \cdot \frac{1}{k_{zp}^2} \begin{bmatrix} -j(k_0^2 - k_x^2)l_{nz} & jk_x k_y l_{nz} & k_x \\ jk_x k_y l_{nz} & -j(k_0^2 - k_y^2)l_{nz} & k_y \\ k_x & k_y & -jk_0^2 l_{nz} \end{bmatrix} \hat{b}\hat{t}. \quad (C.134)$$

Parts I-III Combined

The total result of the integral is the sum of the two residue contributions for each of the three parts.

Pole in $\pm k_{zp}$

The sum of the residue contributions for the three parts in the pole in $\pm k_{zp}$ is

$$\frac{1}{2\pi} \oint\limits_{\pm k_{zp}} \frac{C_{bt}(k_z)}{k_0^2 - k_x^2 - k_y^2 - k_z^2} l_{nz}^2 \operatorname{sinc}^2\left(k_z \frac{l_{nz}}{2}\right) dk_z$$

$$= \frac{j}{2k_{zp}^3} (C_{bt}(+k_{zp})(2 - e^{-jk_{zp} l_{nz}}) - C_{bt}(-k_{zp})e^{-jk_{zp} l_{nz}}). \qquad (C.135)$$
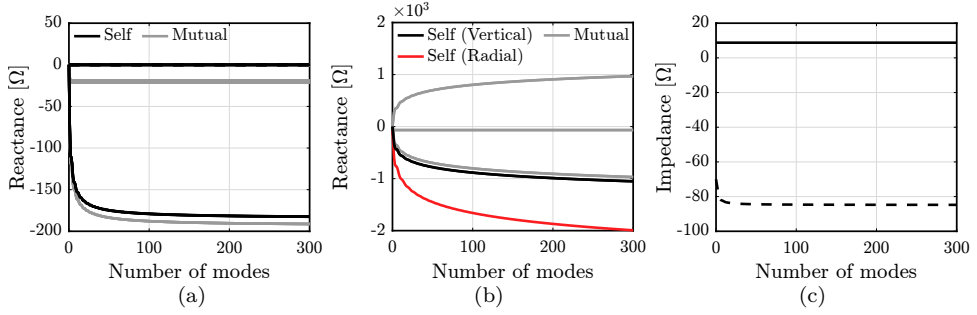
Figure C.1: Mutual and self reactances of (a) the Cartesian basis functions employed in the MoM and (b) the radial basis functions. (c) Self impedance of the combined cylindrical basis function.

Pole in 0

The sum of the residue contributions for the three parts in the pole in 0 is

$$\frac{1}{2\pi} \oint_0 \frac{C_{bt}(k_z)}{k_0^2 - k_x^2 - k_y^2 - k_z^2} l_{nz}^2 \operatorname{sinc}^2\left(k_z \frac{l_{nz}}{2}\right) dk_z$$

$$= j\frac{\zeta}{k_0} \cdot \frac{1}{k_{zp}^2} \begin{bmatrix} (k_0^2 - k_x^2)l_{nz} & -k_x k_y l_{nz} & jk_x \\ -k_x k_y l_{nz} & (k_0^2 - k_y^2)l_{nz} & jk_y \\ jk_x & jk_y & k_0^2 l_{nz} \end{bmatrix} \hat{b}\hat{t}. \qquad \text{(C.136)}$$

Total Expression for Self of Rectangular

The final expression for the self of a rectangular basis function is

$$\frac{1}{2\pi} \int_{-\infty}^{\infty} \frac{C_{bt}(k_z)}{k_0^2 - k_x^2 - k_y^2 - k_z^2} l_{nz}^2 \operatorname{sinc}^2\left(k_z \frac{l_{nz}}{2}\right) dk_z$$

$$= \frac{j}{2k_{zp}^3}(C_{bt}(+k_{zp})(2 - e^{-jk_{zp}l_{nz}}) - C_{bt}(-k_{zp})e^{-jk_{zp}l_{nz}})$$

$$+ j\frac{\zeta}{k_0} \cdot \frac{1}{k_{zp}^2} \begin{bmatrix} (k_0^2 - k_x^2)l_{nz} & -k_x k_y l_{nz} & jk_x \\ -k_x k_y l_{nz} & (k_0^2 - k_y^2)l_{nz} & jk_y \\ jk_x & jk_y & k_0^2 l_{nz} \end{bmatrix} \hat{b}\hat{t}. \qquad \text{(C.137)}$$

C.10 Convergence of Floquet Sums

The Floquet sums in Section C.4.3 have their limits at infinity. To ensure an accurate result is obtained for a finite number of terms, the mutual impedances are

calculated for various sum limits. Since the higher order modes only influence the mutual reactance, the mutual resistance is omitted. The self and mutual reactances of the Cartesian basis functions are shown in Fig. C.1(a), where it is seen that they converge after summing 100 modes. The self and mutual reactances of the cylindrical basis functions are shown in Fig. C.1(b), which do not converge.

As described in Section 4.4.3, the three cylindrical basis functions are summed with equal amplitude to ensure continuity of the current. The resulting reduced matrix is then used to calculate the currents. As such, only the convergence of this reduced matrix is relevant, and the self impedance of the combined basis function is evaluated. Fig. C.1(c) shows that this self impedance already converges for a low number of modes considered.

Appendix D

Basis Functions

This appendix lists various basis functions used in this thesis.

D.1 Cartesian Basis Functions

These basis functions are used in the Cartesian method of moments and are assumed to be a function of x, y, or z. The given Fourier transforms use the following definition:

$$B(k_x) = \int\limits_{-\infty}^{\infty} b(x)e^{jk_x x}dx \tag{D.1}$$

D.1.1 Rectangular

The rectangular basis function is shown in Fig. D.1(a). It can be written as

$$b(x) = \text{rect}\left(\frac{x}{l}\right) = \begin{cases} 1 & \text{if } |x| < l/2, \\ \frac{1}{2} & \text{if } |x| = l/2, \\ 0 & \text{otherwise,} \end{cases} \tag{D.2}$$

where l is the length of the basis function. The Fourier transform of (D.2) is given by

$$B(k_x) = l\,\text{sinc}\left(k_x\frac{l}{2}\right). \tag{D.3}$$
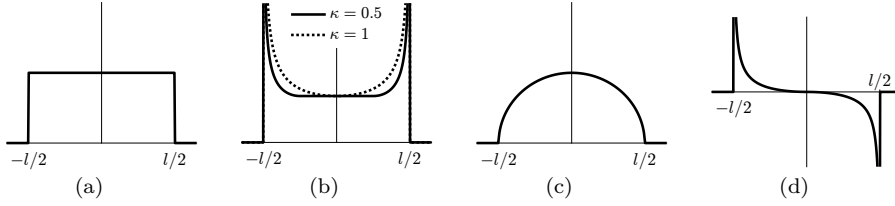
Figure D.1: Cartesian basis functions described in this appendix. (a) Rectangular, (b) adjustable edge singular, (c) inverse edge singular, (d) odd edge singular.

D.1.2 Adjustable Edge Singular

The adjustable edge singular basis function [104] is shown for two values of κ in Fig. D.1(b). It can be written as

$$b(x) = \frac{\text{rect}\left(\frac{2x+l}{l\kappa} - \frac{1}{2}\right)}{\sqrt{1 - \left(\frac{l+2x}{\kappa l} - 1\right)^2}} + \frac{\text{rect}\left(\frac{2x-l}{l\kappa} + \frac{1}{2}\right)}{\sqrt{1 - \left(\frac{l-2x}{\kappa l} - 1\right)^2}} + \text{rect}\left(\frac{x}{l(1-\kappa)}\right)\text{sign}(1-\kappa) \quad \text{(D.4)}$$

where l is the length of the basis function and

$$\text{sign}(x) = \begin{cases} -1 & \text{if } x < 0, \\ 0 & \text{if } x = 0, \\ 1 & \text{if } x > 0. \end{cases} \quad \text{(D.5)}$$

κ is the fraction of the function that is edge singular. The expression is valid for $0 \leq \kappa \leq 2$, where $\kappa = 0$ yields the rectangular function

$$\lim_{\kappa \to 0} b(x) = \text{rect}\left(\frac{x}{l}\right), \quad \text{(D.6)}$$

and $\kappa = 1$ yields the edge singular function

$$\lim_{\kappa \to 1} b(x) = \frac{1}{\sqrt{1 - \left(\frac{2x}{l}\right)^2}}. \quad \text{(D.7)}$$

When $\kappa = 2$, each of the half edge singulars occupy the entire length l, causing them to overlap. The Fourier transform of (D.4) is given by

$$B(k_x) = l\kappa\frac{\pi}{2}\left(J_0\left(k_x\frac{l}{2}\kappa\right)\cos\left(k_x\frac{l}{2}(1-\kappa)\right) - \mathbf{H}_0\left(k_x\frac{l}{2}\kappa\right)\sin\left(k_x\frac{l}{2}(1-\kappa)\right)\right)$$
$$+ l(1-\kappa)\text{sinc}\left(k_x\frac{l}{2}(1-\kappa)\right), \quad \text{(D.8)}$$

where J_ν is the ν-th order Bessel function of the first kind and $\mathbf{H}_\alpha$ is the α-th order Struve function of the first kind.

D.1.3 Inverse Edge Singular

The inverse edge singular basis function is shown in Fig. D.1(c) and is obtained by taking the inverse of the edge singular basis function. It can be written as

$$b(x) = \frac{4}{\pi l} \sqrt{1 - \left(\frac{2x}{l}\right)^2} \, \text{rect}\left(\frac{x}{l}\right) , \tag{D.9}$$

where l is the length of the basis function and the factor $4/(\pi l)$ is used to normalize the area of the basis function to 1. The Fourier transform of (D.9) is given by

$$B(k_x) = \frac{4}{\pi l} \frac{\pi}{k_x} J_1\left(k_x \frac{l}{2}\right) , \tag{D.10}$$

where $\lim_{k_x \to 0} B(k_x) = 1$.

D

D.1.4 Odd Edge Singular

The edge singular basis function is shown in Fig. D.1(d). It can be written as

$$b(x) = \left[\frac{1}{\sqrt{1 - \left(\frac{2x}{l}\right)^2}} - 1\right] \left(\text{rect}\left(\frac{2x}{l} + \frac{1}{2}\right) - \text{rect}\left(\frac{2x}{l} - \frac{1}{2}\right)\right) . \tag{D.11}$$

where l is the length of the basis function. The Fourier transform of (D.11) is given by

$$B(k_x) = e^{jk_x l/2} \left(J_0(k_x l) - j\mathbf{H}_0(k_x l)\right) - e^{-jk_x l/2} \left(J_0(-k_x l) - j\mathbf{H}_0(-k_x l)\right) . \tag{D.12}$$

D.2 Cylindrical Basis Functions

These basis functions are used in the cylindrical method of moments and are assumed to be a function of ρ. The given Hankel transforms use the following definitions:

$$B_{\rho,J_0}(k_\rho) = \int_0^\infty b_\rho(\rho) J_0(k_\rho \rho) \rho \, d\rho \tag{D.13}$$

$$B_{\rho,J_1}(k_\rho) = \int_0^\infty b_\rho(\rho) J_1(k_\rho \rho) \rho \, d\rho . \tag{D.14}$$
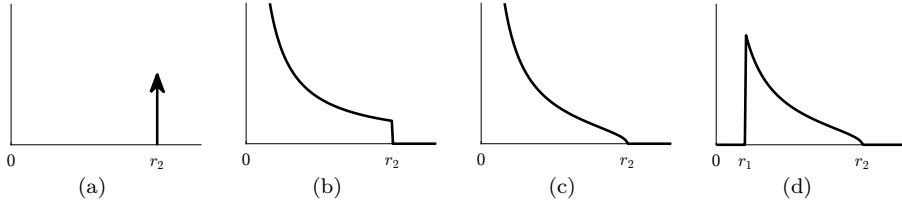
Figure D.2: Cylindrical basis functions described in this appendix. (a) Infinitesimal in ρ, (b) radial spreading, (c) radial spreading with forcing term, and (d) radial spreading with forcing term and zeroed below r_1.

D.2.1 Infinitesimal at $\rho = r_1$

The current of the pin is defined on an infinitesimally thin sheet on its surface at $\rho = r_1$, as shown in Fig. D.2(a). It can be written as

$$b(\rho, \phi) = \frac{1}{2\pi r_1} \delta(\rho - r_1) \,. \tag{D.15}$$

The Hankel transforms of the 0th and 1st order of (D.15) are given by

$$
\begin{aligned}
B_{J_0}(k_\rho) &= \frac{1}{2\pi} J_0(k_\rho r_1) \\
B_{J_1}(k_\rho) &= \frac{1}{2\pi} J_1(k_\rho r_1) \,.
\end{aligned}
\tag{D.16}
$$

D.2.2 Radial Spreading

Suppose there is radial spreading on the x-y plane, defined on the interval $[0, r_2]$, as shown in Fig. D.2(b). It can be written as

$$b(\rho, \phi) = \frac{1}{\rho} \, \text{rect} \left(\frac{\rho}{r_2} - \frac{1}{2} \right) \,. \tag{D.17}$$

The Hankel transforms of the 0th and 1st order of (D.17) are given by

$$B_{J_0}(k_\rho) = \frac{a}{2} \left(\pi J_1(k_\rho r_2) \mathbf{H}_0(k_\rho r_2) + J_0(k_\rho r_2)(2 - \pi \mathbf{H}_1(k_\rho r_2)) \right) \tag{D.18}$$

$$B_{J_1}(k_\rho) = \frac{1 - J_0(k_\rho r_2)}{k_\rho} \,. \tag{D.19}$$

These expressions are valid when

$$
\begin{aligned}
&\text{re}(k_\rho) > 0 \\
&\text{or } \text{re}(k_\rho) = 0 \text{ and } \text{im}(k_\rho) > 0 \,.
\end{aligned}
\tag{D.20}
$$

D.2.3 Radial Spreading with Forcing Term

To ensure the basis function goes to zero at the edge of the patch, r_2, it is multiplied by an inverse edge singular, as shown in Fig. D.2(c). It can be written as

$$b(\rho, \phi) = \frac{1}{\rho} \sqrt{1 - \left(\frac{\rho}{r_2}\right)^2} \, \text{rect}\left(\frac{\rho}{r_2} - \frac{1}{2}\right) . \tag{D.21}$$

The Hankel transforms of the 0th and 1st order of (D.21) are given by

$$B_{J_0}(k_\rho) = \frac{\pi}{4} r_2 \left(J_0\left(k_\rho \frac{r_2}{2}\right)^2 + J_1\left(k_\rho \frac{r_2}{2}\right)^2 \right) \tag{D.22}$$

$$B_{J_1}(k_\rho) = \frac{1 - \text{sinc}(k_\rho r_2)}{k_\rho} . \tag{D.23}$$

D.2.4 Radial Spreading with Forcing Term and Minimum Radius

To model the current on the pin-patch structure, a radial spreading function that runs from an inner radius r_1 to an outer radius r_2 is desired. This can be achieved by zeroing a part of the rectangular function in (D.21) to form

$$b(\rho, \phi) = \frac{1}{\rho} \sqrt{1 - \left(\frac{\rho}{r_2}\right)^2} \left(\text{rect}\left(\frac{\rho}{r_2} - \frac{1}{2}\right) - \text{rect}\left(\frac{\rho}{r_1} - \frac{1}{2}\right) \right) \hat{\rho} . \tag{D.24}$$

However, the integrals of the Hankel transforms of this function do not converge. Instead, the section from 0 to r_1 is removed by subtracting a second-order Taylor series, which is given by

$$\frac{1}{\rho} \sqrt{1 - \left(\frac{\rho}{r_2}\right)^2} \approx \frac{1}{\rho} \left(1 - \frac{\rho^2}{2r_2^2}\right) . \tag{D.25}$$

This is multiplied by a rect function that runs from 0 to r_1 and subtracted from the basis function in (D.21) to form the shape shown in Fig. D.2(d). The resulting expression is

$$b(\rho, \phi) = \frac{1}{\rho} \sqrt{1 - \left(\frac{\rho}{r_2}\right)^2} \, \text{rect}\left(\frac{\rho}{r_2} - \frac{1}{2}\right) - \frac{1}{\rho} \left(1 - \frac{\rho^2}{2r_2^2}\right) \text{rect}\left(\frac{\rho}{r_1} - \frac{1}{2}\right) . \tag{D.26}$$

The Hankel transforms of the 0th and 1st order of (D.26) are given by

$$B_{J_0}(k_\rho) = -\frac{r_1}{2} J_0(k_\rho r_1)(2 - \pi \mathbf{H}_1(k_\rho r_1) \left(1 + \frac{1}{2k_\rho^2 r_2^2}\right) \tag{D.27}$$

$$+ \frac{r_1}{2} J_1(k_\rho r_1)(k_\rho \frac{r_1}{r_2^2} - \pi \mathbf{H}_0(k_\rho r_1) \left(1 + \frac{1}{2k_\rho^2 r_2^2}\right)$$

$$+ \frac{r_2}{4} \pi \left(J_0 \left(k_\rho \frac{r_2}{2}\right)^2 + J_1 \left(k_\rho \frac{r_2}{2}\right)^2 \right)$$

$$B_{J_1}(k_\rho) = \frac{1}{k_\rho} \left(J_0(k_\rho r_1) + \frac{1}{2} \frac{r_1^2}{r_2^2} J_2(k_\rho r_1) - \text{sinc}(k_\rho r_2) \right). \tag{D.28}$$

D

Appendix E

X-pol Cancellation Analysis

As described in Section E.1, an aperture with two orthogonal radiators can be used to realize an arbitrary polarization. This appendix describes the required excitation weights for the two radiators to achieve a certain desired polarization. It also gives some additional results for the effectiveness of the cancellation versus scan angle and frequency when only a single weight is chosen. Finally, the effect of phase and amplitude errors on the purity of circular polarization is shown.

E.1 Cross-Polarization Cancellation

The excitation weights for the two radiators depend on their radiated field and on the desired polarization. First, the excitation weights required to cancel the X-pol as defined by are given. Next, the weights required to realize a linear polarization along an arbitrary slant angle are given, and finally the expressions for circular polarization are given.

E.1.1 Linear Polarization

When linear polarization is considered, the X-pol is often defined using Ludwig's third definition [99]. To achieve perfect linear polarization, the cross-polarized component of a certain radiator is canceled using the co-polarized component of the other radiator in the unit cell. Assuming that a generic x-oriented source is fed with the complex amplitude, or weight, a_x and radiates a total far field that is given by

$$\boldsymbol{E}_{\text{total},x} = a_x \left(E_{\text{co},x} \hat{L}_{3x} + E_{\text{cx},x} \hat{L}_{3y} \right) , \qquad (\text{E.1})$$

where the unit vectors $\hat{L}_{3x}$ and $\hat{L}_{3y}$ represent the directions of the co- and cross-polarized field for the x-oriented source. $E_{\text{co},x}$ and $E_{\text{cx},x}$ are the complex amplitudes
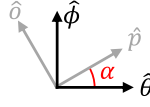
Figure E.1: Definition of $\hat{p}$ and $\hat{o}$ vectors with respect to the $\hat{\theta}$ and $\hat{\phi}$ vectors.

of the field radiated by the source along those two unit vectors. Similarly, for a y-oriented source fed with a complex amplitude a_y, the total radiated field is

$$\boldsymbol{E}_{\text{total},y} = a_y \left(E_{\text{co},y} \hat{L}_{3y} + E_{\text{cx},y} \hat{L}_{3x} \right) , \tag{E.2}$$

where the co-polar and cross-polar unit vectors are now inverted. Summing the two fields and projecting onto the two unit vectors yields

$$(\boldsymbol{E}_{\text{total},x} + \boldsymbol{E}_{\text{total},y}) \cdot \hat{L}_{3x} = a_x E_{\text{co},x} + a_y E_{\text{cx},y} \tag{E.3}$$

$$(\boldsymbol{E}_{\text{total},x} + \boldsymbol{E}_{\text{total},y}) \cdot \hat{L}_{3y} = a_x E_{\text{cx},x} + a_y E_{\text{co},y} . \tag{E.4}$$

To get a total field along a specific polarization (e.g. $\hat{L}_{3y}$), one can impose (E.3) to be equal to 0, which gives the condition

$$a_y = -a_x \frac{E_{\text{cross},x}}{E_{\text{co},y}} . \tag{E.5}$$

When the cross-polarization of the x-oriented source is high, the amplitude of a_y can be higher than the amplitude of a_x, in which case both excitation amplitudes should be scaled such that they are both realizable.

E.1.2 Slant Linear Polarization

The derivation in Section E.1.1 can be generalized to yield a linear polarization at a certain slant angle α. Suppose the radiated fields from the x- and y-oriented radiators are given by

$$\boldsymbol{E}_{\text{total},x} = a_x \left(E_{\theta,x} \hat{\theta} + E_{\phi,x} \hat{\phi} \right) \tag{E.6}$$

$$\boldsymbol{E}_{\text{total},y} = a_y \left(E_{\theta,y} \hat{\theta} + E_{\phi,y} \hat{\phi} \right) , \tag{E.7}$$

where $\hat{\theta}$ and $\hat{\phi}$ are the unit vectors of the spherical coordinate system. The total field can be projected onto two arbitrary orthogonal unit vectors $\hat{p}$ and $\hat{o}$, which are rotated by an angle α with respect to $\hat{\theta}$ and $\hat{\phi}$, respectively [see Fig. E.1. Note that the $\hat{\theta}$ and $\hat{\phi}$ vectors can be replaced by any two orthogonal reference vectors, such as $\hat{L}_{3x}$ and $\hat{L}_{3y}$. Indicating the desired slant linear polarization by $\hat{p}$ and the undesired orthogonal direction with $\hat{o}$, the condition for the total radiated field to be along the $\hat{p}$-direction becomes

$$a_y = -a_x \frac{E_{\phi,x} \cos \alpha - E_{\theta,x} \sin \alpha}{E_{\phi,y} \cos \alpha - E_{\theta,y} \sin \alpha} . \tag{E.8}$$

E.1.3 Circular Polarization

To achieve circular polarization, for any two orthogonal components of the radiated field, such as $\hat{\theta}$ and $\hat{\phi}$ or $\hat{L}_{3x}$ and $\hat{L}_{3y}$, one can define two vectors

$$\hat{R} = \frac{\hat{\theta} - j\hat{\phi}}{\sqrt{2}} \tag{E.9}$$

$$\hat{L} = \frac{\hat{\theta} + j\hat{\phi}}{\sqrt{2}} \ , \tag{E.10}$$

which are the right-handed and left-handed circular polarization unit vectors, respectively. Since these unit vectors are complex, the complex conjugate should be applied in the scalar (dot) product to verify $\hat{R} \cdot \hat{R}^* = 1$ and $\hat{R} \cdot \hat{L}^* = 0$. Projecting the total field onto the two vectors gives

$$E_R = \frac{(a_x E_{\theta,x} + a_y E_{\phi,y}) + j\,(a_x E_{\phi,x} + a_y E_{\phi,y})}{\sqrt{2}} \tag{E.11}$$

$$E_R = \frac{(a_x E_{\theta,x} + a_y E_{\phi,y}) - j\,(a_x E_{\phi,x} + a_y E_{\phi,y})}{\sqrt{2}} \ . \tag{E.12}$$

The tilt angle of the polarization ellipse is given by

$$\tau = \frac{1}{2} \arg\left(\frac{E_R}{E_L}\right) \ , \tag{E.13}$$

and the axial ratio is given by

$$AR = \frac{|E_R| + |E_L|}{|E_R| - |E_L|} \ . \tag{E.14}$$

To obtain perfect right-handed circular polarization, one can impose $AR = 1$, which implies $|E_L| = 0$ and is achieved when

$$a_{y,R} = -a_x \frac{E_{\theta,x} - jE_{\phi,x}}{E_{\theta,y} - jE_{\phi,y}} \ . \tag{E.15}$$

To obtain perfect left-handed circular polarization, one can impose $AR = -1$, which implies $|E_R| = 0$ and is achieved when

$$a_{y,L} = -a_x \frac{E_{\theta,x} + jE_{\phi,x}}{E_{\theta,y} + jE_{\phi,y}} = a_{y,R}^* \ . \tag{E.16}$$

E.2 Circular Polarization with Fixed Weights

The results in Fig. 5.22 use a different combination of weights for each elevation angle θ. This may not be desired as it requires a large look-up table for the weights, as
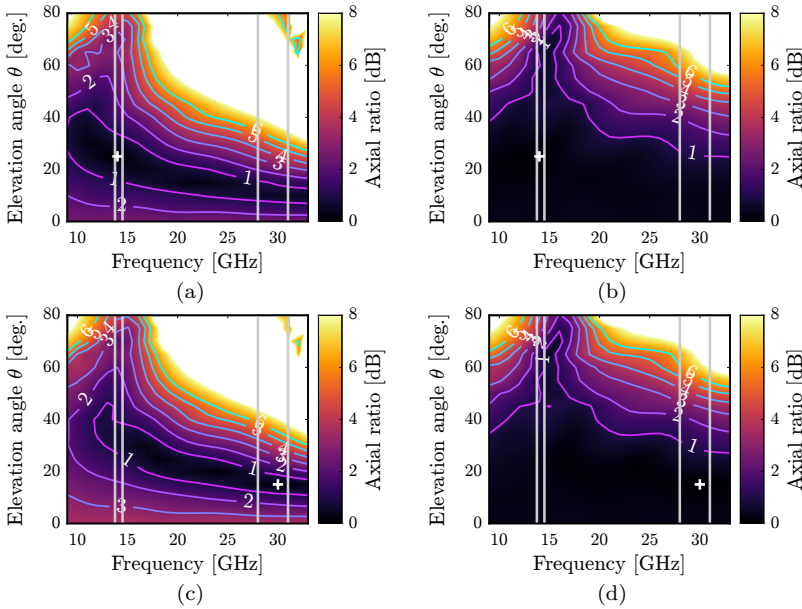
Figure E.2: Axial ratio of the unit cell in Fig. 5.12(b) with the linear polarization weighting condition in (E.5) applied at (top) 14 GHz and $\theta = 25°$ or (bottom) 30 GHz and $\theta = 15°$ on the (left) H-plane and (right) D-plane. The white + marker indicates the angle and frequency for which the weight is calculated. The results for the E-plane are identical to the H-plane and are therefore omitted.

well as prior knowledge of the radiation characteristics of the antenna at each of these angles. As such, the effect of applying the weighting for a single elevation angle θ is investigated, to better highlight the angular and frequency dependence of the polarization properties. The resulting axial ratio vs frequency and elevation angle θ is shown as a color map in Fig. E.2 for both H- and D-plane scanning. The two frequency bands are highlighted, and the frequency and scanning angle at which the weights are calculated are shown with a white plus marker.

Both the angular and frequency variation is higher in the main planes compared to the diagonal plane. Also, as already noted earlier, the frequency dependence of the axial ratio is much lower for small scanning angles and increases for wide scan. When the weighting is applied at 14 GHz and $\theta = 25°$, for either E- or D-plane scanning, it is seen in Fig. E.2(a) and Fig. E.2(b) that the axial ratio is below 3 dB in the entire range $0° < \theta < 60°$ in the Ku-band. The axial ratio is seen to be less stable in the Ka-band, remaining below 3 dB in a smaller range $0° < \theta < 45°$, so a separate pair of weights would be required for the scan range $45° < \theta < 60°$. It is also observed that applying the weighting condition at 30 GHz and $\theta = 15°$ does not significantly change the behavior of the axial ratio.

E.2.1 Variations in Amplitude and Phase

The previous figures assume that the weighting conditions are applied perfectly. To study the effect of variations in amplitude and phase in the excitation of the slots, the axial ratio versus frequency is determined for various error values. First, an amplitude error Δa is introduced by multiplying the weight for the y-oriented slot by a factor $(1+$ error$)$, that is, $a_{y,\Delta a} = a_y(1+\Delta a)$. The resulting axial ratio versus frequency is shown for various scanning angles in Fig. E.3. One can note that amplitude variations of the weights up to 15% still yield axial ratio lower than 3 dB, in both bands. Therefore, the cancellation technique is quite robust in terms of amplitude errors.

The effect of phase errors is studied by multiplying the weight for the y-oriented slot by a phase error term δ, that is, $a_{y,\delta} = a_y e^{j\delta}$. The resulting axial ratio versus frequency is shown for various scanning angles in Fig. E.4. It can be seen that phase variation of $\pm 10°$ still provide axial ratio lower than 3 dB for all considered cases. The required phase accuracy can be safely achieved with current on-chip phase shifters in both Ku- and Ka-band [115–117].

E

Figure E.3: Axial ratio of the unit cell in Fig. 5.12(b) with the circular polarization weighting condition in (E.15) with a ±30% amplitude error. The weight is calculated at (top) 14 GHz or (bottom) 30 GHz, and results are shown for – from left to right – Broadside, H-plane 60°, D-plane 60°, and E-Plane 60°.

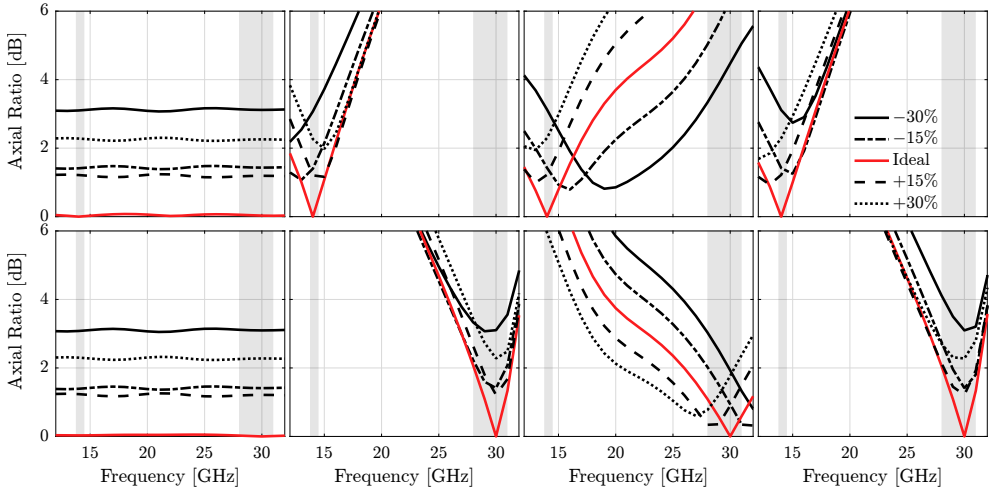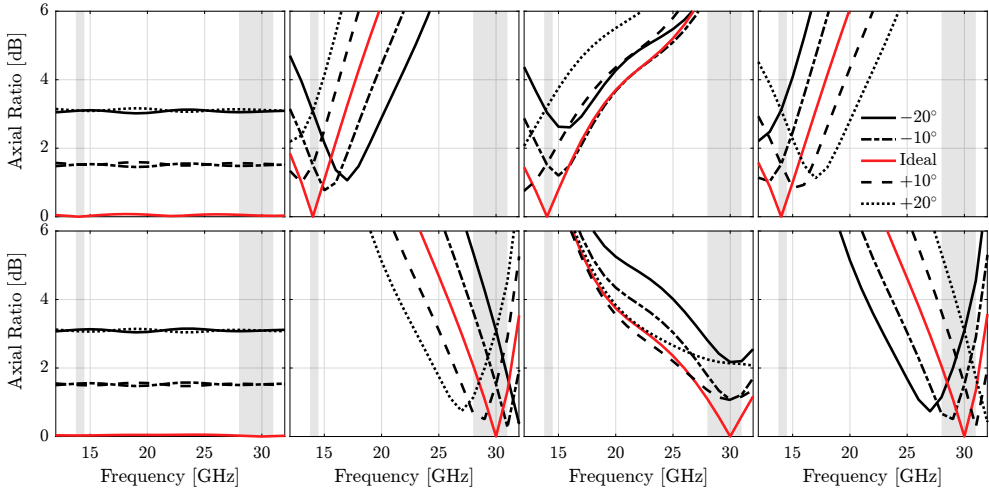
Figure E.4: Axial ratio of the unit cell in Fig. 5.12(b) with the circular polarization weighting condition in (E.15) with a ±20° phase error. The weight is calculated at (top) 14 GHz or (bottom) 30 GHz, and results are shown for – from left to right – Broadside, H-plane 60°, D-plane 60°, and E-Plane 60°.

Bibliography

[1] A. J. Fenn, D. H. Temme, W. P. Delaney, and W. E. Courtney, "The Development of Phased-Array Radar Technology," *Lincoln Laboratory Journal*, vol. 12, no. 2, 2000.

[2] A. Spezio, "Electronic warfare systems," *IEEE Transactions on Microwave Theory and Techniques*, vol. 50, no. 3, pp. 633–644, Mar. 2002.

[3] A. Farina and P. Neri, "Multitarget interleaved tracking for phased-array radar," *IEE Proceedings F Communications, Radar and Signal Processing*, vol. 127, no. 4, p. 312, 1980.

[4] E. Taenzer, "Tracking Multiple Targets Simultaneously with a Phased Array Radar," *IEEE Transactions on Aerospace and Electronic Systems*, vol. AES-16, no. 5, pp. 604–614, Sep. 1980.

[5] T. Kinghorn, I. Scott, and E. Totten, "Recent advances in airborne phased array radar systems," in *2016 IEEE International Symposium on Phased Array Systems and Technology (PAST)*. Waltham, MA, USA: IEEE, Oct. 2016, pp. 1–7.

[6] C. Renard and M. Soiron, "Wideband multifunction airborne antennas," in *2009 International Radar Conference "Surveillance for a Safer World" (RADAR 2009)*, Oct. 2009, pp. 1–3.

[7] H. Bui-Van, J. Abraham, M. Arts, Q. Gueuning, C. Raucy, D. Gonzalez-Ovejero, E. De Lera Acedo, and C. Craeye, "Fast and Accurate Simulation Technique for Large Irregular Arrays," *IEEE Transactions on Antennas and Propagation*, vol. 66, no. 4, pp. 1805–1817, Apr. 2018.

[8] S. W. Ellingson, "Sensitivity of Antenna Arrays for Long-Wavelength Radio Astronomy," *IEEE Transactions on Antennas and Propagation*, vol. 59, no. 6, pp. 1855–1863, Jun. 2011.

[9] D. Sheen, D. McMakin, and T. Hall, "Three-dimensional millimeter-wave imaging for concealed weapon detection," *IEEE Transactions on Microwave Theory and Techniques*, vol. 49, no. 9, pp. 1581–1592, Sept./2001.

[10] M. H. Novak and J. L. Volakis, "Ultrawideband Antennas for Multiband Satellite Communications at UHF–Ku Frequencies," *IEEE Transactions on Antennas and Propagation*, vol. 63, no. 4, pp. 1334–1341, Apr. 2015.

[11] Z. Liu, E. A. Karahan, and K. Sengupta, "Ultra Broadband Phased-Array Transmitter with Low Phase Error of 1.24-2.8° across 36-91 GHz Supporting 10.8 Gbps 64QAM in 90 nm SiGe," in *ESSCIRC 2023- IEEE 49th European Solid State Circuits Conference (ESSCIRC)*. Lisbon, Portugal: IEEE, Sep. 2023, pp. 497–500.

[12] R. J. Bolt, D. Cavallo, G. Gerini, D. Deurloo, R. Grooters, A. Neto, and G. Toso, "Characterization of a Dual-Polarized Connected-Dipole Array for Ku-Band Mobile Terminals," *IEEE Transactions on Antennas and Propagation*, vol. 64, no. 2, pp. 591–598, Feb. 2016.

[13] M. H. Novak, F. A. Miranda, and J. L. Volakis, "Ultra-Wideband Phased Array for Millimeter-Wave ISM and 5G Bands, Realized in PCB," *IEEE Transactions on Antennas and Propagation*, vol. 66, no. 12, pp. 6930–6938, Dec. 2018.

[14] P. Dewdney, P. Hall, R. Schilizzi, and T. Lazio, "The Square Kilometre Array," *Proceedings of the IEEE*, vol. 97, no. 8, pp. 1482–1496, Aug. 2009.

[15] G. W. Kant, P. D. Patel, S. J. Wijnholds, M. Ruiter, and E. Van Der Wal, "EMBRACE: A Multi-Beam 20,000-Element Radio Astronomical Phased Array Antenna Demonstrator," *IEEE Transactions on Antennas and Propagation*, vol. 59, no. 6, pp. 1990–2003, Jun. 2011.

[16] W. Hong, Z. H. Jiang, C. Yu, J. Zhou, P. Chen, Z. Yu, H. Zhang, B. Yang, X. Pang, M. Jiang, Y. Cheng, M. K. T. Al-Nuaimi, Y. Zhang, J. Chen, and S. He, "Multibeam Antenna Technologies for 5G Wireless Communications," *IEEE Transactions on Antennas and Propagation*, vol. 65, no. 12, pp. 6231–6249, Dec. 2017.

[17] Z. Xiao, Z. Han, A. Nallanathan, O. A. Dobre, B. Clerckx, J. Choi, C. He, and W. Tong, "Antenna Array Enabled Space/Air/Ground Communications and Networking for 6G," *IEEE Journal on Selected Areas in Communications*, vol. 40, no. 10, pp. 2773–2804, Oct. 2022.

[18] C. I. Adomnitei, C. E. Lesanu, A. Done, A. Yu, M. Dimian, and A. Lavric, "The Design and Implementation of a Phased Antenna Array System for LEO Satellite Communications," *Sensors*, vol. 24, no. 6, p. 1915, Mar. 2024.

[19] J.-C. S. Chieh, E. Yeo, R. Farkouh, A. Castro, M. Kerber, R. B. Olsen, E. J. Merulla, and S. K. Sharma, "Development of Flat Panel Active Phased Array Antennas Using 5G Silicon RFICs at Ku- and Ka-Bands," *IEEE Access*, vol. 8, pp. 192 669–192 681, 2020.

[20] A. H. Aljuhani, T. Kanar, S. Zihir, and G. M. Rebeiz, "A Scalable Dual-Polarized 256-Element Ku-Band SATCOM Phased-Array Transmitter with 36.5 dBW EIRP Per Polarization," in *2018 48th European Microwave Conference (EuMC)*.   Madrid: IEEE, Sep. 2018, pp. 938–941.

[21] I. Kaplan, I. Marinov, A. Gal, V. Peshlov, M. Gachev, V. Boyanov, and B. Marinov, "Electronically beam steerable antennas for broadband satellite communications," in *The 8th European Conference on Antennas and Propagation (EuCAP 2014)*.   The Hague, Netherlands: IEEE, Apr. 2014, pp. 2450–2454.

[22] A. H. Aljuhani, T. Kanar, S. Zihir, and G. M. Rebeiz, "A 256-Element Ku-Band Polarization Agile SATCOM Receive Phased Array With Wide-Angle Scanning and High Polarization Purity," *IEEE Transactions on Microwave Theory and Techniques*, vol. 69, no. 5, pp. 2609–2628, May 2021.

[23] L. Baggen, S. Vaccaro, D. L. Del Rio, and J. Padilla, "A compact phased array for satcom applications," in *2013 IEEE International Symposium on Phased Array Systems and Technology*.   Waltham, MA, USA: IEEE, Oct. 2013, pp. 232–239.

[24] G. Gultepe, T. Kanar, S. Zihir, and G. M. Rebeiz, "A 1024-Element Ku-Band SATCOM Phased-Array Transmitter With 45-dBW Single-Polarization EIRP," *IEEE Transactions on Microwave Theory and Techniques*, vol. 69, no. 9, pp. 4157–4168, Sep. 2021.

[25] ——, "A 1024-Element Ku-Band SATCOM Dual-Polarized Receiver With >10-dB/K G/T and Embedded Transmit Rejection Filter," *IEEE Transactions on Microwave Theory and Techniques*, vol. 69, no. 7, pp. 3484–3495, Jul. 2021.

[26] X. Luo, J. Ouyang, Z. H. Chen, Y. Yan, L. Han, Z. Wu, T. Yu, and K. Zheng, "A Scalable Ka-Band 1024-Element Transmit Dual-Circularly-Polarized Planar Phased Array for SATCOM Application," *IEEE Access*, vol. 8, pp. 156 084–156 095, 2020.

[27] W. M. Abdel-Wahab, H. Al-Saedi, E. H. Mirza Alian, M. Raeis-Zadeh, A. Ehsandar, A. Palizban, N. Ghafarian, G. Chen, H. Gharaee, M. R. Nezhad-Ahmadi, and S. Safavi Naeini, "A Modular Architecture for Wide Scan Angle Phased Array Antenna for K/Ka Mobile SATCOM," in *2019 IEEE MTT-S International Microwave Symposium (IMS)*.   Boston, MA, USA: IEEE, Jun. 2019, pp. 1076–1079.

[28] X. Gu, D. Liu, C. Baks, O. Tageman, B. Sadhu, J. Hallin, L. Rexberg, P. Parida, Y. Kwark, and A. Valdes-Garcia, "Development, Implementation, and Characterization of a 64-Element Dual-Polarized Phased-Array Antenna Module for 28-GHz High-Speed Data Communications," *IEEE Transactions on Microwave Theory and Techniques*, vol. 67, no. 7, pp. 2975–2984, Jul. 2019.

[29] A. I. Sandhu, E. Arnieri, G. Amendola, L. Boccia, E. Meniconi, and V. Ziegler, "Radiating Elements for Shared Aperture Tx/Rx Phased Arrays at K/Ka Band," *IEEE Transactions on Antennas and Propagation*, vol. 64, no. 6, pp. 2270–2282, Jun. 2016.

[30] C. Ni, M. S. Chen, Z. X. Zhang, and X. L. Wu, "Design of Frequency- and Polarization-Reconfigurable Antenna Based on the Polarization Conversion Metasurface," *IEEE Antennas and Wireless Propagation Letters*, vol. 17, no. 1, pp. 78–81, Jan. 2018.

[31] H. L. Zhu, S. W. Cheung, X. H. Liu, and T. I. Yuk, "Design of Polarization Reconfigurable Antenna Using Metasurface," *IEEE Transactions on Antennas and Propagation*, vol. 62, no. 6, pp. 2891–2898, Jun. 2014.

[32] D. H. Schaubert, S. Kasturi, A. O. Boryssenko, and W. M. Elsallal, "Vivaldi antenna arrays for wide bandwidth and electronic scanning," in *2nd European Conference on Antennas and Propagation (EuCAP 2007)*. Edinburgh, UK: Institution of Engineering and Technology, 2007, pp. 211–211.

[33] J. J. Lee, S. Livingston, and R. Koenig, "A low-profile wide-band (5:1) dual-pol array," *IEEE Antennas and Wireless Propagation Letters*, vol. 2, pp. 46–49, 2003.

[34] W. Elsallal, J. W. West, J. Wolf, R. Freeman, R. Legge, V. Olen, T. W. Darymple, M. B. Longbrake, and P. E. Buxa, "Charateristics of decade-bandwidth, Balanced Antipodal Vivaldi Antenna (BAVA) phased arrays with time-delay beamformer systems," in *2013 IEEE International Symposium on Phased Array Systems and Technology*. Waltham, MA, USA: IEEE, Oct. 2013, pp. 111–116.

[35] R. W. Kindt and J. T. Logan, "Dual-Polarized Metal-Flare Sliced Notch Antenna Array," *IEEE Transactions on Antennas and Propagation*, vol. 68, no. 4, pp. 2666–2674, Apr. 2020.

[36] H. Holter, "Dual-Polarized Broadband Array Antenna With BOR-Elements, Mechanical Design and Measurements," *IEEE Transactions on Antennas and Propagation*, vol. 55, no. 2, pp. 305–312, Feb. 2007.

[37] R. W. Kindt and W. R. Pickles, "Ultrawideband All-Metal Flared-Notch Array Radiator," *IEEE Transactions on Antennas and Propagation*, vol. 58, no. 11, pp. 3568–3575, Nov. 2010.

[38] R. Kindt and R. Pickles, "12-to-1 bandwidth all-metal Vivaldi array element," in *2009 IEEE Antennas and Propagation Society International Symposium*. North Charleston, SC, USA: IEEE, Jun. 2009, pp. 1–4.

[39] J. Lee and S. Livingston, "Wide band bunny-ear radiating element," in *Proceedings of IEEE Antennas and Propagation Society International Symposium*. Ann Arbor, MI, USA: IEEE, 1993, pp. 1604–1607.

[40] M. W. Elsallal and J. C. Mather, "An ultra-thin, decade (10:1) Bandwidth, modular "BAVA" array with low cross-polarization," in *2011 IEEE International Symposium on Antennas and Propagation (APSURSI).* Spokane, WA: IEEE, Jul. 2011, pp. 1980–1983.

[41] J. J. Lee, S. Livingston, R. Koenig, D. Nagata, and L. L. Lai, "Compact light weight UHF arrays using long slot apertures," *IEEE Transactions on Antennas and Propagation*, vol. 54, no. 7, pp. 2009–2015, Jul. 2006.

[42] J. Lee, S. Livingston, and D. Nagata, "A low profile 10:1 (200-2000 MHz) wide band long slot array," in *2008 IEEE Antennas and Propagation Society International Symposium.* San Diego, CA: IEEE, Jul. 2008, pp. 1–4.

[43] J. P. Doane, K. Sertel, and J. L. Volakis, "A Wideband, Wide Scanning Tightly Coupled Dipole Array With Integrated Balun (TCDA-IB)," *IEEE Transactions on Antennas and Propagation*, vol. 61, no. 9, pp. 4538–4548, Sep. 2013.

[44] W. F. Moulder, K. Sertel, and J. L. Volakis, "Ultrawideband Superstrate-Enhanced Substrate-Loaded Array With Integrated Feed," *IEEE Transactions on Antennas and Propagation*, vol. 61, no. 11, pp. 5802–5807, Nov. 2013.

[45] D. Cavallo, A. Neto, and G. Gerini, "Analytical Description and Design of Printed Dipole Arrays for Wideband Wide-Scan Applications," *IEEE Transactions on Antennas and Propagation*, vol. 60, no. 12, pp. 6027–6031, Dec. 2012.

[46] J. T. Logan, R. W. Kindt, M. Y. Lee, and M. N. Vouvakis, "A New Class of Planar Ultrawideband Modular Antenna Arrays With Improved Bandwidth," *IEEE Transactions on Antennas and Propagation*, vol. 66, no. 2, pp. 692–701, Feb. 2018.

[47] E. Yetisir, N. Ghalichechian, and J. L. Volakis, "Ultrawideband Array With 70° Scanning Using FSS Superstrate," *IEEE Transactions on Antennas and Propagation*, vol. 64, no. 10, pp. 4256–4265, Oct. 2016.

[48] Y. S. Kim and K. S. Yngvesson, "Characterization of tapered slot antenna feeds and feed arrays," *IEEE Transactions on Antennas and Propagation*, vol. 38, no. 10, pp. 1559–1564, Oct./1990.

[49] D. H. Schaubert, Joon Shin, and G. Wunsch, "Characteristics of single-polarized phased array of tapered slot antennas," in *Proceedings of International Symposium on Phased Array Systems and Technology.* Boston, MA, USA: IEEE, 1996, pp. 102–106.

[50] D. T. McGrath, N. Schuneman, T. H. Shively, and J. Irion, "Polarization properties of scanning arrays," in *IEEE International Symposium on Phased Array Systems and Technology, 2003.* Boston, Mass, USA: IEEE, 2003, pp. 295–299.

[51] R. Kindt and D. Taylor, "Polarization correction in dual-polarized phased arrays of flared notches," in *2011 IEEE International Symposium on Antennas and Propagation (APSURSI).* Spokane, WA: IEEE, Jul. 2011, pp. 1961–1964.

[52] M. N. Vouvakis, D. H. Schaubert, and F. B. Gross, "Vivaldi antenna arrays," in *Frontiers in Antennas: Next Generation Design & Engineering.* McGraw-Hill New York, NY, USA, 2011.

[53] S. S. Holland, D. H. Schaubert, and M. N. Vouvakis, "A 7–21 GHz Dual-Polarized Planar Ultrawideband Modular Antenna (PUMA) Array," *IEEE Transactions on Antennas and Propagation*, vol. 60, no. 10, pp. 4589–4600, Oct. 2012.

[54] D. Cavallo, W. H. Syed, and A. Neto, "Connected-Slot Array With Artificial Dielectrics: A 6 to 15 GHz Dual-Pol Wide-Scan Prototype," *IEEE Transactions on Antennas and Propagation*, vol. 66, no. 6, pp. 3201–3206, Jun. 2018.

[55] Y. Li, S. Xiao, C. H. Hu, and Z. Yao, "A Low-Profile Light-Weight Wideband Connected Parallel Slot Array for Wide-Angle Scanning," *IEEE Transactions on Antennas and Propagation*, vol. 68, no. 2, pp. 813–823, Feb. 2020.

[56] Y. Li, S. Xiao, and B. Z. Wang, "A Wideband Circularly Polarized Connected Parallel Slot Array in the Presence of a Backing Reflector," *IEEE Access*, vol. 8, pp. 26 517–26 523, 2020.

[57] D. Cavallo and A. Neto, "A Connected Array of Slots Supporting Broadband Leaky Waves," *IEEE Transactions on Antennas and Propagation*, vol. 61, no. 4, pp. 1986–1994, Apr. 2013.

[58] W. H. Syed, D. Cavallo, H. Thippur Shivamurthy, and A. Neto, "Wideband, Wide-Scan Planar Array of Connected Slots Loaded With Artificial Dielectric Superstrates," *IEEE Transactions on Antennas and Propagation*, vol. 64, no. 2, pp. 543–553, Feb. 2016.

[59] R. Ozzola, A. Neto, U. Imberg, and D. Cavallo, "Connected Slot Array With Interchangeable ADL Radome for Sub-8 GHz 5G Applications," *IEEE Transactions on Antennas and Propagation*, vol. 72, no. 1, pp. 992–997, Jan. 2024.

[60] Z. Zhang, X. Guo, Y. Chen, S. W. Qu, and S. Yang, "One-dimensional conformal ultra-wideband connected slot arrays with reduced scattering," *International Journal of RF and Microwave Computer-Aided Engineering*, vol. 31, no. 10, Oct. 2021.

[61] A. Neto and S. Maci, "Green's function for an infinite slot printed between two homogeneous dielectrics. I. Magnetic currents," *IEEE Transactions on Antennas and Propagation*, vol. 51, no. 7, pp. 1572–1581, Jul. 2003.

[62] A. Neto and J. J. Lee, "Ultrawide-Band Properties of Long Slot Arrays," *IEEE Transactions on Antennas and Propagation*, vol. 54, no. 2, pp. 534–543, Feb. 2006.

[63] ——, ""Infinite Bandwidth" long slot array antenna," *IEEE Antennas and Wireless Propagation Letters*, vol. 4, pp. 75–78, 2005.

[64] M. Maggi, R. Fragnier, R. Contreres, R. Sauleau, and M. Ettorre, "Wideband Wide Scan Unit-Cell of a Connected Slot Array for SatCom Applications," in *2023 17th European Conference on Antennas and Propagation (EuCAP)*. Florence, Italy: IEEE, Mar. 2023, pp. 1–3.

[65] E. Magill and H. Wheeler, "Wide-angle impedance matching of a planar array antenna by a dielectric sheet," *IEEE Transactions on Antennas and Propagation*, vol. 14, no. 1, pp. 49–53, Jan. 1966.

[66] N. Alexopoulos and D. Jackson, "Fundamental superstrate (cover) effects on printed circuit antennas," *IEEE Transactions on Antennas and Propagation*, vol. 32, no. 8, pp. 807–816, Aug. 1984.

[67] S. Sajuyigbe, S. Cummer, and D. Smith, "Utilization of metamaterials for wide angle impedance matching (WAIM) in phased array antennas," in *2009 IEEE Antennas and Propagation Society International Symposium*. Charleston, SC: IEEE, Jun. 2009, pp. 1–4.

[68] M. Soltani and G. V. Eleftheriades, "Wide-Angle Impedance Matching of a Patch Antenna Phased Array Using Artificial Dielectric Sheets," *IEEE Transactions on Antennas and Propagation*, vol. 72, no. 5, pp. 4258–4270, May 2024.

[69] W. H. Syed and A. Neto, "Front-to-Back Ratio Enhancement of Planar Printed Antennas by Means of Artificial Dielectric Layers," *IEEE Transactions on Antennas and Propagation*, vol. 61, no. 11, pp. 5408–5416, Nov. 2013.

[70] D. Cavallo, W. H. Syed, and A. Neto, "Closed-Form Analysis of Artificial Dielectric Layers—Part II: Extension to Multiple Layers and Arbitrary Illumination," *IEEE Transactions on Antennas and Propagation*, vol. 62, no. 12, pp. 6265–6273, Dec. 2014.

[71] ——, "Closed-Form Analysis of Artificial Dielectric Layers—Part I: Properties of a Single Layer Under Plane-Wave Incidence," *IEEE Transactions on Antennas and Propagation*, vol. 62, no. 12, pp. 6256–6264, Dec. 2014.

[72] D. Cavallo and C. Felita, "Analytical Formulas for Artificial Dielectrics With Nonaligned Layers," *IEEE Transactions on Antennas and Propagation*, vol. 65, no. 10, pp. 5303–5311, Oct. 2017.

[73] D. Cavallo and R. M. van Schelven, "Closed-Form Analysis of Artificial Dielectric Layers with Non-Periodic Characteristics," in *2019 13th European Conference on Antennas and Propagation (EuCAP)*, Mar. 2019, pp. 1–5.

[74] R. M. van Schelven and D. Cavallo, "Analysis of Nonsquare Artificial Dielectric Layers and Application to the Design of Anisotropic Slabs," *IEEE Antennas and Wireless Propagation Letters*, vol. 21, no. 2, pp. 302–306, Feb. 2022.

[75] C. Craeye and X. Dardenne, "Element pattern analysis of wide-band arrays with the help of a finite-by-infinite array approach," *IEEE Transactions on Antennas and Propagation*, vol. 54, no. 2, pp. 519–526, Feb. 2006.

[76] F. Capolino, A. Neto, M. Albani, and S. Maci, "Edge diffracted Floquet waves at a truncated array of dipoles," in *IEEE Antennas and Propagation Society International Symposium 1997. Digest*, vol. 2, Jul. 1997, pp. 1078–1081 vol.2.

[77] A. K. Skrivervik and J. R. Mosig, "Analysis of finite phase arrays of microstrip patches," *IEEE Transactions on Antennas and Propagation*, vol. 41, no. 8, pp. 1105–1114, Aug. 1993.

[78] A. Neto, S. Maci, G. Vecchi, and M. Sabbadini, "A truncated Floquet wave diffraction method for the full-wave analysis of large phased arrays .II. Generalization to 3-D cases," *IEEE Transactions on Antennas and Propagation*, vol. 48, no. 4, pp. 601–611, Apr. 2000.

[79] C. Craeye, "A Fast Impedance and Pattern Computation Scheme for Finite Antenna Arrays," *IEEE Transactions on Antennas and Propagation*, vol. 54, no. 10, pp. 3030–3034, Oct. 2006.

[80] P. De Vita, A. Freni, F. Vipiana, P. Pirinoli, and G. Vecchi, "Fast Analysis of Large Finite Arrays With a Combined Multiresolution—SM/AIM Approach," *IEEE Transactions on Antennas and Propagation*, vol. 54, no. 12, pp. 3827–3832, Dec. 2006.

[81] D. J. Ludick, R. Maaskant, D. D. Davidson, U. Jakobus, R. Mittra, and D. De Villiers, "Efficient Analysis of Large Aperiodic Antenna Arrays Using the Domain Green's Function Method," *IEEE Transactions on Antennas and Propagation*, vol. 62, no. 4, pp. 1579–1588, Apr. 2014.

[82] O. A. Civi and P. H. Pathak, "Array Guided Surface Waves on a Finite Planar Array of Dipoles With or Without a Grounded Substrate," *IEEE Transactions on Antennas and Propagation*, vol. 54, no. 8, pp. 2244–2252, Aug. 2006.

[83] A. Neto, D. Cavallo, and G. Gerini, "Edge-Born Waves in Connected Arrays: A Finite x Infinite Analytical Representation," *IEEE Transactions on Antennas and Propagation*, vol. 59, no. 10, pp. 3646–3657, Oct. 2011.

[84] D. Cavallo, W. H. Syed, and A. Neto, "Equivalent Transmission Line Models for the Analysis of Edge Effects in Finite Connected and Tightly Coupled Arrays," *IEEE Transactions on Antennas and Propagation*, vol. 65, no. 4, pp. 1788–1796, Apr. 2017.

[85] R. M. van Schelven, D. Cavallo, and A. Neto, "Equivalent Circuit Models of Finite Slot Antennas," *IEEE Transactions on Antennas and Propagation*, vol. 67, no. 7, pp. 4367–4376, Jul. 2019.

[86] H. Wheeler, "Simple relations derived fom a phased-array antenna made of an infinite current sheet," *IEEE Transactions on Antennas and Propagation*, vol. 13, no. 4, pp. 506–514, Jul. 1965.

[87] A. Neto, S. Maci, M. Sabbadini, and G. Vecchi, "Edge fringe approach for the full-wave solution of large finite arrays," in *IEEE Antennas and Propagation Society International Symposium 1997. Digest*, vol. 2, Jul. 1997, pp. 1074–1077 vol.2.

[88] O. Civi, P. Pathak, and H.-T. Chou, "On the Poisson sum formula for the analysis of wave radiation and scattering from large finite arrays," *IEEE Transactions on Antennas and Propagation*, vol. 47, no. 5, pp. 958–959, May 1999.

[89] F. Capolino, M. Albani, S. Maci, and L. Felsen, "Frequency-domain Green's function for a planar periodic semi-infinite phased array .I. Truncated floquet wave formulation," *IEEE Transactions on Antennas and Propagation*, vol. 48, no. 1, pp. 67–74, Jan. 2000.

[90] S. Maci, A. Toccafondi, A. Polemi, and L. Felsen, "High-frequency Green's function for a semi-infinite array of electric dipoles on an infinite grounded stratified dielectric slab: Part II-spatial domain parameterization," *IEEE Transactions on Antennas and Propagation*, vol. 53, no. 4, pp. 1364–1376, Apr. 2005.

[91] L. Felsen, S. Maci, A. Polemi, and A. Toccafondi, "High-frequency Green's function for a semi-infinite array of electric dipoles on an infinite grounded stratified dielectric slab: Part III $phase-matched wave interactions and numerical results," *IEEE Transactions on Antennas and Propagation*, vol. 53, no. 5, pp. 1663–1671, May 2005.

[92] A. Ishimaru, R. Coe, G. Miller, and W. Geren, "Finite periodic structure approach to large scanning array problems," *IEEE Transactions on Antennas and Propagation*, vol. 33, no. 11, pp. 1213–1220, Nov. 1985.

[93] S. Sajuyigbe, M. Ross, P. Geren, S. A. Cummer, M. H. Tanielian, and D. R. Smith, "Wide angle impedance matching metamaterials for waveguide-fed phased-array antennas," *IET Microwaves, Antennas & Propagation*, vol. 4, no. 8, pp. 1063–1072, 2010.

[94] T. R. Cameron and G. V. Eleftheriades, "Analysis and Characterization of a Wide-Angle Impedance Matching Metasurface for Dipole Phased Arrays," *IEEE Transactions on Antennas and Propagation*, vol. 63, no. 9, pp. 3928–3938, Sep. 2015.

[95] T. G. Waterman, "Wideband wide scan antenna matching structure using electrically floating plates," US Patent US8 253 641B1, Aug., 2012.

[96] A. Hoorfar, K. C. Gupta, and D. C. Chang, "Cross-polarization level in radiation from a microstrip dipole antenna," *IEEE Transactions on Antennas and Propagation*, vol. 36, no. 9, pp. 1197–1203, Sept./1988.

[97] C. C. Chen, "Wideband wide-angle impedance matching and polarization characteristics of circular waveguide phased arrays," *IEEE Transactions on Antennas and Propagation*, vol. 22, no. 3, pp. 414–418, May 1974.

[98] D. Cavallo, "Connected Array Antennas: Analysis and Design," Ph.D. dissertation, Technische Universiteit Eindhoven, 2011.

[99] A. Ludwig, "The definition of cross polarization," *IEEE Transactions on Antennas and Propagation*, vol. 21, no. 1, pp. 116–119, Jan. 1973.

[100] D. Cohen and R. Shavit, "Bi-anisotropic Metamaterials Effective Constitutive Parameters Extraction Using Oblique Incidence S-Parameters Method," *IEEE Transactions on Antennas and Propagation*, vol. 63, no. 5, pp. 2071–2078, May 2015.

[101] D. Sievenpiper, L. Zhang, R. Broas, N. Alexopolous, and E. Yablonovitch, "High-impedance electromagnetic surfaces with a forbidden frequency band," *IEEE Transactions on Microwave Theory and Techniques*, vol. 47, no. 11, pp. 2059–2074, Nov. 1999.

[102] A. J. van Katwijk, A. Neto, G. Toso, and D. Cavallo, "Design of Wideband Wide-Scanning Dual-Polarized Phased Array Covering Simultaneously Both the Ku- and the Ka-Satcom Bands," in *2020 14th European Conference on Antennas and Propagation (EuCAP)*. Copenhagen, Denmark: IEEE, Mar. 2020, pp. 1–3.

[103] S. Rao, D. Wilton, and A. Glisson, "Electromagnetic scattering by surfaces of arbitrary shape," *IEEE Transactions on Antennas and Propagation*, vol. 30, no. 3, pp. 409–418, May 1982.

[104] R. O. Ribeiro, M. V. T. Heckler, and A. F. Tinoco-S., "Entire Domain Basis Function With Accurate Edge Condition for Rectangular Microstrip Antennas," *IEEE Antennas and Wireless Propagation Letters*, vol. 18, no. 1, pp. 123–127, Jan. 2019.

[105] D. M. Pozar, *Microwave Engineering*. Wiley, Apr. 2012.

[106] "CST Studio Suite," https://www.3ds.com/products/simulia/cst-studio-suite, Jul. 2023.

[107] "Flann Microwave | Standard Gain Horns Series 240," https://flann.com/products/antennas/standard-gain-horns-series-240/, Apr. 2018.

[108] G. E. Evans, *Antenna Measurement Techniques*. Artech House, 1990.

[109] N. Gagnon and A. Petosa, "Using Rotatable Planar Phase Shifting Surfaces to Steer a High-Gain Beam," *IEEE Transactions on Antennas and Propagation*, vol. 61, no. 6, pp. 3086–3092, Jun. 2013.

[110] X. Zhao, C. Yuan, L. Liu, S. Peng, Q. Zhang, L. Yu, and Y. Sun, "All-Metal Beam Steering Lens Antenna for High Power Microwave Applications," *IEEE Transactions on Antennas and Propagation*, vol. 65, no. 12, pp. 7340–7344, Dec. 2017.

[111] F. Caminita, C. D. Giovampaola, M. Nannetti, G. Minatti, N. Bartolomei, E. Martini, B. Byrne, G. Toso, and S. Maci, "TX/RX Terminal Based on Metascreen Technology for Ka-Band Satcom with Dual Switchable Polarization," in *2024 18th European Conference on Antennas and Propagation (EuCAP)*, Mar. 2024, pp. 1–5.

[112] R. Ozzola, "Advanced Electromagnetic Modelling of the Next Generation (XG) Wireless Communication Systems," Ph.D. dissertation, Delft University of Technology, Delft, 2024.

[113] D. Cavallo, "Parallel-Plate Waveguide-Feeding Structure for Planar-Connected Arrays," *IEEE Antennas and Wireless Propagation Letters*, vol. 21, no. 4, pp. 765–768, Apr. 2022.

[114] M. Abramowitz and I. A. Stegun, *Handbook of Mathematical Functions: With Formulas, Graphs, and Mathematical Tables*. Courier Corporation, Jan. 1965.

[115] K. J. Koh and G. M. Rebeiz, "0.13-Mm CMOS Phase Shifters for X-, Ku-, and K-Band Phased Arrays," *IEEE Journal of Solid-State Circuits*, vol. 42, no. 11, pp. 2535–2546, Nov. 2007.

[116] Q. Zheng, Z. Wang, K. Wang, G. Wang, H. Xu, L. Wang, W. Chen, M. Zhou, Z. Huang, and F. Yu, "Design and Performance of a Wideband Ka-Band 5-b MMIC Phase Shifter," *IEEE Microwave and Wireless Components Letters*, vol. 27, no. 5, pp. 482–484, May 2017.

[117] C. Liu, Q. Li, Y. Li, X. D. Deng, H. Tang, R. Wang, H. Liu, and Y.-Z. Xiong, "A Ka-Band Single-Chip SiGe BiCMOS Phased-Array Transmit/Receive Front-End," *IEEE Transactions on Microwave Theory and Techniques*, vol. 64, no. 11, pp. 3667–3677, Nov. 2016.

List of Publications

Journal Papers

J1. <u>A. J. van Katwijk</u>, A. Neto, G. Toso, and D. Cavallo, "Efficient Semi-Analytical Method for the Analysis of Large Finite Connected Slot Arrays," *IEEE Trans. Antennas Propag.*, vol. 71, no. 1, pp. 402–410, Jan. 2023.

J2. <u>A. J. van Katwijk</u>, A. Neto, G. Toso, and D. Cavallo, "On the Cross-Polarization Levels of Arrays With Wide Angle Impedance Matching Layers," *IEEE Trans. Antennas Propag.*, vol. 72, no. 6, pp. 5078–5087, May. 2024.

J3. <u>A. J. van Katwijk</u>, A. Neto, and D. Cavallo, "Efficient Analysis Method for Artificial Dielectric Layers with Vertical Metal Inclusions Based on a Full-Wave Spectral Domain Approach," *IEEE Trans. Antennas Propag.*, under review.

Conference Papers

C1. <u>A. J. van Katwijk</u> and D. Cavallo, "Analysis and Design of Connected Slot Arrays with Artificial Dielectrics," *IEEE International Symposium on Phased Array Systems & Technology (PAST 2019)*, Oct. 15–18 2019.

C2. <u>A. J. van Katwijk</u>, A. Neto, G. Toso, and D. Cavallo, "Design of Wideband Wide-Scanning Dual-Polarized Phased Array Covering Simultaneously Both the Ku- and the Ka-Satcom Bands," *Proc. 14th Eur. Conf. Antennas Propag. (EuCAP 2020)*, Copenhagen, Denmark, Mar. 15–20 2020.

C3. <u>A. J. van Katwijk</u>, A. Neto, G. Toso, and D. Cavallo, "Dual-Polarized Wide Scan Phased Array Covering Both the Ku- and the Ka-Satcom Bands," *IEEE International Symposium on Antennas and Propagation (APS 2020)*, Montréal, Québec, Canada, Jul. 5–10 2020.

C4. <u>A. J. van Katwijk</u>, A. Neto, G. Toso, and D. Cavallo, "Dual-Polarized Connected Slot Array Design for Satellite Communication," *Proc. 15th Eur. Conf. Antennas Propag. (EuCAP 2021)*, Düsseldorf, Germany, Mar. 22–26 2021.

C5. <u>A. J. van Katwijk</u>, A. Neto, G. Toso, and D. Cavallo, "Dual-Pol Wide Scan Connected Slot Array for Ku- and Ka-band Satcom with Low Cross-Polarization," *IEEE International Symposium on Antennas and Propagation (APS 2021)*, Singapore, Singapore, Dec. 4–10 2021.

C6. <u>A. J. van Katwijk</u>, A. Neto, G. Toso, and D. Cavallo, "Wideband Phased Array Design for Ku/Ka SatCom Applications," *Proc. 16th Eur. Conf. Antennas Propag. (EuCAP 2022)*, Madrid, Spain, Mar. 26–Apr. 01 2022.

C7. <u>A. J. van Katwijk</u>, A. Neto, G. Toso, and D. Cavallo, "Efficient Analysis Method for Finite Connected Arrays," *IEEE International Symposium on Antennas and Propagation (APS 2022)*, Denver, Colorado, United States, Jul. 10–15 2022.

C8. <u>A. J. van Katwijk</u>, G. Toso, and D. Cavallo, "Ku/Ka-Band Wide-Scanning Dual-Polarized Connected Slot Array with Improved Polarization Purity," *Proc. 17th Eur. Conf. Antennas Propag. (EuCAP 2023)*, Florence, Italy, Mar. 26–31 2023.

C9. <u>A. J. van Katwijk</u>, A. Neto, and D. Cavallo, "Spectral Periodic Method of Moment Analysis of Artificial Dielectrics with Vertical Metal Inclusions," *IEEE International Symposium on Antennas and Propagation (APS 2023)*, Portland, Oregon, United States, Jul. 23–28 2023.

C10. <u>A. J. van Katwijk</u>, A. Neto, and D. Cavallo, "Efficient Analysis Method for Artificial Dielectric Layers with Vertical Metal Inclusions," *Proc. 18th Eur. Conf. Antennas Propag. (EuCAP 2024)*, Glasgow, United Kingdom, Mar. 17–22 2024.

C11. <u>A. J. van Katwijk</u>, G. Toso, and D. Cavallo, "Reducing the Cross-Polarization Levels in Artificial Dielectric Layers for Wideband Arrays," *Proc. 18th Eur. Conf. Antennas Propag. (EuCAP 2024)*, Glasgow, United Kingdom, Mar. 17–22 2024.

C12. <u>A. J. van Katwijk</u>, G. Toso, and D. Cavallo, "A Ku/Ka-Band Shared Aperture Connected Array for Satcom Applications," *Proc. 19th Eur. Conf. Antennas Propag. (EuCAP 2025)*, Stockholm, Sweden, Mar. 30–Apr. 4 2024.

Theses Co-Supervised

T1. C. G. van Wamel "Reduction of Cross Polarization Level in Connected Slot Arrays using Artificial Dielectric Layers with Vertical Metallic Inclusions," M.Sc. thesis, Delft University of Technology, Delft, the Netherlands, July 2021.

T2. C. M. Coco Martin "Wideband Flat Lenses Based on Artificial Dielectric Layers," M.Sc. thesis, Delft University of Technology, Delft, the Netherlands, September 2021.

Summary

Wideband wide-scanning antenna arrays have been gaining popularity in the past decade due to their applicability in multiple fields and applications. Wideband arrays are desired due to their ability to combine multiple functions or services in a single aperture. The need for ultra-wideband capability is often paired to the ability to scan over a large conical region. Wide-scanning arrays enable tracking of multiple targets simultaneously, which can be important for radar systems or for communication systems with multiple users. Especially in satellite communication (Satcom) on-the-move applications, wideband wide-scanning array have a key advantage due to their ability to cover multiple bands in a single package while maintaining agile connections to multiple satellites. This type of array has been demonstrated using various technologies, but most of these use a costly and complex assembly process or have considerable cross-polarization (X-pol). One of the proposed concepts is the connected slot array with artificial dielectric layers (ADLs), which offers the required bandwidths and scanning ranges in a low-volume planar structure. Entire connected arrays can be fabricated on a single board using traditional printed circuit board manufacturing techniques, making them relatively low cost and low complexity.

In this work, a dual-polarized 32×32-element connected slot array utilizing ADLs is designed to cover the Ku- and Ka-transmit Satcom bands (13.75–14.5 GHz and 28–31 GHz) in a scan volume of $\pm 60°$ for all azimuths. The ADL superstrate is designed to implement a wideband Chebyshev impedance transformer from the impedance of free space to a lower impedance at the slot plane. A recent analysis technique that enables the analysis of non-periodic ADL stratifications is used to significantly reduce the number of layers required to implement this impedance transformer. Two different designs are presented. The first incorporates a perforated substrate to cover the full scan range and two separate feeding networks to feed the two orthogonal slot arrays independently. Several boards are designed for various scanning configurations. Since the first design posed problems in manufacturing due to thermal and mechanical constraints of the materials, another design is presented.

The second design is aimed at simplifying the manufacturing process. For example, the perforated substrate is omitted and a different substrate material is used to avoid issues with thermal stability. The aperture is designed to radiate circular polarization in the Ka-band using a delay line in the last part of the feeding network, so only one network is needed per board. Two prototype boards are manufactured with two different scan angles; one pointing to broadside and one pointing to 30°.

The two boards are measured in in-house near-field and far-field measurement setups. A directivity close to the theoretical maximum is observed, and the voltage standing wave ratio is below 1.6 in the two bands of interest. The axial ratio of the circular polarization closely matches simulations and is under 2.5 dB and 1.8 dB for the broadside and scanning boards, respectively. The gain of the array is 5–10 dB lower than the directivity due to significant losses in the 1-to-2048 elements feeding network.

To support the design of the arrays, an analysis method for large finite connected slot arrays is developed. The technique uses a Method of Moments (MoM) procedure in which the basis functions represent the spectra of the field that needs to be represented. The method uses one basis function per element plus two per slot together with the analytically known connected slot array Green's function to form a computationally efficient method. This enables modeling of large finite connected slot arrays in arbitrary stratifications which would be infeasible to simulate in available commercial software. The method is found to be in good agreement with commercial software when the results of smaller sample arrays are compared, with a much lower computational cost.

During the design of the superstrates, it was found that the ADLs increase the X-pol of the arrays when scanning on the diagonal plane. This work presents a study of the X-pol behavior of various superstrates in the presence of a magnetic Wheeler current sheet. The main cause of the increased X-pol is found to be in the different behavior of transverse electric and transverse magnetic plane waves in the structure, which is the result of anisotropy in the effective permittivity and permeability tensors. A novel structure is proposed that connects the patches of two layers of ADL together using a vertical pin to form a pin-patch structure. Two prototype ADLs are shown – one with and one without the pins – and the new structure is experimentally shown to reduce the X-pol by 2–5 dB.

To facilitate the use of the pin-patch structure in future antenna designs that use ADL superstrates, an analysis technique based on a MoM is developed. The technique uses entire domain basis functions to analyze the pin-patch structure in a periodic environment. The current on the structure are described using three groups of basis functions, describing a linear, loop, and radial current on the patches. The current on the pin and the radial current are described using an analogous structure consisting of circular patches. The currents on the structure and the reflection coefficients are found using this method and a commercial solver and good agreement is demonstrated with a fraction of the computation time.

Samenvatting

Breedbandige antenne-arrays met een groot gezichtsveld hebben de afgelopen tien jaar aan populariteit gewonnen vanwege hun brede toepasbaarheid. Breedbandige arrays zijn gewenst vanwege hun vermogen om meerdere functies of diensten in één antenne te combineren. De behoefte aan ultrabreedbandcapaciteit gaat vaak gepaard met de behoefte om over een groot gezichtsveld te scannen. Arrays met een breed gezichtsveld maken het gelijktijdig volgen van meerdere doelen mogelijk, wat belangrijk kan zijn voor radarsystemen of voor communicatiesystemen met meerdere gebruikers. Vooral bij toepassingen voor mobiele satellietcommunicatie (Satcom) hebben zulke antennes een belangrijk voordeel vanwege hun vermogen om meerdere banden in één antenne te dekken en tegelijkertijd flexibele verbindingen met meerdere satellieten te behouden. Dit type array is gedemonstreerd met behulp van verscheidene technologieën, maar de meeste hiervan maken gebruik van een kostbaar en complex assemblageproces of hebben een aanzienlijke kruispolarisatie (X-pol). Een van de voorgestelde concepten is de *connected slot array* met kunstmatige diëlektrische lagen (ADL's), die de vereiste bandbreedtes en scanbereiken biedt in een platte structuur met een laag volume. Volledige verbonden arrays kunnen op één bord worden gefabriceerd met behulp van traditionele productietechnieken voor printplaten, waardoor ze relatief goedkoop en weinig complex zijn.

In dit werk is een dubbel gepolariseerde 32×32-elementen connected slot array ontworpen die gebruik maakt van ADL's om de Ku- en Ka-transmissie Satcombanden te dekken (13,75–14,5 GHz en 28–31 GHz) in een scanvolume van $\pm 60°$ voor alle azimuts. Het ADL-superstraat is ontworpen als een breedbandige Chebyshev-impedantietransformator van de impedantie van de vrije ruimte naar een lagere impedantie aan de onderkant. Een recente analysetechniek die de analyse van niet-periodieke ADL-stratificaties mogelijk maakt, wordt gebruikt om het aantal lagen dat nodig is om deze impedantietransformator te implementeren aanzienlijk te verminderen. Er worden twee verschillende ontwerpen gepresenteerd. De eerste bevat een geperforeerd substraat om het volledige gezichtsveld te bestrijken en twee afzonderlijke voedingsnetwerken om de twee orthogonale slotarrays onafhankelijk van elkaar te voeden. Meerdere borden zijn ontworpen voor verschillende scanconfiguraties. Omdat het eerste ontwerp problemen opleverde bij de productie door thermische en mechanische beperkingen van de materialen, is een tweede versie ontwikkeld.

Het tweede ontwerp is gericht op het vereenvoudigen van het productieproces. Zo wordt het geperforeerde substraat weggelaten en wordt een ander substraatmateriaal

167

gebruikt om problemen met de thermische stabiliteit te voorkomen. De opening is ontworpen om circulaire polarisatie in de Ka-band uit te stralen met behulp van een vertragingslijn in het laatste deel van het voedingsnetwerk, zodat er per bord slechts één netwerk nodig is. Er worden twee prototypeborden vervaardigd met twee verschillende scanhoeken; één wijst recht omhoog en één wijst naar 30°. De twee borden worden gemeten in *in-house* nearfield- en farfield-meetopstellingen. De waargenomen directiviteit ligt dicht bij het theoretische maximum en de spanning-staande-golfverhouding ligt lager dan 1,6 in de twee relevante banden. De axiale verhouding van de circulaire polarisatie volgt de gesimuleerde waarden en is onder 2.5 dB en 1.8 dB voor de twee borden. De versterking van de array is 5–10 dB lager dan de directiviteit als gevolg van aanzienlijke verliezen in het voedingsnetwerk van 1 naar 2048 elementen.

Ter ondersteuning van het ontwerp van de arrays is een analysemethode voor grote eindige connected slot arrays ontwikkeld. De techniek maakt gebruik van een Method of Moments (MoM)-procedure waarbij de basisfuncties de spectra vertegenwoordigen van het veld dat moet worden weergegeven. De methode maakt gebruik van één basisfunctie per element plus twee per slot, samen met de analytisch bekende connected slot arrays Green's functie om een rekentechnisch efficiënte methode te vormen. Dit maakt het modelleren van grote eindige connected slot arrays in willekeurige stratificaties mogelijk, wat onhaalbaar zou zijn om te simuleren in beschikbare commerciële software. De methode geeft vrijwel dezelfde resultaten als commerciële software voor kleinere voorbeeldarrays met veel minder vereiste rekenkracht, wat betekent dat hij in staat is dit soort arrays accuraat te analyseren.

Tijdens het ontwerp van de superstraten bleek dat de ADL's de X-pol van de arrays vergroten bij het scannen op het diagonale vlak. Door te kijken naar het X-pol-gedrag van verschillende superstraten in de aanwezigheid van een magnetisch Wheeler-stroomblad wordt de belangrijkste oorzaak van de verhoogde X-pol gevonden in het verschillende gedrag van transversale elektrische en transversale magnetische vlakke golven in de structuur, wat het resultaat is van anisotropie in de effectieve permittiviteits- en permeabiliteitstensoren. Er wordt een nieuwe structuur voorgesteld die de metale patches van twee lagen ADL met elkaar verbindt met behulp van een verticale pin om een pin-patch-structuur te vormen. Er worden twee prototypes van ADL's getoond – één met en één zonder de pinnen – en experimenteel wordt aangetoond dat de nieuwe structuur de X-pol met 2–5 dB reduceert.

Om het gebruik van de pin-patch-structuur in toekomstige antenneontwerpen die ADL-superstraten gebruiken te vergemakkelijken, is een analysemethode gebaseerd op een MoM ontwikkeld. De techniek maakt gebruik van basisfuncties van het hele domein om de pin-patch-structuur in een periodieke omgeving te analyseren. De stroom op de structuur wordt beschreven met behulp van drie groepen basisfuncties, die een lineaire, lus- en radiale stroom op de patches beschrijven. De stroom op de pin en de radiale stroom worden beschreven met behulp van een analoge structuur bestaande uit cirkelvormige patches. Met behulp van deze methode worden de stromen op de structuur en de reflectiecoëfficiënten berekend en vergeleken met de resultaten uit een commerciële oplosser, waarbij een goede overeenstemming wordt aangetoond in slechts een fractie van de rekentijd.

About the Author

Alexander Jacob van Katwijk was born on June 22nd, 1992 in Takoma Park, United States of America. He received his B.Sc. and M.Sc. (cum laude) degrees in Electrical Engineering from the Delft University of Technology, Delft, the Netherlands in 2017 and 2019, respectively.

Since September 2019 he has been with the Delft University of Technology pursuing the Ph.D. degree in the Terahertz Sensing Group. During this time, his research interests included analytical/numerical techniques in electromagnetics, cross-polarization reduction techniques, and wideband connected arrays. This research has been carried out under the supervision of Prof. dr. ing. A. Neto and Dr. D. Cavallo as promotors. The research has resulted in 3 journal publications and 11 contributions at various international conferences. During his Ph.D. he has co-supervised two M.Sc. students in the Terahertz Sensing Group of the Delft University of Technology.